Mémoires de Géologie (Lausanne) No. 44, 2005

The Geology, Geochemistry and Evolution of Nisyros Volcano (Greece). Implications for the Volcanic Hazards

Edited by
Johannes C. Hunziker and Luigi Marini

IMPRIMERIE CHABLOZ S.A., LAUSANNE

ISSN 1015-357

Mémoires de Géologie (Lausanne)

Section des Sciences de la Terre
Université de Lausanne
BFSH-2, 1015 Lausanne, Suisse

44

The Geology, Geochemistry and Evolution of Nisyros Volcano (Greece). Implications for the Volcanic Hazards

Edited by

Johannes C. Hunziker and Luigi Marini

Mémoires de Géologie (Lausanne) No. 44, 2005

Table of Contents

Author’s addresses:

François Bussy: Institut de Minéralogie et Géochimie, BFSH-2, Université de Lausanne, CH-1015 Lausanne, Switzerland. Tel: +41 21 692 44 58, fax: +41 21 692 43 05. E-mail: Francois.Bussy@unil.ch

Jens Fiebig: Geologisch-Paläontologisches Institut, J.W. Goethe Universität, Senckenberganlage 32, D-60325 Frankfurt am Main, Germany. Tel: +49 69 798 23107, fax: +49 69 798 22958 E-mail: Jens.Fiebig@em.uni-frankfurt.de

Pierre Gex: Institut de Géophysique, CP-1, Université de Lausanne, CH-1015 Lausanne, Switzerland. Tel: +41 21 692 44 04, fax: +41 21 692 44 05 E-mail: Pierre.Gex@unil.ch

Jean Hernandez : Institut de Minéralogie et Géochimie, BFSH-2, Université de Lausanne, CH-1015 Lausanne, Switzerland. Tel: +41 21 692 35 01, fax: +41 21 692 43 05. E-mail: Jean.Hernandez@unil.ch

Johannes C. Hunziker: Institut de Minéralogie et Géochimie, BFSH-2, Université de Lausanne, CH-1015 Lausanne, Switzerland. Tel: +41 21 692 43 65, fax: +41 21 692 43 05. E-mail: Johannes.Hunziker@unil.ch

Luigi Marini: Laboratorio di Geochimica, Dip.Te.Ris., Università di Genova, Corso Europa 26, I-16132 Genova, Italy. Tel: + 39-010-3538307, fax: +39-010-352169. E-mail: lmarini@dipteris.unige.it

Claudia Principe: Istituto di Geoscienze e Georisorse, Area della Ricerca CNR-Pisa San Cataldo Via G. Moruzzi 1, I-56124 (Pisa), Italy. Tel: + 39-050-3152335, fax: +39-050-3152360. E-mail: c.principe@igg.cnr.it

Loÿc Vanderkluysen: SOEST, Geology & Geophysics Dept., VGP, POST room #606, 1680 East-West Road, Honolulu, HI 96822, USA. Tel: +1 808 956 2581, fax: +1 808 956 5512. E-mail: loyc@hawaii.edu

Marino Vetuschi Zuccolini: Laboratorio di Geochimica, Dip.Te.Ris., Università di Genova, Corso Europa 26, I-16132 Genova, Italy. Tel: + 39-010-3538136, fax: +39-010-352169. E-mail: zucco@dipteris.unige.it

Alain C. M. Volentik: Department of Geology, SCA 528, University of South Florida, 4202, E. Fowler Ave., Tampa, FL 33647, USA. Tel: +1 813 974 8756. E-mail: avolenti@mail.usf.edu

1. Introduction

Compared to Kos, Nisyros is a very small island, how is it possible there is something interesting in that isle? ... This was thinking one of us (LM) when he was approaching Nisyros for the first time on a small boat together with the late Prof. Giorgio Marinelli. He was full professor at the University of Pisa, from 1961 to 1992; very good teacher and very bright scientist, he promoted and led several research projects on volcanology and geothermics both in Italy and abroad, including several areas along the South Aegean volcanic arc. At that time, in the '80s, Nisyros island was the site of a geothermal exploration project aimed to generate electricity. Indeed, based on the positive indications gathered through suitable surface surveys carried out by the Institute of Geological and Mineral Exploration (IGME), under the supervision of Giorgio Marinelli, the Greek Energy Authority (PPC) decided to drill two deep geothermal wells in the southern Lakkì plain of Nisyros, near the area of the hydrothermal craters. Actually, Giorgio Marinelli was aware of the high geothermal potential of Nisyros and he also understood the dynamics of the hydrothermal eruptions that occurred in this geologically fascinating place.

After some researches carried out in the early '90s on the hydrothermal eruptions and on the chemistry of fumarolic effluents and thermal waters, we decided to work together on fluid geochemistry, enriching this subject with stable isotope geochemistry and measurements of CO_2 fluxes from soil and soil temperatures in the area of the hydrothermal craters. These researches were brillianty carried out first by Tatjana Brombach, in the framework of her PhD Thesis and afterwards by Jens Fiebig as part of his post-doctoral stage both at Lausanne University.

During one of the field visits together with Claudia Principe, it became evident that knowledge of Nisyros geology was far from satisfactory. First, all the previous geological maps were prepared on a merely geolithological basis. Second, the reconstruction of tephra stratigraphy and facies analysis was uncomplete. Therefore, we charged two students of Lausanne University, Loÿc Vanderkluysen and Alain Volentik, with geological mapping and related volcanological studies under the supervision of both Claudia Principe, IGG-CNR, Pisa and one of us (JCH). This work attracted more students and we ended the work with seven persons in the field.

A further weak point in the geological work previously performed on Nisyros were the scarce and not very conclusive age determinations, so that a further PhD Thesis was assigned to Annett Büttner under the supervision of Igor Villa, University of Bern. Unfortunately, we had to find out that their investigations were not adequate for elucidating the geochronology of Nisyros volcanic rocks, which is a subject deserving further careful studies.

In 1999 we started, as a full member of the European three-year project GEOWARN (Geo-spatial warning systems Nisyros volcano [Greece]. An emergency case study. IST-12310), a collaboration of Greek, German, Italian and Swiss geoscientists. As work with Lausanne students had started two years prior to GEOWARN outlasting this european project, and mapping, geochemistry of rocks and minerals, and geochronology were not included and financed by the GEOWARN project, we decided to assemble all these data in the present volume of the Mémoires de Géologie (Lausanne). Partially the results have been published in different journals but the huge amount of data backing these results merit a proper documentation in this synthesis.

The major result of volcanological investigations is a new geological map in the 1:12,500 scale, which represents the pivotal subject of this monography. Thirty-six stratigraphic units were defined, including 9 pyroclastic sequences, 16 lava flow units, 7 epiclastic units, 2 lacustrine deposits, as well as 1 debris avalanche deposit, on the basis of their physical characters, the stratigraphic position of each deposit and the presence of discontinuities, erosional surfaces, palaeosoils and epiclastic deposits within the reconstructed stratigraphic sequence. In contrast to previous maps, this new geological map is based on the use of Unconformity Bounded Stratigraphic Units (UBSU) in compliance with the guidelines of the International Subcommission on Stratigraphic Classification. UBSU are separated by discontinuities in the stratigraphic succession, which emphasise the major breaks in the evolution of the volcano and its spatial and temporal geometry. This approach greatly improves the understanding of the geological history of the island and highlights changes in the eruptive styles as well as the localisation of the volcanic centres through time. These topics are exhaustively discussed in chapters 2 and 3.

Further results of the volcanological investigations concerning tectonic and volcano-tectonic and petrology and rock geochemistry are presented in chapters 4 and 5, respectively, whereas the reconstructed eruptive history of Nisyros is dealt with in chapter 6. All together chapters 2 to 6 constitute the first part of the monography, which is devoted to the geological history of Nisyros volcano.

The second part of the monography has an applied component, namely the mitigation of the volcanic hazard both for the permanent residents of the island and for the annually over 50,000 visiting tourists mostly without awareness of the entire risk situation. It presents the results of a geophysical surveys (chapter 7) and of several geochemical studies (chapters 8, 9, and 10) which were carried out during the last fifteen years. Indeed, an impulse in geochemical investigations occurred during and after the increase in activity that took place in 1995-1998 comprising intense seismicity, with earthquakes of magnitude between 4.1 to 5.5 on the Richter scale, ground deformations, as well as remarkable variations in the chemistry of fumarolic effluents. In spite of these considerable efforts of the scientific community that led to the publication of several papers, a thorough review and synthesis of the existing geochemical information was still lacking. Chapter 9 is aimed to fill this gap. The need for the stochastic approach in the evaluation of the fluxes of CO_2 from soil and the total output of carbon dioxide is emphasized in chapter 8, thanks to the contribution of Marino Vetuschi Zuccolini, the first who understood the importance of this geostatistical technique, in spite of what other people claim. Chapter 10 is devoted to evaluate the timing of argillic alteration and advanced argillic alteration by using reaction path modeling and to infer possible consequences for debris avalanches induced by flank collapse and hydrothermal eruptions. Finally, the implications for mitigating the volcanic hazard at Nisyros drawn from all the geological, geophysical, and geochemical data presented and reviewed in this monography are discussed in Chapter 11.

We hope that our work may be of help for the people who live on this Earthly Paradise or just spend some time there. We would like to thank the population of Nisyros for their warm hospitality, that always turned our field seasons into wonderful experiences. Special thanks are due to Roberto Cioni of IGG-CNR, Pisa and Roberto Moretti of OV-INGV, Napoli for laboratory chemical analyses and field assistance, respectively. The internationally composed GEOWARN group contributed to the success of our work, many fruitful discussions helped to clear our views on our proper work and also helped with many important details. Last but not least we sincerely thank Lorenz Hurni, who allowed us to use the topographic map as base of our geology.

Johannes C. Hunziker and Luigi Marini

Lausanne, 10 October 2005

2. Explanatory notes on the "Geological Map of Nisyros Volcano (Greece)"

Alain C. M. Volentik(1), **Claudia Principe**(2),
Loÿc Vanderkluysen(1), **Johannes C. Hunziker**(1)

(1) Institut de Minéralogie et Géochimie, BFSH-2, Université, CH-1015 Lausanne, Switzerland.

(2) Istituto di Geoscienze e Georisorse, Area della Ricerca CNR-Pisa San Cataldo Via G. Moruzzi 1, I-56124 (Pisa), Italy.

Abstract - The stratigraphy proposed in the new 1:12,500 map of Nisyros consists of a succession of lavas, tephra, deposits of hydrothermal explosions, lacustrine beds, and epiclastites that have been grouped in 36 cartographic units, for a total of 8 synthems and 6 sub-synthems, on the basis of the definition of Unconformity Bounded Stratigraphic Units (UBSU), as given by the International Subcommission on Stratigraphic Classification (Salvador, 1987). Owing to the scarcity of available absolute age determinations for Nisyros rocks, the division in UBSU is especially important, since it outlines the discontinuities representing the end of phases of activity and important changes in the island's morphology. In particular, it emphasises the clustering in time of the volcanic activity and links volcanic eruptions to main geological events revealed by epiclastic deposits, erosional discontinuities, and lacustrine sediments.

2.1. Morphological outline

Nisyros is located at the easternmost end of the Aegean volcanic arc, in the Dodecanese archipelago between the islands of Kos and Tilos (Fig. 2.1-A) (Mercator 36°35' N, 27°10' E; UTM 514900 E, 4048600 N, zone 35 S). The island is almost circular in shape, with an average diameter of 8 km and covers an area of about 42 km^2. Culminating at 698 m a.s.l., it rests on a basement of Mesozoic limestone (Geotermica Italiana, 1983 & 1984; Varekamp, 1993) and a thinned crust, with the Moho discontinuity located at a depth of about 27 km (Makris & Stobbe, 1984). The main morphological feature of Nisyros is the circular 4-km-diameter caldera depression (Fig. 2.1-B, C), whose western portion is filled by a number of domes. These likely constitute the youngest magmatic event on Nisyros. The Lakkì plain, which occupies the remaining third of the caldera floor, has been the scene of intense hydrothermal activity in historic times. The related hydrothermal craters are the main touristic attraction of Nisyros, with a flux of 200 to 1000 visitors per day between May and September. The chief town in the island is the little village of Mandraki (that in ancient Greek means a place closed and protected, that is not necessarily an harbour), on the NW coin of the island (Fig. 2.1-B). The other inhabited villages are Palì, Nikià and Emboriò (Fig. 2.1-B). To be mentioned also the Loutrà thermae on the coast between Mandraki and Palì, and the small abandoned arbour of Avlaki, on the southern coast (Fig. 2.1-B).

2.2. Historical excursus on the cartography of Nisyros from ancient times to the Italian presence

According to the Greek myths (as referred by *Strabo*, into *Geographia*, lib. X, chap. V, and in the *Library,* attributed to *Apollodorus* from Athens, I century B.C.) the formation of Nisyros (named *Porphyris* in very ancient times, that is an intriguing name for geologists) took place as a consequence of the battle between Gods and Giants. Poseidon (the God of sea), after defeating the Giant Polybotes, caught him up, near Kos. With his trident, Poseidon broke off a piece of the western portion of Kos and hurled it at the giant. The piece of land pinned Polybotes down. Nisyros was born. Lying underneath Nisyros as he does, Polybotes sometimes sighs and groans, generating earthquakes and volcanic phenomena. From this description it can be supposed that the dismembering of the Kos island is a mythological memory of the important caldera collapse that followed to the Kos Plateau Tuff (KPT) eruption at about 161 ka ago (Allen & Cas, 2001), by far the most important eruption on this volcanic zone. This account highlights the common volcanic origin of Nisyros and of the western portion of the

Kos Island. As a matter of fact, a similar derivation from the war from Gods and Giants has been postulated for a number of other Mediterranean volcanoes, including Etna in Sicily.

After late Latin times, Italian people coming from Venice are known to have had commercial trades into the Dodecanese Islands (also named Southern Sporades) starting at least from the XI century. In 1082 they established a commercial station in Rhodes. During the XIII century Nisyros has been dominated by Genoa, that in 1309 sold the island to the Order of the Knights of Saint John from Jerusalem.

Even if the Nisyros thermae were well known and publicized from the times of Hippocrates from Kos (the father of medicine), the first detailed description, with the first rudimentary maps, we have of Nisyros Island is into the "*Librum Insularum Archipelagi*" published by Cristoforo Bondelmonti, from Florence, in 1420 (Fig. 2.2-A). However, his mention of the passage from Nisyros of Cleopatra and Antonius testifies that actually Bondelmonti description refers to information extracted from previous Latin texts[1]. This text describes hydrothermal activity occurring inside the caldera depression, more intense than nowadays, with frequent hydrothermal explosions and significantly higher soil temperatures and fumarole temperatures, leading to abundant sulphur deposition and production. Small sulphur flows were emitted inside an area which seems to coincide with the present hydrothermally altered Lofos Dome (Fig. 2.3). The hydrothermal crater of Polyvotis hosted a little lake which lead to the formation of varved lacustrine deposits, which today are covered by the 1873 debris flow deposits (Marini et al., 1993 and Fig. 2.27-C).

No new information related to Nisyros is reported into the "*Geografia*" of Francesco Boringhieri (1480) and into the"*Isolario*" of Bartolomeo Zamberli (1485). Then, after a famous siege, in 1523 Nisyros passed to the Turkish domination and the Knights of Saint John moved to Malta to give origin to the more famous Order of the Malta Knights. We have very few news on Nisyros for all the four-century-long period of the Turkish domination. The only notable source dates to the late Turkish times and consists in the map (Fig. 2.2-B) and related description[2] by the archaeologist Ludwig Ross who visited Nisyros on 9-11 August 1841 (Ross, 1843). The Turkish domination on the fifteen Dodecanese islands ended with the military occupation by the Italians. On May 12th 1912 the

---

[1] *Hic Flaminius, consul, rediens de partibus Orienti set accedens pugnaturus contra Gallos, auguratus est victoriam obtenire, et sic factum in luce resolvit. Itaque insula haec semper benevola Romanis habita est. Per hanc etiam transiens Cleopatra cum Antonio, et nolentes cives praeceptis ipsorum obedire, totam insulam delevere. Et XVIII cir. Mi. et quinque videntur oppida, quorum duo principaliora apparent Mandrachi et Palaeocastro, et Pandenichi, Nicea et Argos sunt in circuitu. Circa medium mons erigitur altissimus, quo in summitate per subterraneos meatus sulphureus ignis die ac nocte eructat in altum, ut in insula Strongili apud Liparum habetur. In descensu vero montis, ad iactum lapidis, fons calidissimus emanat in imum, et in plano circa lacum profundissimumque obscurum aquae descendunt ; ibique colentes quantitatem maximam sulphuris mercatoribus praeparant. Et quia in tantum viget intensitas caloris, de medio usque verticem nullus est ausus sine sotularibus accedere ligneis. Est etenim hic tanta foecunditas ficuum, quod in anno naves onerantur parvae. Ad trionem in pede montis, contigua maris, spelunca consistit, ad quam circustantes, doloribus oppressi, accedunt et, diu morati, in patriam incolumes revertuntur. Et quia cava, ut praesumitur, haec insula habetur, saepe saepius tot et tanta terraemota ubique regnant, quod forenses ob hoc perterriti, locum, cito maledicentes, derelinquunt, et procul accedere gaudent. Colentes vero tale sterminium pro nihilo reputant et in eo non advertere curant."*

"Here [in Nisyros], Flaminius consul, coming back from Orient has been predicted to win in the coming fighting against Galics, as actually happened. For this reason the island has been always considered of good omen by Latin people. Also Cleopatra and Antonius passed by Nisyros and razed to the ground the island as its inhabitants refused to obey their orders. The island is eighteen miles in circumference and there are five towns to be seen there: Mandrachi and Paleocastro are the largest, Pandenichi, Nicea and Argos are found elsewhere around the island. In the centre of the island there is a very high mountain which belches out sulfur fire from underground passages day and night, as it happens in the island of Stromboli, near Lipari. Just a stone's throw down from the summit there is a hot spring whose waters descend into a hidden deep lake on the plain below. The islanders gather the sulfur in great amounts and sell it to passing traders. From half way up the mountain to its summit, heat is so intense that no one dares to ascend without wooden shoes. The island produces abundant figs, too many each year for the passing ships to carry them away. In the northern portion of the island there is a cave, in which sick people reside until they go back home recovered. Because people think that in this island there are a lot of underground caves, very often there are so many and so strong earthquakes that foreign people gladly go away damning. In contrast, the inhabitants consider this rumour nothing and do not care of it. [*translation from latin by Clara Ardu Principe*].

[2] We synthesize here the Ross description of Mandraki and Loutrà thermal area (as reported in Martelli, 1917) that look a little bit different than in present times: "At Bondelmonti times [XVI century] inside Paleokastro walls there was a village. Nowadays all this place is occupied by vineyards and figs and almonds trees. A thermal spring [Loutrà spa] is present at a walking distance of half an hour East of Mandraki, which is the main village and arbour of the island. To reach the spa, we pass through a plain land that twenty years ago was a swampy region, and has been reclaimed for the construction of a little pier [that still exists]. This because the ancient arbour, named by Strabo, has been progressively filled by sediments during the past two millennia. Near the spa, at distances of some hundred steps [ancient unit of measurement of distance, corresponding to ~170-190 cm] in all places you dig, salt and 'spicy' waters pour out, used by women for washing. In past times a number of strong earthquakes took place but since 30 years ago they diminished both for intensity and frequency".

Italian "*Reali Carabinieri*" disembarked from the "*Regia Nave Roma*" to get hold of the island. At that time, Nisyros (then Italianized in *Nisiro*) was populated by 4300 inhabitants versus the 916 residents of nowadays[3]. Following the Lausanne treatise, the "*Regio Decreto n. 1854*" in 1925 assigned the Italian nationality to all the inhabitants of the Dodecanese, that became a portion of Italy until the German occupation, during the Second World War. Only the 28th October 1947, Nisyros finally became part of Greece.

After the Turkish domination, the Italian presence represented a moment of intense development, with the construction of new roads and public edifices as well as new spaces for agriculture by means of land terraces, water reservoirs for irrigation, etc. For all these works a detailed cartographic and geological knowledge of the territory was needed.

With the exception of some small-scale nautical charts, with some details along the coasts but none inland, which were produced by the Hydrographic Office of the Admiralty in London during the XIX century (e.g., the map: "The Island of Kos, Niseros and Piscopia", scale 1:116,000, compiled by Graves and Bacon in 1841 and revised by Spratt in 1863, edited in 1848 and 1890, respectively), no detailed maps of the Dodecanese archipelago was available at that time, even for the major island of Rhodes. It is during the first years of the Italian presence that cartographers of the Istituto Geografico Militare (IGM) and Istituto Idrografico della Marina (IIM) (Traversi, 1965) performed a systematic field work on all the Dodecanese islands. One of the best cartographic results obtained during these years is the topographic map of Rhodes at the 1:50,000 scale, whose 4 sheets were printed in 1927. It was based on a detailed survey performed during 1922-24 at the 1:20,000 scale, and originally printed in 21 sheets at the 1:25,000 scale. In 1929, Captain Aiello Rosetto carried out a topographic survey of Nisyros at 1:20,000, which led to the preparation of the 1:25,000 map printed by IGM in the same year. A relief model of Nisyros at the 1:10,000 scale was also produced and, last but not least, a nautical map of Nisyros and the neighbouring islands prepared in 1933 and printed in 1939 ("*Carta nautica di Nisiro e delle isole minori*"), comparable to the present digital and 3-D maps.

2.3. The new 1:12,500 geological map

At the same time, geographic and geological surveys of Nisyros were performed by Italian geologists, namely Alessandro Martelli in 1917 (Fig. 2.3) and Ardito Desio during his stay in Dodecanese from 1922 to 1924 (Desio, 1931).

After these pioneering works, in modern times, the geology of Nisyros was studied in detail by Di Paola (1974), who produced a geo-lithological map at the scale 1:10,000, and, more recently, by Papanikolaou et al. (1991) and Vougiukalakis (1993). The geological map of Nisyros at the scale 1:12,500 we present in this monography derives from a completely new geological survey, performed between 1999 and 2003 at the 1:10,000 scale and focused on the use of the *Unconformity Bounded Stratigraphic Units* (UBSU). As topographic base we used the new digital topographic map at the 1:10,000 scale produced in 2001 by the Institute of Cartography of the Swiss Federal Institute of Technology (ETH), Zürich, to which we added some elements as toponyms and elevations of contour lines.

2.3.1. Unconformity Bounded Stratigraphic Units (UBSU)

We applied the Unconformity Bounded Stratigraphic Units (UBSU) criteria to group stratigraphic units into hierarchically more important entities, following the recommendations of the International Subcommission on Stratigraphic Classification (Salvador, 1987).

An unconformity-bounded unit is a body of rock bounded above and below by clearly evident discontinuities in the stratigraphic succession.

This implies that in defining a UBSU unit, neither the lithological character of the rocks that compose the unit nor the time span it represents enter into its definition and recognition. In the volcanic environment, this means that the presence of bedding planes between each depositional unit is not by itself a valid criterion for subdividing such a sequence in UBSU and neither is the occurrence of palaeosoils. The hierarchy for the UBSU is based on the structural angularity, the time span of the stratigraphic hiatus represented by the discontinuity, and the geographical extension of the discontinuity, three criteria often independent of one another (Salvador, 1987).

Other kinds of stratigraphic units are frequently used in volcanic areas. One example is the "eruptive

---

[3] According to a Turkish census, the number of inhabitants of the whole Dodecanese was about 100,000 in 1890. The inhabitants became 150,000 in the Greek census dated 1912, and were 103,169 in the Italian census of 1922. In 1927 this population attained 118,000 units. 78% of these were Greeks of orthodox religion and the others were Turkish people (Muslims), Jewish people (from Spain), and Italians of catholic religion (Treccani enc.).

unit" that groups all the deposits attributed to the same eruption or eruptive phase (De Rita et al., 1998; 2000). However, this unit typology requires an interpretation of the observed stratigraphic relationships. Unconformity bounded units, in contrast, entail no such genetic or causal interpretation. They are "objective, non-interpretative units" and for these reasons the strict application of the UBSU concepts results in a clearer and more pragmatic approach to stratigraphic analysis and in a better, more descriptive and more lucid interpretation of geologic history (Salvador, 1987).

For these reasons, the UBSU classification has been adopted in cartographic projects, such as the new geological map of Italy at the scale 1:50,000 (Commissione CNR, 1992).

2.3.2. Stratigraphic units

Here we present the new complete stratigraphic sequence of the volcanic deposits cropping out on Nisyros Island. By means of the UBSU criteria the whole stratigraphic sequence has been subdivided into 8 synthems and 6 sub-synthems (Fig. 2.1-C). Figure 2.4 summarizes the main characters of the synthematic boundaries we identified in the Nisyros' stratigraphic succession. These discontinuities are due to volcanic, volcano-tectonic, and purely tectonic accidents, such as the formation of a caldera depression and its filling by means of lacustrine sediments, the occurrence of a debris avalanche and the related sector collapse of the volcanic edifice, the effects of the activation of a tectonic trend, that in at least one case has been able to induce the enlargement of the pre-existing caldera morphology and the redoubling of a large portion of the stratigraphy of the caldera walls. In some cases, epiclastic deposits were used for subdividing two synthems, i.e. when epiclastics (because of their composition and distribution, and independent of their thickness) are clearly indicative of an important morphological reorganisation of the hydrological pattern of the whole island.

The facies analysis of the volcanic deposits and the identification of eruptive units led to the definition of finer subdivisions within each UBSU, resulting in a total of 36 stratigraphic units. This larger number of stratigraphic units in comparison with previous works (Di Paola, 1974; Papanikolaou et al., 1991; St. Seymour & Vlassopoulos, 1992; Vougioukalakis, 1993; Francalanci et al., 1995) derives essentially from the particular attention that has been devoted to the study of tephra deposited between lava flows and used as stratigraphic markers (Volentik et al., 2002).

The main features of the 36 units that compose the stratigraphy of Nisyros are summarised in Table 3.1, while our stratigraphic succession is depicted in Fig. 3.1. Chemical names in the following text are derived from the classificative TAS diagram of Fig. 5.2 (Vanderkluysen et al.(a), this volume). While Table 5.4 (Vanderkluysen et al.(a), this volume) and Fig.3.10 (Volentik et al.(b), this volume) summarise the main mineralogical components for each unit and the lithics content respectively.

Kanafià synthem

ho$_a$ - This unit has already been recognised by many authors as the lowest one in the stratigraphic succession of the island. It is made of basalt-andesitic pillow lavas and hyaloclastites, cropping out along the north-western coast of the island. The most representative outcrop is located below the Monastery of Aghios Spiliani (Fig. 2.5), and the maximum thickness of this unit is 40-50 m.

ho$_j$ - This epiclastic deposit reworks the material of **ho**$_a$ in an aqueous medium (stream or river). It only occurs along the north-western coast of Nisyros and is interbedded within **ho**$_a$. This interbedding is ascribable to episodes of emersion likely due to tectonic activity (see Vanderkluysen (b) et al , this volume). The deposit is 5-10 m thick and in places intensely affected by hydrothermal alteration, along N030°-trending faults.

Kremastò synthem

lf^1 - The only outcrops of this basalt-andesitic lava flow are found below the road, at the bottom of the north-eastern caldera wall and are 35 m in thickness. N070°-trending dykes feeding the overlying lava flows (**lf**^{2} and **lf**^{5}) cut the unit. The lava flow appears to be strongly tectonised. As previously recognised by Volentik et al. (2002), this unit is the lowest outcropping unit along the caldera walls but, in our opinion, there is no evidence supporting a relation between this unit and the **ho**$_a$ pillow lavas, as proposed by Papanikolaou et al. (1991).

ka (Lakkì A pyroclastics) - This unit marks the first explosive aerial event recorded in the volcanic succession. A 3.5-m-thick fall deposit is found at the base. It is overlain by flow (Fig. 2.6-A) and surge units, and a final lapilli fallout (Fig. 2.6-B). The magmatic fraction is black, poorly vesiculated, crystal-poor, and basalt-andesitic in composition. The maximum thickness of this unit is 30 m, along the northern caldera walls, representing the only place where this unit crops out. Lithics consist of andesite fragments only, either unaltered or affected by argillic alteration.

lf^2 - It consists of an andesitic lava flow with a maximum thickness of 40 m, limited to the north-eastern part of the caldera. It is cut by dykes (N070°-trending) that feed the **lf5** lava flow.

kb (Lakkì B pyroclastics) - We attribute this explosive unit to the same eruptive cycle of **ka**, because of their similar mineralogy, chemical composition, vesiculation, eruptive facies, and because of the lack of discontinuities between **ka**, **lf**^{2} and **kb**. The base comprises a 5-m-thick surge deposit, followed by a 40 cm lapilli fall deposit, a thick (about 20 m) and massive pyroclastic flow deposit, a 3-m-thick coarse-grained surge deposit, which is overlain by a final thick (about 30 m) and massive pyroclastic flow deposit (Fig. 2.6-C). This unit crops out in two different locations along the caldera cliffs, but the most representative outcrop is located south of the neck feeding the Nikià lavas (**nlf**; [N.] on Fig. 2.1-B). The entire deposit reaches about 60 m in thickness. Lithic fragments are similar to those of the Lakkì A (**ka**) deposits.

Katò Lakkì synthem

First lake sub-synthem

fl$_l$ (Lacustrine deposits) - This unit is made up of lacustrine varved deposits with a dominant volcanic contribution, accompanied by a few intercalations of black, manganese-rich layers (Fig. 2.7-A & B). Their detailed stratigraphy has been described in Volentik et al. (2002).

lf^3 - These basalt-andesitic lavas were emplaced above the **fl**$_l$ lacustrine beds, resulting in load cast structures within these water-saturated sediments. They are found along the north-eastern caldera walls.

Second lake sub-synthem

sl$_l$ (Lacustrine deposits) - After **lf**^{3}, lacustrine sedimentation resumes in a manner similar to that of **fl**$_l$ and ends with the deposition of a lapilli fallout and fine surges (Fig. 2.7-C). These beds are limited in their lateral extension to the north-eastern portion of the caldera.

lf^4 (scoria-rich lava) - This unit, with a maximum thickness of 70 m, along the cliffs below Emboriò, comprises several basalt-andesitic lava flows with scoriaceous base and top. This stratigraphic unit is ubiquitous along the caldera walls.

ms (Melisserì pyroclastics) - This andesitic pyroclastic unit is found throughout the island, and displays its most proximal facies along the northern caldera wall. It is characterised by pinkish red pumices and scoriae and displays a fallout level at its base (Fig. 2.8-A), followed in the most proximal section by a 30-m-thick pyroclastic flow deposit (Fig. 2.8-B), and finally a 3.5-m-thick succession of fall, surges, and pyroclastic flows. Pyroclastic flow deposits with a maximum thickness of 5 m displaying distinct lower vesicularity, larger vesicle size and higher porphyric index of the magmatic fraction have been found locally below the main pyroclastic flows of the Melisserì eruption (Evangelistra sub-unit).

Lies synthem

Afionas sub-synthem

ms$_j$ - This unit reworks the Melisserì and Evangelistra sequence (**ms**), typically depositing 1 to 2 m of epiclastites. It can be found below the village of Emboriò and along the caldera road.

lf^5 - This andesitic lava flow extends all the way around the caldera, in an almost complete stratigraphic continuity. Representative outcrops are located near the road on the north-eastern side of the caldera and in general in the north-eastern part of Nisyros.

xlf$_b$ (enclave-rich lava) - This lava flow (Fig. 2.9) has the peculiarity of incorporating up to 30% of enclaves, mainly andesitic blebs of various colours, ranging from red to dark grey, which appear in relief compared to the erosion surface, which make it an excellent stratigraphic marker. It is found throughout the northern portion of the caldera cliffs, from Emboriò up to the neighbourhood of Nikià as well as along the road to the volcano, below Emboriò and in a deep valley between the Lies beach and the military tower of control ([M. T.] in Fig. 2.1-B). Its most illustrative outcrop is located just above the road upon entering the caldera from Mandraki.

lf^6 - An andesitic lava flow with a thick base of red scoriae. It is found mainly in the northern part of the caldera and in the north-eastern part of the entire island (Fig. 2.10). Together **lf**^{5}, **xlf**$_b$ and **lf**^{6} constitute a widespread lava sequence that we will refer to as the Ellinika lavas.

sv (Stàvros pyroclastics) - The main characteristic of this basalt-andesitic unit is its base, which is made up of surge beds of grey lapilli. It is followed by pyroclastic flows and surges, with a substantial dominance of the latter. Fresh andesitic fragments are found as lithics, in particular in the flow deposits. Its thickest section (30 m) is exposed below the Monastery of Stàvros, along the southern wall of the caldera. This unit becomes substantially thinner northwards, until it totally disappears North of Nikià.

alf (Argos lava flows) - In terms of volume, this unit is dominantly represented by lava flows and domes and by minor associated block and ash flow deposits. The lava flow is a dark grey rhyolitic lava, which sometimes presents reddish banding and perlitic textures (Fig. 2.11-A & B). The thickest sections are found in the southern sector of the caldera, where a neck of Argos lava crops out ([A.] in Fig. 2.1-B). This unit can be found all around the southern flanks of Nisyros, from Avlaki to Lefkos Cove.

$\mathbf{lf^7}$ - This light grey dacitic lava flow is found in only one location on the island, between the beaches of Lies and Pahia Ammos. Its thickness does not exceed 10 m.

pa (Pahia Ammos Tuff cones) - This unit is mainly composed of light grey surge deposits (Fig. 2.12-A), with impact sags, pisolitic ashes, proximal andesite to dacite fallout deposits and minor pyroclastic flow deposits, with a number of intercalated palaeosoils. In the proximal fallout deposits, lithics are common and include fresh andesitic lavas, limestones, marbles, skarns and magmatic cumulates. The maximum thickness of this unit is about 80 m and its deposits can be found between the beaches of Lies and Pahia Ammos (Fig. 2.12-B), along the eastern shore of Nisyros. Keller et al. (1990) and Innocenti et al. (2002) defined a detailed stratigraphy of this unit. We have also attributed to this unit some hydrothermally altered outcrops on the western shore of Nisyros.

Xolante sub-synthem

$\mathbf{pa_j}$ - This unit is made up of reworked material of **pa** and is composed of debris flow and hyper-concentrated flow deposits. They show flow structures, channel and pinch out structures, typical of a deposition in a stream-like environment. These deposits are found above **pa** in the lowest topographic levels of the eastern part of Nisyros (Fig. 2.13).

$\mathbf{vs_n}$ - This unit is composed of a basalt-andesitic fallout deposit (possibly resulting from a violent strombolian eruption), showing proximal characteristics (high thickness and poor sorting) near the caldera rim. Its thickness decreases quickly along the slopes of the volcano moving towards the sea, where it presents a good sorting. The most representative outcrops are located on the top of the tuff cones in the area between the Monastery of Panagia Kyra and the beach of Lies (Fig. 2.14). This deposit is about 3-m-thick on the caldera rim, and about 1.5-m-thick in the area of the Monastery of Panagia Kyra. Note that this unit is not indicated in the geological map owing to its limited thickness and the small numbers of places where it crops out.

xo - This basalt-andesitic pyroclastic unit is composed of four different deposit types vented from a number of strombolian cones distributed at this stratigraphic level all around the island (see chapter 7a). $\mathbf{xo_{n1}}$ is a red scoriae fallout deposit (Fig. 2.15) with proximal characteristics (spatter cone facies with agglutinated fragments of fresh lava); $\mathbf{xo_{n2}}$ is a black scoriae fallout deposit resulting from the same eruptive activity, but representing the most distal facies (strombolian cone facies); $\mathbf{xo_h}$ is a facies of planar bedded surge deposits; $\mathbf{xo_c}$ is a facies of pyroclastic flow deposits, in particular, a violet pyroclastic flow deposit (basalt-andesitic in composition) including pockets of red scoriae spatter cone fragments (up to 2 m), with a strong erosive contact at its base. No lithics were found in the red scoriae horizons. In contrast, the scoria cone deposits contain abundant lithics, such as fresh andesitic lavas, limestones, marbles and magmatic cumulates. Lithics fragments in the pyroclastic flows are composed essentially of Argos lava fragments. Usually, the thickness of $\mathbf{xo_{n1}}$ and $\mathbf{xo_{n2}}$ together does not exceed 10-15 m, whereas $\mathbf{xo_c}$ reaches a maximum thickness of 5-7 m in valleys. The extension of $\mathbf{xo_{n1}}$ and $\mathbf{xo_{n2}}$ is limited to the area around the vents.

$\mathbf{lf^8}$ - This unit is related to the previous one, in that it is composed of several basalt-andesitic lava flows flowing out of the **xo** spatter cones and scoria cones and interposed to the **xo** deposits. This unit does not exceed 5-10 m in thickness and occurs at the same location as the related explosive deposits, namely Aghia Irini, the Monastery of Stàvros and Avlaki.

Fournià synthem

$\mathbf{pc_j}$ (Paleocastro epiclastic deposits) - This unit is composed of epiclastic deposits, both proximal debris flow deposits and more distal hyper-concentrated flow deposits, related to a period of rest in volcanic activity, during which intense erosion, reworking, and re-sedimentation of the previous volcanic deposits occurred. Flow structures, load casts, channels, and pinch out structures are common. This unit reaches a thickness of 15-20 m in palaeo-valleys, such as in the area of Kàrdia, and shows a remarkable extent throughout the island (Fig. 2.16).

blf (Aghia Basilei lava flows) - These basalt-andesitic to andesitic lava flows, with a thick red scoriae base and top, directly overlay the previous epiclastic deposits (**pc**$_{j}$) (Fig. 2.16 & 2.17). In some places, agglutinated red scoriae deposits suggest the proximity of the volcanic vent (for instance on the western part of the caldera walls or on the western flanks of the volcano). The maximum thickness of this lava flow succession is 20-25 m in the western part of the caldera cliffs. This unit is chiefly located on the western flanks of the volcano, from Mandraki to the valley of Kàrdia.

emb (Emboriò lava domes) - This unit can be found all along the northern part of Nisyros volcano (Fig. 2.18), from the castle of Paleocastro (above Mandraki) to Emboriò. The dominant facies of this unit is a typically light grey dacite that includes 1-2% of andesitic enclaves. This unit consists of characteristic lava domes and associated dome collapse pyroclastic deposits (block and ash flows) of the same juvenile composition. Currently, the best exposed dome is the 150-m-high hill of Akimaronas, which dominates the village of Emboriò ([Ak.] in Fig. 2.1).

Kàrdia synthem

Loutrà sub-synthem

vu$_{l}$ (Vunàri debris avalanche deposits) - This unit is composed of a deposit characterised by rounded blocks (ranging from less than 1 cm^3 to more than 1 m^3 and showing jigsaw fractures) within a fine matrix (Fig. 2.19). The blocks in the deposit vary in lithology from dacites (the most abundant ones, compositionally related to the underlying **emb**, the Emboriò lava domes) to andesites from one or more of the other previous units, with occasional red scoriae pockets. The unit produced a hummocky topography, with each hummock being in general 20-30 m high. These hummocks are found all along the northern shore of Nisyros volcano, from Mandraki to Palì. Based on these characteristics, we interpret this deposit as the result of a debris avalanche event, although it was formerly interpreted as a block and ash flow deposit due to dome collapses (Limburg & Varekamp, 1991; Vougioukalakis, 1993; Francalanci et al., 1995). A palaeosoil caps the Vunàri debris avalanche deposit.

llf (Lubunià lava flow) - This lava flow, outpouring from a fracture which opened inside the scarp morphology resulting from the Vunàri debris avalanche, has the peculiarity to be the last andesitic event in the evolution of Nisyros volcano. The outcropping area is located between Loutrà and Mandraki (Fig. 2.20).

lp (Lower Pumice pyroclastics) - This unit starts with a basal pumice fallout deposit (**lp**$_{n}$) (Fig. 2.21-A & B) (see Volentik (b) et al, this volume, for a discussion on the depositional facies of this units), showing a reverse grading of the magmatic fraction (rhyolitic pumice) and an increasing amount of lithic fragments towards its top (Fig. 2.21-A). This fallout has been found only in three different locations: (i) along the road from Mandraki to Loutrà (Fig. 2.21-A); (ii) along the road climbing from Palì to Emboriò (Fig. 2.21-B at the elevation of 180 m) and (iii) in the valley from Cape Katsuni to Emboriò (at the elevation of 100 m). The fallout is overlain by pyroclastic density current deposits, characterised by pumice-rich, lithic-poor and almost matrix-free pyroclastic flow deposits (Fig. 2.21-A & C) in the North of the island (**lp**$_{f}$). On the southern coast of the island, the sequence comprises a lithic-lag breccia (**lp**$_{d}$) (Fig. 2.21-D) that is overlain by wavy surge deposits with impact sags (**lp**$_{o}$) and topped by a matrix-rich pyroclastic flow deposit (**lp**$_{c}$) (Fig. 2.21-D). A ground layer deposit is associated with **lp**$_{c}$ and is found at its base. A widespread light brown palaeosoil tops the unit. Lithic fragments in this unit are made up of fresh andesites and rhyolites, sub-intrusive rocks, fumarolised lava fragments, skarns, epidote-bearing lithics, amphibole-bearing lithics. Limburg & Varekamp, (1991) found in this unit also clinopyroxene-garnet fragments, clinopyroxenites, and tremolite-bearing limestones.

Palì sub-synthem

pl$_{j}$ - Unit **pl**$_{j}$ is composed of debris flow deposits that rework **emb** to **lp**, over which **pl**$_{j}$ lies unconformably (Fig. 2.22). The deposits are made up of canalised pumices (locally displaying current structures) and Emboriò lava fragments floating in a sandy matrix. These epiclastic deposits are typically 2-3 m thick (but up to 20 m thick in the area of Avlaki) and occur principally in the northern part of Nisyros. The top of the unit is affected by pedogenetic processes.

nlf (Nikià lava flows) - Thick rhyolitic lava flows constitute this unit, which covers the whole eastern flank of the island (Fig. 2.23-A), all the way from the rim of the caldera to the sea (from the beach of Pahia Ammos to Avlaki). The flow facies can locally vary to be more vitrophyric and perlitic. Large amphibole-bearing enclaves of basalt-andesitic composition reaching 1.5 m in size (Fig. 2.23-B) are widespread within the flows. A palaeosoil covers the upper blocky surface of the flows. Typical outcrops are found near the

Monastery of Aghios Ioannis Theologos and near the village of Nikià, where its thickness can reach 150 m. A neck that fed one of these flow units is exposed along the caldera wall ([N.] in Fig. 2.1-B). We estimate the total volume at slightly more than 1 km^3, in agreement with Hardiman (1999).

up (Upper Pumice pyroclastics) - The tephrostratigraphy (see also Volentik (b) et al., this volume) of this rhyodacitic pyroclastic unit outlines different deposit typologies: a 2 to 10-m-thick pumice-rich pyroclastic flow deposit ($\mathbf{up_f}$), lithic-poor and almost matrix free (Fig. 2.24-A & B); a succession of wavy surges ($\mathbf{up_o}$) and pumice-rich pyroclastic flows ($\mathbf{up_c}$); a pyroclastic flow deposit ($\mathbf{up_e}$) with a 3-4 m thick level enriched in lithics (Fig. 2.24-C) (interpreted as the breaking up of the hydrothermal reservoir by Limburg & Varekamp, 1991) overlying $\mathbf{up_c}$ in the section of Cape Katsuni); an ash flow deposit ($\mathbf{up_g}$), comprising two other lithic-rich lenses; a final phreatomagmatic surge deposit ($\mathbf{up_h}$) with planar-bedded structures (Fig.2.24-D), reaching a maximum thickness of 5-8 m. Lithic fragments within the **up** pyroclastic unit are made up in majority of skarns, with subordinate fresh lava fragments and sub-intrusive rocks that have been affected to a different extent by argillic alteration. Limburg & Varekamp (1991) found also epidote-bearing lithics, pyroxenites and limestones. The most complete exposures are located along the road between Palì and Lies beach at Cape Katsuni and in the abandoned quarry at Loutrà, that represents the most proximal outcrop of this pyroclastic unit.

Profitis Illias synthem

$\mathbf{up_j}$ - This epiclastic unit reworks the previous pumice deposit (**up**). It is composed of debris flow deposits, such as those of $\mathbf{pl_j}$.

$\mathbf{ya_j}$ (Yalì fallout) - Aphyric and extremely finely vesiculated pumices characterise the magmatic fraction of this lithic-free eruption. The Yalì fallout layer (Allen & McPhie, 2000, Fig. 2.25-A, B & C) is only found remobilized within the talus fans at several locations on Nisyros island (Volentik et al., 2002; see Volentik (b) et al., this volume for more details on Yalì pumices). The best exposure lies along the road to the caldera floor, where the total thickness of the fallout reaches 2 m, but it shows several reversely graded beds, superimposed atop each other owing to remobilization (Fig. 2.25-D). This deposit is also found along the road to the castle of Paleocastro and to Kàrdia.

pfi (Post-caldera lava domes) - These domes, up to 600 m in height (Mt Profitis Illias, Fig. 2.26-A), fill two-thirds of the caldera on its western side. They are rhyodacitic in composition and present andesitic enclaves up to 20-30 cm in size (Fig. 2.26-B). The stratigraphic succession of the domes is described in Limburg & Varekamp (1991) and is reported in Fig. 2.1-C. Typical outcrops are found along the trail that leads from the Monastery of Evangelistra to the hydrothermal craters' area in the southern part of the Lakkì caldera depression.

Gorceix synthem

gx - A number of hydrothermal explosions took place in the southern Lakkì plain (Fig. 2.27-A & B), the last of which occurred in 1871-1873 and in 1887 (Gorceix, 1873; Martelli, 1917). Related deposits are made up of debris flow deposits with variable amounts of matrix (Fig. 2.27-C). Lava fragments inside the deposits vary in size from a few centimetres to a few metres, and are generally affected by fumarolic alteration processes preceding the eruption. The matrix is clayey to sandy in granulometry and yellow in colour. Its main characteristic is the presence of variable amounts of secondary sulphur and euhedral gypsum crystals (Marini et al., 1993).

Marine terrace (uncertain stratigraphic position)

Marine terrace deposits, first reported by Rehren (1988) and composed of rounded lava blocks (10-15 cm on average, and up to 1 m) of varied origin in a sandy matrix (Fig. 2.28), are found at an elevation of about 30-60 m above sea level along the western coast of Nisyros. The deposit is mainly cut into **blf** and preceding ones. Nevertheless, its stratigraphic position cannot be determined with certainty, since both the nature of the deposit may prevent it from being preserved in younger units (**lp** to **pfi**) due to their particular lithological characteristics, and tectonic movements may have specifically affected the area of Mandraki and the western sector of the island (see Volentik (c), this volume) leading to terrace emersion and uplifting in this sector only.

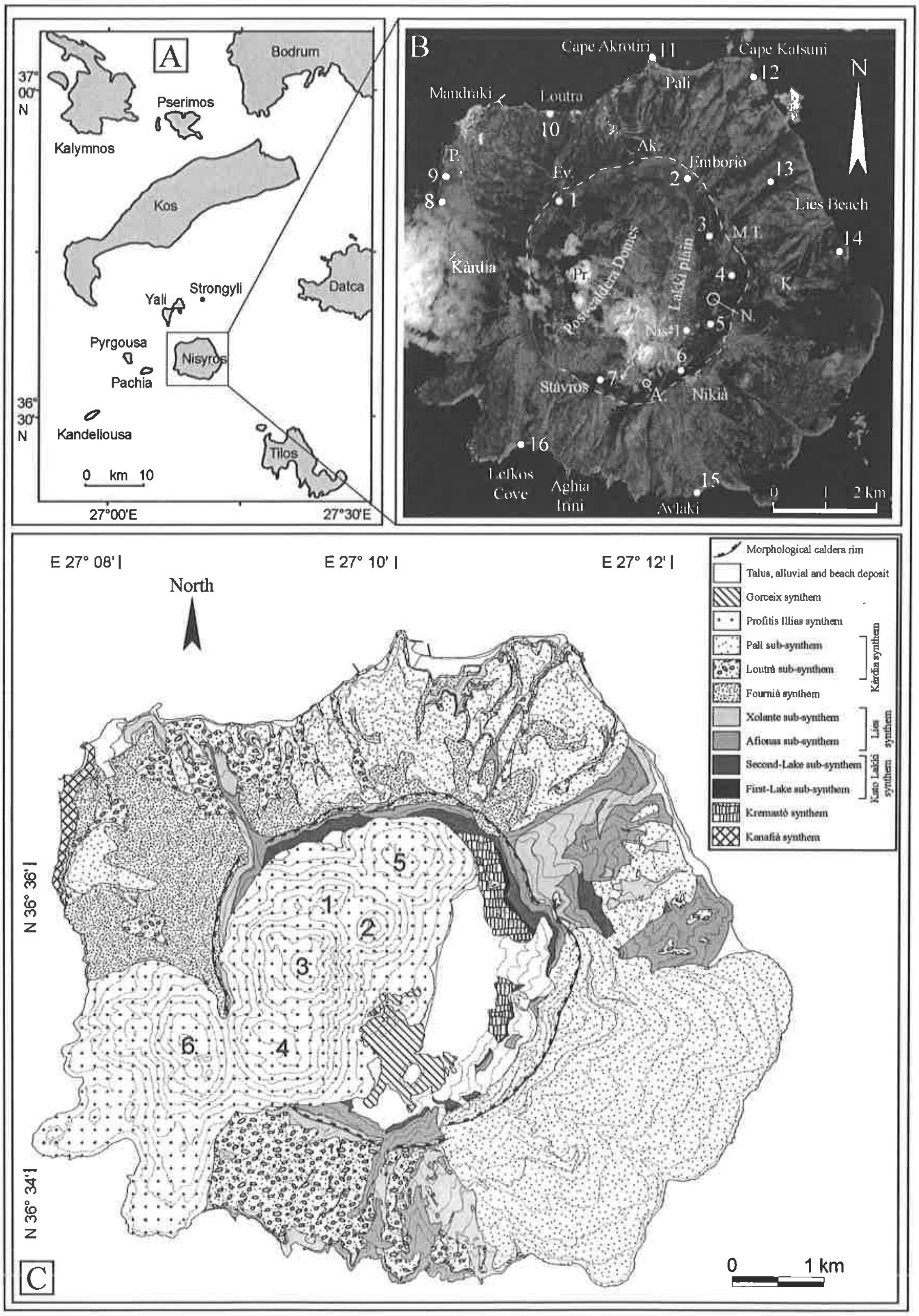

Fig. 2.1: (A) Localisation of Nisyros Island in the Aegean Sea. (B) IKONOS satellite image of Nisyros, by courtesy of the GEOWARN group. Numbers 1 to 16 refer to stratigraphic sections detailed in Volentik et al. (b) (this volume). [A.] Neck of Argos. [Ak.] Dome of Akimaronas. [E.] Village of Emboriò. [Ev.] Monastery of Evangelistra. [K.] Monastery of Panagia Kyra. [M. T.] Military tower of control. [N.] Neck. [P.] Ruins of Paleocastro. [Pr.] Mt Profitis Illias. [S.] Monastery of Stàvros. (C) Geological synthematic sketch map of Nisyros. Numbers refer to the time-sequence of the post-caldera domes, after Limburg & Varekamp (1991).

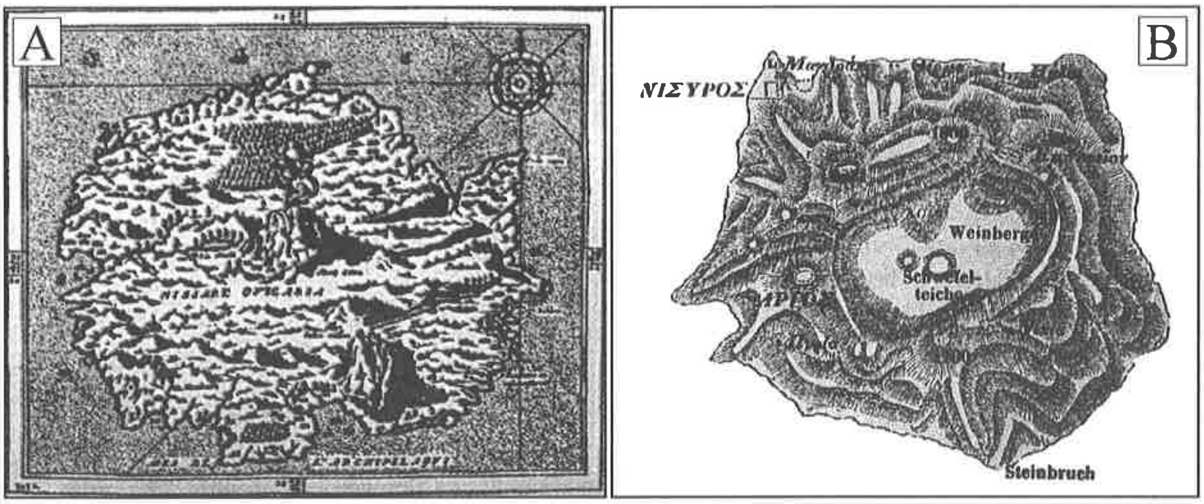

Fig. 2.2: A: Cristoforo Bondelmonti's map of Nisyros, 1420; B: Ludwig Ross' map of Nisyros, 1841.

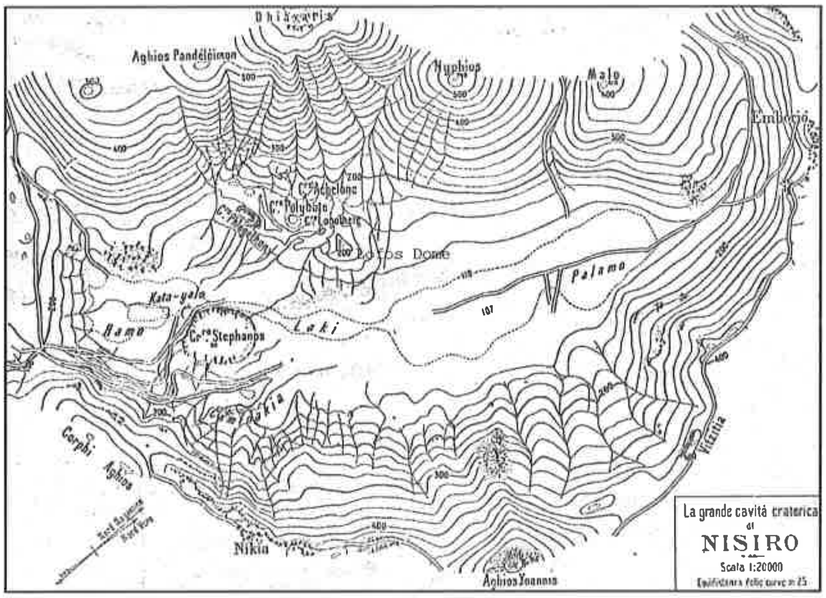

Fig. 2.3: Topographic map of the caldera depression drawn by Martelli in 1912 and published in 1917.

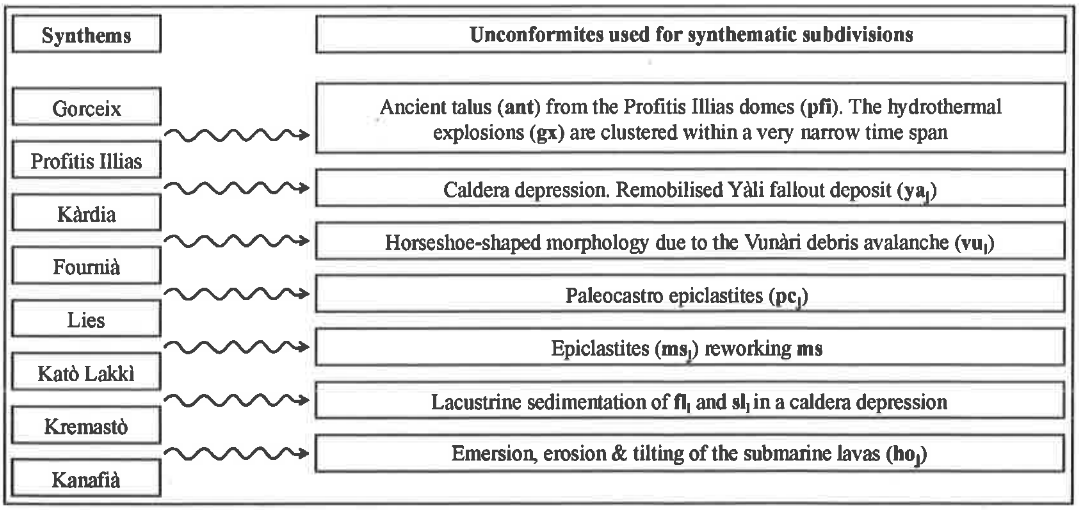

Synthems	**Unconformites used for synthematic subdivisions**
Gorceix	
	Ancient talus (**ant**) from the Profitis Illias domes (**pfi**). The hydrothermal explosions (**gx**) are clustered within a very narrow time span
Profitis Illias	
	Caldera depression. Remobilised Yàli fallout deposit ($\mathbf{ya}_l$)
Kàrdia	
	Horseshoe-shaped morphology due to the Vunàri debris avalanche ($\mathbf{vu}_l$)
Fournià	
	Paleocastro epiclastites ($\mathbf{pc}_l$)
Lies	
	Epiclastites ($\mathbf{ms}_l$) reworking **ms**
Katò Lakkì	
	Lacustrine sedimentation of $\mathbf{fl}_l$ and $\mathbf{sl}_l$ in a caldera depression
Kremastò	
	Emersion, erosion & tilting of the submarine lavas ($\mathbf{ho}_l$)
Kanafià	

Fig. 2.4: Summary of criteria used to define synthems in text.

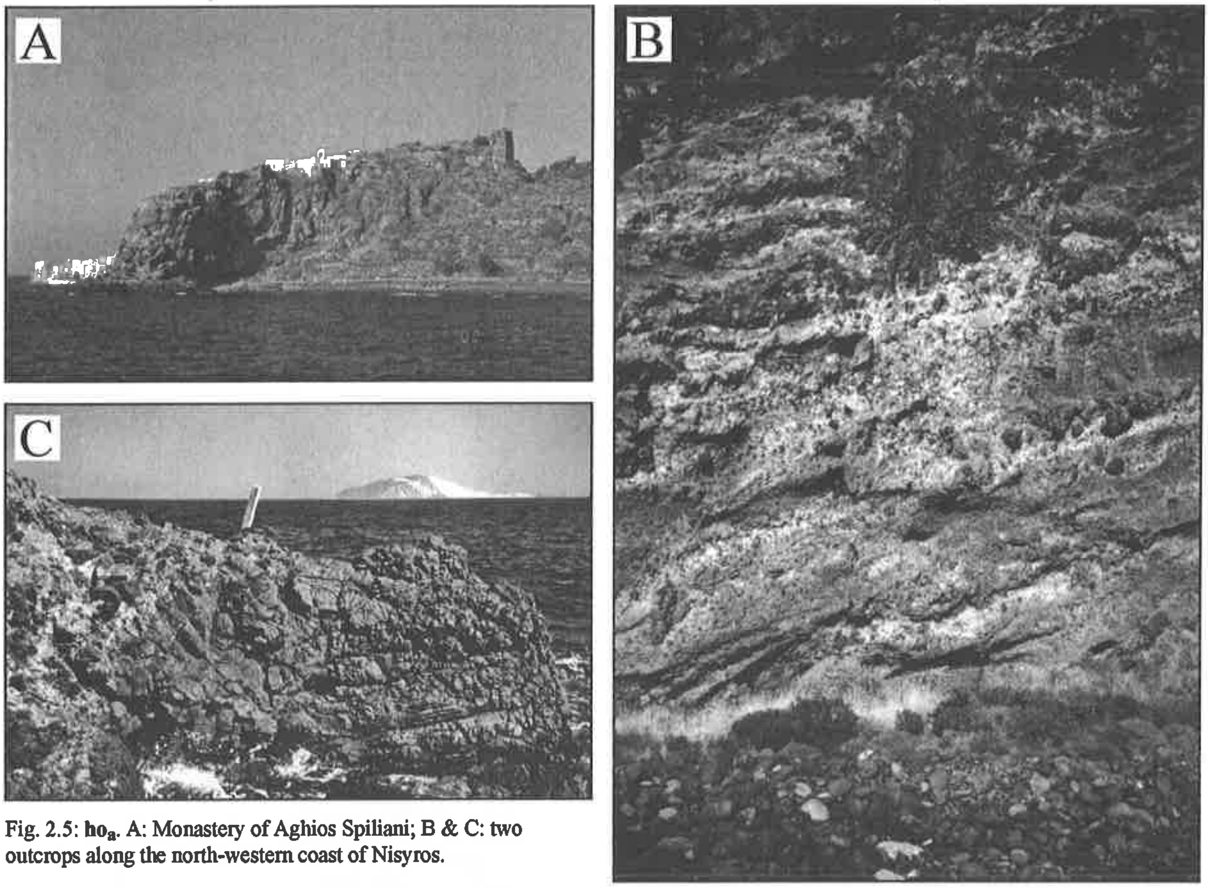

Fig. 2.5: **ho$_a$**. A: Monastery of Aghios Spiliani; B & C: two outcrops along the north-western coast of Nisyros.

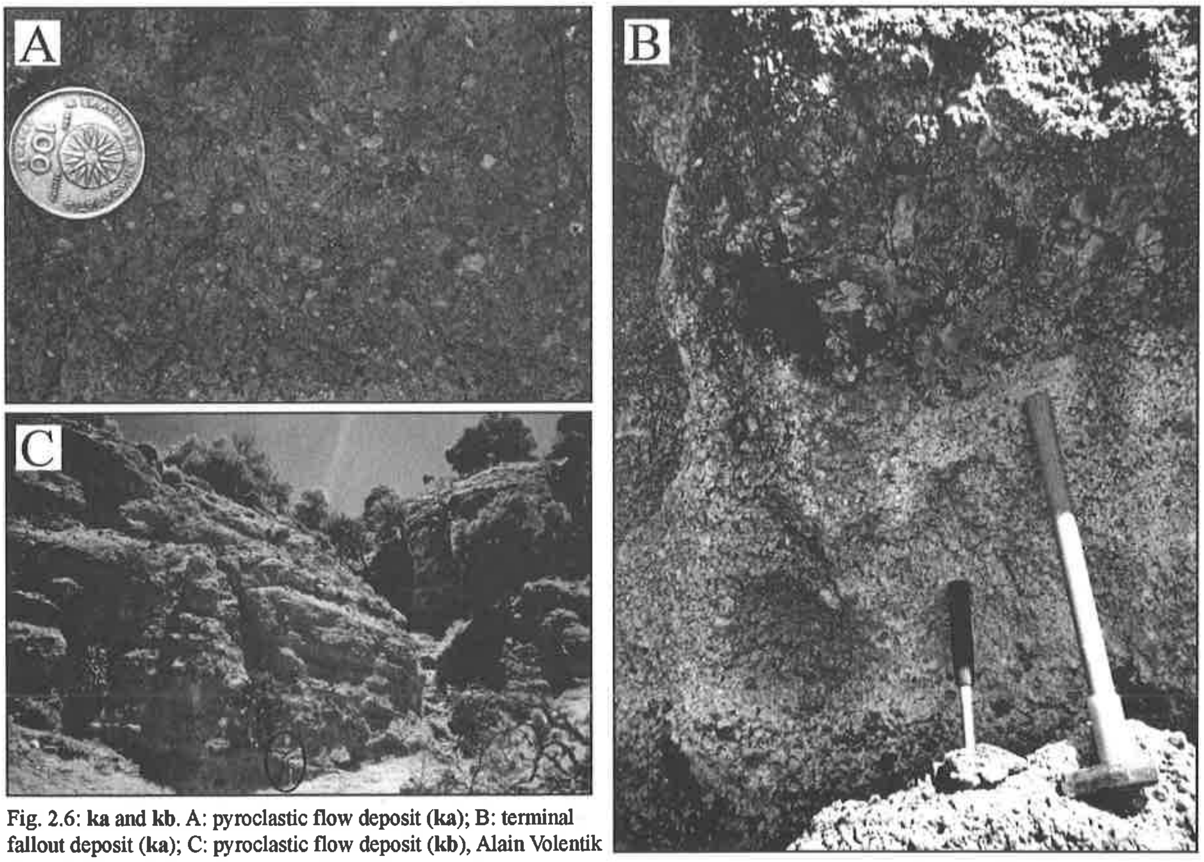

Fig. 2.6: **ka** and **kb**. A: pyroclastic flow deposit (**ka**); B: terminal fallout deposit (**ka**); C: pyroclastic flow deposit (**kb**), Alain Volentik for scale.

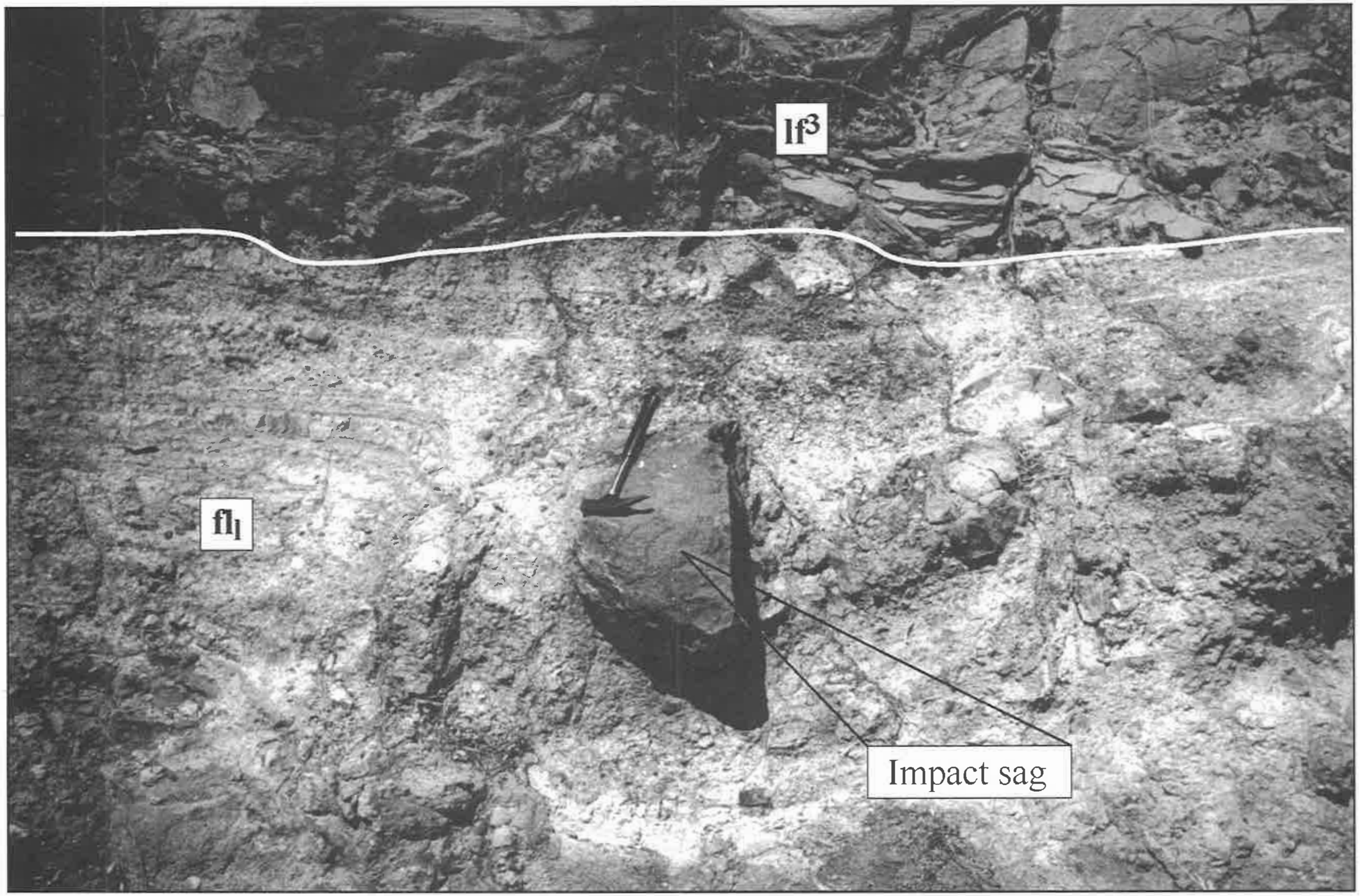

Fig. 2.7: $\mathbf{fl_l}$ (first lacustrine deposit) and $\mathbf{lf^3}$. Note the impact sag in the soft lacustrine beds.

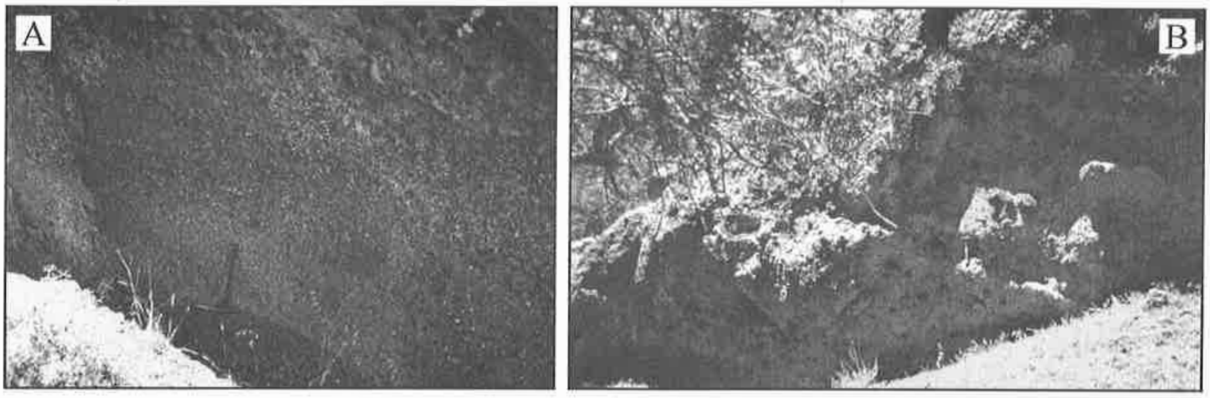

Fig. 2.8: **ms**, Melisserì pyroclastics. A: fallout deposit; B: pyroclastic flow deposit. The hammer for scale is 32 cm long.

Fig. 2.9: **xlf**$_b$, enclave-rich lava flow, Remo Chiesa for scale.

Fig. 2.10: **lf**^{6}, andesitic lava flow, flowing above a lava neck, which fed an older lava flow (**lf**^{5}).

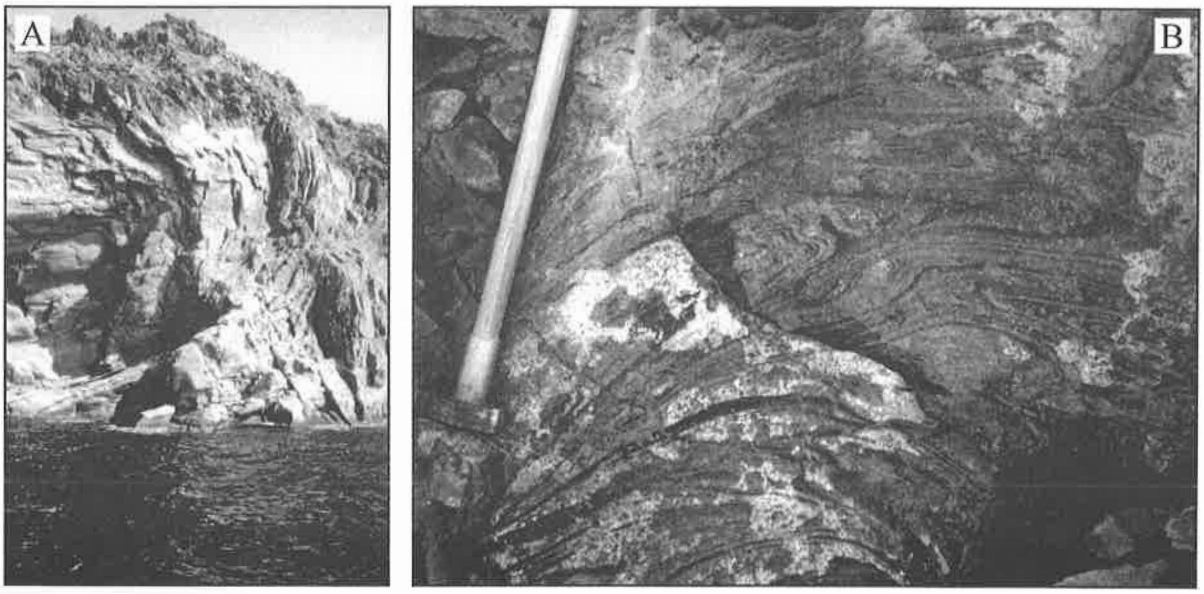

Fig. 2.11: **alf**, Argos rhyolitic lava flows. A: **alf** entering the sea (south coast of Nisyros) showing typical "onions" structures; B: flux structures in **alf** (road from Lakkì to the Monastery of Stavròs).

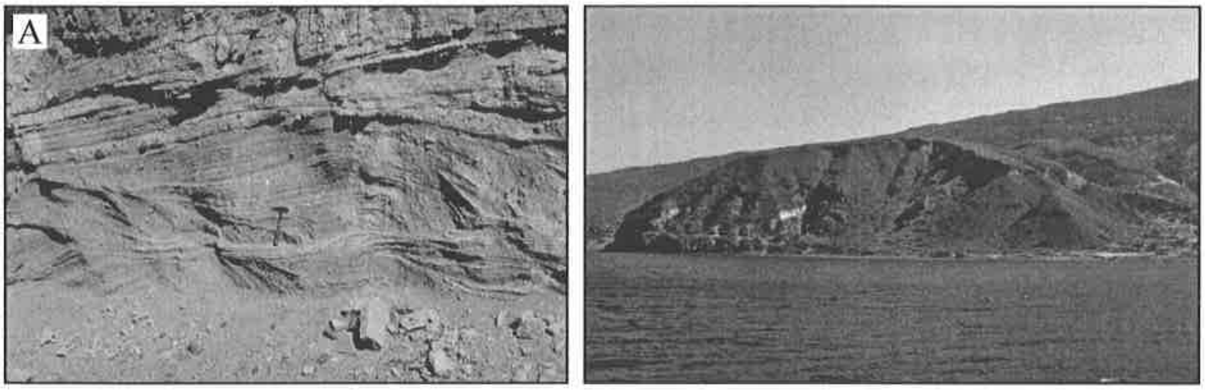

Fig. 2.12: **pa** (Pahia Ammos Tuff Cones). A: Surge deposits, showing nice dunes and anti-dunes structures,hammer for scale is 32 cm long; B: Tuff cone between the beaches of Lies (right) and Pahia Ammos (left).

Fig. 2.13: **pa_j**, Prof. Johannes Hunziker for scale (in the circle).

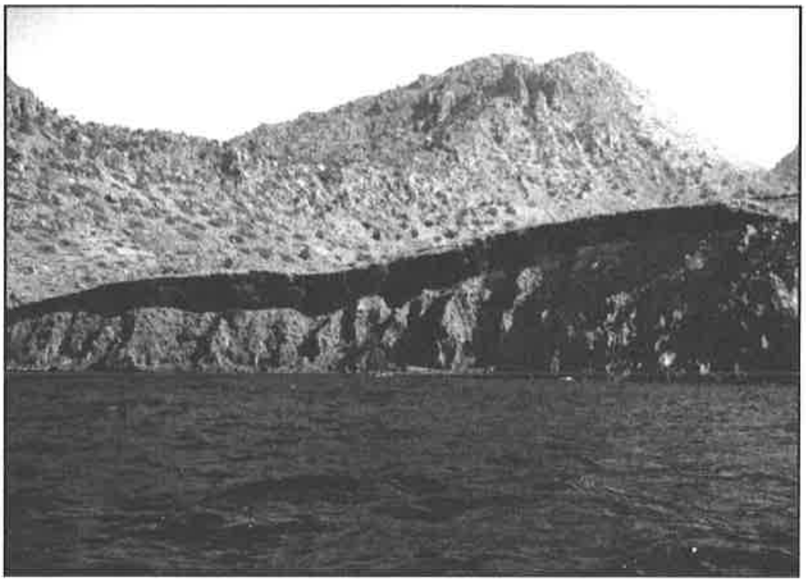

Fig. 2.15: **xo_{n1}**, proximal red scoriae fallout deposit, between Aghia Irini and Lefkos Cove, southern coast of Nisyros.

Fig. 2.14: vs_n, violent strombolian fallout deposit. A and B: Outcrops between the Monastery of Panagia Kyra and Lies beach, hammer (32 cm long) and Claudia Principe for scale.

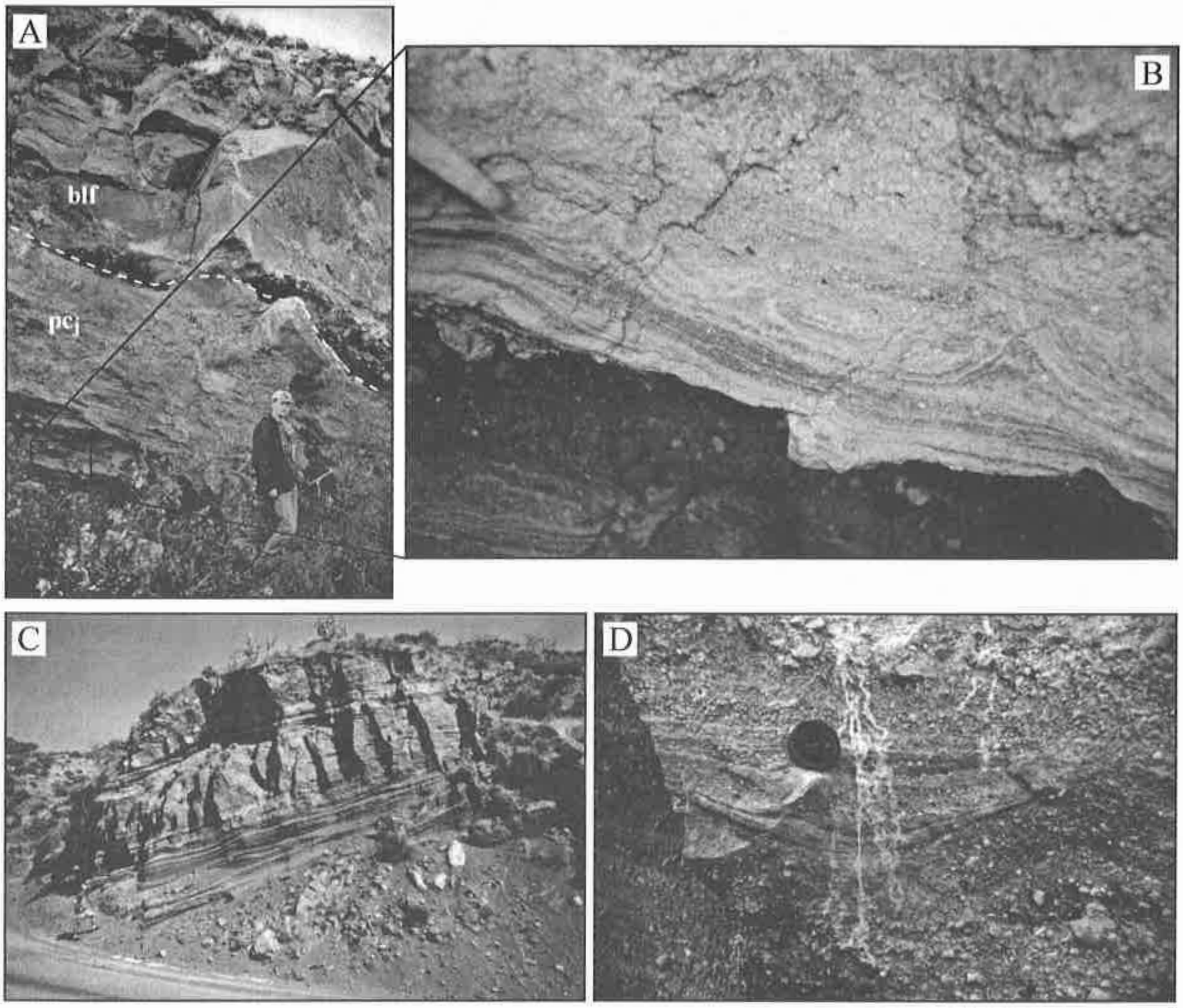

Fig. 2.16: **pc$_j$**, Paleocastro epiclastic deposits. A: debris flow deposits overlaid by **blf** (Aghia Basilei lava flows) in the area of Kàrdia, Loÿc Vanderkluysen for scale; B: detail of A showing load casts and slump structures; C: interbedding of surge deposits (**xo$_h$**) with Paleocastro epiclastic deposits (**pc$_j$**), along the road above Pali, Loÿc Vanderkluysen for scale; D: channel strucutres in debris flow deposits (**pc$_j$**), in a valley above Pali.

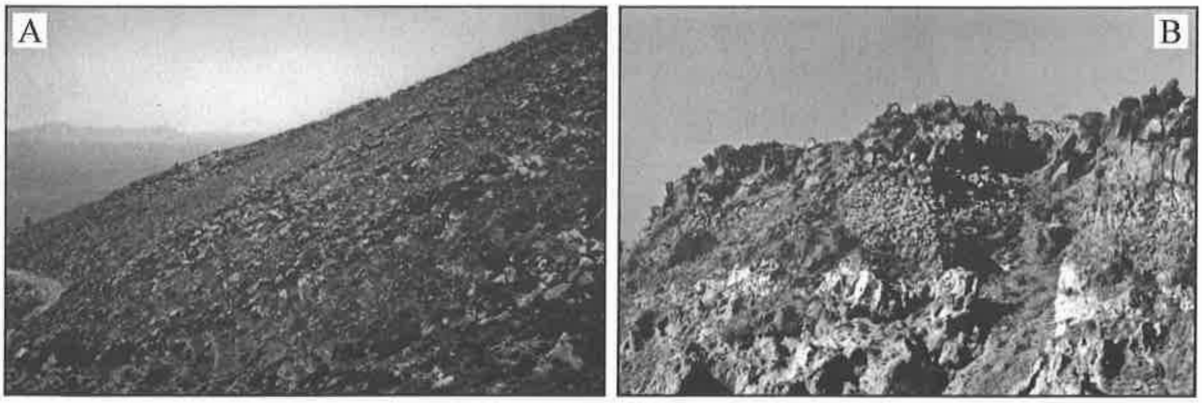

Fig. 2.17: **blf**, Aghia Basilei lava flows. A: Succession of lava flows on the upper western slope of the volcano; B: One of the lava flows on the top of the cliff on the western coast of Nisyros, note the thick red-scoriae top of the flow and the prismatic cooling suggesting the front of the flow.

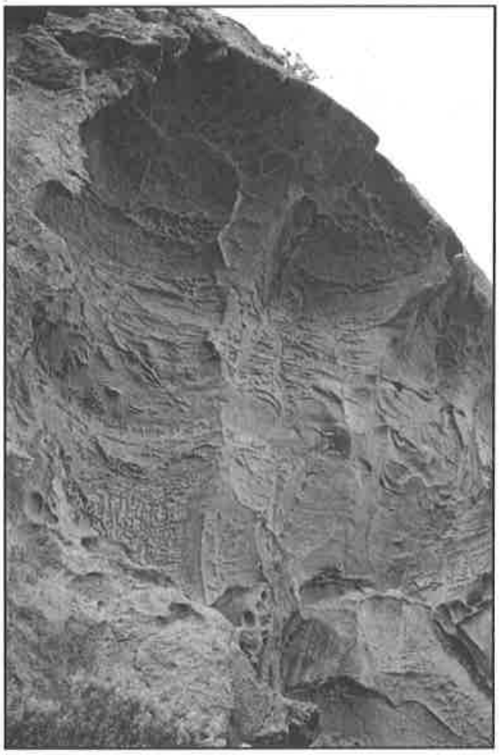

Fig. 2.18: **emb**, Emboriò lava flow, outcrop on the caldera walls, along the path from Evangelistra to Emboriò.

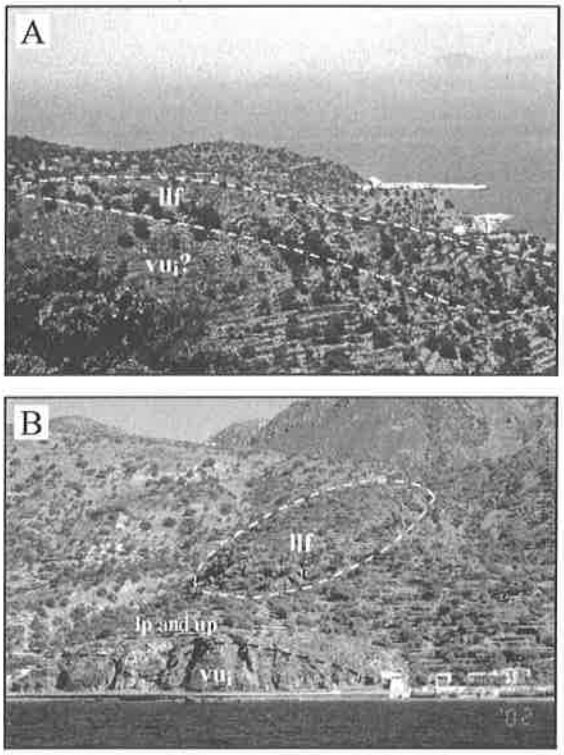

Fig. 2.20: **llf**, Lubunià Lava flow. A: View from Akimaronas to the West. B: View from the North, outcrop above Loutrà.

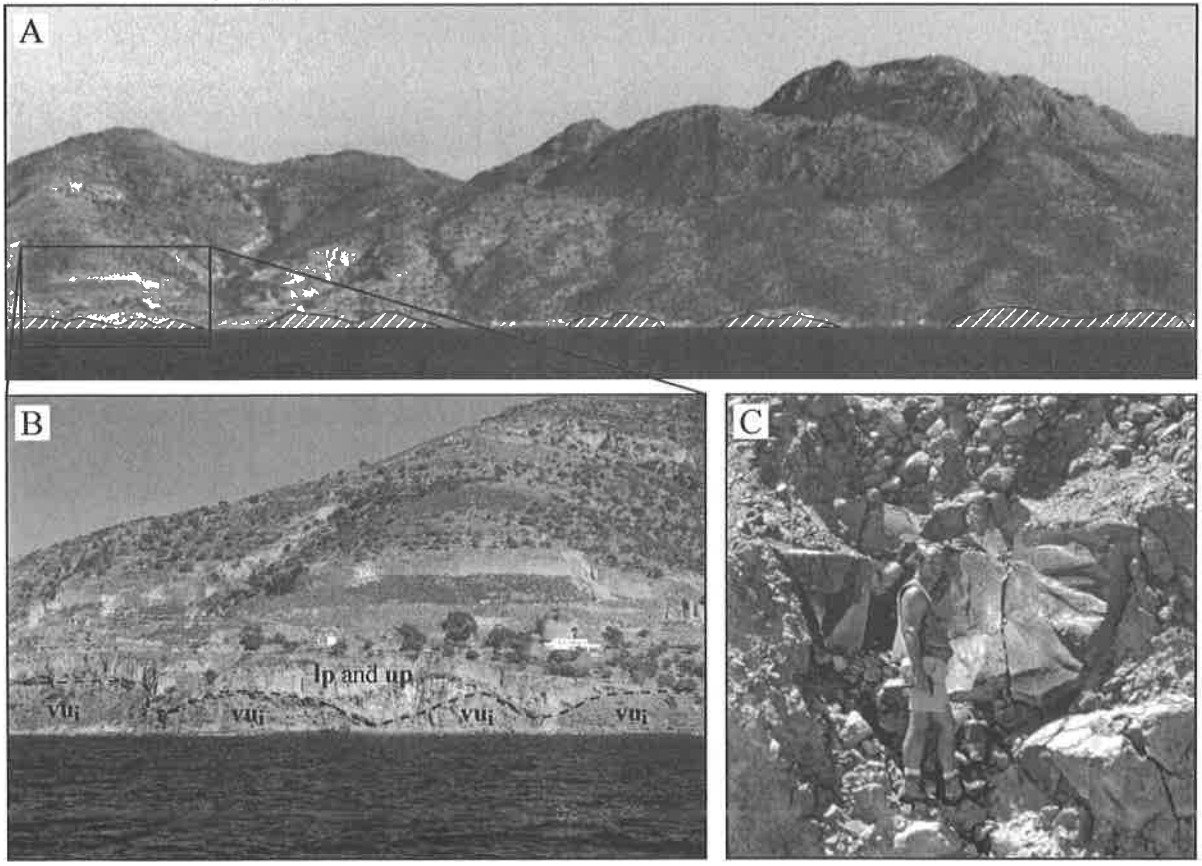

Fig. 2.19: **vu**$_l$, Vunàri debris avalanche. A: General view of the northern coast of Nisyros, note the hummocky topography of the shoreline; B: Detail of the shoreline with two hummocks clearly evident; C: Block (> 1m^3) with jigsaw fractures within the deposit (Loutrà), Alain Volentik for scale.

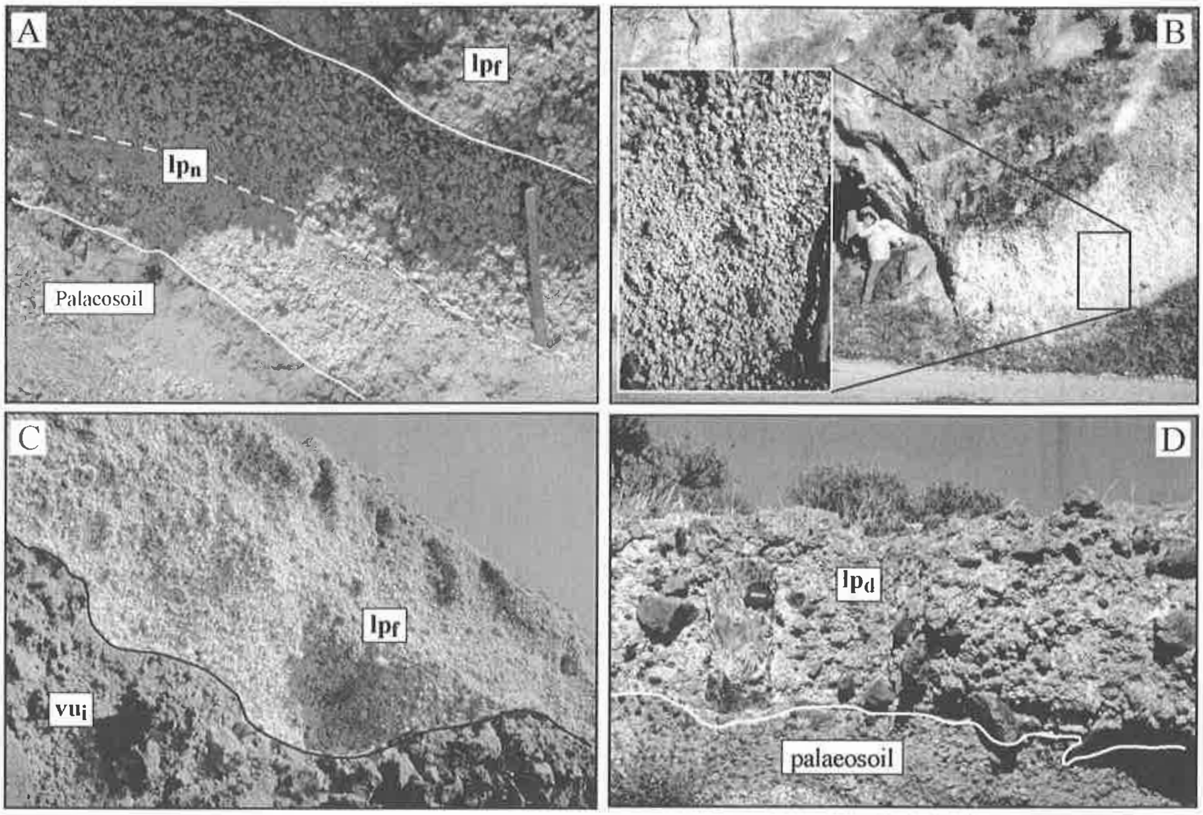

Fig. 2.21: **lp**, the Lower Pumice. A: Fallout deposit (**lp$_n$**) at he base of the unit (Loutrà); B: Proximal fallout deposit (**lp$_n$**) along the road from Pali to Emboriò; C: Pumice-rich pyroclastic flow deposit (**lp$_f$**), Cap Akrotiri; note the erosional features at the base of the deposit; D: Lithic-lag breccia deposit (**lp$_d$**), along the road to Avlaki, southern coast of Nisyros.

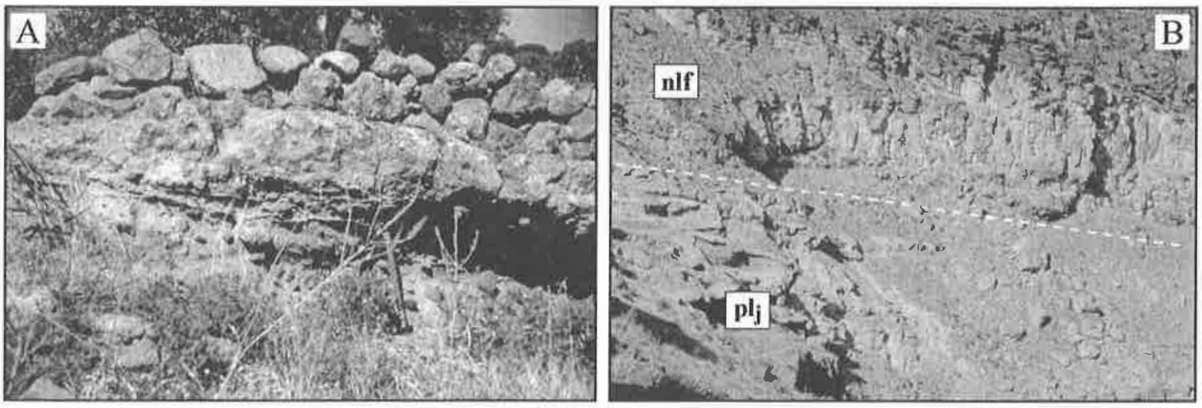

Fig. 2.22: **pl$_j$**. A: Debris flow deposits (above Mandraki); B: Thick debris flow deposits suggesting a palaeovalley (Avlaki).

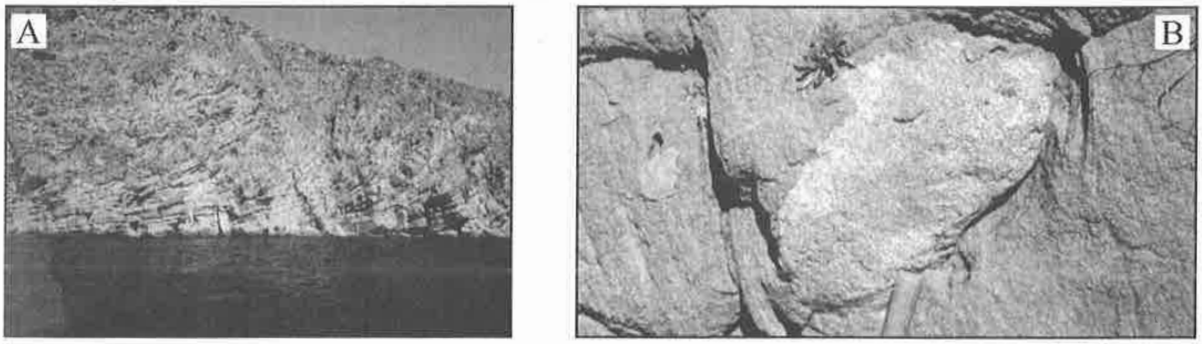

Fig. 2.23: **nlf**, Nikià lava flows. A: "Onion" strucutres suggesting the boundary of one flow; B: Mafic enclave within the rhyolitic Nikià lava flows (**alf**), note the cauliflower-shaped boundary.

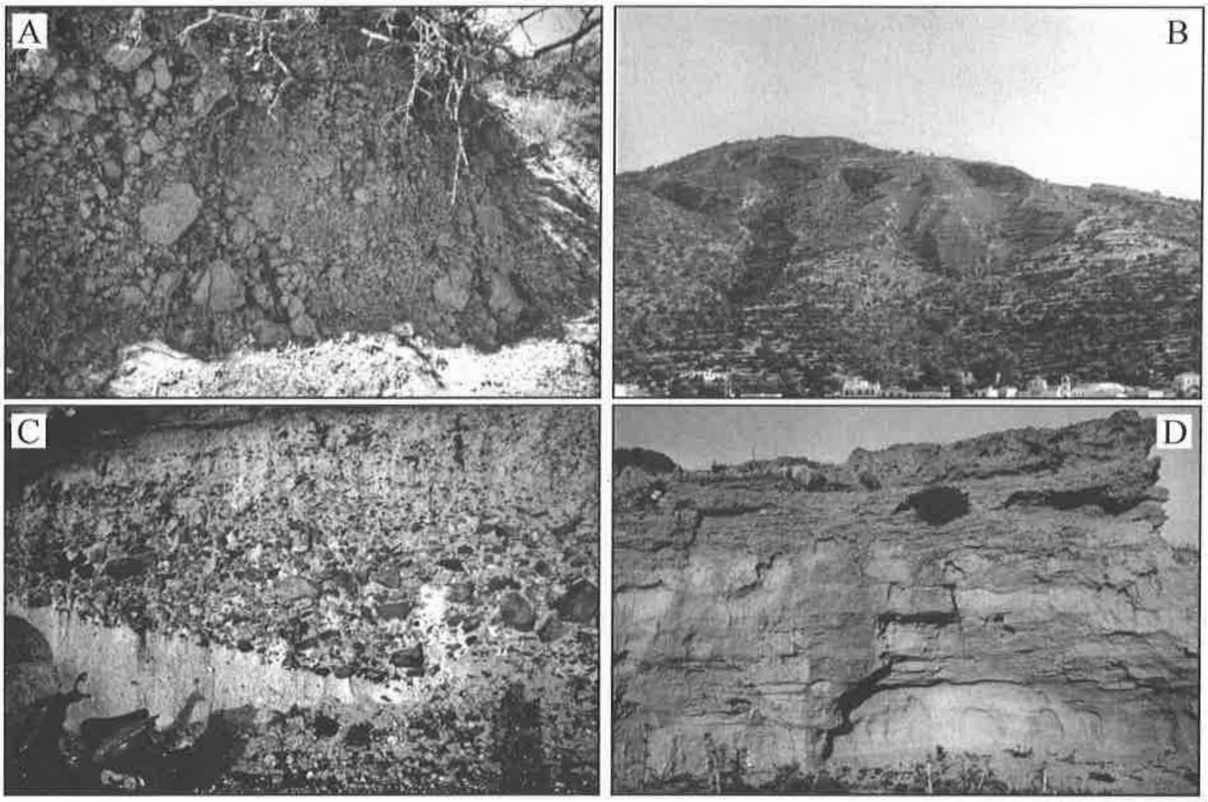

Fig. 2.24: **up**, The Upper Pumice. A: Proximal pumice-rich pyroclastic flow deposits (**up**$_{\mathbf{f}}$), between Pali and Emboriò; B: Lobes of pyroclastic flow deposits (**up**$_{\mathbf{f}}$) above Pali; C: Lithic-lag breccia deposits (**up**$_{\mathbf{d}}$), Cap Katsuni. D: Surge deposits (**up**$_{\mathbf{h}}$), Cap Katsuni.

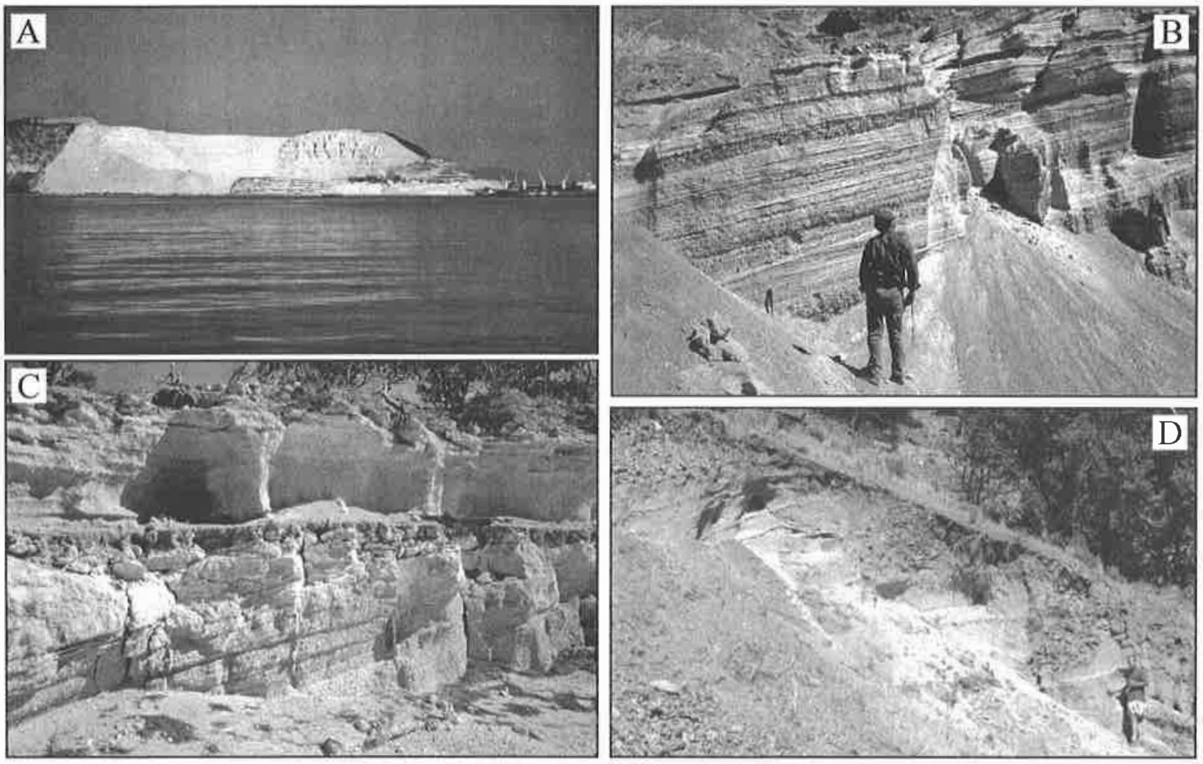

Fig. 2.25: **ya**$_{\mathbf{j}}$. Yali fallout. A: Yali island, north of Nisyros; the quarry is cut in the submarine tuff cone; B: Stratified pumice deposit of the submarine tuff cone of Yali, Jean Hernandez for scale; C: The subaerial Yali pumice fallout (found remobilized on Nisyros, see D) tops the volcanic sequence on Yali and is seperated from the submarine tuff cone by a brown palaeosoil deposit; D: The Yali fallout (**ya**$_{\mathbf{j}}$), remobilized within a talus fan, Alain Volentik for scale.

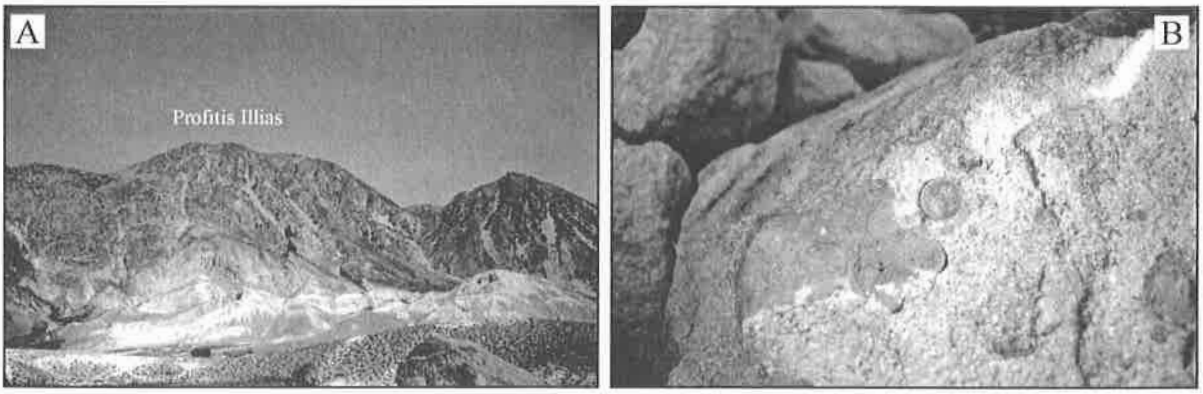

Fig. 2.26: **pfi**, Post-caldera lava domes. A: Profitis Illias from the hydrothermal area; B: Mafic enclave within the rhyodacitic lava (**pfi**).

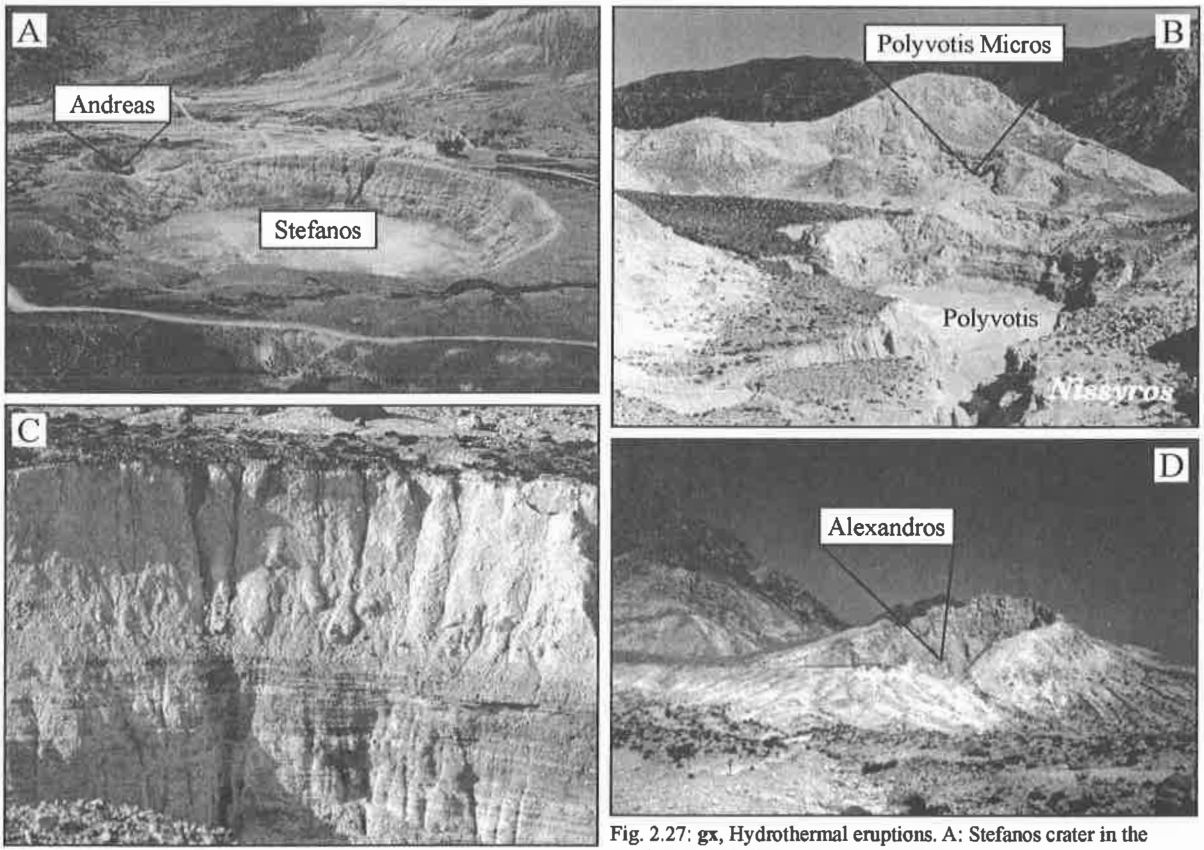

Fig. 2.27: **gx**, Hydrothermal eruptions. A: Stefanos crater in the southern Lakki Plain, view from Nikià; B: Polyvotis Megalos crater, with Polyvotis crater in the middle and Polyvotis Micros crater behind it; view to the east; C: section within Polyvotis crater, showing debris flow deposits related to the 1873 hydrothermal eruptions; note the thick vaved lacustrine deposits underlying the 1873 debris flow deposits, testifying the occurence of a "long-lived" crater lake. Photograph by Prof. Giorgio Marinelli. D: Alexandros crater, view from the south-east.

Fig. 2.28: Marine terrace outcrop along the north-western shore of Nisyros island, south of Paleocastro; Loÿc Vanderkluysen for scale.

3. Stratigraphy of Nisyros Volcano (Greece)

Alain C. M. Volentik(1), **Loÿc Vanderkluysen**(1), **Claudia Principe**(2), **Johannes C. Hunziker**(1)

(1) Institut de Minéralogie et Géochimie, BFSH-2, Université, CH-1015 Lausanne, Switzerland.

(2) Istituto di Geoscienze e Georisorse, Area della Ricerca CNR-Pisa San Cataldo Via G. Moruzzi 1, I-56124 (Pisa), Italy.

Abstract - A new complete stratigraphic record was reconstructed for Nisyros volcanics through the application of a modern volcanological approach, which is very different from those followed by previous authors, in that it incorporates the use of: (i) the UBSU criteria for the unit subdivision, (ii) the tephra deposits as stratigraphic markers, and (iii) the facies analyses to reconstruct eruptive sequences. The occurrence of a major sector collapse, represented by the Vunàri debris avalanche, in the northern sector of Nisyros, is an other innovative result we obtained. Investigating the tephra deposits, we found that three explosive eruptions (i.e., Lakkì, Melisserì and Lower Pumices) contributed to the formation of the present caldera. By means of an accurate facies analysis the eruptive sequences of the Lower and Upper Pumices, their source areas and relations with the Nisyros caldera formation were redefined as well as the role and distribution of the widespread volcanic activity producing spatter cones and scoria cones, with associated small lava flows, that is restricted to a limited stratigraphic interval.

3.1. Introduction

In this chapter we detail the stratigraphy of Nisyros volcanics we reconstructed through both the application of the UBSU criteria and the facies analysis of tephra deposits, including epiclastites. The new stratigraphy we present here implies a number of differences with respect to the previous literature both in the number and definition of the stratigraphic units and in the interpretation of the depositional facies. In particular, facies analyses allowed us to perform stratigraphic correlations between tephra deposits at different distances from their vents, and to subdivide lava flow units according to their stratigraphic position instead than group them based on their chemistry, as done in some previous works. The resulting picture has a number of differences with the previous stratigraphic reconstructions, that are discussed in detail hereunder.

3.2. Geochronology of Nisyros, a still unsolved problem

The timing of the different volcanic events of Nisyros volcano represents a crucial point in the deciphering of its complex history. First order open question remains the starting point of this magmatism, was it a quasi continuum, or can we detect breaks in the magmatic history? Further interesting questions – is there a periodicity in the magmatic activity, if so, are the active periods decreasing with time or increasing? Such facts considerably help in the evaluation of the implications for the volcanic risk.

During the last 30 years numerous attempts to get a grasp on the geochronology of Nisyros have been made (Di Paola 1974; Wagner et al. 1976; Federman & Carey 1980; Vinci 1983; 1985; Barberi et al. 1988; Rehrens 1988; Keller et al. 1990; Limburg & Varenkamp 1991; Vougioukalakis 1993; 1998; Smith et al. 1996; Hardiman 1999; Matsuda et al. 1999). All these dating attempts have so far been without clear results although together they represent a multimethod approach of 13 papers reporting 13 radiometric ages. Up to present the following methods have been applied: ^{14}C, fission tracks on volcanic glass, K-Ar on whole rocks, ^{40}Ar/^{39}Ar on sanidine, plagioclase, and volcanic glass, U-Th disequilibrium on soils, rocks and minerals.

This shows a typical case of grab sampling, which in a so complex case has never led to meaningful results. Some papers do not even bother to specify the locality where the sample was taken, the method or even the laboratory where these measurements were performed, not to speak about the analytical uncertainties. Beside the above mentioned methodological problems, further uncertainties do not help to clarify the picture.

^{14}C: Already the fact that stratigraphical succession often does not correlate with the measured succession of measured ^{14}C ages poses a problem. Then the authors do never state if they are reporting corrected ages or raw data, and last but not least- can we really assume, that on an island degassing CO_2 in the order of over 1000 tons/day the scarce ^{14}C did not at all exchange with the ^{12}C of the passing CO_2 (ratio of 12/14 in the order of 10^{12}-10^{15}) ? In other words the ^{14}C ages of Nisyros volcano are to be taken cum grano salis.

Fission tracks on volcanic glass: In the early days of fission track dating, experts have originally used volcanic glass for dating, but with time have left this technique due to difficulties in distinction between real tracks of fission and elongated gas micro-bubbles in the glass. Today most specialists do not apply this method any more on volcanic glass or even on pumice. In order to believe in these ages one would like to see a stratigraphic succession measured and yielding successive ages, and not only 2-3 isolated determinations.

K-Ar: So far no systematic work on K-Ar has been performed. Only whole rock measurements have been reported. In order to find out if a system is datable, mineral separates, glassy matrix as well as whole rock analyses would be required, and this on a stratigraphic profile and not on isolated samples. No such work was reported.

^{40}Ar/^{39}Ar: The only reliable age determination is the Kos plateau tuff (KPT) dated on Kos by Smith et al. (1996), yielding 161±1 ka.

The whole age situation not being very clear, a PhD thesis of A. Büttner on the subject was started in 2000 by Prof. I. Villa in Bern. In her PhD thesis Büttner (2004) reports only 8 pumice? samples on Nisyros (3 plagioclases, 2 glasses and 3 not specified samples) -one would really like to know what exactly was analysed there, but the precise locality where the rocks have been taken was not reported. All these samples show highly discordant spectra ranging between 10 ma and negative ages. Büttner (2004) concluded, that strangely, the high temperature plagioclases are extremely poor in potassium and most of the potassium is in the glass matrix, which includes considerable amounts of parentless ^{40}Ar. She states, that as a consequence the age spectra of the plagioclases and glasses did not provide a reliable chronological framework. We cannot decide if these facts are due to a poor choice of the measured samples, to underestimated blank problems of the used furnace, (sample sizes range between 7 and 110 mg), or simply due to parentless ^{40}Ar as suggested by Büttner (2004). One thing however seems quite clear: the measured spectra have the peculiarity that the radiogenic ^{40}Ar component is mostly in the order of 0-6%. In addition the non radiogenic "atmospheric" Argon 40/36 ratio is very often in the range of 160-260 and not as generally accepted 295.5. These problems have not been addressed in the thesis. As no Ar/Ar correlation plots are reported for the Nisyros samples, but instead only a Ca/K-Cl/K diagram, this anomaly most likely remained undetected.

The over 400 feldspar electron microprobe analyses of the Lausanne group from all the different outcropping rocks of Nisyros, show that plagioclases normally have around 0.4-0.5 weight % of K_2O, but also that in some not too rare cases, the Or component is higher, yielding up to 1.8% K_2O and not as stated by Büttner (2004) lower than 0.7%. The over 100 amphibole analysis show K_2O contents up to 0.7% and whole rocks show contents up to 4% K_2O. These rocks must contain in the micro-crystalline or glassy matrix components with high potassium contents. Here the question arises if another sample choice instead of only pumices would not have improved the results considerably. For a Swiss PhD thesis one would have expected a wider choice of samples that to our knowledge had been collected on Nisyros and also a greater number of analyses.

In the original proposal of the PhD-thesis of A. Büttner there was a suggestion to increase the signal to background ratio of these most likely extremely young rocks by using a laser ablation system-this could also have changed the results. In a future study of the age relations of Nisyros volcano these points need to be clarified in order to hopefully come to more meaningful solutions.

A further approach of dating the Nisyros rocks was undertaken by Büttner (2004) with the U-Th disequilibrium method on 6 paleosols sandwiched between volcanic rocks and 3 rocks, 2 lavas and a pumice. Here also the obtained ages are highly discordant, ranging between 400 and 10 ka and orders of magnitude younger than the intercalated Ar/Ar ages. The given interpretation of open system behaviour of the paleosols and of not suitable U/Th ratios of these soils show that we are still far from solving the age problems on Nisyros. Here again we can state that in a PhD thesis a methodology newly developped in a laboratory should first be tested on a perfectly calibrated geologic section-this would be a geologists approach! Obviously not considered important.

3.2.1. Age range of the volcanic succession

Based on previous discussion, it is evident that the duration of volcanic activity on Nisyros is poorly constrained by few and in some cases contrasting absolute ages, as already underscored by Limburg & Varekamp (1991), Francalanci et al. (1995) and Pe-Piper & Piper (2002).

Table 3.1 summarises the available age data. Since the 31-ka-old Yalì pumice fall has been found remobilized on the talus deposits inside the caldera walls (Volentik et al., 2002), but neither above the post-caldera domes nor interlayered within the dome-related detritus cones, these domes, which are the stratigraphically youngest igneous unit, are younger than 31 ka (but are still undated). Similarly, the Kos Plateau Tuff (KPT), which has been found on Nisyros both as scattered pumices into the epiclastites capping the pillow lavas sequence of Holaki by Keller (1971) and at the base of the volcanic succession in the geothermal well Nisyros-1 (see below), sets the onset of Nisyros' subaerial activity at less than 161 ka ago (Smith et al., 1996).

3.3. Stratigraphic units

We applied the Unconformity Bounded Stratigraphic Units (UBSU) criteria to group stratigraphic units into hierarchically more important entities, following the guidelines of the International Subcommission on Stratigraphic Classification (Salvador, 1987); see Volentik et al.(a) (this volume) for a detailed discussion of the UBSU criteria.

The main features of the 36 units that compose the stratigraphy of Nisyros (see Volentik et al.(a), this volume, for a complete description of the different units) are summarised in Table 3.2, while Fig. 3.1 synthesizes our stratigraphic data. For the sake of clarity, the correspondence between the codes given in this paper and the unit numbers previously defined by Volentik et al. (2002) has been also reported in Table 3.2.

Stratigraphic correlations between the most representative measured sections are presented in Figs. 3.2a and 3.2b (see Fig. 2.1-B in Volentik et al.(a), this volume for the location of all the stratigraphic sections discussed in this chapter).

The most ancient portion of the stratigraphic sequence (Figs. 3.2a, 3.2c and 3.3 to 3.7), with the exception of the submarine deposits (logs 8 & 9 in Fig. 3.2b, and Fig. 3.8), crops out along the caldera walls. The main results achieved through the study of the sequences exposed along the caldera cliff are: (i) the finding of a lacustrine sequence emplaced after the deposition of the Lakkì pyroclastics, hinting at the existence of an early summit depression, possibly formed by such an eruption (Volentik et al., 2002); (ii) the localization of the source of the Melisserì/Evangelistrà eruption (Volentik et al., 2002) in the eastern sector of Nisyros as inferred from the variations in both facies and thickness as well as from the typology and volume of the explosive deposits.

Most of the stratigraphic units exposed along the caldera walls crop out also in the sea cliffs and in the deeply eroded valleys of Nisyros Island (Fig. 3.9), while the stratigraphically highest tephra (Fig. 3.2b) mantle the present morphology.

3.3.1. Kanafià synthem

The lowermost stratigraphic unit on Nisyros (**ho**$_{a}$) is constituted by the basalt-andesitic hyaloclastites and pillow lavas of Holaki (Keller, 1971) (log 8 & 9 in Fig. 3.2b and Fig. 3.8), cropping out along the north-western coast of the island. The most representative outcrop is located below the Monastery of Aghios Spiliani (Fig. 2.5 in Volentik et al.(a), this volume), and the thickness of this unit is 40-50 m. A 5-10 m thick epiclastic deposit (**ho**$_{j}$) reworks the material of **ho**$_{a}$ in a fresh water medium (stream or river). It only occurs along the north-western coast of Nisyros and is interbedded within **ho**$_{a}$ (log 8 in Fig. 3.2b, and Fig. 3.8). All these deposits are in places intensely altered by hydrothermal activity, which occurs along N030°-trending faults.

3.3.2. Kremastò synthem

Deposits related to this synthem crop out mainly at the interior of the Nisyros caldera and have been extensively studied by Volentik et al. (2002) to whom the reader is referred for a detailed description.

The lowermost unit cropping out on the caldera floor is represented by the strongly tectonized lavas of **lf**^{1} (log 3, Fig. 3.2a, and Fig. 3.4). As previously stated by Volentik et al. (2002), there is no evidence for correlating this unit with the pillow lavas of **ho**$_{a}$, as proposed by Papanikolaou et al. (1991).

The other relevant feature of this synthem is the occurrence of the Lakkì explosive sequence (Fig. 3.2c-A & B) to which Volentik et al. (2002) attributed the formation of the first summit caldera depression on Nisyros. Lithic and magmatic fraction contents of the **ka** deposits are presented in Fig. 3.10-A & B.

3.3.3. Katò Lakkì synthem

It essentially consists of the Melisserì deposits (**ms**), as well as the lacustrine deposits (Fig. 3.11 and Fig. 2.7 in Volentik et al.(a), this volume) lying into an early caldera depression presumably formed as a consequence of the Lakkì explosive eruptions. The Melisserì andesitic pyroclastic unit is found throughout the island, and displays its most proximal facies along the northern caldera wall. It is characterised by pinkish red pumices and scoriae and displays a fallout level at its base (Figs. 3.2c-C and 3.5), followed in the most proximal sections by a 30-m-thick pyroclastic flow deposit, and finally by a 3.5 m succession of fall, surges, and pyroclastic flows (Fig. 2.8 in Volentik et al.(a), this volume). Lithic and magmatic fraction contents of the **ms** deposits are shown in Fig. 3.10-C & D.

Pyroclastic flow deposits of a maximum thickness of 5.0 m displaying distinctly lower vesicularity, larger vesicle size and higher porphyric index of the magmatic fraction (Evangelistra sub-unit) have been locally found below the main body of pyroclastic flows of the Melisserì eruption, indicating an initial volatile-rich phase in the Melisserì eruptive episode.

3.3.4. Lies synthem

This synthem begins with the epiclastic deposits of the $\mathbf{ms_j}$ unit, attaining a maximum thickness of 2-3 m along the northern caldera walls below Emboriò. Lies is the most complex synthematic unit defined on Nisyros. It comprises 12 stratigraphic units, most of which were first recognized along the caldera walls (Fig. 3.2a-c and Figs. 3.3 to 3.7) and described in Volentik et al. (2002).

A number of these units also crop out extensively outside of the caldera, like $\mathbf{lf^6}$, an andesitic lava flow with a thick sole of red scoriae that is found mainly in the northern part of the caldera (Fig. 2.6 in Volentik et al.(a), this volume) and in the north-eastern part of the entire island. Together with lavas $\mathbf{lf^5}$ and $\mathbf{xlf_b}$ it constitutes a widespread lava sequence that we will refer to as the Ellinika lavas (Figs. 3.2a and 3.4 to 3.6).

The most characteristic feature of this synthem is the scattering of the eruptive centres all around the island that resulted in the formation of a number of tuff cone and scoria cone deposits (Figs. 3.9 & 3.12). The Pahia Ammos sequence (**pa**), which has been stratigraphically detailed by Keller et al. (1990) and Innocenti et al. (2002), is a typical illustration thereof (Fig. 3.12).

This complex unit is composed principally of light grey surge deposits, with impact sags, pisolitic ashes, proximal andesite to dacite fallout deposits and minor pyroclastic flow deposits, with a number of intercalated palaeosoils. In the proximal fallout deposits, lithics are common and include fresh andesitic lavas, limestones, marbles, skarns and magmatic cumulates (Fig. 3.10-E, F, G & H). The maximum thickness of this unit is about 80 m and typical deposits can be found between the beaches of Lies and Pahia Ammos, along the eastern shore of Nisyros (Fig. 2.12 in Volentik et al.(a), this volume). We have also attributed to this unit some hydrothermally altered outcrops on the western shore of Nisyros, that consist of laminated surge deposits and accretionary lapilli, still recognizable in less altered outcrops.

Unit $\mathbf{pa_j}$ reworks the **pa** deposits. It is composed of debris flow and hyper-concentrated flow deposits of limited extension that mark the subdivision of the Lies synthem into the sub-synthems of *Aphionas* and *Xolante*. These epiclastites display flow structures as well as channel and pinch out structures, which are typical of deposition in a stream-like environment. These deposits are located in the lowest topographic levels of the eastern part of Nisyros, lying above **pa**.

Unit $\mathbf{vs_n}$ is composed of a basalt-andesitic fallout deposit (possibly resulting from a violent strombolian eruption), showing proximal characteristics (high thickness and poor sorting) near the caldera rim, and decreasing in thickness quickly along the slopes of the volcano towards the sea, where a well-sorted fallout deposit is recognisable. The most representative of the few available outcrops is located at the top of the tuff cones in the area between the Monastery of Panagia Kyra and the beach of Lies (Fig. 2.14 in Volentik et al.(a), this volume). The thickness of the deposit is about 3 m on the caldera rim and about 1.5 m in the area of the Monastery of Panagia Kyra. It must be underscored that this unit is not indicated in the geological map owing to its limited thickness and the small numbers of places where it crops out.

The basalt-andesitic pyroclastic unit **xo** is composed of four different deposit types. The first type of deposit ($\mathbf{xo_{n1}}$) was vented from a number of strombolian cones distributed at this stratigraphic level all around the island: it is a red scoriae fallout deposit with proximal characteristics (spatter cone facies with agglutinated fragments of fresh lava); $\mathbf{xo_{n2}}$ is a black scoriae fallout deposit resulting from the same eruptive activity, but with distal features (strombolian cone facies); $\mathbf{xo_h}$ is a facies of planar bedded surge deposits; $\mathbf{xo_c}$ is a facies of pyroclastic flow deposits; in particular, a violet pyroclastic flow deposit (basalt-andesitic in composition) including pockets of red scoriae spatter cone fragments (up to 2 m), with a strong erosive contact at its base, is recognisable. No lithics were found in the red scoriae horizons, whereas lithics are common in the scoria cones and comprise andesitic lavas, limestones, marbles, and magmatic cumulates (Vanderkluysen & Volentik, 2001). Lithics in the pyroclastic flows are composed essentially of Argos lava fragments. Usually, the thickness of $\mathbf{xo_{n1}}$ and $\mathbf{xo_{n2}}$ together does not exceed 10-15 m, and $\mathbf{xo_c}$ reaches a maximum thickness of 5-7 m in valleys. The spatial distribution of $\mathbf{xo_{n1}}$ and $\mathbf{xo_{n2}}$ is limited to the areas around the vents.

Unit $\mathbf{lf^8}$ ends the Lies synthem and is related to the previous unit, in that it is composed of several lava flows flowing out of the spatter cones and the scoria cones. As several such edifices can coexist in one area, the cone-related deposits can display interfingering relationships (e.g. Fig. 3.13). These lavas are basalt-andesitic in composition and do not exceed 5-10 m in thickness. Aghia Irini, the Monastery of Stàvros (Fig. 3.7), and Avlaki (Fig. 3.13) are some locations to observe nicely exposed relations between **xo** and $\mathbf{lf^8}$.

3.3.5. Fournià synthem

A period of rest in the volcanic activity is responsible of intense erosion, reworking and re-sedimentation of the previous volcanic deposits, which generated the Paleocastro epiclastic deposits ($\mathbf{pc_j}$). This unit is composed of different epiclastic deposits, such as proximal debris flow deposits and more distal hyper-concentrated flow deposits. Flow structures, load casts, channel and pinch out structures are common. This unit reaches a thickness of 15-20 m in palaeo-valleys, such as in the area of Kàrdia, and shows a remarkable extent around the island.

The basalt-andesitic to andesitic lava flows of Aghia Basilei (**blf**), with a thick red scoriae sole and top, directly overlay the Paleocastro epiclastic deposits. In some places, agglutinated red scoriae deposits suggest proximity to the volcanic vent (for instance along the western part of the caldera walls or on the western flanks of the volcano, Fig. 3.3). The maximum thickness of this lava flow succession is 20-25 m along the western part of the caldera cliffs. This unit is located principally on the western flanks of the volcano, from Mandraki to the valley of Kàrdia.

At the end of the synthem, the dacitic activity of Emboriò (**emb**) took place all along the northern part of Nisyros volcano, from the castle of Paleocastro (above Mandraki) to Emboriò (Figs. 3.3 & 3.5). The dominant facies of this unit is a typically light grey dacite that includes 1-2% of andesitic enclaves. This unit forms characteristic lava domes and associated dome collapse pyroclastic deposits (block and ash flows). Indeed, the composition of the Emboriò lava dome is the same as that of the lava blocks within the underlying block and ash flows. Currently, the best exposed dome is the 150-m-high hill of Akimaronas, which dominates the village of Emboriò ([Ak.] in Fig. 2.1-B, in Volentik et al.(a), this volume). A debris avalanche, possibly triggered by the domes' growth, signals the beginning of a new sythem

3.3.6. Kàrdia synthem

This synthem include the Vunàri debris avalanche deposits ($\mathbf{vu_l}$) and the two explosive eruption of the Lower (**lp**) and Upper (**up**) pumices. The debris avalanche deposit is capped by a palaeosoil and another palaeosoil subdivides the Lower from the Upper pumices.

The Vunàri debris avalanche deposit ($\mathbf{vu_l}$) is characterised by rounded blocks (ranging from less than 1 cm^3 to more than 1 m^3 and showing jigsaw fractures) within a fine matrix. The blocks in the deposit vary in composition from dacites (by far the most abundant ones, compositionally related to **emb**, the Emboriò lava domes) to andesites, from previous lava units; occasional red scoriae pockets are also present. After the debris avalanche event, volcanic activity resumed in the scarp area with the emplacement of the Lubunià lava flow (**llf**), which has the peculiarity to be the last andesitic event in the evolution of Nisyros volcano. The outcropping area is located between Loutrà and Mandraki.

The stratigraphic sequence of the Lower Pumice (**lp**) starts with a basal pumice fallout deposit (layer $\mathbf{lp_n}$) (Fig. 3.15), showing a reverse grading of the magmatic fraction, which is made up of rhyolitic pumices, and an increasing amount of lithic fragments towards the top of the deposit (Fig. 3.15-C & E). This fallout was found only in three different locations: (i) along the road from Mandraki to Loutra; (ii) along the road climbing from Palì to Emboriò (at 180 m elevation) and (iii) in the valley from Cape Katsuni to Emboriò (at 100 m elevation). In the northern part of the island, the fallout is overlain by pyroclastic density current deposits (layer $\mathbf{lp_f}$), characterised by pumice-rich, lithic-poor and almost matrix-free pyroclastic flow deposits (Figs. 3.15 to 3.17). In contrast, on the southern coast of the island, the sequence comprises a lithic-lag breccia (layer $\mathbf{lp_d}$) (Figs. 3.13 & 3.18) that is overlain by wavy surge deposits with impact sags (layer $\mathbf{lp_o}$) and topped by a matrix-rich pyroclastic flow deposit (layer $\mathbf{lp_c}$) (logs 15 and 16 in Fig. 3.2b). A ground layer deposit is associated with layer $\mathbf{lp_c}$. A widespread light brown palaeosoil tops the unit. Lithic fragments in this unit are made of fresh andesites and rhyolites, sub-intrusive rocks, fumarolised lava fragments, skarns, epidote- and amphibole-bearing lithics (Fig. 3.10). Limburg & Varekamp (1991) also report the presence of clinopyroxene-garnet fragments, clinopyroxenites and tremolite-bearing limestones as lithics in this unit.

Unit $\mathbf{pl_j}$ is composed of debris flow deposits that rework **emb** and **lp,** over which $\mathbf{pl_j}$ lies uncomformably (Fig. 3.15). The $\mathbf{pl_j}$ deposits are made of canalized **lp** pumices (locally displaying current structures) and Emboriò lava fragments floating in a sandy matrix. These deposits are typically 2-3 m thick and occur principally in the northern part of Nisyros. The top of $\mathbf{pl_j}$ is pedogenised.

Thick rhyolitic lava flows constitute the voluminous Nikià lava (**nlf**), which covers the whole eastern flank of the island all the way from the caldera rim to the sea, from the beach of Pahia Ammos to Avlaki. Vitrophyric and perlitic facies are locally found. Large amphibole-bearing enclaves of basalt-andesitic composition reaching 1.5 m in size are widespread within the lava flows. A palaeosoil covers the summit of the blocky surface of the lava flows. Typical outcrops are found near the Monastery of Aghios Ioannis Theologos and near the village of Nikià, where the thickness of **nlf** reaches 150 m. A neck that fed one of these flow units is exposed along the caldera wall ([N.] in Fig. 2.1-B, in Volentik et al.(a), this volume). We estimate the total volume at slightly more than 1 km^3, in agreement with Hardiman (1999).

The stratigraphic succession inside the Kàrdia synthem ends with the Upper Pumice pyroclastic unit (**up**). This rhyolitic pyroclastic unit comprises 4 different deposit typologies. The most complete exposures are located along the road between Palì and Lies beach at Cape Katsuni and in the abandoned quarry at Loutrà. In the section of Cape Katsuni (Fig. 3.17) this unit comprises:

$\mathbf{up_f}$: a 2-10 m thick pumice-rich pyroclastic flow deposit, lithic-poor and almost matrix free;

$\mathbf{up_o}$: a succession of wavy surges (Fig. 3.17-A$_3$);

$\mathbf{up_c}$: a pumice-rich pyroclastic flow;

$\mathbf{up_e}$: a pyroclastic flow deposit with a 3-4 m thick level enriched in lithics (Fig. 3.17-A$_4$);

$\mathbf{up_g}$: an ash flow deposit, comprising two other lithic-rich lenses;

$\mathbf{up_h}$: a final phreatomagmatic surge deposit with planar-bedded structures, reaching a maximum thickness of 5-8 m (Fig. 3.17-D).

Lithic fragments within the **up** pyroclastic unit are made up in majority of skarns, with subordinate fresh lava fragments and sub-intrusive rocks that have undergone various levels of argillization (Fig. 3.10). Limburg & Varekamp (1991) also report the presence of epidote-bearing lithics, pyroxenites, and limestones in the deposits of this unit.

3.3.7. Profitis Ilias synthem

The main feature of this synthem is represented by a number of rhyodacitic domes grown inside the western half of Nisyros caldera and partly outpouring from its southwestern rim. The stratigraphic succession of the domes has been described in Limburg & Varekamp (1991) and numbered accordingly in Fig. 2.1-C in Volentik et al.(a) (this volume). These domes are covered by exceptionally abundant active and ancient talus deposits. This fact is likely due to the reorganization into the talus fans of the dome carapace, destabilized by the frequent earthquakes that took place on Nisyros since their emplacement to recent times.

3.3.8. Yalì pumices

The little island of Yalì lies about 5 km North of Nisyros (Fig.3.19-A). Yalì deposits comprise mainly: (i) a thick rhyolitic pumice succession in the south, including the Yalì pumice breccia and the units overlying it, and (ii) rhyolitic obsidianaceous lavas in the north. These two portions of the island have been relatively recently connected by a sandy isthmus, named Mandra in Fig. 3.19-A. Phreatomagmatic surges are also found in the easternmost corner of the island. Based on stratigraphic field relations, obsidianaceous lavas appear to be younger than pumices and older than the easternmost phreatomagmatic deposits. The stratigraphic succession of Yalì pumices has been recently studied in detail by Allen & McPhie (2000) (Fig. 3.19-B). In their reconstruction, the >150 m-thick pumice breccia deposit (see Fig. 2.25-A in Volentik et al.(a), this volume) is the emerged remnant of a submarine tuff cone. The upper 1 m of the Yalì pumice breccia is cemented by carbonate and passes gradationally to a fossiliferous limestone, topped by brown soils of sandy silt and bioclastic sandstone (see Fig. 2.25-C in Volentik et al.(a), this volume). The overlaying pumice lapilli layer has been correlated by Allen & McPhie (2000) with the reworked pumices attributed to Yalì that are present on Nisyros (Keller et al., 1990; Limburg & Varekamp, 1991; Francalanci et al., 1995). This Yalì pumice fallout is at least 2.8 m thick, with a maximum diameter of pumices of 7-8 cm and shows a good sorting. These characteristics make unlikely that the eruptive vent is located on Yalì or in the nearby submarine area. As already mentioned the Yalì pumices are found on Nisyros only in few and limited outcrops, reworked in talus fans (see Fig. 2.25-D in Volentik et al.(a), this volume).

3.3.9. Gorceix synthem

A number of hydrothermal explosions took place in the southern Lakkì plain, some in historical times (Gorceix, 1873; Martelli, 1917, see Fig. 3.20). Related deposits (**gx**) are made up of debris flow deposits with variable, age-related amounts of matrix. Lava fragments inside the deposits vary in size from a few centimetres to a few metres, and are generally affected by fumarolic alteration processes preceding the eruption. The matrix is clayey to sandy in granulometry and yellow in colour. Its main characteristic is the presence of a variable amount of secondary sulphur and euhedral gypsum crystals (Marini et al., 1993). These debris flow deposits of hydrothermal origin were sampled in order to investigate their physical characters and the variations in these parameters with the distance from craters (Fig. 3.21). Granulometric analyses of Polyvotis, Alexandros and Stefanos proximal (sampled at the crater edges) debris flow deposits (Fig. 3.21-A, B & E) show the presence of ballistic and fallout components. This feature disappears with the increase in distance from the craters together with an increase in the fine matrix amount (Fig. 3.21-F). Disaggregation of matrix lumps in granulometric analyses performed under a water flow (Fig. 3.21-D) causes an increase in fine fractions with respect to dry granulometric tests (Fig. 3.21-C).

3.4. Discussion of stratigraphic data

3.4.1. Comparison between different stratigraphic successions

After the work of Di Paola (1974), the stratigraphy of Nisyros Volcano was investigated by Papanikolaou et al. (1991) and Vougioukalakis (1993). In the study of Di Paola (1974), the stratigraphic reconstruction was mainly based on the lithology of the few units he recognised. More detailed works were performed by Papanikolaou et al. (1991) and Vougioukalakis (1993) but the very same lithostratigraphic approach was applied again. In Table 3.3 the stratigraphic sequences reconstructed by Papanikolaou et al. (1991) and Vougioukalakis (1993) are compared with that obtained in the present work. We remark that the stratigraphy of Vougioukalakis (1993) bears some similarities with that presented here, except for a few details deriving from both Vougioukalakis' (1993) grouping of lavas of different stratigraphic position but similar composition into the same unit and to the use of UBSU criteria, tephrostratigraphy, and facies analysis of tephra deposits in the present study. We note also that the approach of Papanikolaou et al. (1991), based on the lithological facies only, resulted in the grouping of a large number of our stratigraphic units in few lithological subdivisions (Table 3.3). In addition, there are in Papanikolaou et al. (1991) some inconsistencies, such as the splitting of a single stratigraphic unit into more than one lithostratigraphic member. For instance, the Argos rhyolites (**alf**) belong to both lavas B and C in the lithostratigraphy proposed by Papanikolaou et al. (1991).

3.4.2. From sub-aqueous to sub-aerial activity

The volcanic activity on Nisyros began in the north-western sector of the present-day island, with the emission of submarine pillow lava flows (**ho$_a$**). The epiclastic deposits of **ho$_j$** rework the materials of the lower portion of **ho$_a$** in a fresh-water medium, which implies the development of an hydrographic network. These deposits only occur along the north-western coast of Nisyros where they are interbedded within ho$_a$ (Fig. 3.2b, log 8). These epiclastic deposits are 5-10 m thick and in places are intensely altered by hydrothermal activity, which occurs along N030°-trending faults. This depositional sequence implies that: (i) after the first effusive episode of **ho$_a$**, the palaeo-Nisyros was lifted up above sea level by a still unspecified event (see below) and (ii) erosion and re-sedimentation of part of the pillow lava pile as debris flow deposits took place afterwards. After the erosional episode, the area sank again below sea level and sub-marine effusive activity resumed with the emplacement of new pillow lavas. We propose here two hypotheses for explaining these movements, either (i) a tectonic activity which first lifted up the pillow lava sequence and then collapsed these products under the sea level or (ii) a magmatic process, such as the inflation of a magma chamber, perhaps the KPT magma chamber (if the KPT pumices found by Keller [1971] on top of the submarine sequence correspond to the epiclastic deposit **ho$_j$**), or the intrusion of a plutonic body beneath the area, which was followed by deflation afterwards. Of course, a magmatic uplift followed by a tectonic collapse is also possible. Similar movements have been proposed elsewhere nearby Nisyros, such as for the origin of Yalì island (Keller, 1971; Allen & McPhie, 2000; Pe-Piper et al., 2005; Pe-Piper & Piper, 2005).

Into the litho-stratigraphic log of the Nisyros-1 geothermal well (Geotermica Italiana, 1983), which was drilled inside the Nisyros caldera (Nis-1 in Fig. 2.1-B of Volentik et al.(a), this volume), a "fine tuff or tuffite" was met directly over the non volcanic basement, from 590 to 650 m depth (from -480 to -540 meters with respect to sea level) and a "quartz rich tuff with palagonitic matrix" was found from 650 to 695 m depth (from -540 to -585 meters with respect to sea level). We interpret these deposits as related to the transition from submarine-to subaerial deposition of the pyroclastic density currents of the KPT eruption, in the area presently occupied by Nisyros island. If this hypothesis is correct, it implies both the limited extension toward the East of the submarine pillow lava flows (**ho$_a$**), since they are lacking in the well log, and a post-KPT age for the subaerial volcanic activity of Nisyros.

3.4.3. First explosive episode: Lakkì pyroclastics

After the build-up of the first sub-aerial volcanic edifice, Nisyros experienced its first explosive activity, namely the Lakkì eruption (**ka** and **kb**) (Vanderkluysen & Volentik 2001 and Volentik et al.

2002). This eruption is characterized by two explosive episodes (**ka** and **kb**) divided by an effusive stage (**lf**^{2}), whose products are found in the northern part of the present caldera depression.

In Fig. 3.2c-A & B, the sequence of pyroclastic deposits within **ka** and **kb** is shown. The Lakkì eruption seems to have started with a typical sub-plinian phase, resulting in a convective plume, which produced airfall deposit (Walker et al. 1971). The size of the magmatic fraction suggests a magmatic fragmentation, with a low amount of water entrained in the system. The plinian phase waned and ended with a 5 cm thick ash fall deposit. The plinian column became then unstable, because of either widening of the vent or increase in magma discharge rate or loss of volatiles (Sparks and Wilson 1976, Wilson et al. 1980 and Varekamp 1993) and the eruption vented then a sequence of pyroclastic flows and surges, showing both an increase in the water/magma ratio (decreasing size of the magmatic fraction, planar bedded structures in the surge deposits). The first explosive phase ended with a thick fallout deposit, well sorted, but showing proximal features, such as rare, big scoriae fragments. The inferred vent was certainly in the north-eastern sector of the present island.

This explosive stage was followed immediately by the effusion of an andesitic lava (**lf**^{2}), overlying conformably the pyroclastics of Lakkì A, without any evidence of time gap between them.

A new explosive event took place and its product covered the andesitic lava of **lf**^{2}. It began with a thick layer of surge deposits, showing a high water/magma interaction ratio. A short fallout event occurred in the surge sequence, suggesting either a provisional increase in the magma discharge rate or that less water was entrained in the conduit. The eruption produced then two thick pyroclastic flow deposits, with a 3-m-thick surge layer interbedded within.

The number of exposures for these explosive units are limited to locations along the caldera cliffs, so we have no idea of the distribution and the evolution of the Lakkì deposits in their distal facies and as a consequence of this, the volcanological interpretation is not accurate.

Nevertheless, we believed that a relatively small caldera collapse, confined to the northern sector of Nisyros (Fig. 6.1-C in Vanderkluysen et al.(b), this volume), occurred after the Lakkì eruptive cycle, as already proposed by Vanderkluysen & Volentik (2001) and Volentik et al. (2002). This hypothesis is supported by: (i) **lf**^{2} dips inwards with respect to the current caldera depression, suggesting the presence of a low in palaeo-morphology; (ii) the occurrence of two lake episodes, whose deposits are exposed along the northeastern sector of the current caldera cliff and (iii) the strong lithic content of the Lakkì B pyroclastic sequence.

3.4.4. Second explosive episode: Melisserì

After the Lakkì eruptive cycle, the caldera left by it was filled up by the thick lava flows of **lf**^{4}, and an other volcanic cone was built. Then a new explosive eruption took place on Nisyros, again in the northern sector of the current caldera, determining the deposition of the Melisserì pyroclastics (**ms**). Fig. 3.2c-C shows the detailed stratigraphy of the pyroclastic products of this eruption. It started with a sub-plinian phase, with a convective eruptive plume, resulting in a 2.5 to 3-m-thick fallout deposit (Walker et al. 1971), with some surge events interbedded, suggesting the instability of the eruptive column. The subsequent generation of a thick pyroclastic flow deposit, with minor surge events interbedded, was caused by the collapse of the eruptive column (Sparks & Wilson 1976 and Wilson et al. 1980) which, in turn, can reflect widening of the vent, increase in the magma discharge rate and/or decrease in volatiles in the magma. The presence of a final thin fallout deposit on the top of the Melisserì succession suggests the occurrence of a final magmatic pulse.

As for the Lakkì eruption, the number of outcrops is limited for the Melisserì unit as well, but we found some exposures outside the current caldera, which suggest a good distribution of this unit all around the island. This observation is very important to understand the meaning of such an eruption and its potential of caldera forming.

Hence, we suggest that an other small caldera collapse occurred after the Melisserì eruption (Fig. 6.1-D in Vanderkluysen et al.(b), this volume), even if no field evidence was found, because of burying by the most recent caldera collapse.

The Melisserì eruption is topped by a sequence of epiclastic deposits, which reworked and re-deposited the tephra deposits of Melisserì as debris flow layers (**ms**$_{l}$). This epiclastic sequence represents a period of quiescence in the volcanic activity of Nisyros, resulting in the erosion and re-organisation of the volcanic products and in a drastic change in the palaeo-morphology of the island. Volcanic activity resumed with the eruption of the Ellinika lavas on the north-eastern part of Nisyros.

3.4.5. Southern volcanic activity

Later on in the history of the volcano, another explosive eruption occurred, that of Stàvros, **sv** (Fig. 3.2c-D). This eruption started with an almost 10-m-thick lapilli-surge deposit, with planar-bedded structures, suggesting an initial phreatomagmatic stage. This explosive phase was not powerful enough to stabilize a plinian column and produced a succession of pyroclastic flows, when no water was involved in the eruption, and surges, when water/magma interaction occurred.

The number of exposures is restricted to the southern area of the present caldera cliffs, just below the Monastery of Stàvros, where the pyroclastic deposits show proximal characteristics. Consequently, we hypothesise that the location of the vent was in the southern part of the current caldera depression.

Following the eruption of the Stàvros pyroclastics, extrusion of rhyolitic magma (**alf**, Argos lava) occurred as lava flows and domes with minor associated block and ash flow deposits generated by gravitational dome collapse. This lava unit covered all the southern flanks of the volcano.

3.4.6. Off-centre volcanic activity

Rehren (1988), Keller et al. (1990) and Vougioukalakis (1998) have already described this volcanic activity, but all of them have grouped all these events in a single formation, known as the Kyra Pyroclastics Series. They proposed that the Kyra succession was produced by several strombolian to Plinian eruptions (whose source was in the current caldera) which brought about a caldera collapse afterwards.

According to our interpretation, off-centre volcanic activity began in the eastern part of Nisyros, through the extrusion of dacitic lavas (**lf**^{7}), which was followed by phreatomagmatic activity occurring on N340°-trending faults. This activity formed at least two tuff cones (**pa**) along the present eastern coast of Nisyros. Occurrence of accretionary lapilli in these tephra deposits denotes an important water/magma interaction either in the conduit or at the vent. This phreatomagmatic activity produced base surge deposits with impact sags, suggesting the proximity to the source and also minor pyroclastic flow deposits. When external water did not enter the conduit anymore, normal strombolian fallout deposits were erupted from the vent.

Reworking of the tephra and re-deposition of the volcanic products in a succession of debris flow deposits (**pa**$_{j}$) took place shortly after the end of the phreatomagmatic activity. Then a violent strombolian event (**vs**$_{n}$) occurred, whose source is inferred to be somewhere along the eastern N030°-trending faults cutting the current caldera depression. It deposited a thick black scoriae airfall layer on the eastern sector, suggesting a wind blowing from west to east. Typical column height for such an event is less than 10 km, perhaps around 5 km (Arrighi et al. 2001).

Spatter cones and strombolian cones, widespread all around the island and located on major tectonic faults (Fig. 6.1-D in Vanderkluysen et al.(b), this volume) vented red and black scoriae proximal fallout (**xo**$_{n1}$ and **xo**$_{n2}$ respectively) and minor density currents, such as phreatomagmatic surge and pyroclastic flow deposits (**xo**$_{h}$ and **xo**$_{c}$ respectively). Such events are thought to have tapped deeper magma reservoirs (see Vanderkluysen et al.(a), this volume), due to the strong regional tectonic activity occurring at this time.

3.4.7. The Fournià synthem

This synthem is characterized by a well-developed epiclastic series (**pc**$_{j}$) that remobilized the underlying units (**xo**, **lf**^{8}) and is ubiquitous on Nisyros. The presence of widespread epiclastites, partly filling palaeovalleys, denotes a period of volcanic rest sufficiently long to reorganise the morphology of the island. The volcanic activity resumed with the eruption of the Aghia Basilei lava flows (**blf**), which cover the western flanks of Nisyros.

3.4.8. The Vunari debris avalanche

Unit **vu**$_{j}$ was formerly interpreted as a block and ash flow deposit due to dome collapses (Limburg & Varekamp, 1991; Vougioukalakis, 1993; Francalanci et al., 1995). However the deposition of this unit produced a hummocky topography (Figs. 3.14 & 3.15), with each hummock being in general 20-30 m high, that extends into the sea, as suggested by the bathymetry between Palì and Mandraki. The core of some hummocks has been exposed along the northern shore of Nisyros, from Mandraki to Palì, cut by the sea cliff. Some show intact internal structures, such as layering, and reverse grading of blocks within the hillock, suggesting that the hummocky upper surface is original, and was not generated by post-emplacement alteration or erosion, although a palaeosoil caps the unit. Because of (i) the polymict nature of the deposit, which is composed of scoriae, andesitic, and prevailing dacitic blocks (as already recalled in section 3.6), (ii) its hummocky surface and (iii) its spatial confinement within a depression defined by two well known normal faults (Di Paola, 1974; Papanikolaou et al., 1991), we interpret this deposit as the result of a debris avalanche event. In the past, the detachment circus of the sector collapse has been interpreted as a graben-like structure (Di Paola, 1974). Results of field mapping (Fig. 3.14) have revealed a more curved structure, consistent with the debris avalanche hypothesis.

Pre-collapse morphology was likely dominated by scoriae from **xo** and lavas of **lf**^{8}, overlying lavas from previous units **lf**^{5} to **lf**^{6}, as is the case elsewhere in the northern part of the volcano, on which Emboriò dacites (**emb**) had grown. One of these domes or cryptodomes may have acted as a trigger for the avalanche, explaining the dominance of dacitic blocks within the deposit. Some other factors could have contributed to the triggering of the **vu**$_j$ debris avalanche, like (i) multiple faulting in the area of the sector collapse (see Volentik et al.(c), this volume; Vidal et al., 2000; Pe-Piper et al., 2005) and (ii) generation of hydrothermal clay minerals acting as a lubricant for the collapse (Principe et al.(a), this volume).

The collapse structure did not cut levels deeper than the scoriae of **xo**, suggesting that this unconsolidated deposit acted as the main detachment surface for the debris avalanche event. The presence of subordinate andesitic blocks and scoriae would then reflect the involvement of rocks interposed between **xo** and **emb**.

3.4.9. The Lower Pumices (lp)

The Lower Pumice eruption was the first explosive event involving rhyolitic magma on Nisyros, as a magma of this type was previously discharged only in the effusive eruption of Argos, **alf** (see above). The **lp** eruption followed a period of quiescence (revealed by the existence of a palaeosoil underlying the Lower Pumice pyroclastic deposits) after the catastrophic **vu**$_j$ debris avalanche.

Initial fall and flow stage

This explosive eruption was plinian-like, with a fall-flow-surge-flow sequence (Cas & Wright 1987). A steady convective plume (Fig. 3.22-A) developed at the beginning of the eruptive phase, resulting in the deposition of a pumice fallout deposit (**lp**$_n$), which shows reverse grading, suggesting an increase in both eruption intensity (due to conduit erosion) and eruption column height with time, before the sudden onset of the pyroclastic flow formation (Sparks & Wilson 1976, and Wilson et al. 1980). The distribution of this fallout layer is not accurate, because of the small number of exposures around the island, but it seems to exist (or have existed) only in the north, north-eastern part of Nisyros, which suggests a dispersal axis to the north, north-east (Fig. 3.23-A). The initial inferred vent of the Lower Pumice appears to be located in the eastern-central part of the current caldera depression (Fig 3.23-A).

The plinian column then became unstable, because of either widening of the vent or increase in the magma discharge rate or decrease in the initial particle velocity, and collapsed (Sparks & Wilson 1976 and Wilson et al. 1980), thus forming pumice-rich, lithic-poor pyroclastic flows (**lp**$_f$), directed towards the North, North-East sector of the island (Fig.3.22-B).

The lithic content remained low during the whole first phase of the eruption, even in the upper part of the initial pumice fallout deposit (Pumice/Lithic ratio ≥ 0.9). The data on the pumice fallout deposit are too scarce to compute column height and the total amount of discharged magma. It is worth recalling that Wilson (1976) and Carey & Sigurdsson (1989) proposed column heights and magma discharge rates of 20-30 km and 1.6×10^6 to 1.1×10^9 kg/s, respectively, for typical Plinian eruptions.

Limburg & Varekamp (1991) estimated an eruption column height of 15-20 km and an approximate DRE volume of 2-3 km^3 for the Lower Pumice eruption, based on calculations done for the Upper Pumice eruption.

Lithic-lag breccia and ignimbrite-type deposits

The main change in the eruptive conditions at the onset of the lag-breccia (**lp**$_d$) is reflected both in the nature and areal distribution of the deposits as well as in their lithic content. This lag-breccia is distributed on the southern flanks of the volcano, with more proximal features near the current caldera rims and in the area of Avlaki and more distal characteristics in Lefkos Cove (Figs. 3.22-C and 3.23-A), which suggests a source in the eastern sector of the present caldera depression. This layer is associated with the two overlaying deposits: (i) wavy surge deposits (Unit **lp**$_o$), showing impact sags and restricted to the neighborhood of Avlaki; (ii) a ignimbrite-type pyroclastic flow deposit (**lp**$_c$) with its associated ground layer (Sparks et al. 1973) at the base; **lp**$_c$ is characterized by a pumice- and matrix-rich pyroclastic flow deposit, showing the same proximal and distal characteristics as the lag-breccia deposit.

Barberi et al. (1988), Limburg & Varekamp (1991) and Vanderkluysen & Volentik (2001) attributed the higher lithic content in the **lp**$_d$ products to downward migration of the fragmentation level during the eruption. See Fig. 3.10 for a description of the lithic content of the **lp** deposits.

Accepting our interpretation, at this stage, the eruptive processes changed and magma discharge was not occurring through a single vent anymore but rather through a N030°-trending regional fault situated in the eastern sector of the current caldera depression. A similar process was already proposed by Druitt (1985) and Druitt & Sparks (1984) for the eruption of the Cap Riva pyroclastics at Santorini. Indeed, they predicted the occurrence of two distinct eruptive phases for many large ignimbrite eruptions. Magma pressure in an overpressured magma chamber is bound to decrease with time owing to progressive magma discharge if refilling of the magma chamber either does not occur or does not keep pace. The roof of the magma chamber is supported by the underlying magma as long as overpressure is maintained. In contrast, if the magma chamber becomes underpressured and the roof's strength is exceeded, the roof fractures and collapses. The eruption may continue through new vents activated by roof collapse.

Indeed, the existence of two distinct sets of **lp** deposits, a northern one and a southern one, fits with the hypothesis of an eruption process requiring the activation of multiple vents.

Summing up, the model for the Lower Pumice eruption (Fig. 3.22) involves: (i) an initial Plinian eruption from a single vent, with subsequent collapse of the convective plume, leading to the deposition of the pumice-rich pyroclastic flow; (ii) onset of the caldera collapse accompanied by deposition of the lithic lag-breccia and of the pyroclastic flows and surges. The lithic-lag breccia is much coarser and lithic-rich than the previous pyroclastic flow deposit, which suggests an increase in the magma discharge rate as a consequence of the caldera collapse (Druitt & Sparks 1984 and Walker 1985). The hypothetical caldera shape left by the Lower Pumice eruption is illustrated in Fig. 3.23-A.

3.4.10. The Nikià rhyolitic lava flows (nlf)

The existence of a 10 to 20-cm-thick palaeosoil between the top of the Lower Pumice pyroclastics and the overlying Nikià lava flows suggests an important period of volcanic rest before the extrusion of these rhyolitic lavas.

The Nikià lava flows were erupted along the N030°-trending fault cutting the current caldera depression and flowed towards the southeast (Fig. 6.1-F in Vanderkluysen et al.(b), this volume). As already recalled, we estimated the total volume of magma erupted by means of a simple geometrical model obtaining slightly more than 1.0 km^3, in a good agreement with Hardiman (1999). The extrusion of this huge volume of magma could have been responsible of an incremental collapse (to the east) of the caldera left by the **lp** eruption, as already suggested by Hardiman (1999).

A palaeosoil covers the blocky surface of the Nikià lava flow (Fig. 3.16-E), suggesting a long period of volcanic rest before the next volcanic activity on Nisyros.

3.4.11. The Upper Pumices (up)

This is the second explosive event involving rhyolitic magma on Nisyros. The first phase of this eruption is represented by pumice-rich pyroclastic flow and wavy surge deposits ($\mathbf{up_f}$ and $\mathbf{up_o}$). It is a purely magmatic stage, as indicated by: (i) the size of the juvenile magma fraction, which is typical of a purely magmatic fragmentation process; (ii) wavy surge deposits, showing dune and anti-dune structures, which are also typical of magmatic eruptions.

The ratio of pyroclastic flow/surge deposits decrease from the inferred source to the east, as expected, because of the stronger transport energy of surges with respect to pyroclastic flows. The average sizes of the three biggest pumices and lithics in these deposits are similar.

In the north-eastern part of Nisyros (Cape Katsuni, see Fig. 3.17), matrix-rich pyroclastic deposits ($\mathbf{up_c}$) overlie the first pyroclastic products. The contact between $\mathbf{up_c}$ and $\mathbf{up_f}$ is conformable and the lack of evidence for any time break between these two units suggests they were vented during the same volcanic event; $\mathbf{up_c}$ is covered by an other matrix-rich pyroclastic flow deposit ($\mathbf{up_e}$), which includes a 3-m-thick, lithic-rich lense.

The overlying thick ash flow deposit ($\mathbf{up_g}$) presents a decrease in size of the juvenile magma, suggesting an increase in water/magma interaction in the conduit, which is confirmed by the final phreatomagmatic surge deposits ($\mathbf{up_h}$). The latter was produced under a high water/magma interaction ratio, as indicated by the strong fragmentation of the juvenile magma and by the planar-bedded structures of the deposits (Fisher & Schmincke 1984).

Based on the available data, the eruptive model for the Upper Pumice eruption is not accurate, because of the complexity of the eruptive processes and the distribution of the deposits. A more detailed study is needed to elaborate an accurate eruptive model for the Upper Pumice eruption.

Nevertheless, we reject the previous reconstruction of an eruption beginning at a central vent with a convecting plume, resulting in a pumice fallout deposit, and ending with a major caldera collapse (Barberi et al. 1988, Keller et al. 1990, Limburg & Varekamp 1991, Vougioukalakis 1998). In fact, the distribution and the physical characteristics of the Upper Pumice deposits suggest the occurrence of both (i) outpouring of pumice-rich pyroclastic flows from an off-centred vent localised on the northern slopes of Nisyros (Fig. 3.23-B), as already proposed by Hardiman (1999) and (ii) a fissural eruption along N030°-trending faults cutting the eastern sector of the current caldera depression, producing the pumice-rich pyroclastic flow deposit overlying the Nikià lava flow on the eastern slopes of the island (Fig. 3.23-B). We believe that the first stage of the Upper Pumice eruption was characterised by fountaining of the eruption column, which built up a tuff cone on the northern slopes of Nisyros. The distribution of **up_c** and **up_h**, which is restricted to the northeast sector of Nisyros, confirms the hypothesis of an inferred vent situated in the northern part of the island.

The outpouring of a lag-breccia concomitant with the drastical decrease in the magmatic fraction (**up_e** and **up_g**) may be related to either (i) an important input of water in the eruption conduit or (ii) the foundering of the roof of the magma chamber, consecutive to the pressure drop caused by prolonged magma discharge (see section 4.8). Barberi et al. (1988) attributed this possible increase in water/magma interaction ratio to the downward migration of the fragmentation level in the conduit during the course of the eruption. Limburg and Varekamp (1991) accredited this change in eruptive style to the massive addition of geothermal water, subsequent to hydrothermal break up. In our opinion, the presence of two distinct sequences of **up** deposits, also showing a different areal distribution, supports the second hypothesis, similar to the lp case (see section 4.8).

A column height of 15-20 km and an approximate pumice volume (DRE) of 2-3 km^3 were proposed by Limburg & Varekamp (1991), based on the thickness and distribution of the pumice fall deposit and the presence of a 7-cm-thick ash layer at 120 km distance (Vinci 1983). New field evidence gathered in this work demonstrates that the Upper Pumice eruption did not experience the sustained convective plume which is needed to produce a pumice fallout. Consequently, the eruption characteristics computed by Limburg & Varekamp (1991) represent overestimates.

A minor caldera collapse incremented certainly the size of the caldera depression at the end of the Upper Pumice eruption (Fig. 3.23-B), but it was much smaller than the major event proposed by Limburg & Varekamp (1991). Indeed, such an event should have included an important amount of Nikià lavas among the lithics, which is not the case for the Upper Pumice pyroclastic deposits, with the exception of minor Nikià lithics hosted in the eastern pyroclastic flow deposits, which were vented from the N030°-trending fault cutting the Nikià rhyolites.

3.4.12. Comparison between different interpretations of the Lower and Upper Pumices

Although Limburg & Varekamp (1991) and Hardiman (1999) studied in great detail the uppermost volcanic sequence on Nisyros, we propose a divergent interpretation of lithofacies to account for all the physical characters of the deposits (Table 3.4). The physical characters supporting our interpretation of Unit 4 of Limburg & Varekamp (1991) and LP-A of Hardiman (1999) as a pumice-rich pyroclastic flow deposit (**lp_f**) instead of a plinian fallout deposit are: the presence of an erosional surface at its base (Fig. 3.16-C), the low angularity of the pumices, the low degree of sorting (Fig. 3.15-D), the existence of a ground layer at the base of **lp_f** (Fig. 3.16-C), the presence of carbonized wood fragments and tree holes oriented along the flux direction (similar to those observed for **up_f**, see Fig. 3.16-F), and the marked increase in thickness of this unit in morphological depressions, e.g., from 0 to 20 m in thickness over 20 m of horizontal distance, as shown in Fig. 3.16-B – this is not possible for a fallout deposit!

We agree with Hardiman's (1999) interpretation of **lp_d** (unit 3 and LP-B of Limburg & Varekamp (1991) and Hardiman (1999), respectively) as a lithic lag breccia deposit, however Table 3.4 highlights some differences existing in the description and interpretation of the other deposits related to the **lp** eruption.

Following the same line of reasoning as for **lp_f**, the physical properties of **up_f** (5A in Limburg & Varekamp, 1991) (Fig. 3.16-D) characterize a pumice flow rather than a pumice fall deposit.

This wrong interpretation of the deposits of both the Lower and Upper Pumice eruptions has led previous authors to an erroneous evaluation of isopach maps, erupted magma volume and magnitude of this kind of eruptions at Nisyros.

3.4.13. The marine terrace

The marine terrace deposits described by Keller (1971) and Rehren (1988) are composed of rounded lava blocks (10-15 cm on average and up to 1 m) of varied origin in a sandy matrix. They are found at an elevation of about 30-60 m above sea level along the western coast of Nisyros (Fig. 2.28 in Volentik et al.(a), this volume). The terrace is mainly cut into **blf** and previous units. Nevertheless, its stratigraphic position cannot be determined with certainty. In fact, the nature of the deposit may prevent its preservation in some younger units, such as **lp** and **up**, due to their particular lithological characteristics. Besides, tectonic movements may have specifically affected the area of Mandraki and the western sector of the island (Pe-Piper & Piper, 2005), leading the terrace to emersion in this sector only. At any rate, the present position of the marine terrace, some tens of meters above sea level, testifies that at least this portion of the island experienced important vertical displacements in recent times.

3.5. Conclusions

Based on a new reconstruction of the stratigraphy of Nisyros volcanics, which was obtained through a modern volcanological approach, we recognised the following major points of interest in the volcanological evolution of Nisyros.

The basal pillow lava sequence **ho** was uplifted by an emersion stage as testified by the erosion of these submarine lavas and their re-deposition as subaerial debris flows; this implies that: (i) the emerged submarine volcanic edifice was large enough to develop an hydrographical system; (ii) important tectonic and/or magmatic events, possibly related with the KPT eruption, occurred before and after the erosive event.

Two successive volcanic cones grew afterwards (eastward with respect to the submarine structure) and occupied different areas. The first edifice, presumably smaller than the second one, was truncated by a caldera collapse as a consequence of the Lakkì eruption (**ka** and **kb**). The second cone was presumably affected by an other caldera collapse after the Melisserì eruption (**ms**).

A widespread volcanic activity coeval with $\mathbf{lf}^7$ to $\mathbf{lf}^8$ took place all around the island, producing spatter cones and scoria cones, with small associated lava flows. This volcanic activity was aligned along the major tectonic trends.

An ubiquitous epiclastic deposit ($\mathbf{pc}_\mathbf{J}$) denotes a period of volcanic rest, long enough to restructure the morphology of the island.

A major sector collapse, represented by the Vunàri debris avalanche ($\mathbf{vu}_\mathbf{J}$) occurred in the northern sector of Nisyros, connected to both the growth of the dacitic domes of Emboriò (**emb**) and the activation of multiple faulting in the area where the sector collapse originated.

A new eruptive model is proposed for the Lower Pumice (**lp**) eruption based on: (i) the recognition of the *true* fallout deposit ($\mathbf{lp}_\mathbf{n}$) of this eruption; (ii) the correct interpretation of the volcanic facies of the subsequent deposits.

The potential of caldera forming of the voluminous Nikià lava flows was confirmed. Indeed, this eruption brought about an increment in the size of the caldera left by the **lp** eruption, as already suggested by Hardiman (1999).

A new eruptive model is suggested for the Upper Pumice (**up**) eruption, which probably had two distinct volcanic vents. It appears to have contributed in a minor way to the formation of the present caldera, through an increment in the size of the pre-existing caldera.

Acknowledgments - We would like to thank Georgia Pe-Piper of the Department of Geology, Saint Mary's University at Halifax (Canada) who kindly provided a pre-print of the paper "The South Aegean active volcanic arc: relationships between magmatism and tectonics" that is expected to be printed in Developments in Volcanology. We are also grateful to Alessia Arias who kindly performed the sieving analysis of the hydrothermal debris flow deposits from the southern Lakkì plain.

Stratigraphy	Age	Method	Reference
Yalì obsidian	24 ka	FT on volcanic glass	Wagner et al., 1976
Yalì pumice fall	31 ka	Oxygen-isotope stratigraphy	Federman & Carey, 1980
Upper Pumice (**up**)	> 44 ka	^{14}C	Limburg & Varekamp, 1991
	110 ± 40 ka	FT on volcanic glass	Barberi et al., 1988
	24 ka	extrapolation of sed. rate	Vinci, 1983; 1985
Lower Pumice (**lp**)	35 ka	extrapolation of sed. rate	Hardiman, 1999
Palaeosoil	24.26 ± 0.56 ka	^{14}C (on charcoal)	Rehren, 1988
Kyra formation (**pa**)	37 ± 24 ka	K-Ar (on plagioclase)	Rehren, 1988
	39 ± 26 ka	K-Ar (on groundmass)	Rehren, 1988
Argos lava flow (**alf**)	200 ± 50 ka	K-Ar (on bulk rock)	Di Paola, 1974
	66.6 ± 2 ka	K-Ar (on plagioclase)	Rehren, 1988
Andesites	100 ± 100 ka	K-Ar (on bulk rock)	Matsuda et al., 1999
	800 ± 700 ka	K-Ar (on bulk rock)	Matsuda et al., 1999
Kos Plateau Tuff (KPT)	161 ± 1 ka	^{40}Ar/^{39}Ar (on sanidine)	Smith et al., 1996

Table 3.1. Summary of available age data for the volcanic rocks of Nisyros and nearby islands. The stratigraphic position of the palaeosoil dated at 24 ka by Rehren (1988) is not clear, but is thought to lie between **xo** (this study) and the Lower Pumice (**lp**) deposits.

Synthem	Sub-synthem	Unit	General description	Thickness (m)	Tectonics	Chemical composition	Most representative outcrop	Unit numbers of Volentik et al. (2002)
Gorceix		**gx**	Debris flow deposits related to hydrothermal eruptions; the matrix is clayey to sandy and yellow in colour and its characteristic is the presence of a variable amount of secondary sulphur and euhedral gypsum crystals (Marini et al., 1993)	30-40	N030°		southern part of the Lakkì plain and Ramos area	
Profitis Ilias		**pfi**	*Post-caldera* lava domes and dome coulées including andesitic enclaves up to 30 cm in size.	600	N030°	rhyodacitic	Mt Profitis Ilias	23
		ya$_j$	Pyroclastic deposit: the Yàli fallout layer is found remobilized within the talus fans around the island	2		rhyolitic	along the road to the caldera floor	22
		up$_j$	Epiclastic deposit reworking **up**	2				
Kàrdia	Pali	**up**	*Upper Pumice* pyroclastic deposits: flow-wavy surge-flow-planar bedded surge sequence	up to 30	N030°	rhyodacitic	Loutrà, Pali	
		nlf	*Nikià* lava flows; a palaeosoil covers the top of the blocky surface of the flows	150	N030°	rhyolitic	Monastery of Aghios Theologos and near Nikià	21
		pl$_j$	Epiclastic deposits composed of debris flow deposits that rework **emb** to **vu**$_l$; the top is pedogenised	5 and up to 20			Loutrà, Avlaki	
	Loutrà	**lp**	*Lower Pumice* pyroclastic deposits: fall-flow-wavy surge-flow sequence topped by a widespread palaeosoil	up to 20	N030°, N120°	rhyolitic	Loutrà, Pali, Avlaki	20
		llf	*Lubunià* lava flow	7	N340°	andesitic	northern flank of Nisyros (above Loutrà)	
		vu$_l$	*Vunàri* debris avlanche deposit: rounded blocks showing jigsaw fractures within a fine matrix producing a hummocky topography	20-30	N030°, N070°, N340°		northern coast of the island	
Fournià		**emb**	*Emboriò* lava flows and domes with minor block and ash flow deposits, including 1-2% of andesitic enclaves	150	N030°, N340°	dacitic	northern flank of Nisyros (Akimaronas Hill)	19
		blf	*Aghia Basilei* lava flows with thick red scoriae sole and top	up to 25	N030°	basalt-andesitic to andesitic	western flank of Nisyros	
		pc$_j$	*Paleocastro* epiclastic deposits reworking the previous volcanic deposits, resulting in the deposition of debris flow and hyper-concentrated flow	up to 20			western flank of the volcano in the area of Kàrdia	
Lies	Xolante	**lf**^{s}	Lava flows related with the previous explosive unit	up to 10	N030°, N070°, N120°, N340°	basalt-andesitic	widespread all around the island	17-18
		xo	Pyroclastic deposits: red and black scoriae fallout, planar bedded surges, and violet pyroclastic flow	up to 15	N030°, N070°, N120°, N340°	basalt-andesitic	widespread all around the island	15-16
		vs$_n$	Pyroclastic deposit: (violent strombolian?) fallout deposit	1	N070°	basalt-andesitic	between the Monastery of Kyra and the beach of Lies	
		pa$_j$	Epiclastic deposits reworking **pa**, resulting in debris flow and hyperconcentrated flow deposits; displays flow and channel and pinch out structures	20			in deep valleys in the eastern flank of Nisyros	

Table 3.2. Summary of the stratigraphy of Nisyros volcano.

Synthem	Sub-synthem	Unit	General description	Thickness (m)	Tectonics	Chemical composition	Most representative outcrop	Unit numbers of Volentik et al. (2002)
Lies	Afionas	**pa**	*Pahia Ammos* pyroclastic deposits: light grey surges, proximal fallout and minor pyroclastic flow, with a number of intercalated palaeosoils	80	N070°, N340°	andesitic to dacitic	between the beaches of Lies and Pahia Ammos	17
		$\mathbf{lf}^{7}$	Light grey lava flow	10	N070°, N340°	dacitic	between the beaches of Lies and Pahia Ammos	
		alf	*Argos* lava: dark grey lava flows and domes with minor block and ash flow deposits; reddish banding and perlitic textures	up to 60	N030°, N070°, N120°	rhyolitic	southern caldera walls below Monastery of Stàvros	14
		sv	*Stàvros* pyroclastic deposits: show a surge-flow sequence (note the lack of airfall deposit)	30	N030°, N070°	basalt-andesitic	southern caldera walls below Monastery of Stàvros	13
		$\mathbf{lf}^{6}$	Lava flow with a thick sole of red scoriae	up to 40	N030°, N070°	andesitic	north-eastern part of Nisyros	12
		$\mathbf{xlf}_{b}$	Lava flow with the peculiarity of incorporating up to 30% of enclaves (mainly andesitic blebs)	up to 25	N030°, N070°	dacitic	north-eastern part of Nisyros	11
		$\mathbf{lf}^{5}$	Lava flow	up to 40	N030°, N070°, N340°	andesitic	north-eastern part of Nisyros	10
		$\mathbf{ms}_{j}$	Epiclastic deposit reworking **ms**	2			northern and north-eastern caldera walls (below Emboriò)	9
Kato Lakki	Second lake	**ms**	*Melisseri* pyroclastic deposits: fall-flow-fall-surge-flow succession; magmatic fraction is composed of pinkish red pumices and scoriae	35	N030°	andesitic	northern caldera walls below Emboriò	8
		$\mathbf{lf}^{4}$	Scoria-rich lava flows	70	N030°	basalt-andesitic	north-eastern caldera walls (ubiquitous around the caldera)	7
		$\mathbf{sl}_{l}$	Lacustrine deposits: same deposits as $\mathbf{fl}_{l}$ but the sequence ends with deposition of subaqueus lapilli fallout and fine sand-waved surges	5			north-eastern caldera walls	6
	First lake	$\mathbf{lf}^{3}$	Lava flow emplaced on the top of the lacustrine beds, resulting in load cast structures within the water-saturated sediments	5	N030°	basalt-andesitic	north-eastern caldera walls	5
		$\mathbf{fl}_{l}$	Lacustrine deposits: varved deposits of dominant volcanic input with few intercalations of black, Mn-rich layers	5			north-eastern caldera walls	4
Kremastò		**kb**	*Lakkì B* pyroclastic deposits: show a surge-fall-flow-surge-flow sequence; same magmatic fraction as **ka**	60	N030°	basalt-andesitic	eastern caldera walls	
		$\mathbf{lf}^{2}$	Lava flow	40	N030°, N070°	andesitic	north-eastern caldera walls	3
		ka	*Lakkì A* pyroclastic deposits: show a fall-flow-surge-fall succession; the magmatic fraction is black, poorly vesiculated and crystal-poor (cpx and fds).	30	N030°	basalt-andesitic	north-eastern caldera walls	2
		$\mathbf{lf}^{1}$	Lava flow; strongly tectonised in some places	35	N030°	basalt-andesitic	north-eastern caldera floor	1
Kanafià		$\mathbf{ho}_{a}$	Epiclastic deposits reworking and interbedded within $\mathbf{ho}_{a}$; intense hydrothermal alteration in some places	10			north-western coast	
		$\mathbf{ho}_{a}$	*Holaki* hyaloclastites and pillow lavas	40-50	N030°	basalt-andesitic	Monastery of Aghios Spiliani	

Table 3.2. continued

Papanikolaou et al., 1991	**This work**	**Vougioukalakis, 1993**	**This work**
3: Caldera deposits	**gx**	19: Intra-caldera deposits	**gx**
		18: Yali upper pumices	**ya$_i$**
4: Profitis Ilias dacite	**pfi**	17: Post-caldera rhyodacitic domes	**pfi**
5: White pumice	**lp$_n$, lp$_f$, pl$_i$, up$_f$, ya$_i$**	16: Upper pumice	**up**
6: Nikia rhyolite	**nlf**	15: Nikia rhyolite	**nlf**
		14: Reworked lower pumice	**pl$_i$**
7: Pumice with volcanic breccia	**lp$_d$, lp$_o$, lp$_c$**	13: Lower Pumice	**lp**
		12: Dome collapse breccias	**emb, vu$_i$**
8: Pyroclastic D	**xo**		
		11: Upper dacitic lavas	**lf^7, emb**
9: Lavas D	**lf^8, blf**	10: Upper andesitic lavas and pyroclastics	**xlf$_b$, lf^6, xo, lf^8**
10: Grey pumice with rounded volcanic pebbles	**up$_o$, up$_e$, up$_g$**		
11: Grey pyroclastic	**pa, pa$_i$, xo**	9: Panagia Kyra pyroclastic series	**pa, pa$_i$, xo**
12: Lavas C	**lf^5, xlf$_b$, lf^6, alf, blf, emb, llf**	8: Middle rhyodacitic lavas	**xlf$_b$?, alf, lf^8?**
13: Pyroclastic B	**sl$_l$, ms, ms$_i$, sv, pa, pa$_i$, pc$_i$, vu$_i$**	7: Middle basic pyroclastics	**ms, ms$_i$**
14: Lavas B	**lf^2, lf^3, lf^4, lf^5, alf, lf^7, lf^8, blf**	6: Middle andesitic lava flows	**?**
		5: Castro conglomerate	**pc$_i$**
		4: Lower dacitic lavas	**lf^2**
15: Pyroclastic A	**ho$_i$, ka, kb, fl$_l$**	3: Lower basic pyroclastics	**ka, kb**
		2: Lower andesitic lava flows	**lf^1, lf^8**
16: Lavas, pillow lavas A	**ho$_a$, lf^1**	1: Submarine andesitic lavas and pyroclastics	**ho$_a$, ho$_i$**

Table 3.3. Comparisons of stratigraphic successions of Nisyros from this work and those of Papanikolaou et al. (1991) and Vougioukalakis (1993).

This work	**Limburg & Varekamp (1991)**	**Hardiman (1999)**
$\mathbf{up_h}$: surge deposits	Unit 5-D: surge deposits	UP-F: phreatomagmatic surge deposits
$\mathbf{up_g}$: ash flow deposit	Unit 5-D: surge deposits	UP-E: lapilli ash flow deposit
$\mathbf{up_e}$: lithic-rich pyroclastic flow deposit	Unit 5C: pyroclastic flow, with lag-breccia	UP-C: lithic-lag breccia
$\mathbf{up_c}$: pumice-rich pyroclastic flow deposit	Unit 5C: pyroclastic flow, with lag-breccia	UP-D: pumiceous flow deposit?
$\mathbf{up_o}$: pyroclastic flow/surge deposits	Unit 5B: surge deposits	UP-B: pumiceous surge deposits
$\mathbf{up_f}$: pumice flow	Unit 5A: pumice fall deposit	UP-A: lapilli-pumice fall deposit
$\mathbf{lp_c}$: pyroclastic flow deposit	Minor ash flows	LP-C: lapilli-pumice pyroclastic flow deposit
$\mathbf{lp_o}$: surge deposits	-	-
$\mathbf{lp_d}$: lithic-lag breccia deposit	Unit 3: plinian fallout deposit	LP-B: lag breccia or ground breccia
$\mathbf{lp_f}$: pumice flow deposit	Unit 4: plinian fallout deposit	LP-A: lapilli pumice fall deposit
$\mathbf{lp_n}$: pumice fall deposit	-	-

Table 3.4. Comparisons of stratigraphic successions of **lp** and **up** from this work and those of Limburg & Varekamp (1991) and Hardiman (1999).

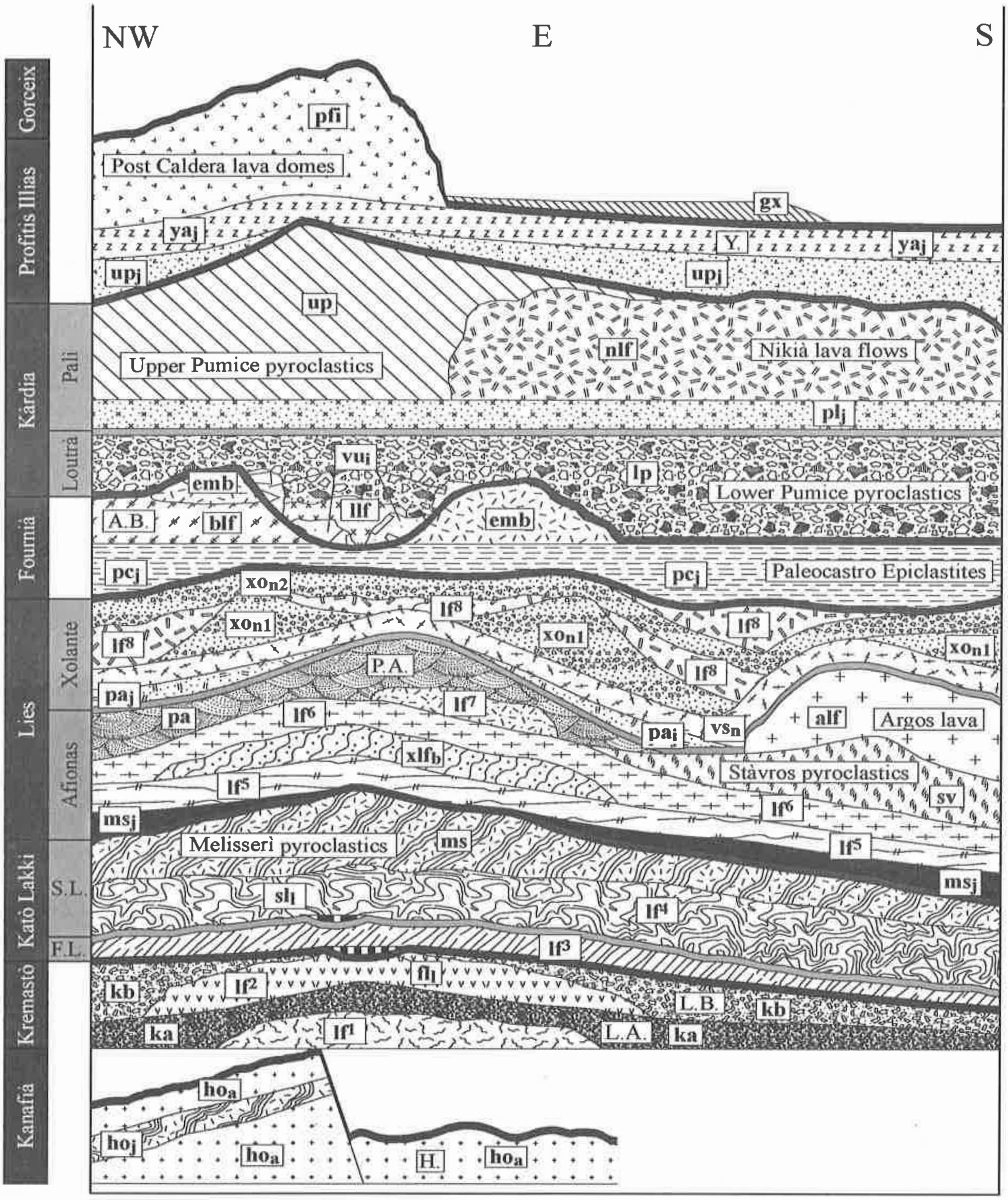

Fig. 3.1: Synthetic stratigraphic section. Names and numbers refer to the units defined in Volentik et al.(a) (this volume). Dark grey lines: synthematic boundaries. Grey lines: sub-synthematic boundaries. Names of synthems and sub-synthems appear in the left boxes, dark grey and grey, respectively. [F. L.] First Lake, [S. L.] Second Lake. [A.B.] Aghia Basilei lava flows; [H.] Holaki hyaloclastites and pillow lavas; [L.A.] Lakkì A pyroclastics; [L.B.] Lakkì B pyroclastics; [P.A.] Pahia Ammos Tuff cones; [Y.] Yalì fallout.

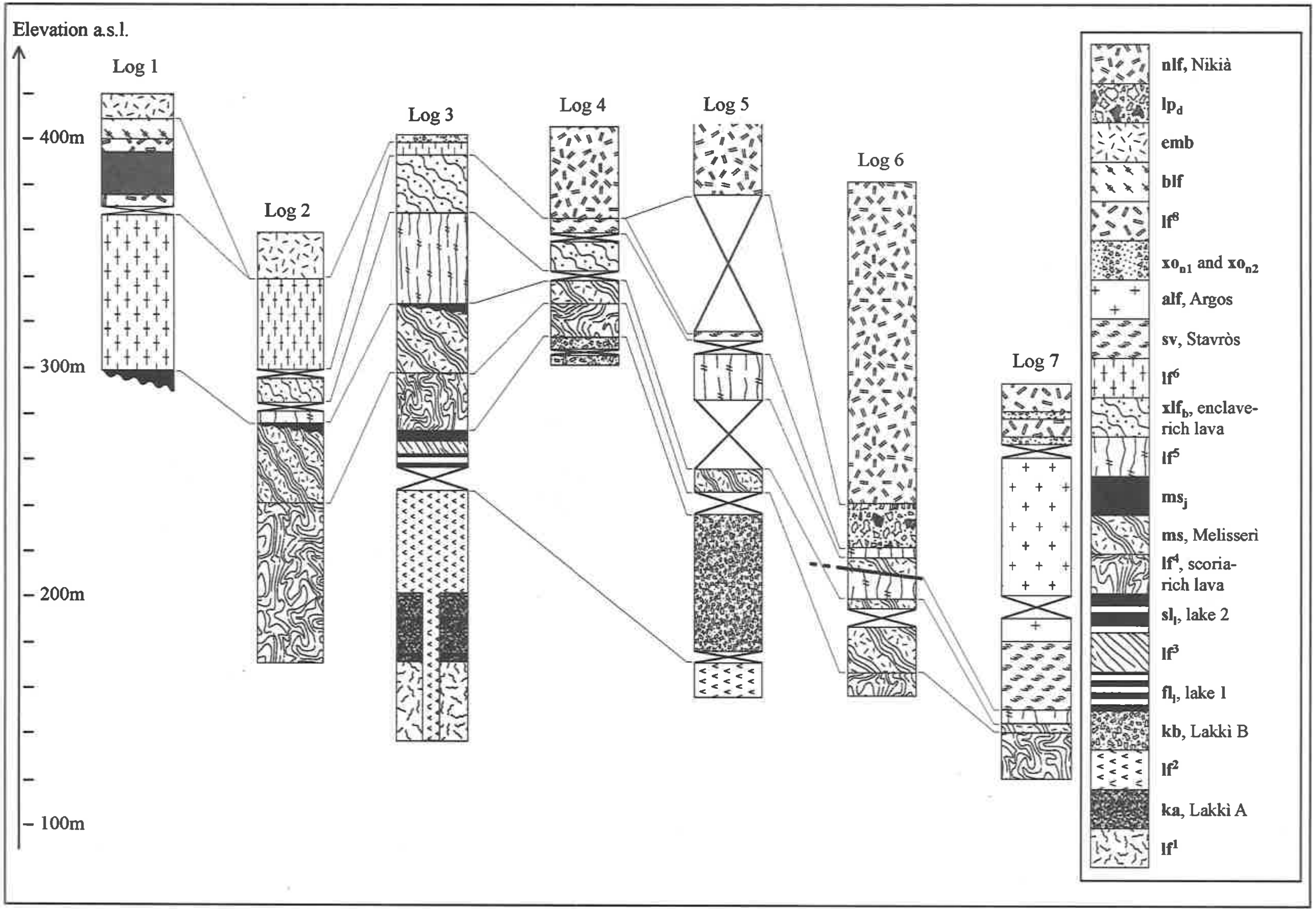

Fig. 3.2a: Correlations between representative stratigraphic sections along the caldera walls of Nisyros volcano. Location of stratigraphic logs in Fig. 2.1-B in Volentik et al.(a), (this volume). Bold alphanumeric codes from Volentik et al.(a) (this volume).

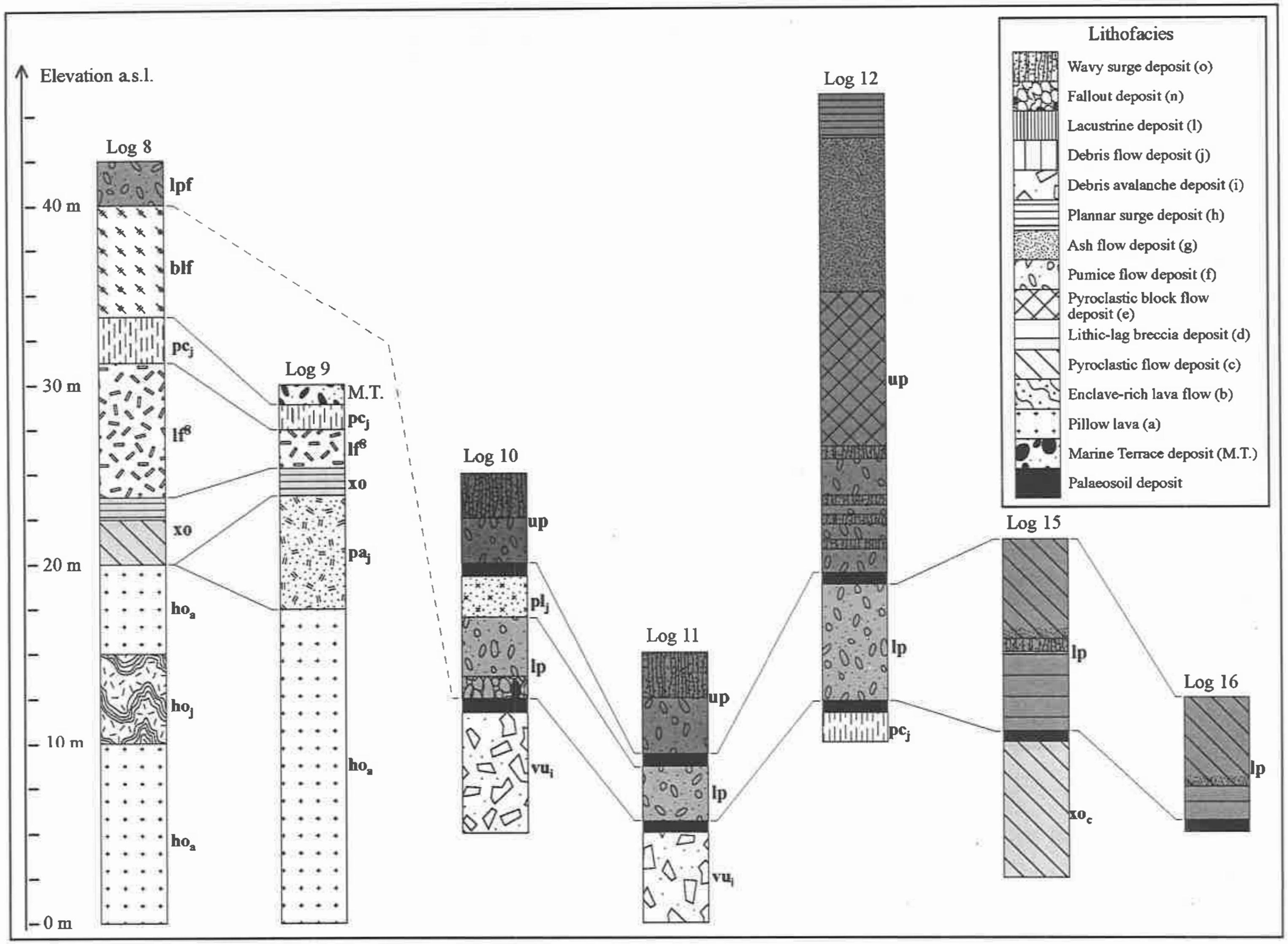

Fig. 3.2b: Correlations between representative stratigraphic sections on the flanks of Nisyros volcano. Location of stratigraphic logs in Fig. 2.1-B in Volentik et al.(a), (this volume). Bold alphanumeric codes from Volentik et al.(a) (this volume). Light grey areas, **xo** eruptive sequence; grey areas, **lp** eruptive sequence; dark grey areas, **up** eruptive sequence.

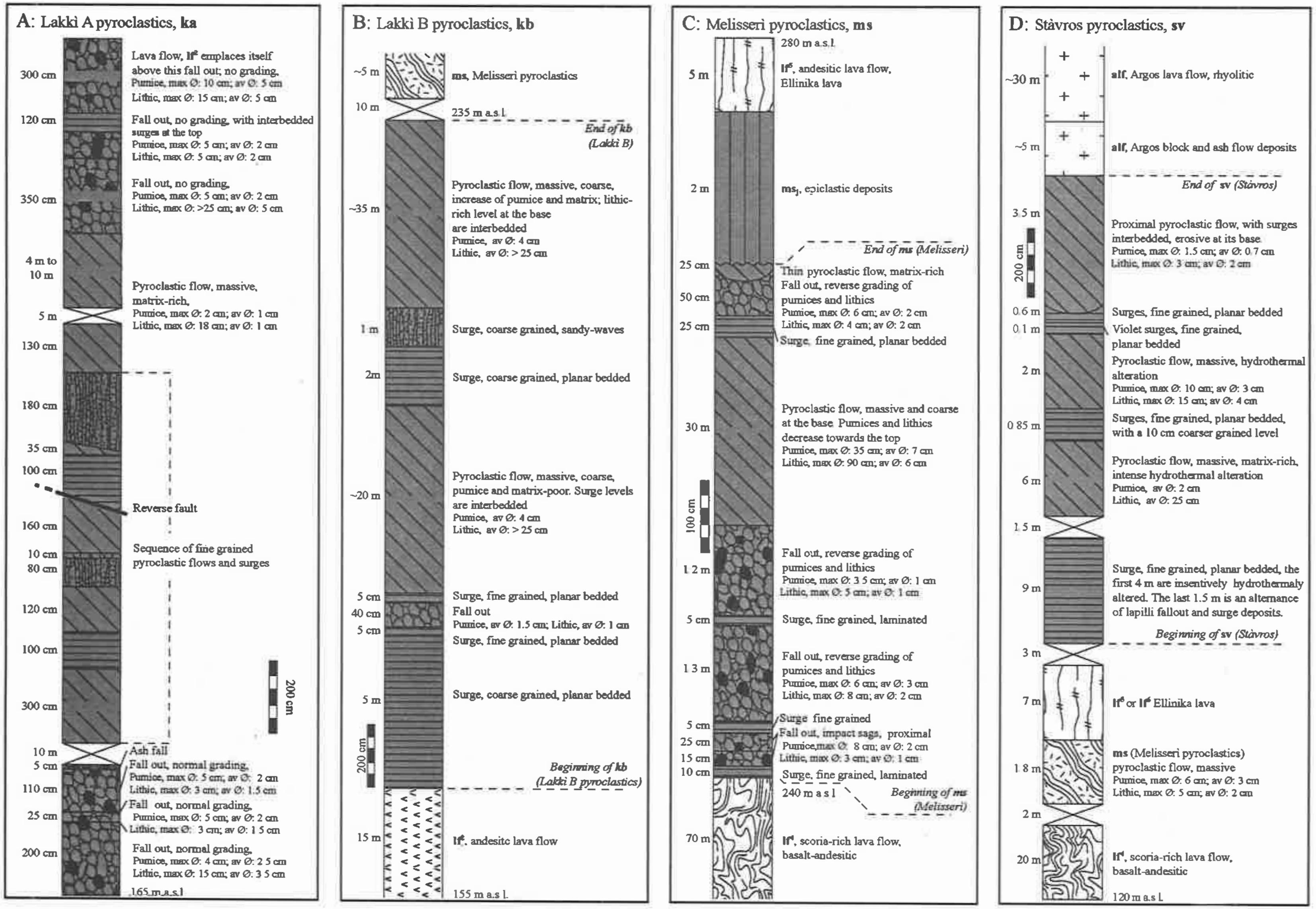

Fig. 3.2c: Tephrostratigraphic sections of: (A), Lakkì A unit (**ka**) (in log 3); (B) Lakkì B unit (**kb**) (in log 5) ; (C) Melisserì unit (**ms**) (in log 2); (D) Stàvros unit (**sv**) (in log 7). The grey area highlight the different pyroclastic units. See Fig. 2.1-B in Volentik et al.(a) (this volume) for the location of the different logs.

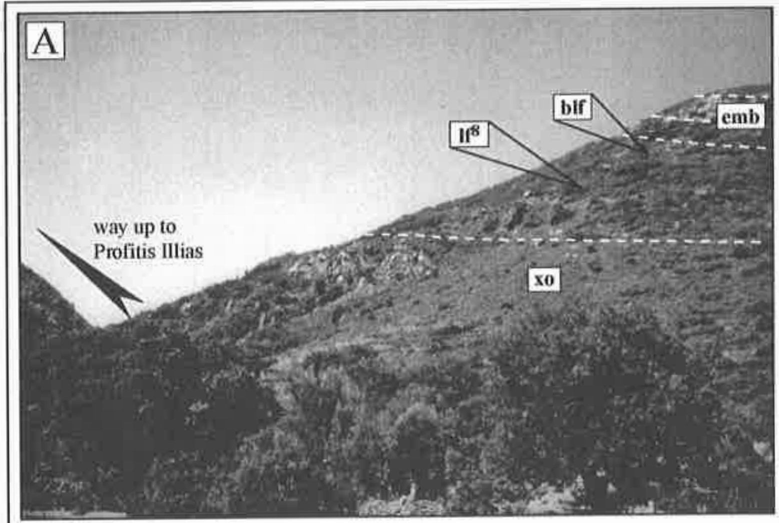

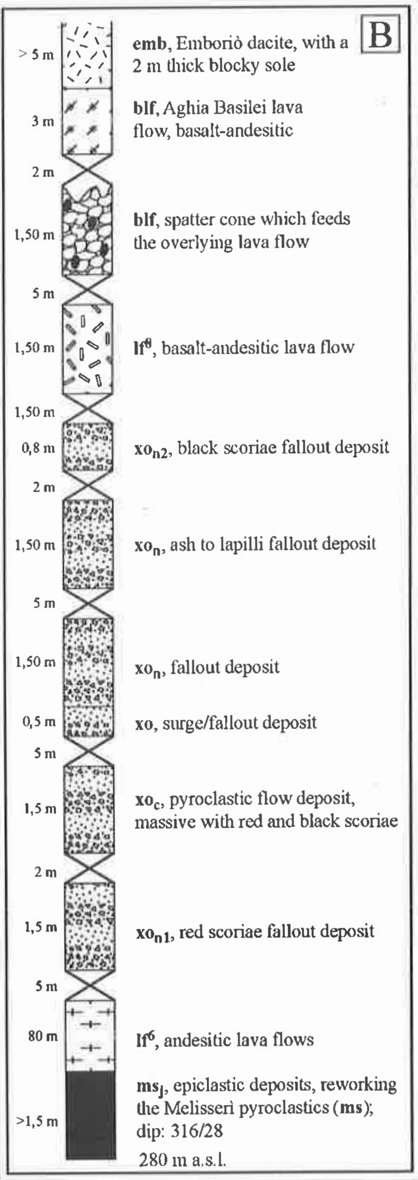

Fig. 3.3: Section 1 (Fig. 2.1-B in Volentik et al.(a), this volume), Evangelistra. A: General view of the caldera cliff above the Monastery of Evangelistra; B: Detailed stratigraphical section of this area. See legend in Fig. 3.1.

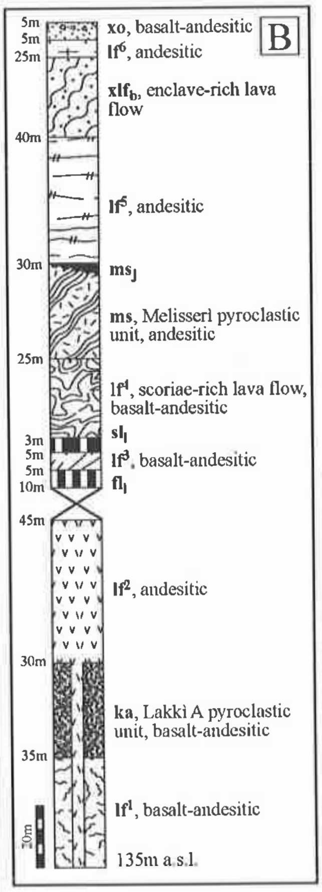

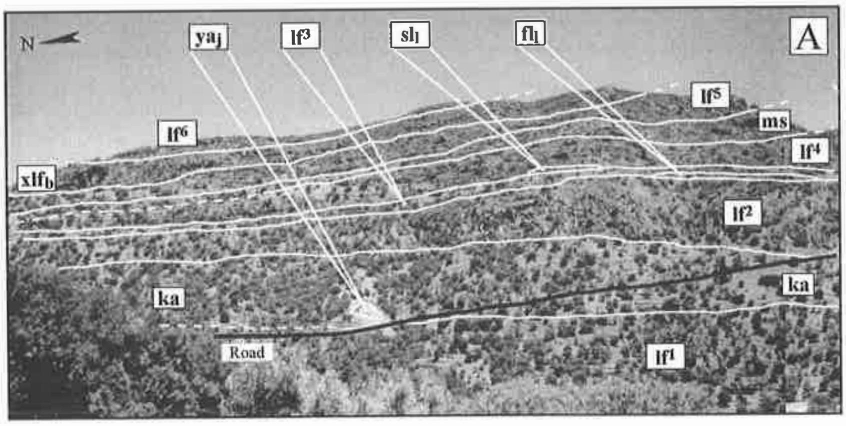

Fig. 3.4: A: Section 3 (Fig. 2.1 in Volentik et al.(a), this volume). A: General view of the north-eastern caldera cliff along the road down to the Lakki plain; B: Detailed stratigraphy of this sector of the caldera cliff. See legend in Fig. 3.1.

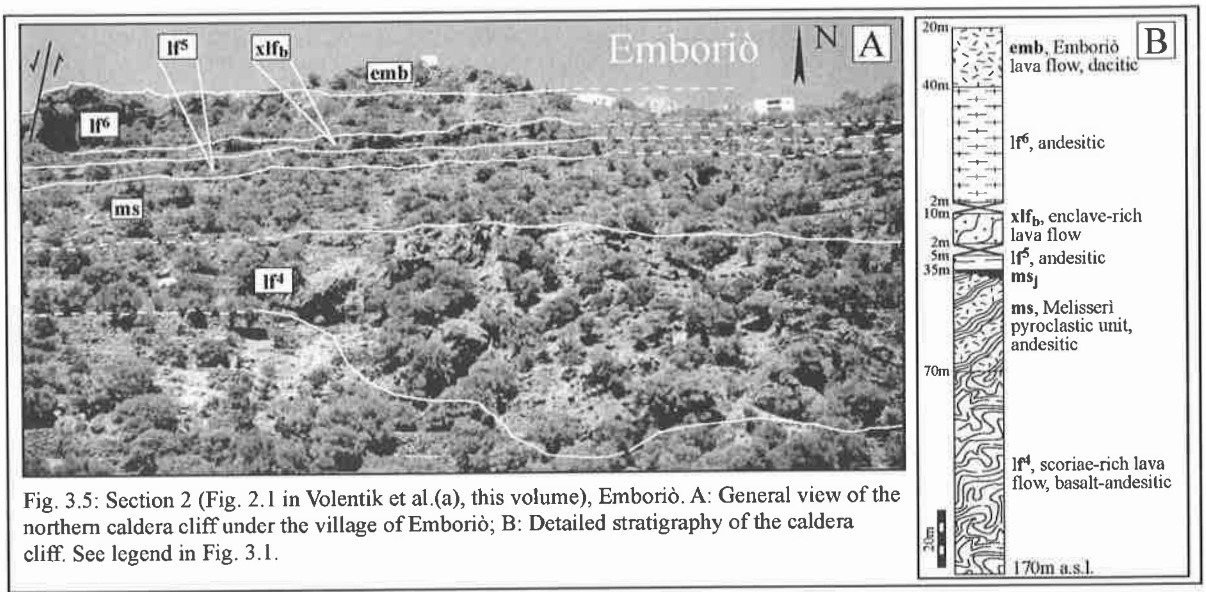

Fig. 3.5: Section 2 (Fig. 2.1 in Volentik et al.(a), this volume), Emboriò. A: General view of the northern caldera cliff under the village of Emboriò; B: Detailed stratigraphy of the caldera cliff. See legend in Fig. 3.1.

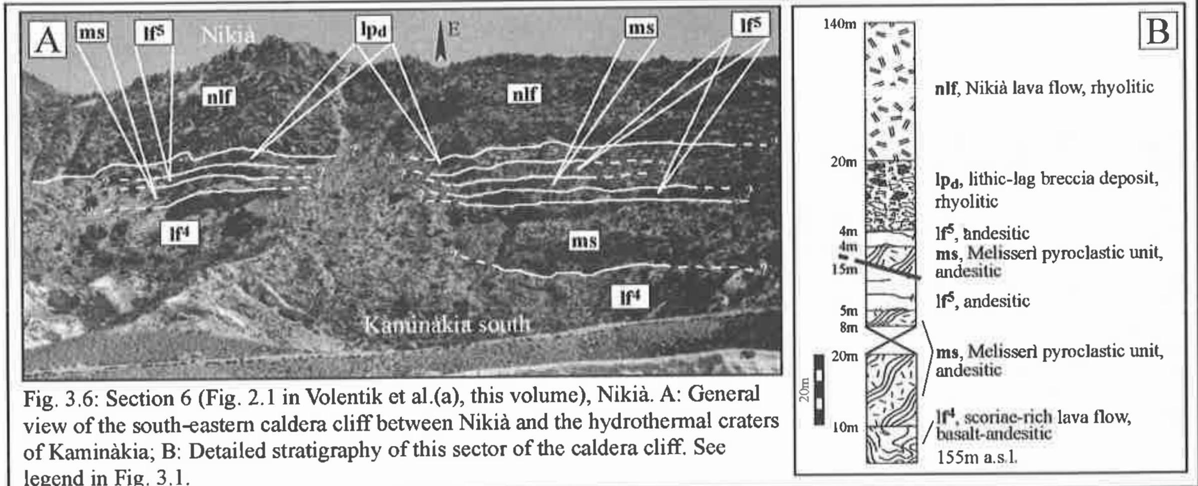

Fig. 3.6: Section 6 (Fig. 2.1 in Volentik et al.(a), this volume), Nikià. A: General view of the south-eastern caldera cliff between Nikià and the hydrothermal craters of Kaminàkia; B: Detailed stratigraphy of this sector of the caldera cliff. See legend in Fig. 3.1.

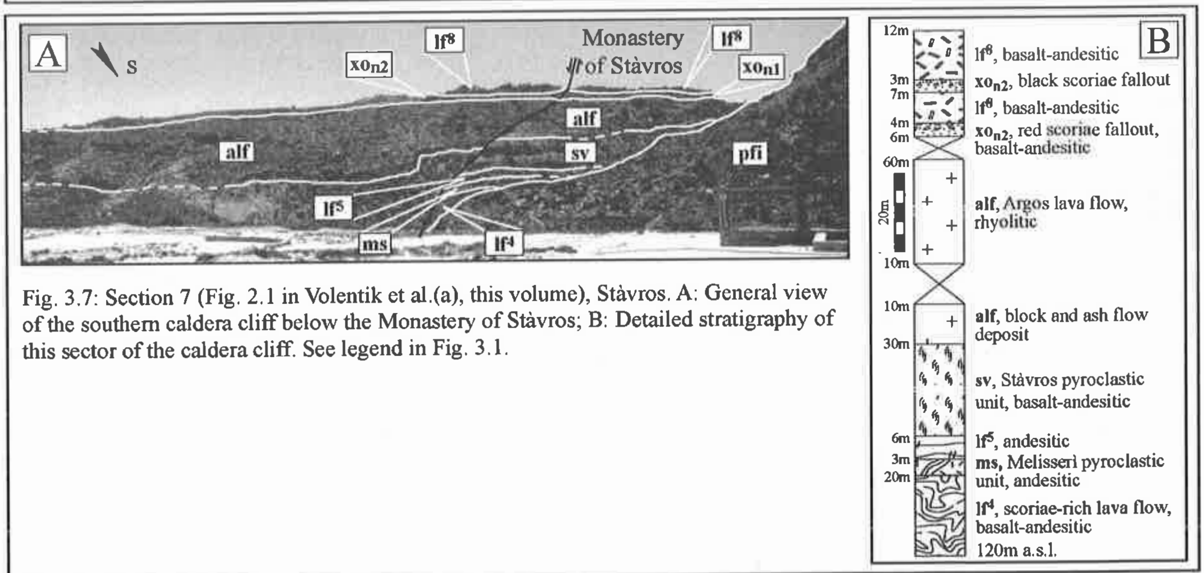

Fig. 3.7: Section 7 (Fig. 2.1 in Volentik et al.(a), this volume), Stàvros. A: General view of the southern caldera cliff below the Monastery of Stàvros; B: Detailed stratigraphy of this sector of the caldera cliff. See legend in Fig. 3.1.

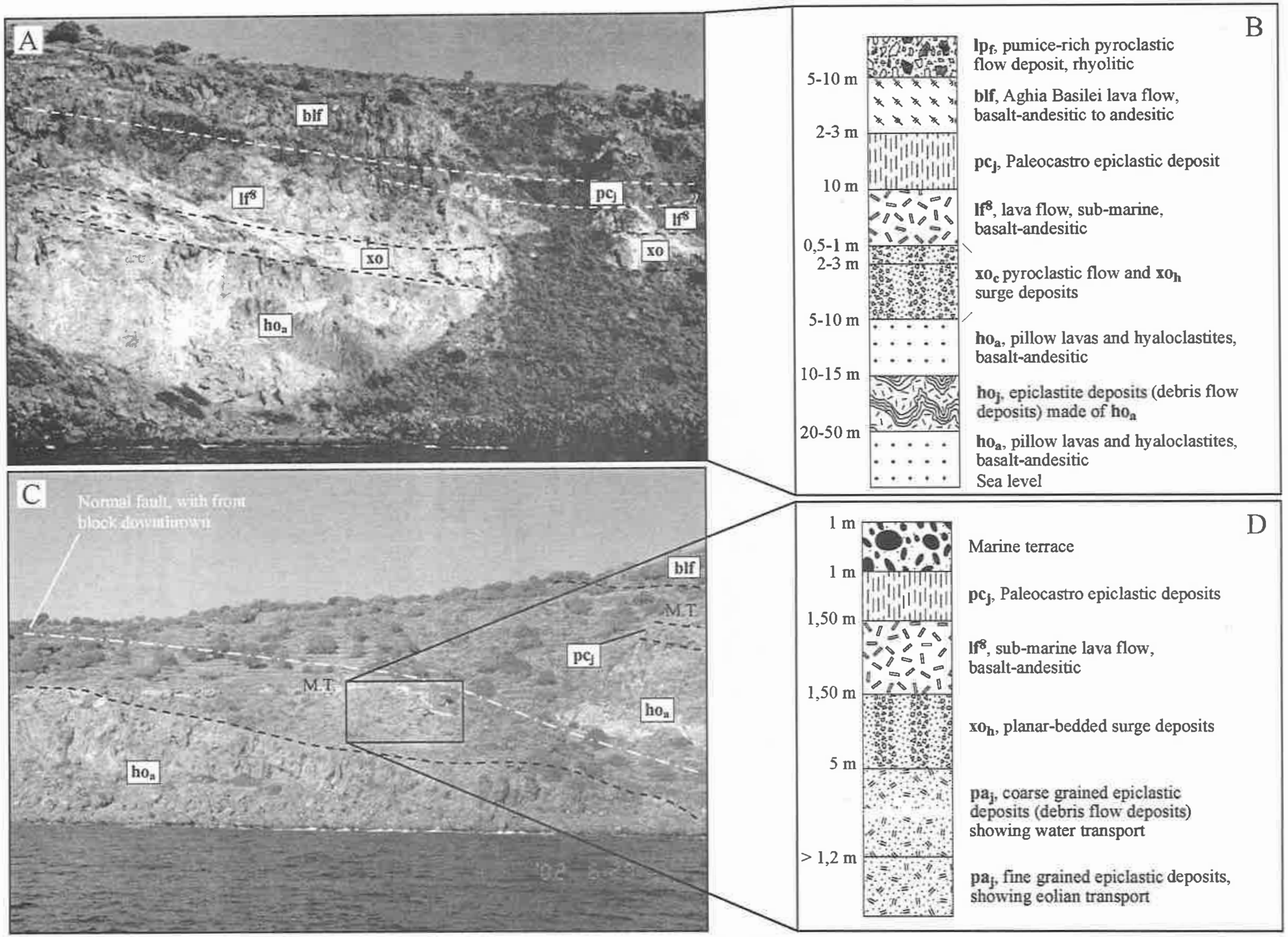

Fig. 3.8: Sections 8 & 9 (Fig. 2.1-B in Volentik et al.(a), this volume), western coast of Nisyros. A: General view of the cliff, where the best stratigraphic succesion is exposed; B: Synthetic stratigraphical section of A; C: General view of a teconized sector along the coast (south of Paleocastro castle), where the normal fault has 20-30 m of throw (note the throw of the marine terrace deposit [M.T.] on the right), its dip is 303/82.

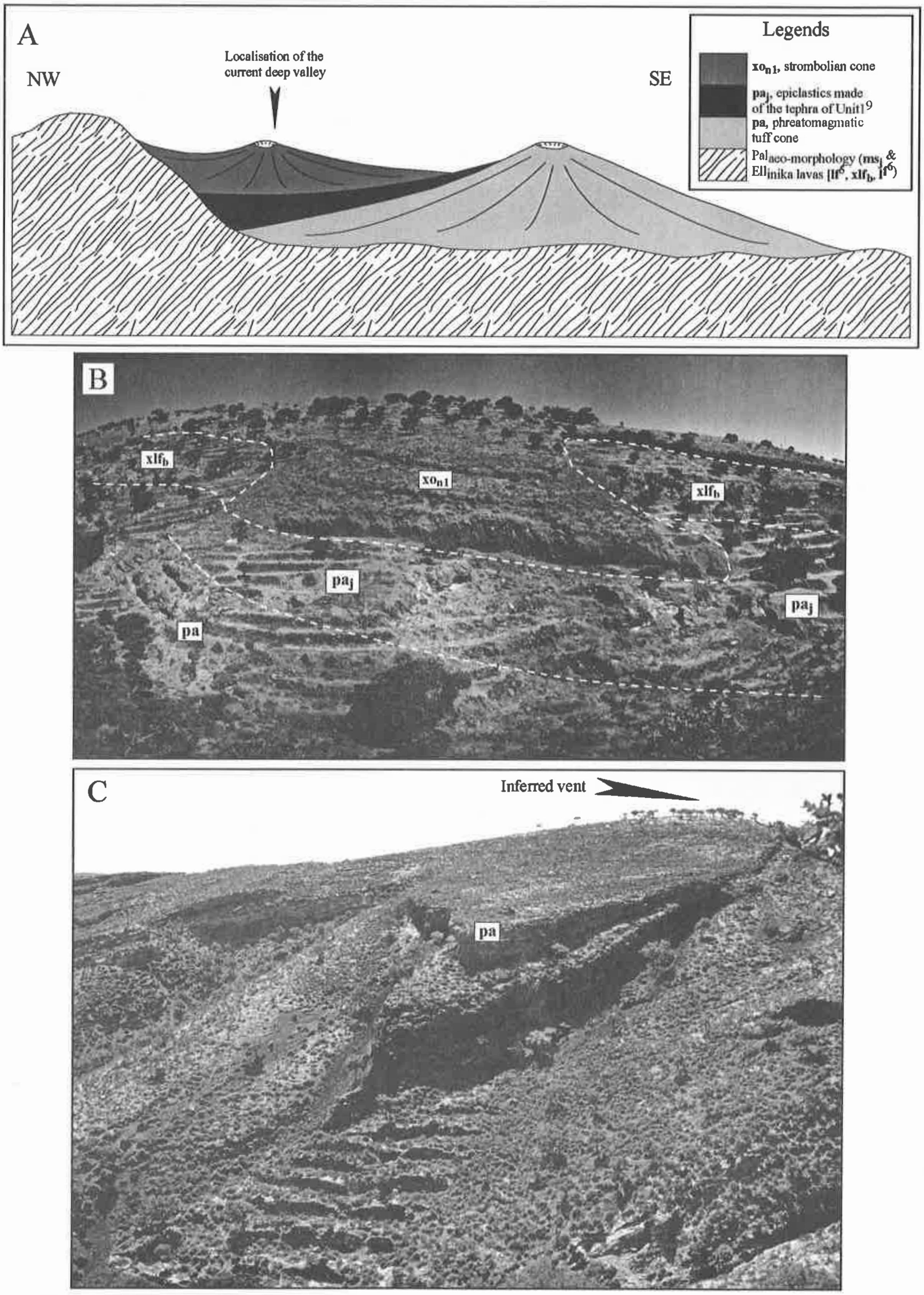

Fig. 3.9: Section 13 (Fig. 2.1-B in Volentik et al. (a), this volume), Lies deep valley. A: schematic cross-section of the valley; B: Strombolian cone (**xo**) on the northern part of the valley; C: Tuff cone (**pa**) on the southern part of the valley

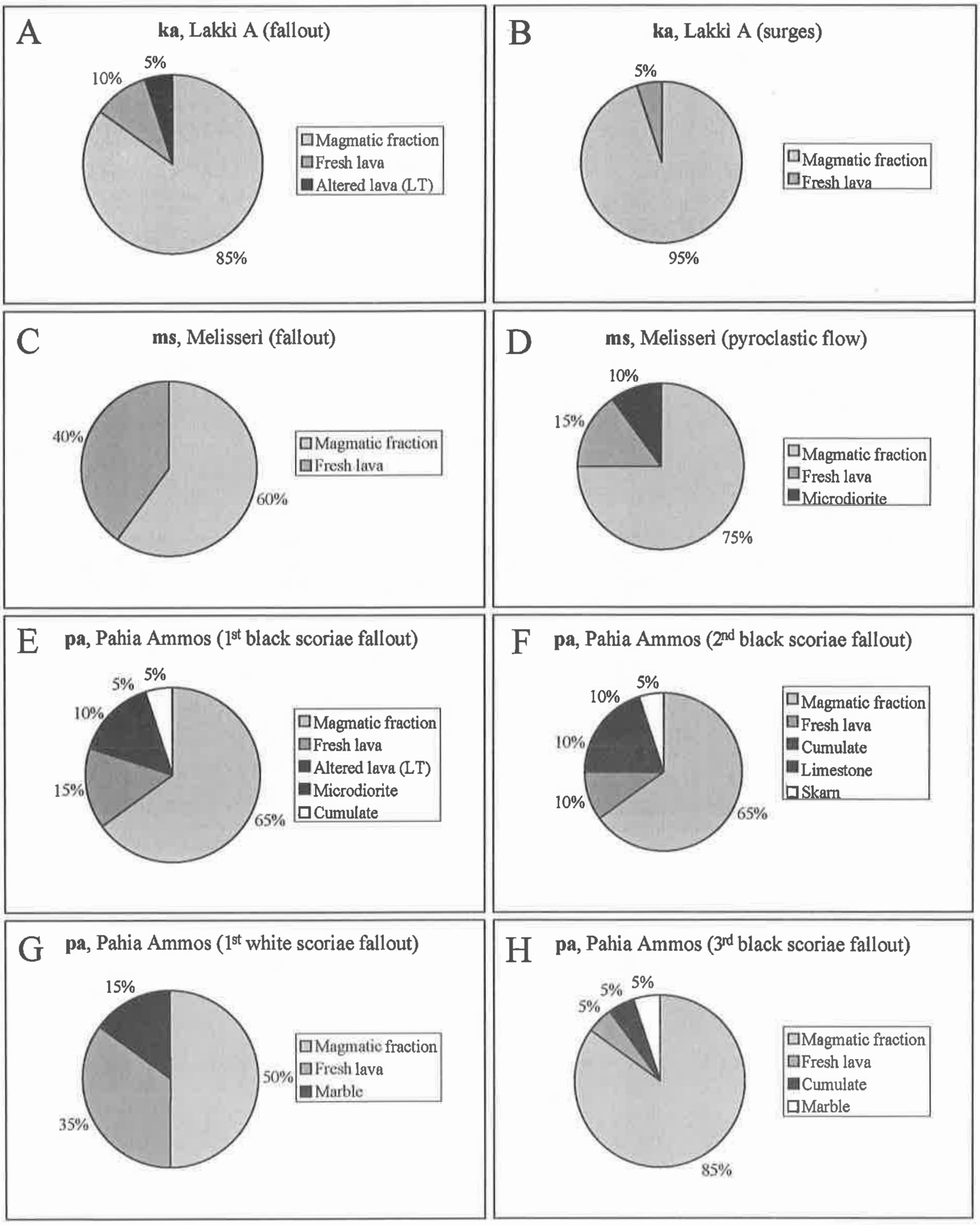
A
ka, Lakkì A (fallout)
5%
10%
85%
Magmatic fraction
Fresh lava
Altered lava (LT)
B
ka, Lakkì A (surges)
5%
95%
Magmatic fraction
Fresh lava
C
ms, Melisserì (fallout)
40%
60%
Magmatic fraction
Fresh lava
D
ms, Melisserì (pyroclastic flow)
10%
15%
75%
Magmatic fraction
Fresh lava
Microdiorite
E
pa, Pahia Ammos (1st black scoriae fallout)
5%
5%
10%
15%
65%
Magmatic fraction
Fresh lava
Altered lava (LT)
Microdiorite
Cumulate
F
pa, Pahia Ammos (2nd black scoriae fallout)
5%
10%
10%
10%
65%
Magmatic fraction
Fresh lava
Cumulate
Limestone
Skarn
G
pa, Pahia Ammos (1st white scoriae fallout)
15%
50%
35%
Magmatic fraction
Fresh lava
Marble
H
pa, Pahia Ammos (3rd black scoriae fallout)
5%
5%
5%
85%
Magmatic fraction
Fresh lava
Cumulate
Marble

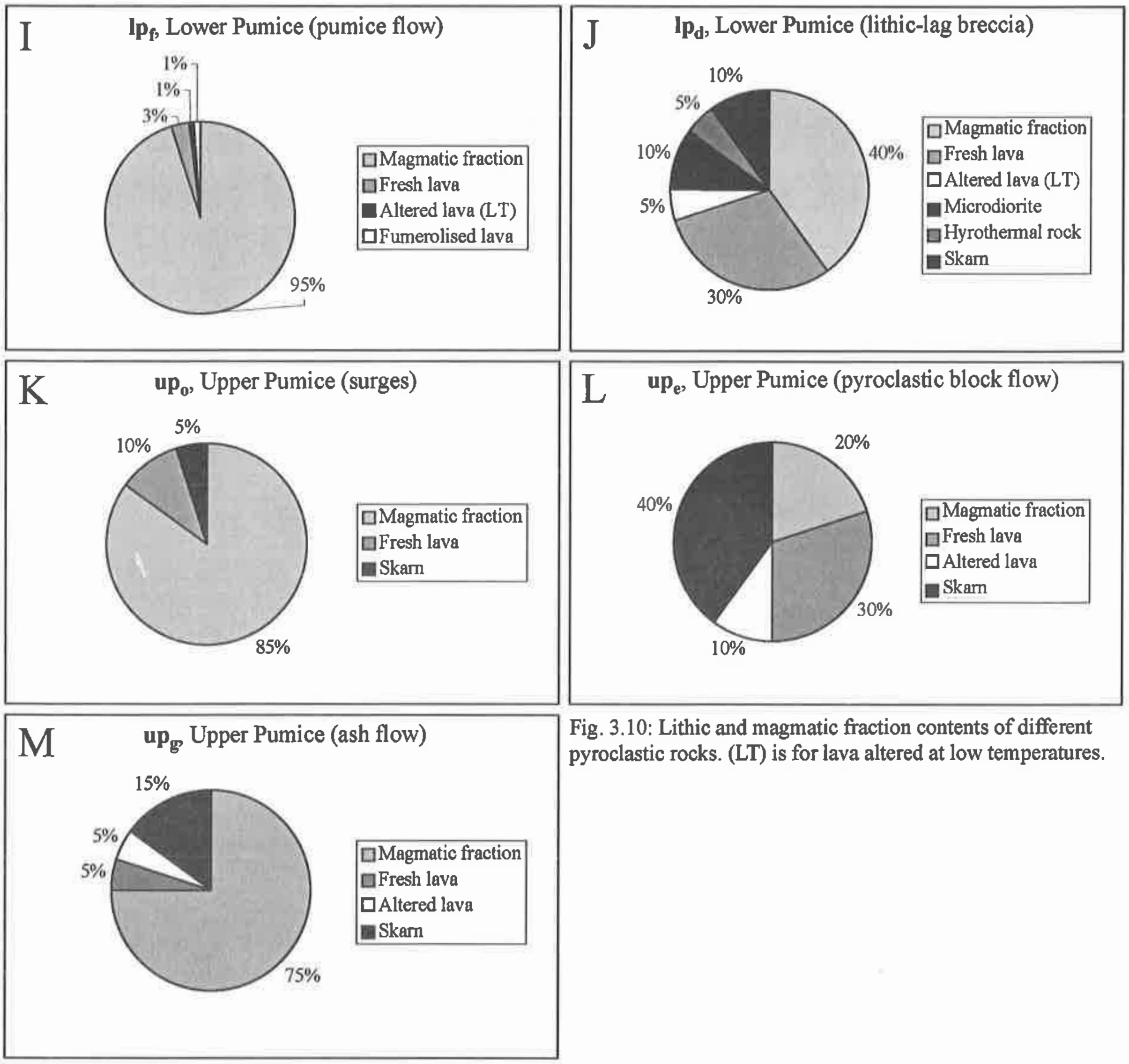

Fig. 3.10: Lithic and magmatic fraction contents of different pyroclastic rocks. (LT) is for lava altered at low temperatures.

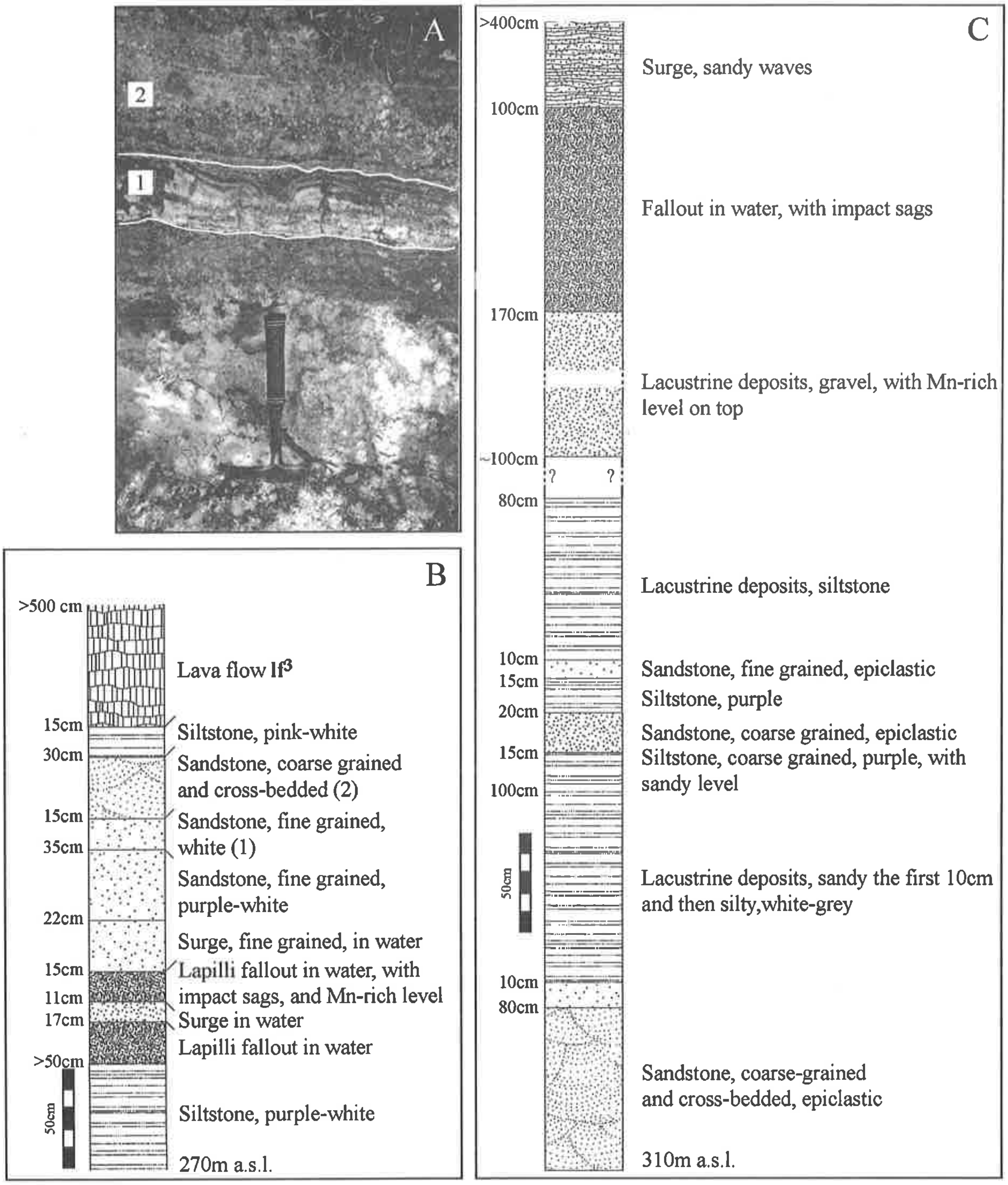

Fig. 3.11: **fl**$_l$ and **sl**$_l$, lacustrine deposits. A: Photograph of the **fl**$_l$, the first lacustrine layer; B & C: Detailed stratigraphy of the two lacustrine episodes (**fl**$_l$ and **sl**$_l$ respectively) outcropping on the northern caldera cliff. Modified from Volentik et al. (2002).

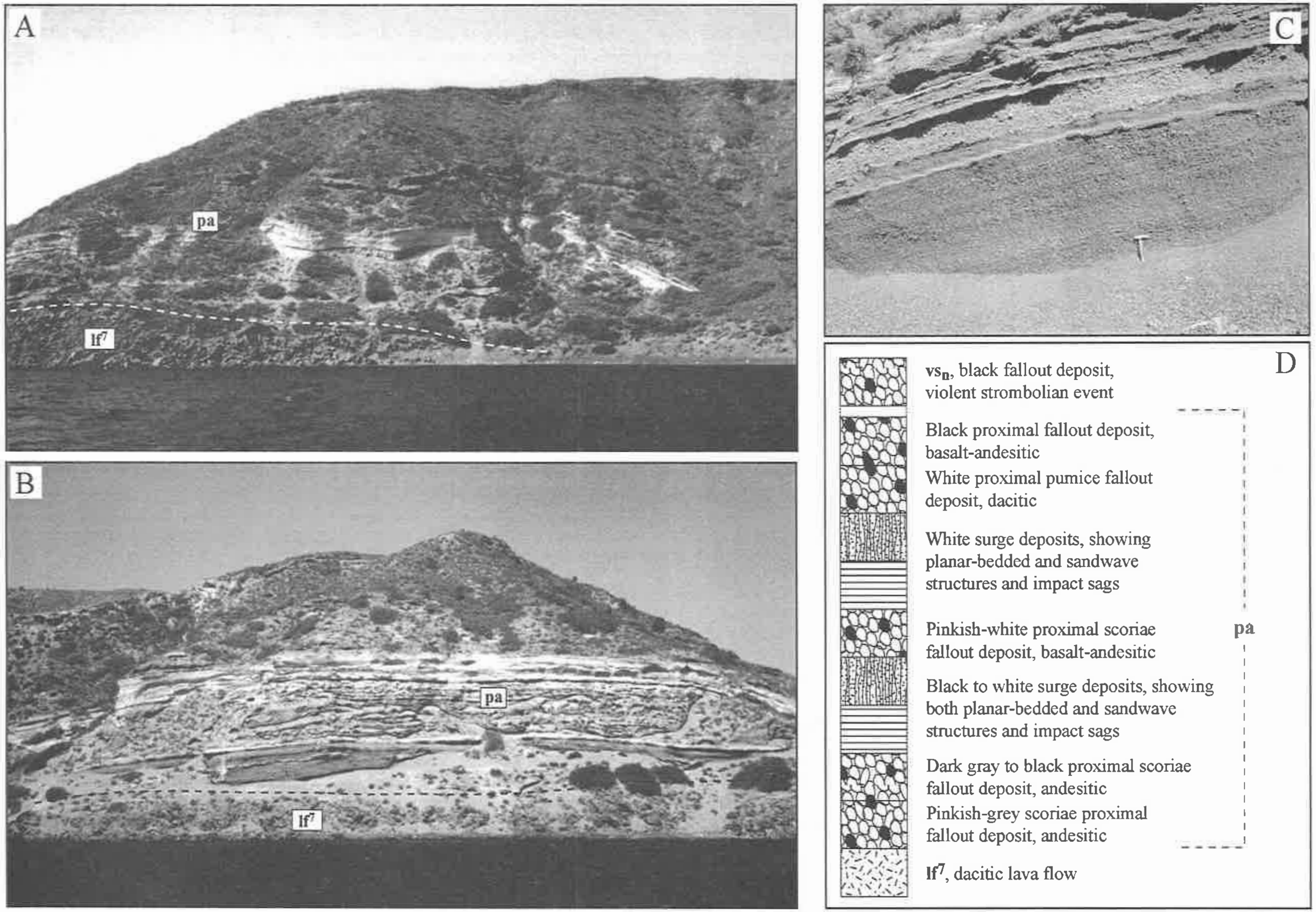

Fig. 3.12: Section 14 (Fig. 2.1 in Volentik et al.(a), this volume), Pahia Ammos. A & B: Tuff cone located between the beaches of Lies and Pahia Ammos (eastern coast of Nisyros); C: Violent strombolian fallout deposit (**vs$_n$**) overlying the tephra of **pa**; D: Simplified stratigraphy of **pa**, note the change in compostion in the fallout sequence.

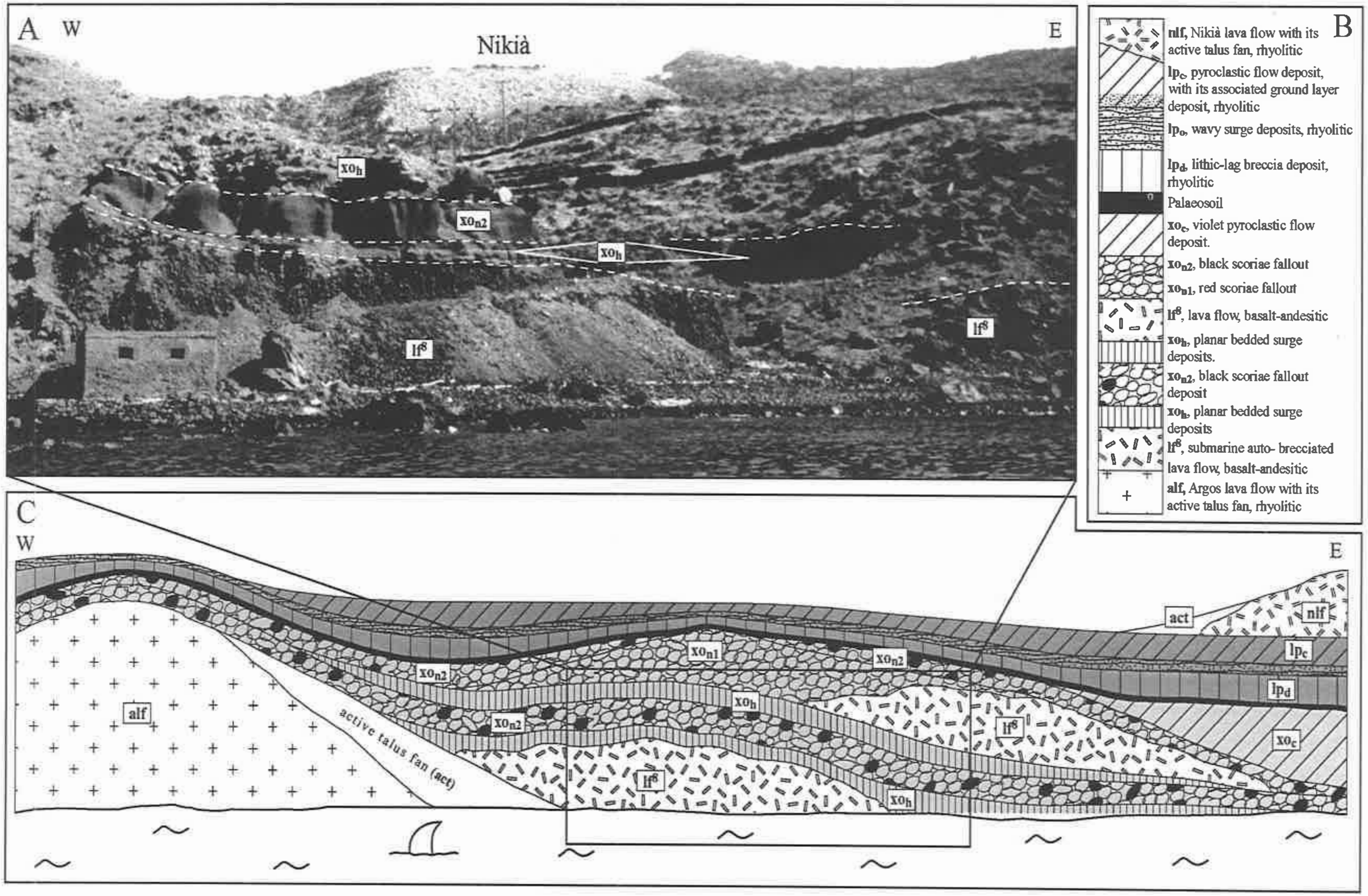

Fig. 3.13: The harbor of Avlaki: (A) Picture of the outcrop seen from the sea; (B) Corresponding schematic stratigraphic section (Location 15 in Fig. 2.1-B in Volentik et al.(a), this volume); (C) Schematic representation of the outcrop. In (A), note the brecciation of **lf**^{8}, suggesting that it is a subaerial flow that entered shallow waters. Light grey areas, **xo** eruptive sequence, grey areas, **lp** eruptive sequence.

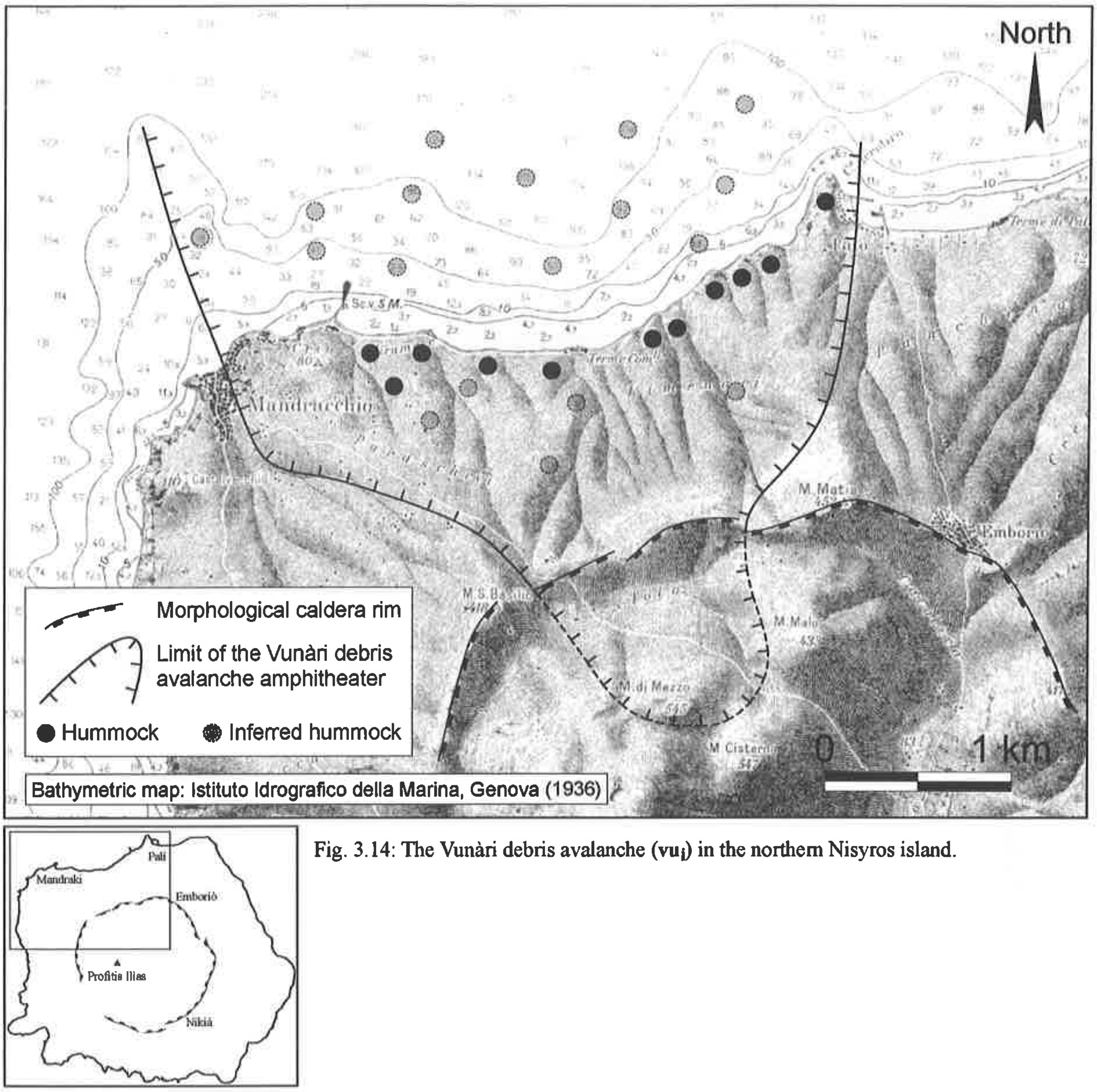

Bathymetric map: Istituto Idrografico della Marina, Genova (1936)

Fig. 3.14: The Vunàri debris avalanche (vu$_1$) in the northern Nisyros island.

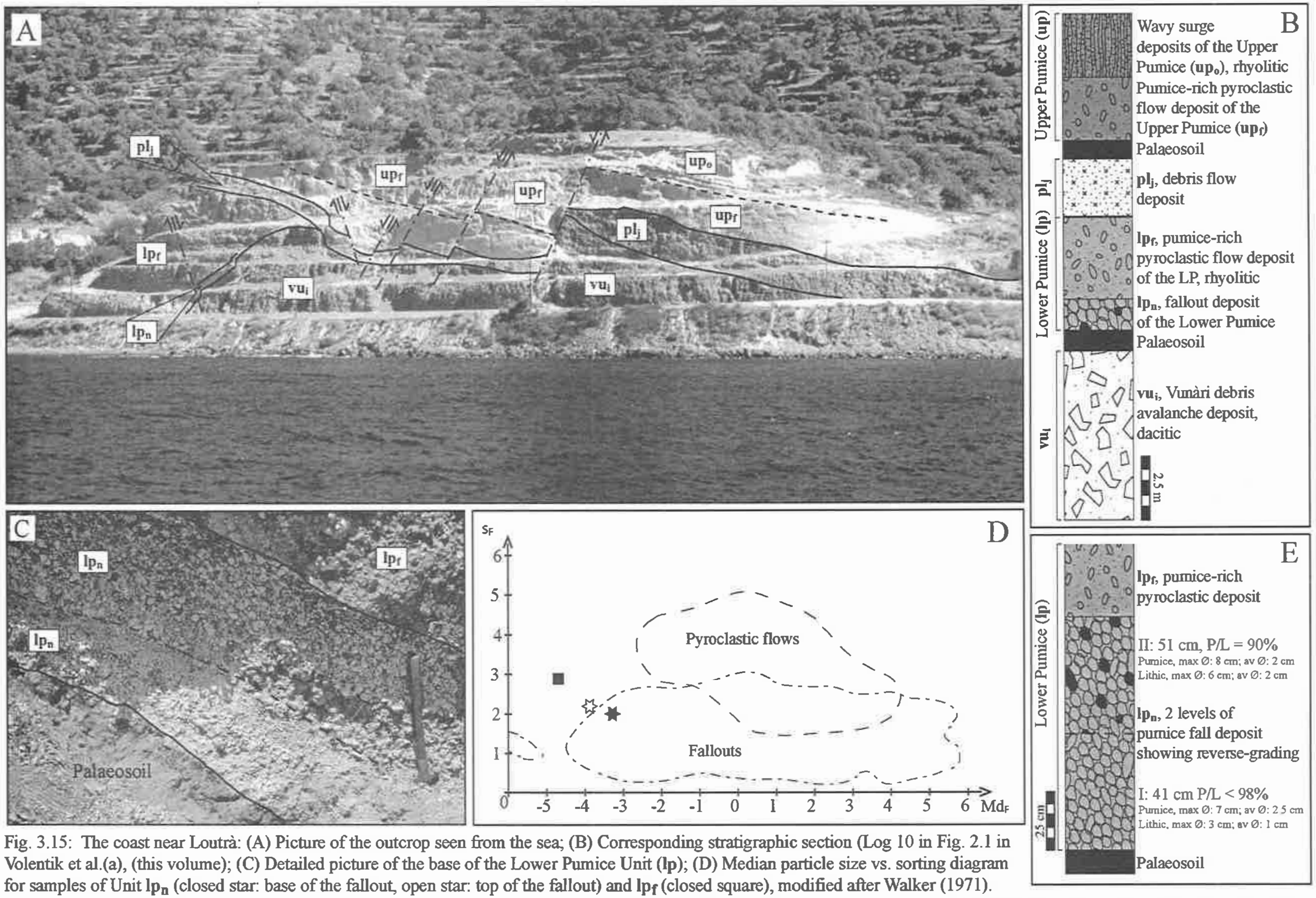

Fig. 3.15: The coast near Loutrà: (A) Picture of the outcrop seen from the sea; (B) Corresponding stratigraphic section (Log 10 in Fig. 2.1 in Volentik et al.(a), (this volume); (C) Detailed picture of the base of the Lower Pumice Unit (**lp**); (D) Median particle size vs. sorting diagram for samples of Unit **lp$_n$** (closed star: base of the fallout, open star: top of the fallout) and **lp$_f$** (closed square), modified after Walker (1971). The poor sorting of the **lp$_f$** sample disqualifies it as a fallout sequence, as formerly proposed by Limburg & Varekamp (1991); (E) Detailed stratigraphic section of the deposits at the base of unit **lp**. Bold letters from Volentik et al. (a) (this volume). Grey areas, **lp** eruptive sequence; dark grey areas, **up** eruptive sequence.

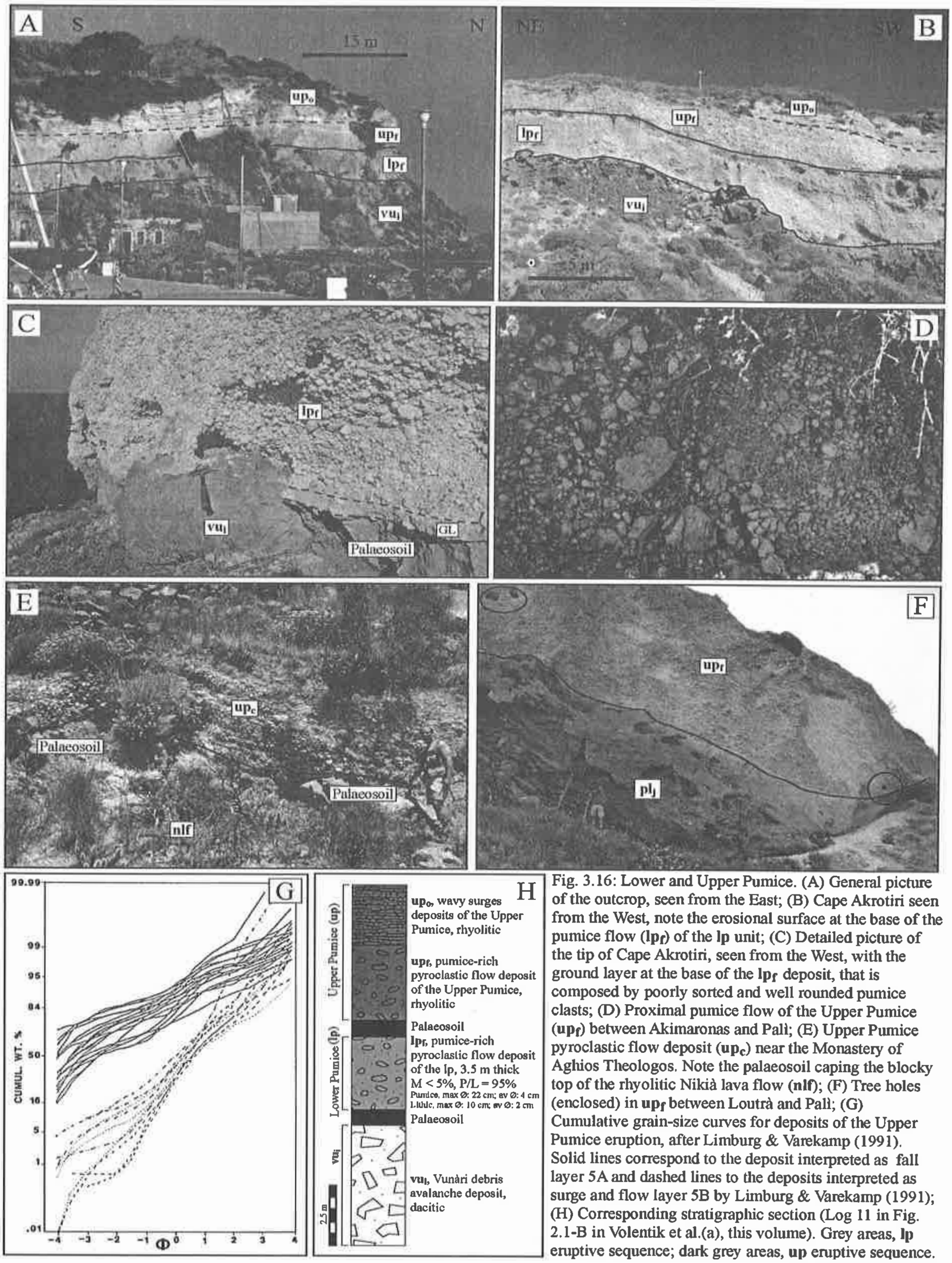

Fig. 3.16: Lower and Upper Pumice. (A) General picture of the outcrop, seen from the East; (B) Cape Akrotiri seen from the West, note the erosional surface at the base of the pumice flow (**lp$_f$**) of the **lp** unit; (C) Detailed picture of the tip of Cape Akrotiri, seen from the West, with the ground layer at the base of the **lp$_f$** deposit, that is composed by poorly sorted and well rounded pumice clasts; (D) Proximal pumice flow of the Upper Pumice (**up$_f$**) between Akimaronas and Palì; (E) Upper Pumice pyroclastic flow deposit (**up$_c$**) near the Monastery of Aghios Theologos. Note the palaeosoil caping the blocky top of the rhyolitic Nikià lava flow (**nlf**); (F) Tree holes (enclosed) in **up$_f$** between Loutrà and Palì; (G) Cumulative grain-size curves for deposits of the Upper Pumice eruption, after Limburg & Varekamp (1991). Solid lines correspond to the deposit interpreted as fall layer 5A and dashed lines to the deposits interpreted as surge and flow layer 5B by Limburg & Varekamp (1991); (H) Corresponding stratigraphic section (Log 11 in Fig. 2.1-B in Volentik et al.(a), this volume). Grey areas, **lp** eruptive sequence; dark grey areas, **up** eruptive sequence.

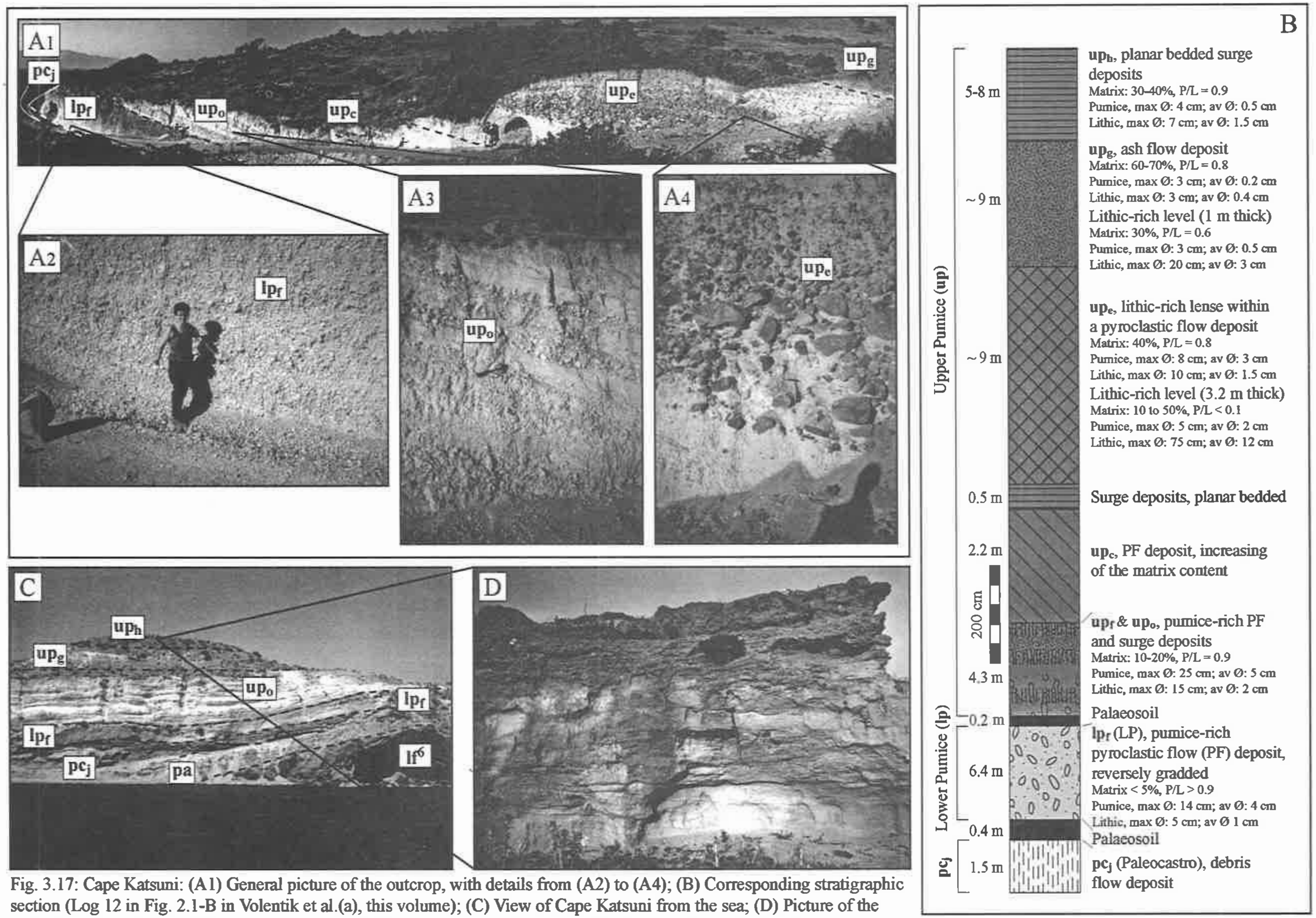

Fig. 3.17: Cape Katsuni: (A1) General picture of the outcrop, with details from (A2) to (A4); (B) Corresponding stratigraphic section (Log 12 in Fig. 2.1-B in Volentik et al.(a), this volume); (C) View of Cape Katsuni from the sea; (D) Picture of the surge deposits at the top of the **up** sequence (**up$_h$**). Grey areas, **lp** eruptive sequence; dark grey areas, **up** eruptive sequence.

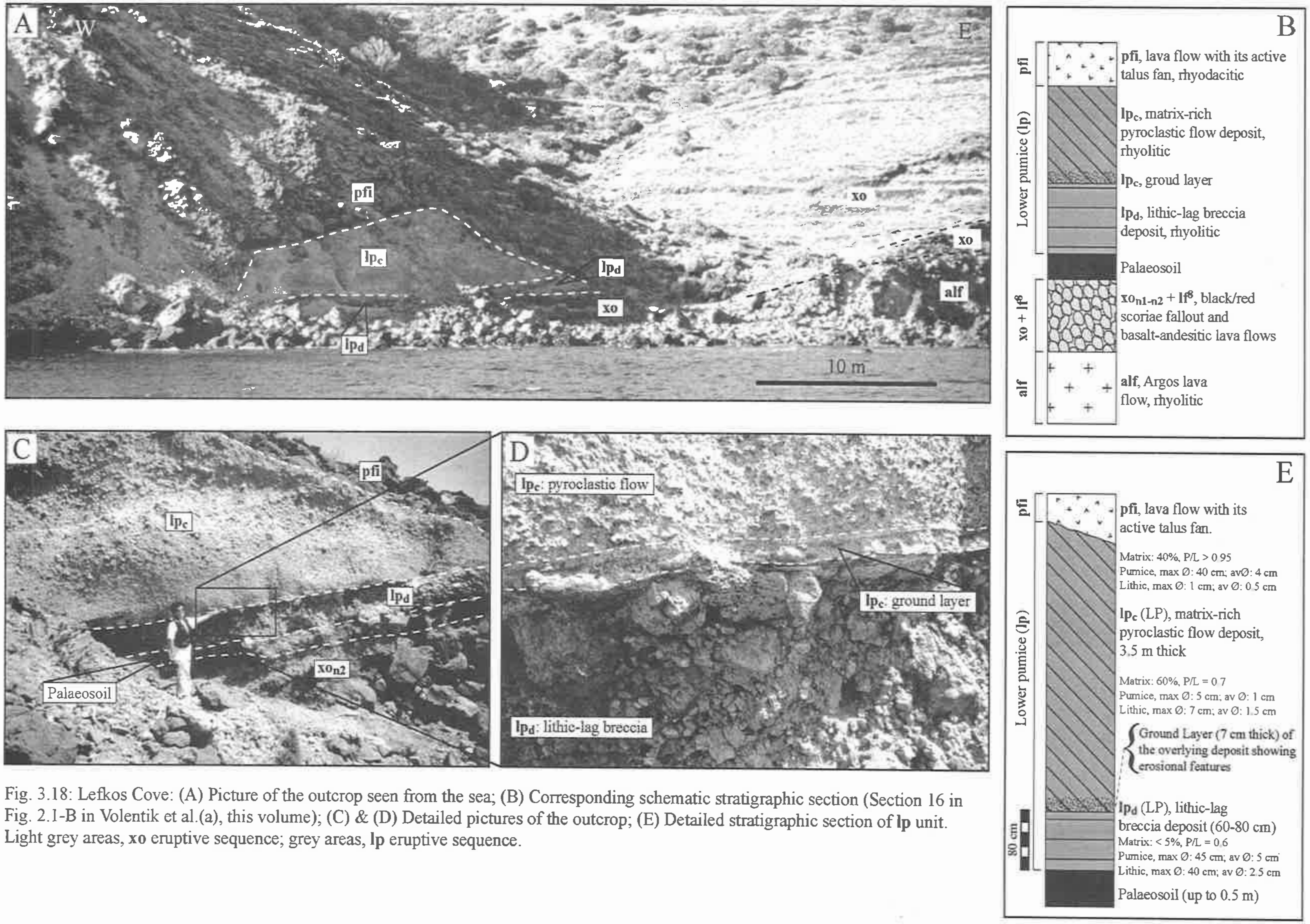

Fig. 3.18: Lefkos Cove: (A) Picture of the outcrop seen from the sea; (B) Corresponding schematic stratigraphic section (Section 16 in Fig. 2.1-B in Volentik et al.(a), this volume); (C) & (D) Detailed pictures of the outcrop; (E) Detailed stratigraphic section of **lp** unit. Light grey areas, **xo** eruptive sequence; grey areas, **lp** eruptive sequence.

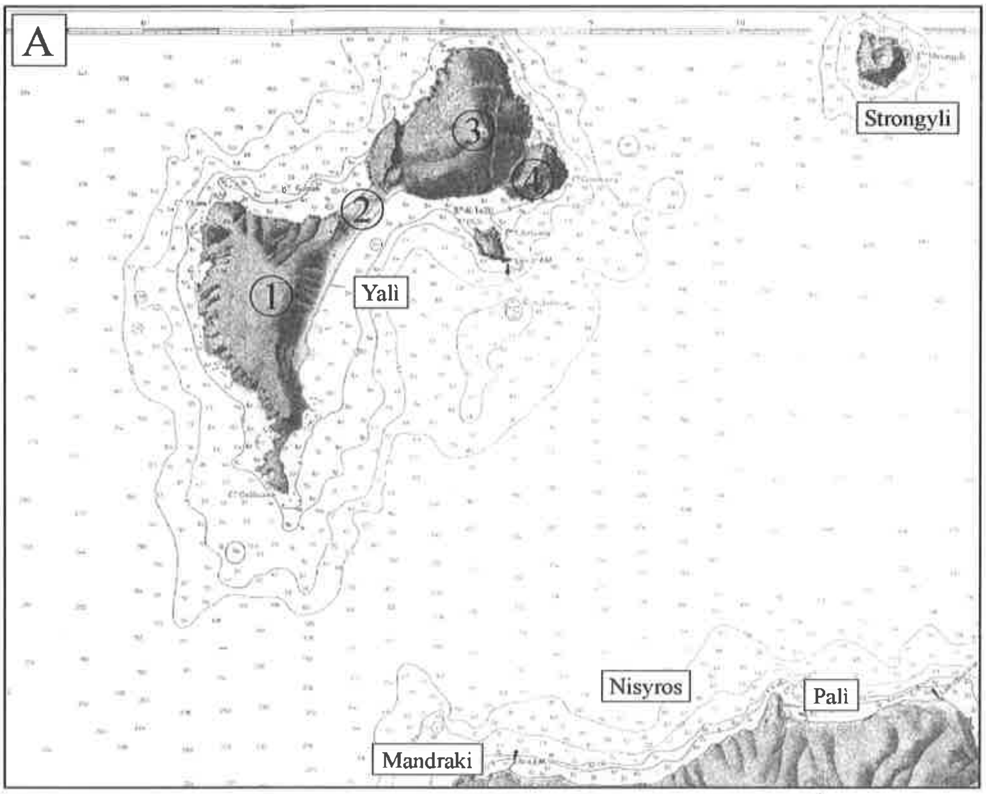

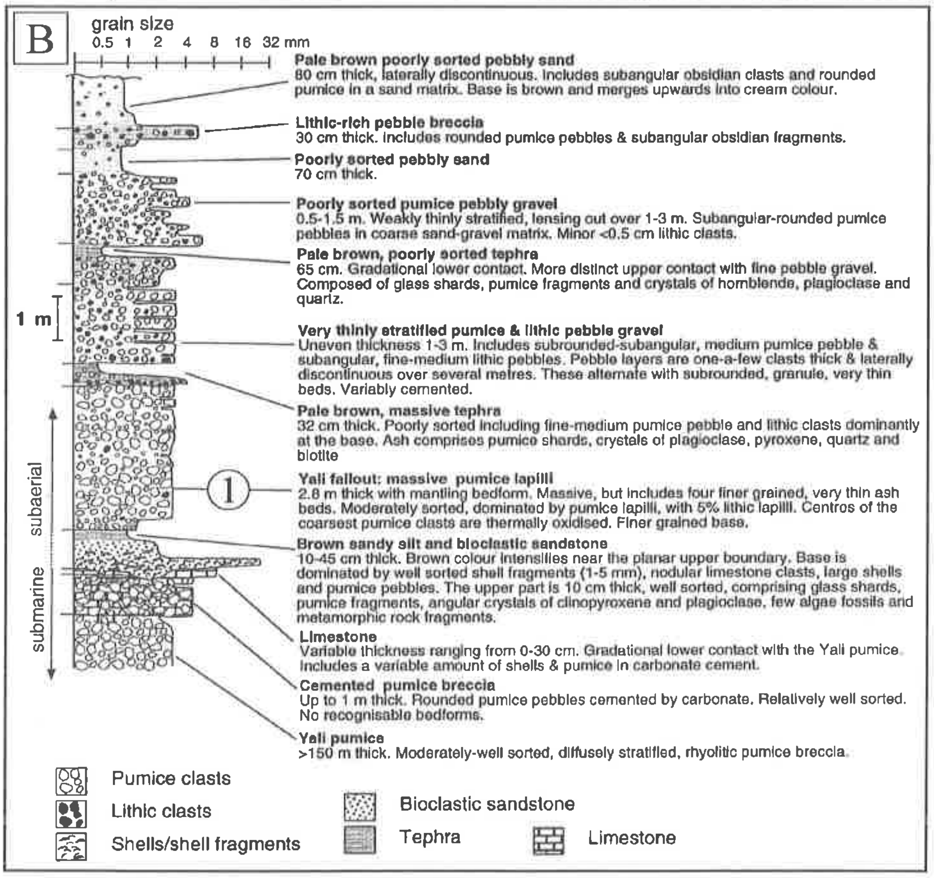

Pale brown poorly sorted pebbly sand
80 cm thick, laterally discontinuous. Includes subangular obsidian clasts and rounded pumice in a sand matrix. Base is brown and merges upwards into cream colour.

Lithic-rich pebble breccia
30 cm thick. Includes rounded pumice pebbles & subangular obsidian fragments.

Poorly sorted pebbly sand
70 cm thick.

Poorly sorted pumice pebbly gravel
0.5-1.5 m. Weakly thinly stratified, lensing out over 1-3 m. Subangular-rounded pumice pebbles in coarse sand-gravel matrix. Minor <0.5 cm lithic clasts.

Pale brown, poorly sorted tephra
65 cm. Gradational lower contact. More distinct upper contact with fine pebble gravel. Composed of glass shards, pumice fragments and crystals of hornblende, plagioclase and quartz.

Very thinly stratified pumice & lithic pebble gravel
Uneven thickness 1-3 m. Includes subrounded-subangular, medium pumice pebble & subangular, fine-medium lithic pebbles. Pebble layers are one-a-few clasts thick & laterally discontinuous over several metres. These alternate with subrounded, granule, very thin beds. Variably cemented.

Pale brown, massive tephra
32 cm thick. Poorly sorted including fine-medium pumice pebble and lithic clasts dominantly at the base. Ash comprises pumice shards, crystals of plagioclase, pyroxene, quartz and biotite

Yali fallout: massive pumice lapilli
2.8 m thick with mantling bedform. Massive, but includes four finer grained, very thin ash beds. Moderately sorted, dominated by pumice lapilli, with 5% lithic lapilli. Centros of the coarsest pumice clasts are thermally oxidised. Finer grained base.

Brown sandy silt and bioclastic sandstone
10-45 cm thick. Brown colour intensifies near the planar upper boundary. Base is dominated by well sorted shell fragments (1-5 mm), nodular limestone clasts, large shells and pumice pebbles. The upper part is 10 cm thick, well sorted, comprising glass shards, pumice fragments, angular crystals of clinopyroxene and plagioclase, few algae fossils and metamorphic rock fragments.

Limestone
Variable thickness ranging from 0-30 cm. Gradational lower contact with the Yali pumice. Includes a variable amount of shells & pumice in carbonate cement.

Cemented pumice breccia
Up to 1 m thick. Rounded pumice pebbles cemented by carbonate. Relatively well sorted. No recognisable bedforms.

Yali pumice
>150 m thick. Moderately-well sorted, diffusely stratified, rhyolitic pumice breccia.

Fig. 3.19: The Yalì fallout. A: Yalì Island, north of Nisyros. (1) Remnant of the pumice breccia cone, overlied by the Yalì pumice fallout, (2) Mandra isthmus, (3) Obsidian lava flows and (4) Phreatomagmatic surges. B: Detailed stratigaphic sequence of the upper part of the Yalì pumice breccia. The sequence represents an upward progression from submarine to subaerial depositional environments. Number (1) represents the equivalent proximal fallout that is found remobilized within talus fans on Nisyros. After Allen & McPhie (2000).

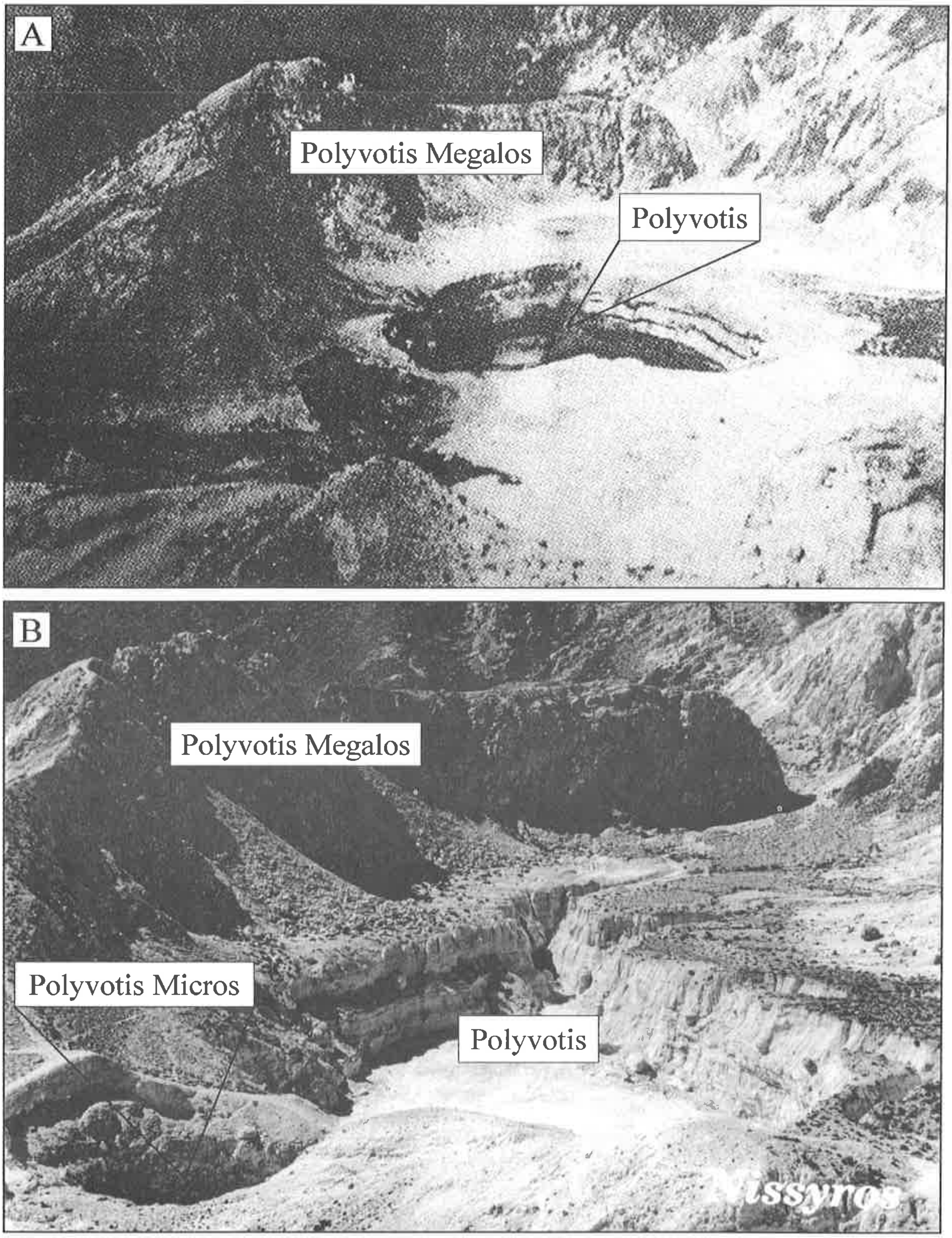

Fig. 3.20: The Polyvotis Megalos hydrothermal area. A: Photograph taken by Martelli in 1912. B: Current view of the area, taken from the same spot. Note the strong enlargement of the Polyvotis crater caused by erosion.

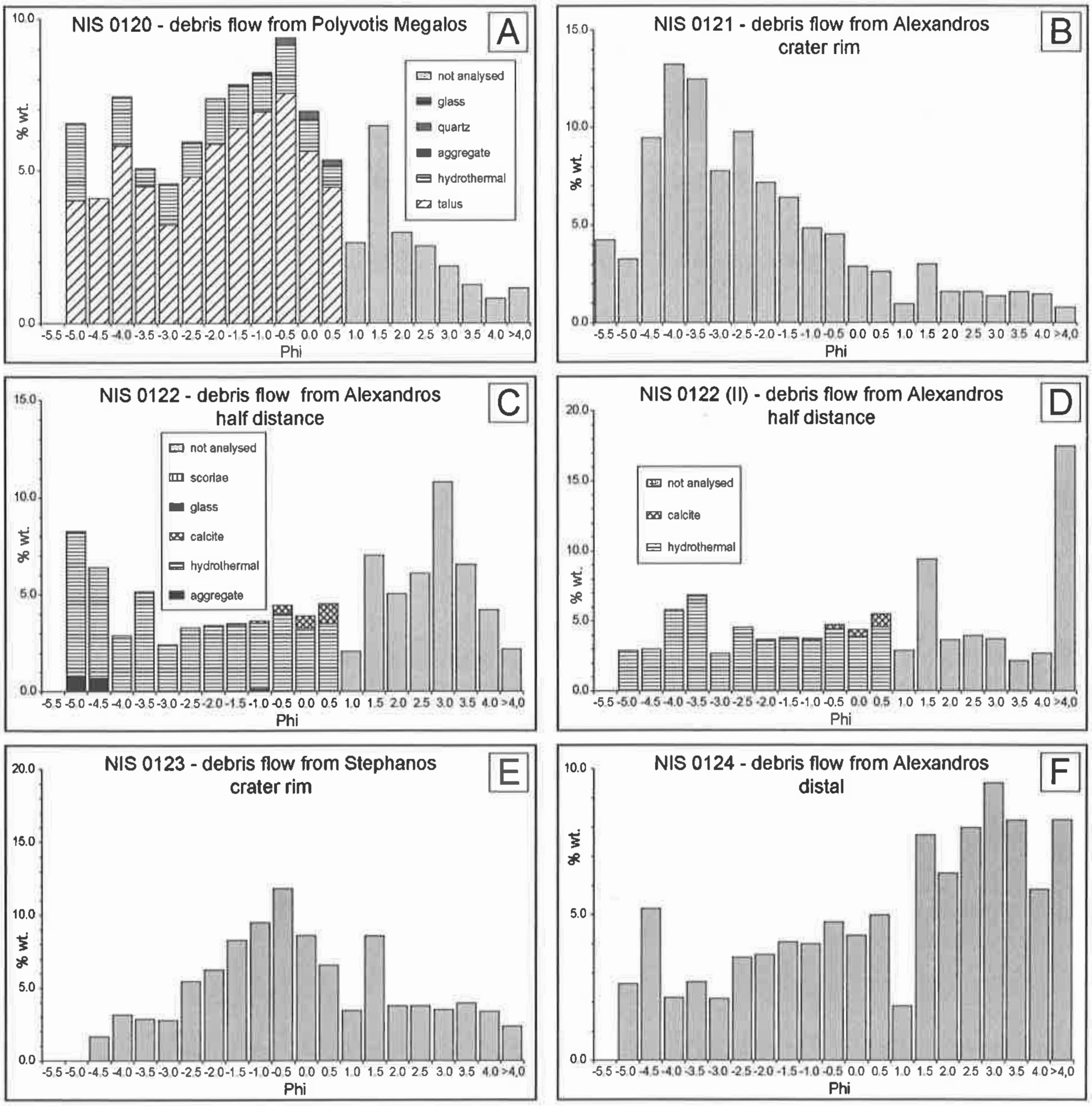

Fig. 3.21: Granolumetric analysis of the hydrothermal debris flow deposits. Note that sample NIS 0122 (C & D) was sieved twice: (C) in dry conditions and (D) under a water flow, in order to dissovle matrix aggregates. The resulting histogram (D) shows an increase in fine fragments due to the disaggregation of matrix lumps, without changing the general trend, characterised by an increase in the fine matrix with the distance from the source and the absence of the big blocks of ballistic origin inside the distal debris flows deposits.

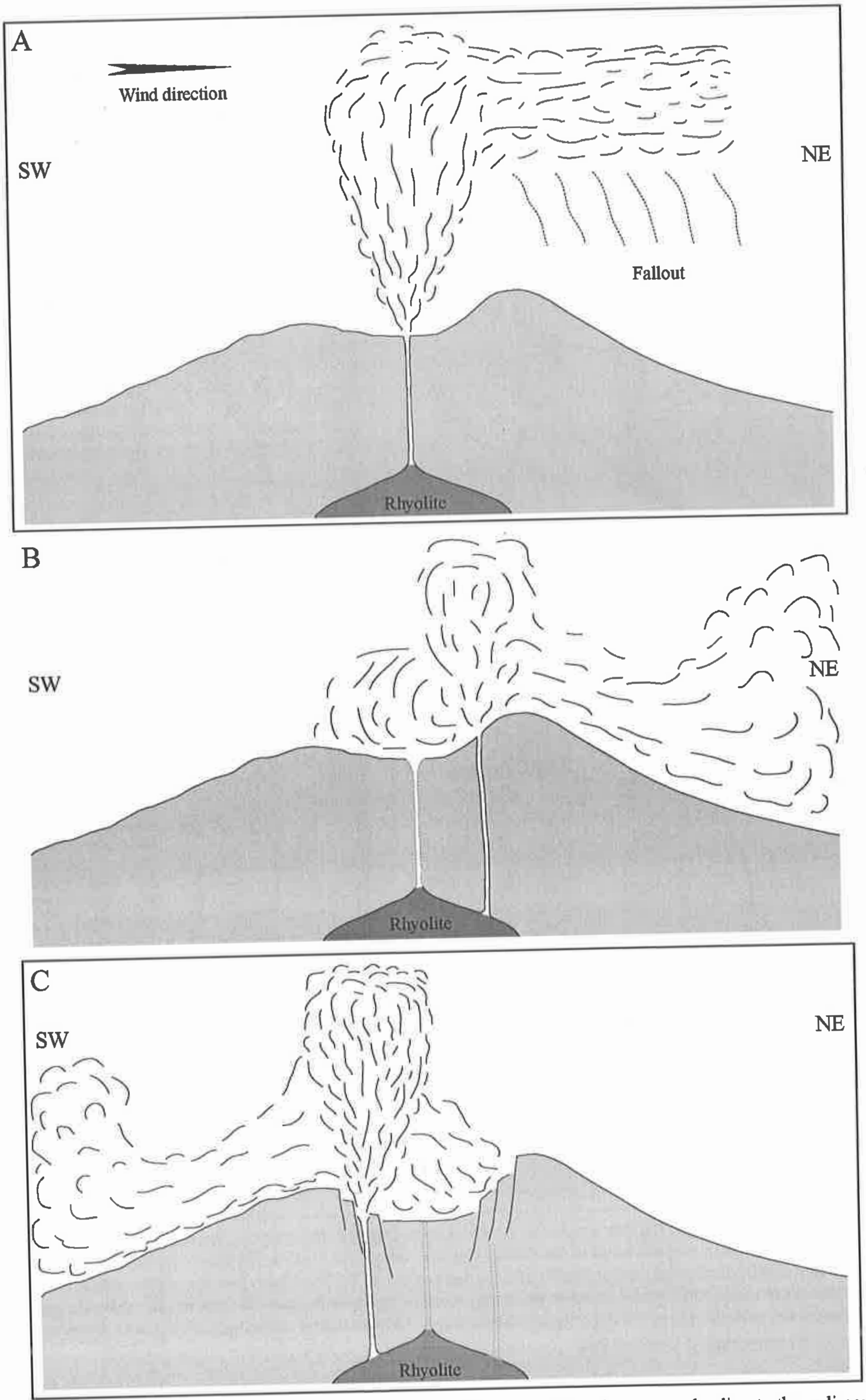

Fig. 3.22: Eruptive model of the Lower Pumice eruption. A: Plinian convective plume stage leading to the sedimentation of the fallout deposit (**lp$_n$**); B: Column collapse and fountaining, generating pumice-rich pyroclastic flows (**lp$_f$**); C: Early caldera collapse, formation of the lithic-lag breccia (**lp$_d$**) and subsequent surges (**lp$_o$**) and pyroclastic flows (**lp$_c$**).

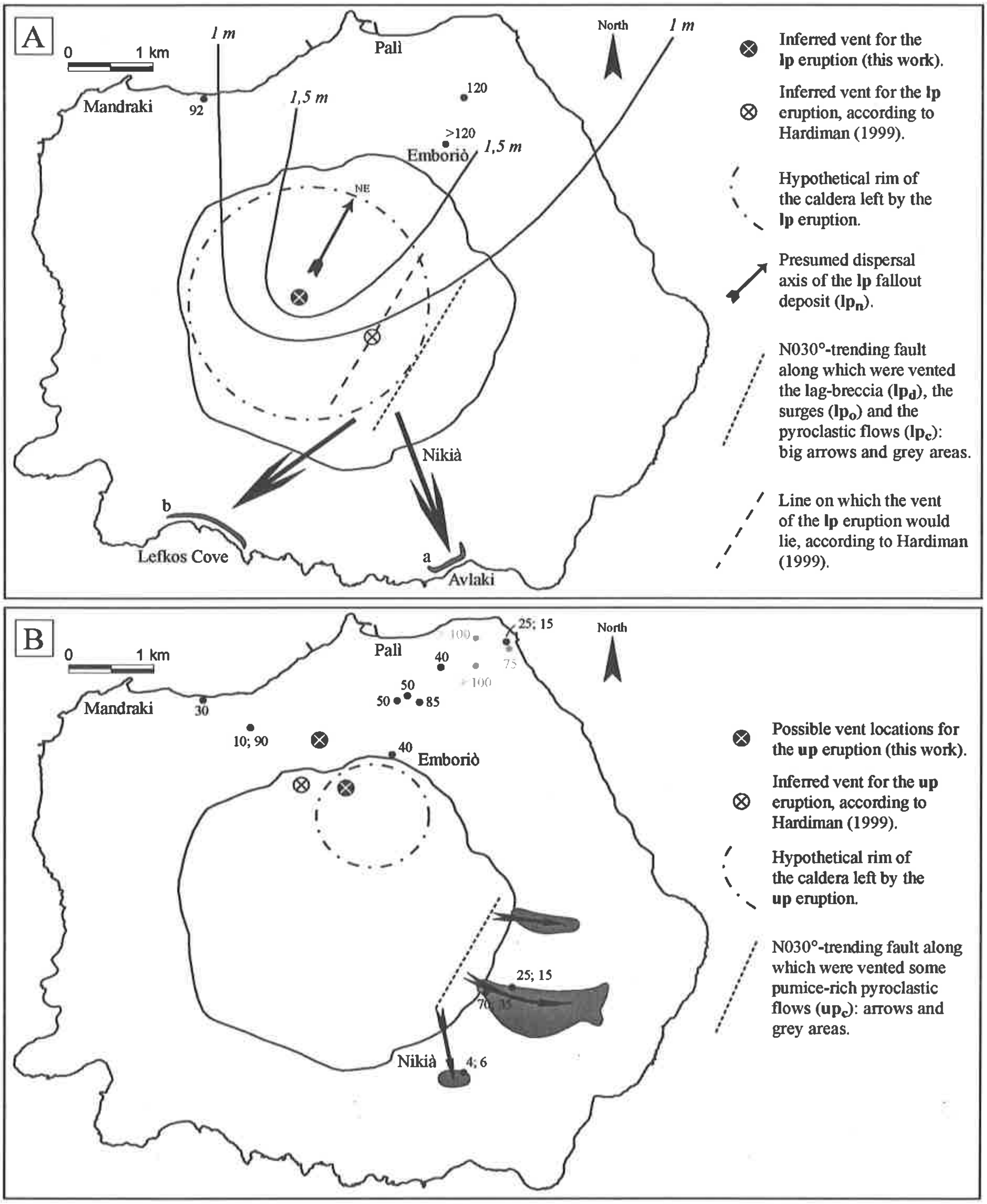

Fig. 3.23: The Lower and Upper Pumice eruptions. A: The Lower Pumice (**lp**) erutpion. Measured thickness of the pumice fallout deposit (**lp**$_{\mathbf{n}}$), isopach lines of the fallout deposit. Grey area localise the lithic-lag breccia (**lp**$_{\mathbf{d}}$), the surges (**lp**$_{\mathbf{o}}$) and the pyroclastic flows (**lp**$_{\mathbf{c}}$) in (a) Avalki and (b) Lefkos Cove. B: The Upper Pumice (**up**) eruption. Isopleth data: the first number close to the solid circles refers to the average size of the three biggest pumices in **up**$_{\mathbf{f}}$, while the second number indicates the average size of the three biggest lithic in **up**$_{\mathbf{f}}$. Numbers close to the light grey cirlces refers to the average size of the three biggest lithics in **up**$_{\mathbf{e}}$.

4. The role of tectonic and volcano-tectonic activity at Nisyros Volcano (Greece)

Alain C. M. Volentik(1), **Loÿc Vanderkluysen**(1),
Claudia Principe(2), **Johannes C. Hunziker**(1)

(1) Institut de Minéralogie et Géochimie, BFSH-2, Université, CH-1015 Lausanne, Switzerland.

(2) Istituto di Geoscienze e Georisorse, Area della Ricerca CNR-Pisa San Cataldo Via G. Moruzzi 1, I-56124 (Pisa), Italy.

Abstract - Tectonic events (either as a result of regional tectonics or induced by volcanic activity) have played a major role on Nisyros. They influenced dyke orientations, caldera collapse events (Volentik et al., 2002) and, more recently, hydrothermal eruptions (Marini et al., 1993) and the opening of fractures within the caldera depression which became apparent as recently as December 2001 (Vougioukalakis, 2003). We present, in this contribution, the tectonic and volcano-tectonic data we collected on Nisyros and their distribution in time. From this data set it can be inferred the existence on the island of 4 families of trends: N030°, N070°, N340°, N120°. The relationships between these elements and the previously defined stratigraphic units results in a strong correlation between the switches in the location of volcanic centres, changes in the dominant tectonic trends, and the synthematic subdivision applied to the stratigraphic record, suggesting a tectonic control of the main phases of volcanic activity on the island.

4.1. The general trend

Nisyros is situated at the eastern termination of the South Aegean island arc which comprises, from west to east, Crommyonia, Methana, Poros, Aegina, Milos, Santorini, the Columbo Bank, Kos, and Nisyros, as well as several minor eruptive centers four of which are localized close to Nisyros island (Keller, 1982). Subduction of the African plate below the Anatolian-Aegean plate has been taking place since Pliocene along the South Aegean island arc and is responsible of volcanism and seismicity (Piper and Perissoratis, 2003). Earthquake hypocenters clearly outline the Benioff plane and seismic tomography investigations have carried out to map the subducting slab (Pe-Piper & Piper, 2005 and references therein). The South Aegean island arc is characterised by a high rate of extension and crustal thinning of the Anatolian-Aegean plate as indicated by the presence of the Moho at comparatively shallow depths. All the volcanic centers of the South Aegean island are situated where the depth to the Benioff zone ranges from 130 to 150 km, suggesting that subduction controls magma generation, most likely through release of fluids entering the overlying mantle wedge, where partial melting under hydrous conditions occurs.

Several studies have shown that tectonics is very active in the Aegean region (Fig. 4.1-A & B) and that Nisyros was affected by numerous tectonic events that still go on at present (Papazachos & Panagiotopoulos 1993, Papazachos et al. 1993, Hanus & Vanek 1993, Lagios et al. 1998, Papadopoulos et al. 1998, Lagios et al. 2001, Sachpazi et al. 2002, Piper & Perissoratis 2003). Most authors interpreted major tectonic trends on Nisyros as the result of regional tectonics, owing to the nearby Kerme graben, or to roll-back of the African plate (Meijer & Wortel 1997, Nakamura & Uyeda 1980).

Recently, a detailed study of the fault patterns in the area comprising Kos and Nisyros led Pe-Piper et al. (2005) to hypothesize how ENE-trending faulting promoted explosive volcanism. According to Pe-Piper & Piper (2005), in the Nisyros-Yalì region a regional motion on the ENE sinistral shear zones led to extension on the older NW-trending lineament which acted as a step-over zone (Fig. 4.2-A & B).

4.2. Previous state of the knowledge on Nisyros tectonics

Looking in more details at the tectonic and volcano-tectonic elements recognizable on the island of Nisyros, Di Paola (1974) was the first to publish a modern geological map of the island, on which a number of faults and fractures are indicated.

Dominant directions of these faults are N340°, N070° and N040°, although the author did not state that tectonic features systematically follow these trends. Papanikolaou et al. (1991) highlighted that the two tectonic trends N340° and N040° are dominant on the island. Simaiakis (1992) released a report mainly confirming the existence of the three tectonic trends noted above. Vougioukalakis (1993) published a tectonic scheme of Nisyros, on which faults and fractures take on a more radial nature, although the author admitted the existence of some dominant trends. Stiros (2000) proposed an entirely different interpretation, in that most of the faults of Nisyros are radial, and caused by the emplacement of the recent caldera-filling domes. Lagios et al. (2001) recognised the existence of 5 families of fractures, oriented at N030°, N340°, N090°, N180° and N120°. However, they interpreted the caldera as a merely volcanic structure with no tectonic influence. Finally, Vanderkluysen & Volentik (2001) and Volentik et al. (2002) reported again the existence of faults oriented at N030°, N070° and N340°, but also pointed out the volcano-tectonic nature of the Nisyros caldera.

4.3. Volcanic and volcano-tectonic structures

In the sketch map of Fig. 4.3, the volcanic and volcano-tectonic features observed in the field (e.g., Figs. 4.4 and 4.5) and those inferred from a geophysical survey (see Vanderkluysen & Gex, this volume) are reported. Besides, necks and vents are subdivided according to the main stratigraphic units they are related to. From this map, it can be inferred the existence on the island of 4 families of trends, namely N030°, N070°, N340°, and N120°.

The timing of each trend's activity is summarised in Table 4.1 and detailed hereunder (numbers on Fig. 4.3 refer to this list; bold alphanumeric codes refer to the mapped unit as defined in Volentik et al.(a), this volume).

(1) A dyke feeding **lf**^{2} lavas with orientation at N070° (Fig. 4.6-A_1 & A_2)

(2) N070° trending dykes found both inside and outside the caldera. It is unclear what units are fed by these dykes (if any), but they must necessarily be included between units **lf**^{5} and **lf**^{8}; it is also certain that this trend was still active after the emplacement of unit **pa**, since a dyke with this direction cuts through the **pa** tuff cone deposits found near the Lies Beach (Fig. 4.6-B)

(3) A dyke in the South-Eastern caldera wall, with N340° direction, feeding the lava **lf**^{5}.

(4) The neck of the Argos rhyolite (**alf**) (Fig. 4.7-A), which is located at the intersection of two majors faults, oriented at N120° and N030°.

(5) N030° tectonic elements strongly tilting the pillow lavas of Mandraki (**ho**$_a$), at some time after their emplacement and before the eruption of **pa** tuff cone deposits, which are unaffected by these movements.

(6) Sources of the dacitic **lf**^{7} lava flow and **pa** tephra in the North-East of the island; these vents are aligned along N340°-trending lines.

(7) Centres of activity of **xo** and **lf**^{8}; these vents are located at the intersections of faults following N030°, N070°, N120° and N340° directions (a normal fault oriented at N070° is illustrated in Fig. 4.4)

(8) A N030°-trending fissure from which the lavas of Aghia Basilei (**blf**) were erupted.

(9) A neck on a N030°-trending line, from which the Emboriò dacites (**emb**) were discharged; N340° structures are superimposed to the N030° line in some outcrops.

(10) The scars of the Vunàri debris avalanche (**vu**$_l$) following N340°, N070° and N030° directions. Stratigraphic evidence suggests that the flank collapse took place along previously existing faults of N340° and N070° directions.

(11) A N340° lineament controlling the emplacement of the Lubunià (**llf**) lavas.

(12) A N030° fissure, situated near the centre of the present caldera, presumably acting as the vent of the first phase of the **lp** eruption and a N030° line in the eastern side of the present caldera, probably representing the vent of the second phase of the same eruption.

(13) The caldera collapse subsequent to the **lp** eruption. It is thought to have followed N030° directions to the East (and possibly to the West) and N120° faults in the South.

(14) A N030° fissure, located on the Eastern part of the caldera (Fig. 4.7-C), from which the Nikià rhyolite (**nlf**) was erupted.

(15) Incremental caldera collapse after the eruption of **nlf**, that re-used the N030° trend.

(16) A N030° fissure acting as vent of the Eastern pyroclastic flows of the **up** eruption.

(17) N030° lineaments inside the caldera and a N340° lineament outside the caldera, from which the caldera-filling rhyodacitic domes (**pfi**) were erupted.

Further tectonic features cutting through the youngest deposits of Nisyros can be observed in some outcrops. We will present below the observations made along the road connecting the villages of Mandraki and Loutrà, about 200-300 m before the latter (Fig. 4.5-A & B). Two families of normal faults were observed here, showing the same N030° direction, within ±10°. However, they dip in opposite directions (one to the East, one to the West), crossing at an angle of 30°. These could represent conjugated faults related to a N120°-

oriented extensional stress. Filling of the fissures may indicate syn- and/or post-**up** activity.

The two main volcano-tectonic structures of the whole Nisyros Island are the central caldera depression and the Vunàri debris avalanche scarp.

At first sight, the caldera of Nisyros appears as an almost perfectly round structure (Fig. 4.3). This morphological characteristic and the striking appearance of Lower and Upper pumices deposits (**lp** & **up**) led several previous authors to relate the caldera depression to these two explosive events (Hardiman, 1999; Vougioukalakis, 1998; Papanikolaou et al., 1991; Keller et al. 1990; Di Paola, 1974), or even to the last one of these explosive eruptions (Limburg & Varekamp, 1991). The stratigraphic reconstruction made by Volentik et al (2002) pointed out that on the present caldera walls are recognisable the deposits of at least two other explosive events capable of inducing caldera collapses, i.e., the pyroclastic units of Lakkì (**ka & kb**) and of Melisserì (**ms**) (see Volentik et al. (a), this volume). Although the Lakkì deposits crop out only in two sections, they show a thick, typical plinian sequence of pumice fallout, surges and pyroclastic flow deposits. In addition to this fact, it must be underscored that the lava flows emplaced after the Lakkì eruption ($\mathbf{lf^2}$ & $\mathbf{lf^3}$) dip in the direction of the present caldera depression, suggesting the presence of a morphological depression topping an ancient, beheaded, volcanic edifice. The existence of such a depression is further testified by the two lacustrine units $\mathbf{fl_1}$ and $\mathbf{sl_1}$ cropping out inside the north-eastern present caldera cliff only. Indeed, these lacustrine deposits do not continue on the eastern sector of the cliff. On the basis of these evidences, Volentik et al, (2002) advanced the hypothesis that a first relatively small caldera was formed during the early periods of volcanic activity in the northern sector of Nisyros as a consequence of the Lakkì eruption.

A second important explosive sequence (up to about 30 m thick) is represented by the Melisserì pyroclastic unit (**ms**), diffusely cropping out on the present caldera walls as well as outside of the caldera, on the slopes of the volcano. The stratigraphic sequence of this eruption includes pumice fallout and huge pyroclastic flow units that crop out all along the caldera wall and decline in thickness moving southward (see Volentik et al.(b), this volume). This decrease in thickness corresponds to a reduction in the juvenile scoriae dimension, indicating that the source region of the flow has to be placed in the north-western sector of the present caldera depression. Epiclastic deposits top the Melisserì sequence ($\mathbf{ms_j}$) marking the reorganization of the morphology after this devastating eruption. This eruptive sequence and the large volume of the deposits cropping out on caldera walls led Volentik et al. (2002) to propose the occurrence, at the end of this eruption, of a second caldera collapse whose position was more centred with respect to the present caldera.

According to the previous literature and based on our findings, a large caldera formed again as a consequence of the explosive eruption that produced the deposits of the Lower Pumice (**lp**). The remnants of this caldera collapse are constituted by the curved morphology that forms the northern half of the present caldera rim.

Even the last phase of explosive magmatic activity (the Upper Pumice eruption) is tectonically controlled. The **up** related deposits formed a tuff cone (Volentik et al., 2002) located outside the **lp** caldera rim (Fig. 4.3) and inside the collapsed area related to the emplacement of the Vunàri debris avalanche. Pyroclastic density current deposits of the **up** eruptive episode poured out from N030° fractures and locally lie on the Nikià lavas (Fig. 4.3).

Finally, the southern sector of the present caldera depression is clearly affected by a stratigraphic doubling (Volentik et al., 2002). It formed as the result of the enlargement of the former nested calderas by faults linked to the major tectonics trends (i.e., N030°) at least after the effusion of the Nikià lava flow (**nlf**).

The area interested by the Vunàri ($\mathbf{vu_i}$) debris avalanche collapse was recognised as interested by major tectonic elements by numerous authors. Both Allen & Cas (2001) and Pe-Piper et al. (2005) postulated the remnants in this area of a portion of the caldera related to the KPT eruption (Fig.4.2-B).

The mechanism of formation of the $\mathbf{vu_i}$ (see Volentik et al.(b) and Principe & Marini, this volume) imply a tectonic stress in the direction of the mass failure (Vidal & Merle, 2000) and consequently tectonic elements perpendicular to the direction of such a movement. These elements are represented in the tectonic sketch map of Fig 4.3 by the N070° faults that still exist in the area indicated as the $\mathbf{vu_i}$ source area, based on our reconstruction. In other words, these ENE tectonic trends can be assumed to have been responsible of the triggering of the Vunàri debris avalanche, which travelled in a NNW direction.

An interesting observation is that the hummocky morphology (see Volentik et al.(a), this volume) related to the $\mathbf{vu_l}$ deposits brough about the presence in past time of a little swamp along the coast from Mandraki to Palì. This swamp was reclaimed at the beginning of the XIX century as testified by Ross (1843) (see note 2 in Volentik et al.(a), this volume).

Finally, an erosional surface is ubiquitous all along the north-western shore of Nisyros as a result of marine erosion followed by the emplacement of marine terrace deposits. As already stated by Volentik et al.(a) (this volume), the terrace is mainly cut into **blf** deposits and preceding ones. According to Pe-Piper & Piper, (2005) tectonic movements may have specifically affected the area of Mandraki and the western sector of the island, leading the terrace to emersion in this sector only. In any case, the present position of the marine terrace, some tens of meters above sea level, testifies that at least this portion of the island experienced important vertical displacements in recent times.

The comparative analysis shown in Table 4.1 demonstrates a strong correlation between the switches in the location of volcanic centres, changes in the dominant tectonic trends, and the synthematic subdivision applied to the stratigraphic record.

There is no clear information on the tectonic control at the beginning of the Nisyros volcanic activity, when the submarine lavas of the Kanafià synthem were emplaced. In contrast, it is apparent that in the subsequent stages of the evolution of Nisyros (Kremastò and Katò Lakkì synthems), the activity is restricted to the northern sector of the island and is mainly dominated by a N030° tectonic trend. The following Lies synthem is the most complex, in that it displays the most complicated relationships between tectonics and volcanic activity. Starting from the northern part of the island, the venting migrated to the South and then to the East and was accompanied by changes in the active tectonic trends. At the end of this synthem, the activation of all tectonic trends is simultaneous to a widespread volcanic activity from scattered strombolian centres. The transition to the Fournià synthem coincides with the activation of a N030° trend and the presence of a source restricted to the north-western sector of the island. The Kàrdia synthem sees the shift to a central vent that will characterise the end of Nisyros activity. In the terminal phase of the volcano's history, the N030° trend once more becomes the prevailing one. This trend seems to be the most important general trend active on Nisyros, dominating almost all phases with short hiatuses chiefly during the Lies synthem.

In a more general way, the north/north-east section of the island seems to have been the preferred site of volcanic activity during much of the island's past, as testified by the concentration of vents in this area throughout Nisyros' history and by the greater number of dykes that alimented the lava flows found along this sector of the caldera wall (Volentik et al., 2002). Eruptive vents moved toward a more central location only during the latest stages of the volcanic evolution of the island.

4.4. Modern tectonic events

On December 5th, 2001, a 350 m long fissure opened in the middle of the Lakkì plain (Fig. 4.8-A & B). No seismic nor tectonic activity was recorded at that time, and the crack was interpreted as the result of surface and subterranean erosion of the ground partly as a result of the torrential rain the island experienced during the winter of 2001 (E. Lekkas, 2001 press release). Our observations in the field revealed (Fig. 4.8-C) that the fracture system follows three trends: N030°, N070° and N340°. The presence of this kind of void areas under the ground in the Lakkì plain, revealed by the heavy rains occurring on the island during that winter, can be related to chemical weathering governed by acidic steam condensates whose flow rate was estimated to be close to 1420 t/d (Caliro et al., 2005). The same mechanism of weathering can be invoked for the formation during winter periods of holes of several cm in diameter, that repeatedly appeared on the floor of the Stephanos crater (Fig. 4.9), which is the area most affected by hydrothermal alteration inside the caldera floor. Incidentally, these holes were already recognized and described by Martelli (1917).

Even though the 2001 fissure probably did not open at that time, its presence and elongation indicates that all the three mentioned tectonic trends were still active in very recent times. This finding confirm the results of the geophysical self-potential and VLF surveys carried out in the Lakkì area (Vanderkluysen & Gex, this volume) and the observed localization of the recent and historical hydrothermal craters at the crossing of elements related to these active tectonic trends (Fig. 4.3).

		Kanafià	Kremastò				Katò Lakkì			Lies										Fournià		Kàrdia					Illias	Gorceix
		ho_a	lf^1	ka	lf^2	kb	lf^3	lf^4	ms	lf^5	xlf_b	lf^6	sv	alf	lf^7	pa	vs_n	xo	lf^8	blf	emb	vu_i	llf	lp	nlf	up	pfi	gx
Dominant tectonic trend	N030°		▒	▒	▒	▒	▒	▒	▒	▒	▒	▒	▒	▓				▓	▓	▓	▓	▓		▓	▓	▓	▓	▓
	N070°				▓					▒	▒	▒	▒	▒	▒	▒	▒	▓	▓			▓						
	N340°									▓					▓	▓		▓	▓		▓	▓	▓					
	N120°													▓				▓	▓					▒				
	Unconformable units		ho_j				fl_l	sl_l		ms_j							pa_j			pc_j					pl_j		ya_j	

Table 4.1: Tectonic trends in effect at the time of each volcanic event on Nisyros. Light grey: evidence supported by single observations of dyke orientation or tectonic lineament measurement. Grey: evidence supported by multiple dyke orientation measurements and correlated with field observation of tectonic lineaments. Black lines: synthematic boundaries; thin lines: sub-synthematic boundaries. Units marking synthematic and sub-synthematic breaks are reported at the bottom.

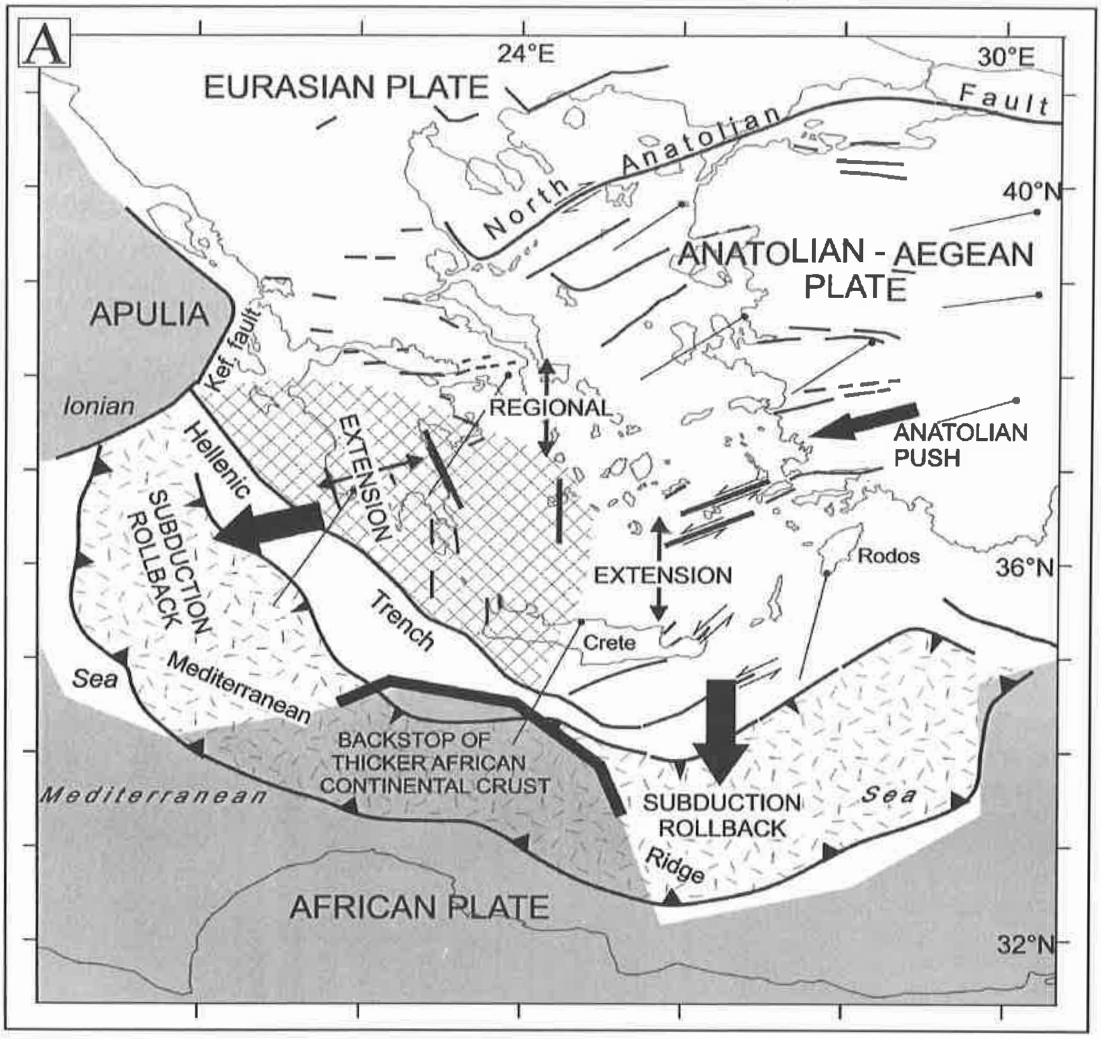

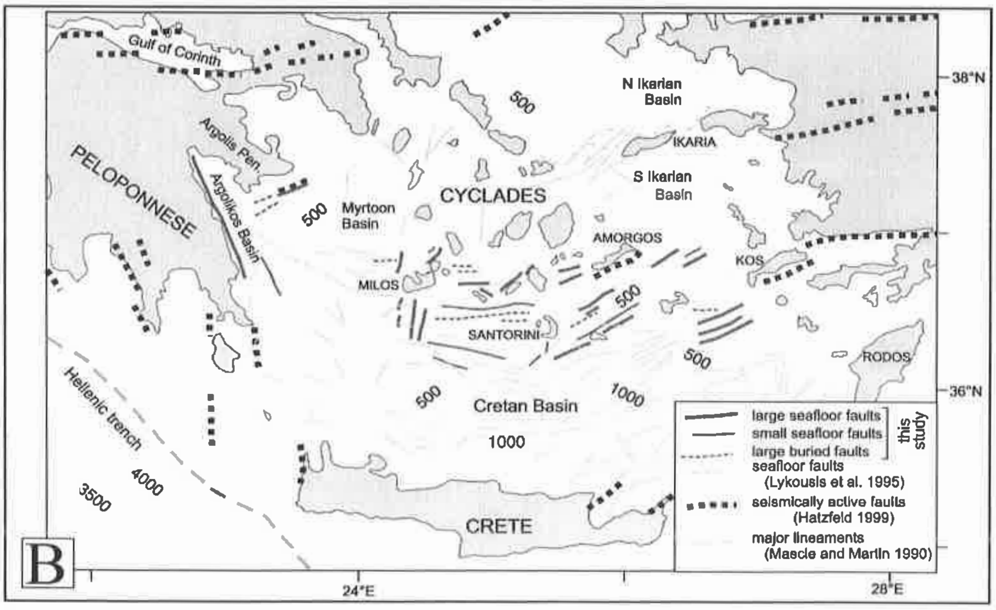

Fig. 4.1:
A: Schematic tectonic interpretation of the South Aegean arc (from Piper & Perissoratis, 2003);
B: Map of faults in the South Aegean arc (from Piper & Perissoratis, 2003).

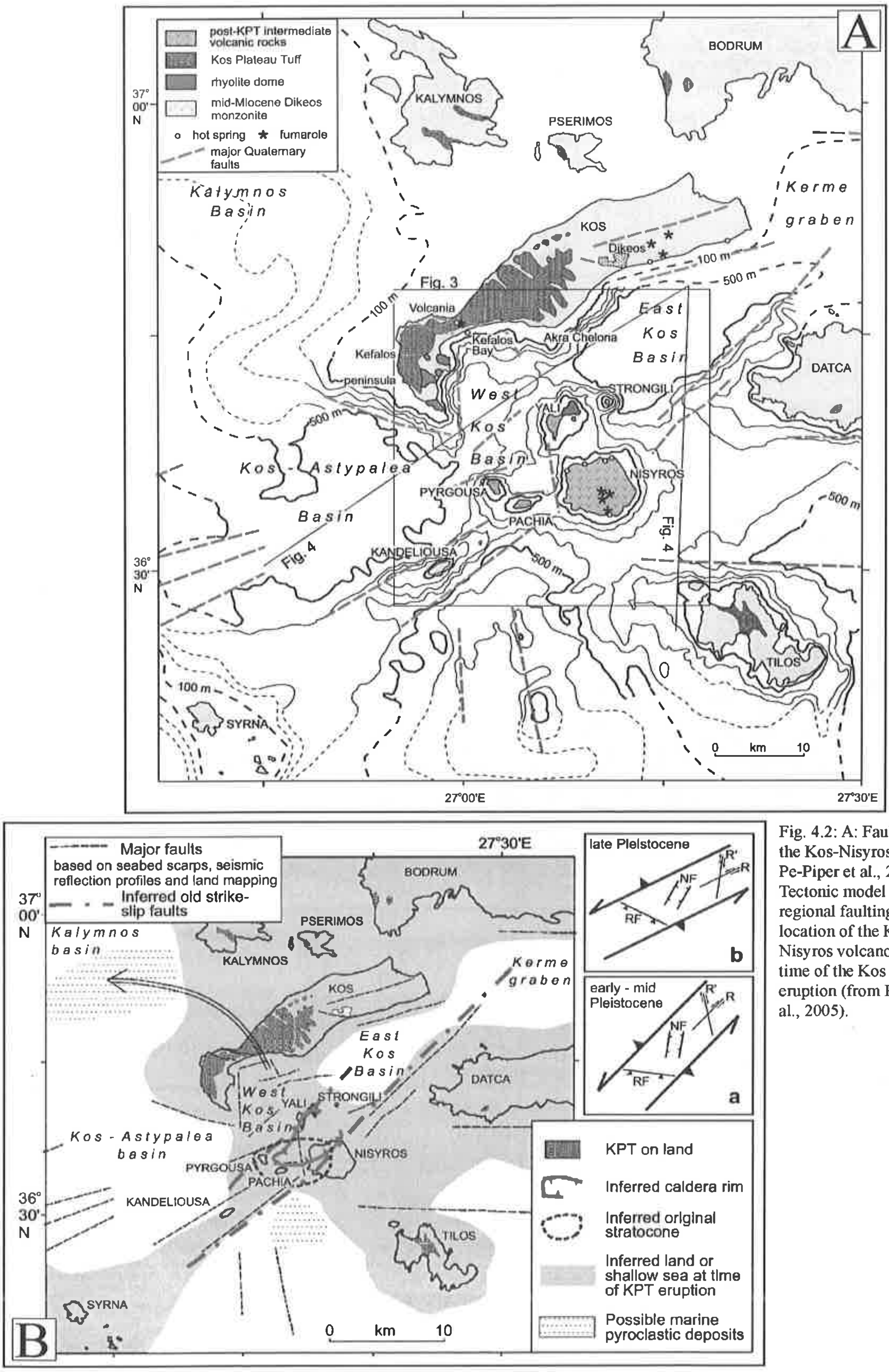

Fig. 4.2: A: Fault patterns in the Kos-Nisyros area (from Pe-Piper et al., 2005); B: Tectonic model for the role of regional faulting in the location of the Kos-Yali-Nisyros volcanoes, at the time of the Kos Plateau Tuff eruption (from Pe-Piper et al., 2005).

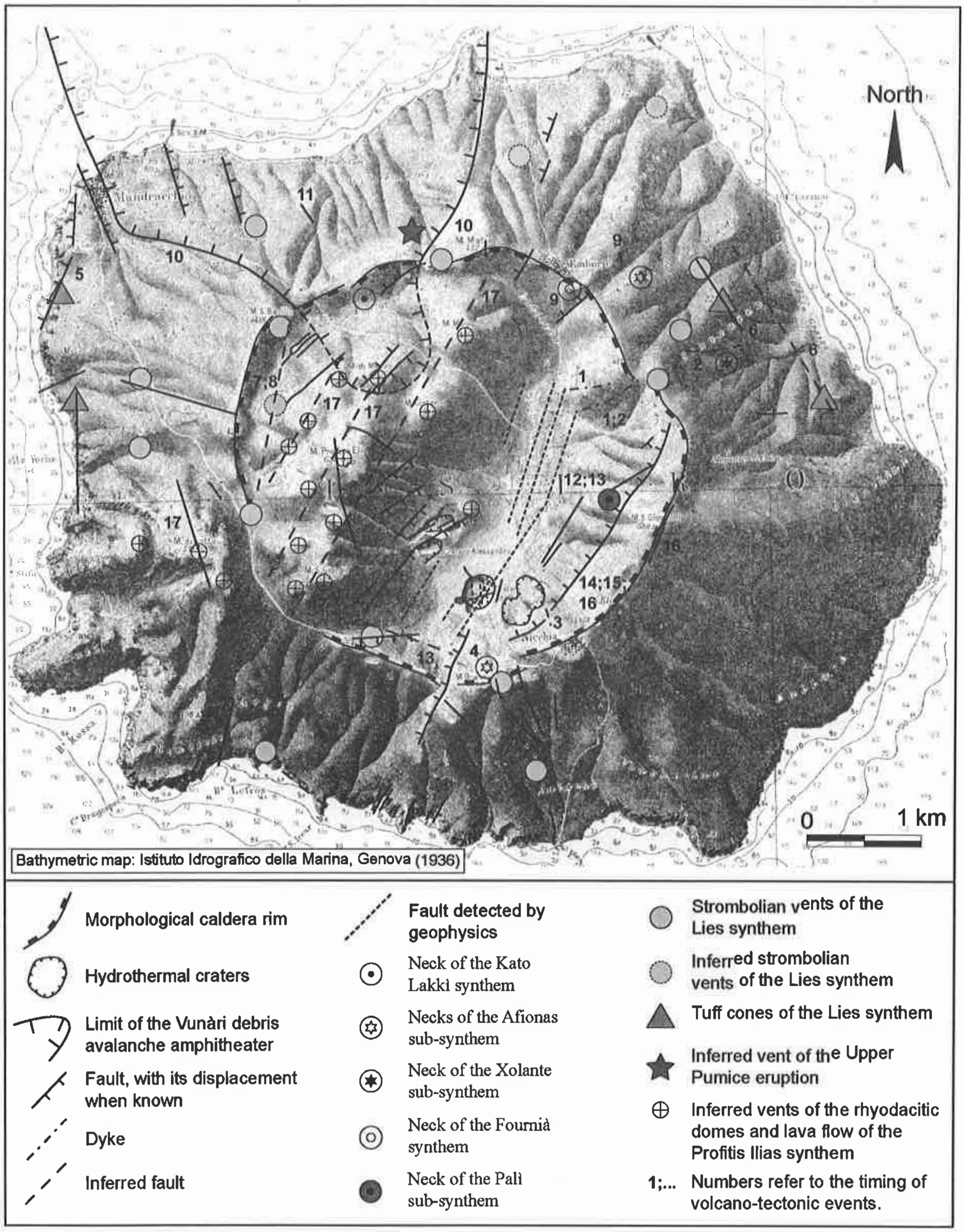

Fig. 4.3: Map of recognised volcanic centres and tectonic elements on Nisyros.

Fig. 4.4: Along the road from the beach of Lies to the Monastery of Panaghia Kyra. Normal fault oriented N 070°, which cuts the pyroclastic deposits of **pa**, A. Volentik for scale.

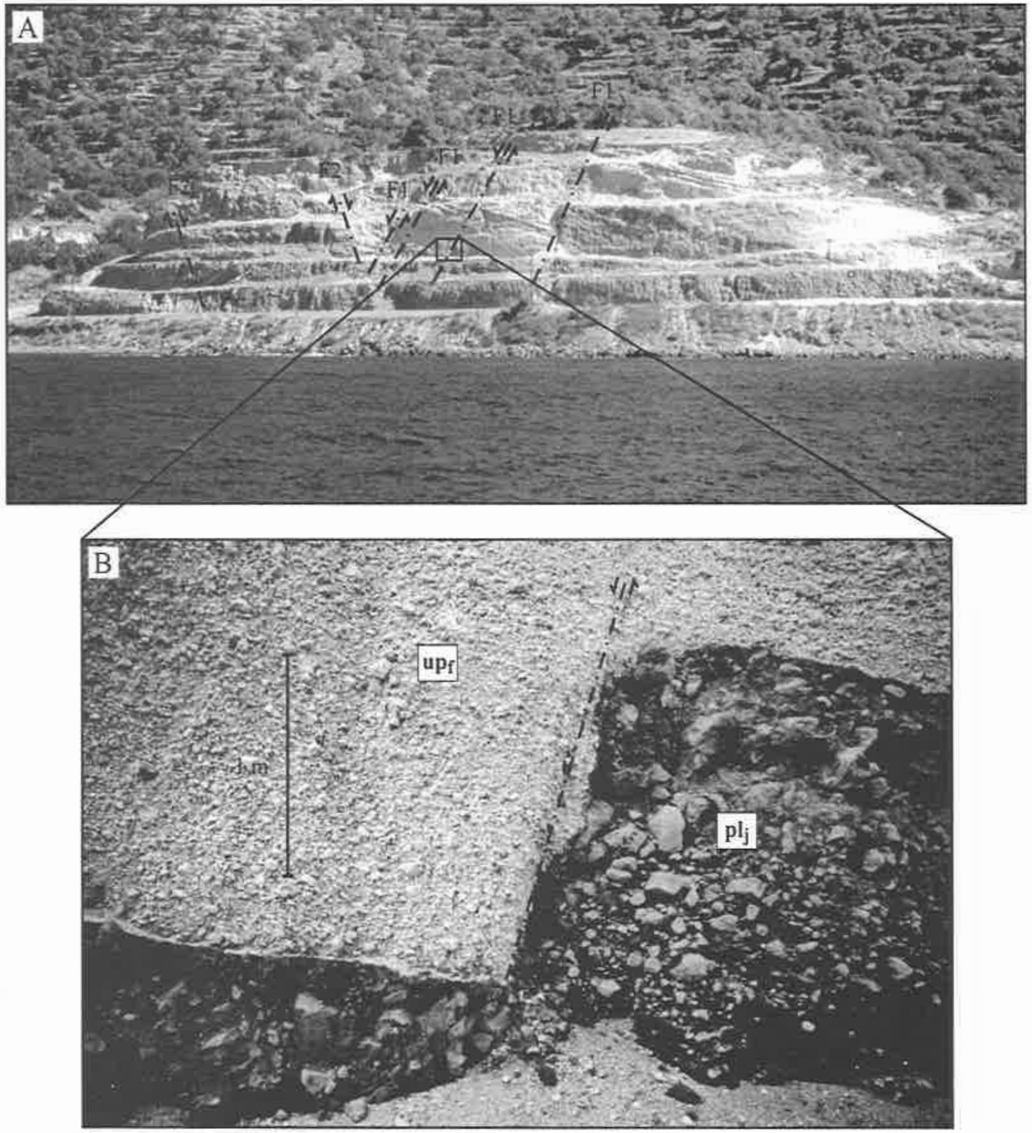

Fig. 4.5: Tectonic structures in the outcrop of Loutrà. A: General view of the outcrop showing the two families of faults (F1 = 110/80; F2 = 275/80); B: Detailed photograph of a F1 normal fault.

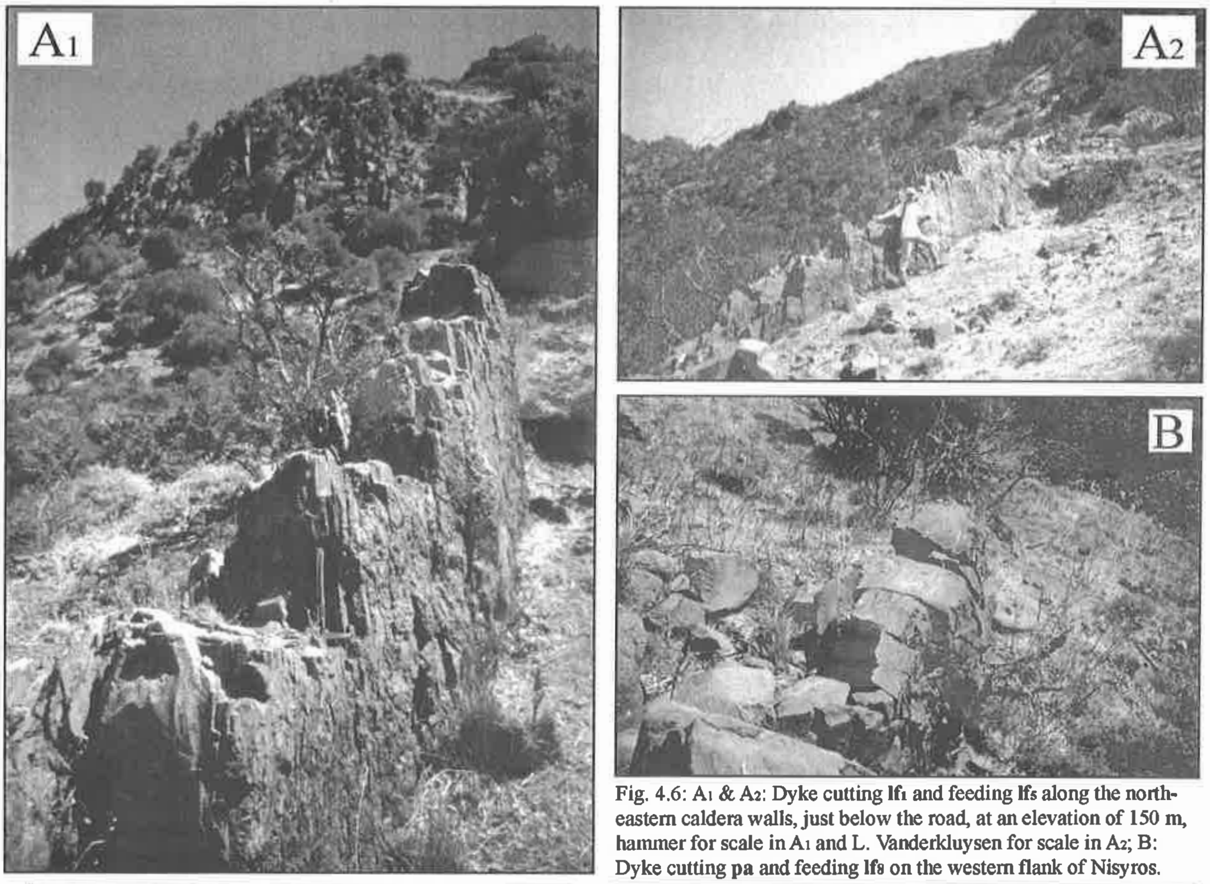

Fig. 4.6: A$_1$ & A$_2$: Dyke cutting **lf$_1$** and feeding **lf$_5$** along the north-eastern caldera walls, just below the road, at an elevation of 150 m, hammer for scale in A$_1$ and L. Vanderkluysen for scale in A$_2$; B: Dyke cutting **pa** and feeding **lf$_8$** on the western flank of Nisyros.

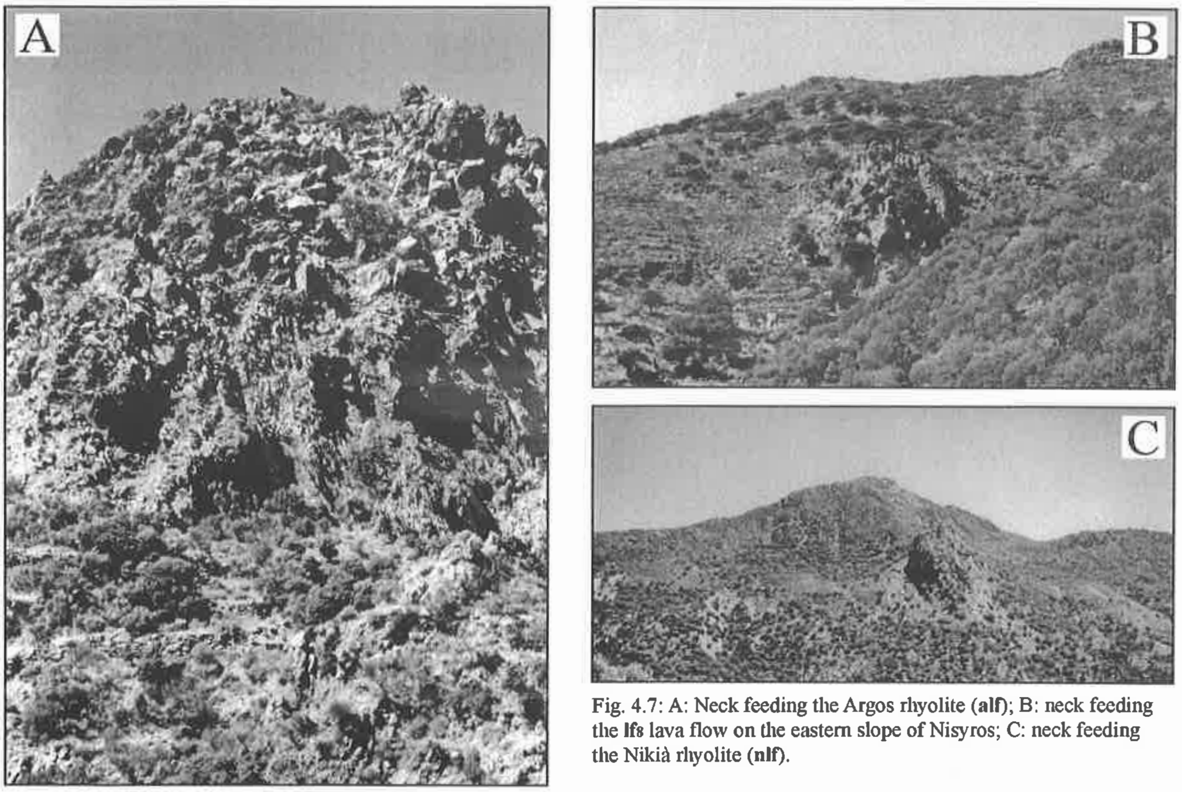

Fig. 4.7: A: Neck feeding the Argos rhyolite (**alf**); B: neck feeding the **lf$_8$** lava flow on the eastern slope of Nisyros; C: neck feeding the Nikià rhyolite (**nlf**).

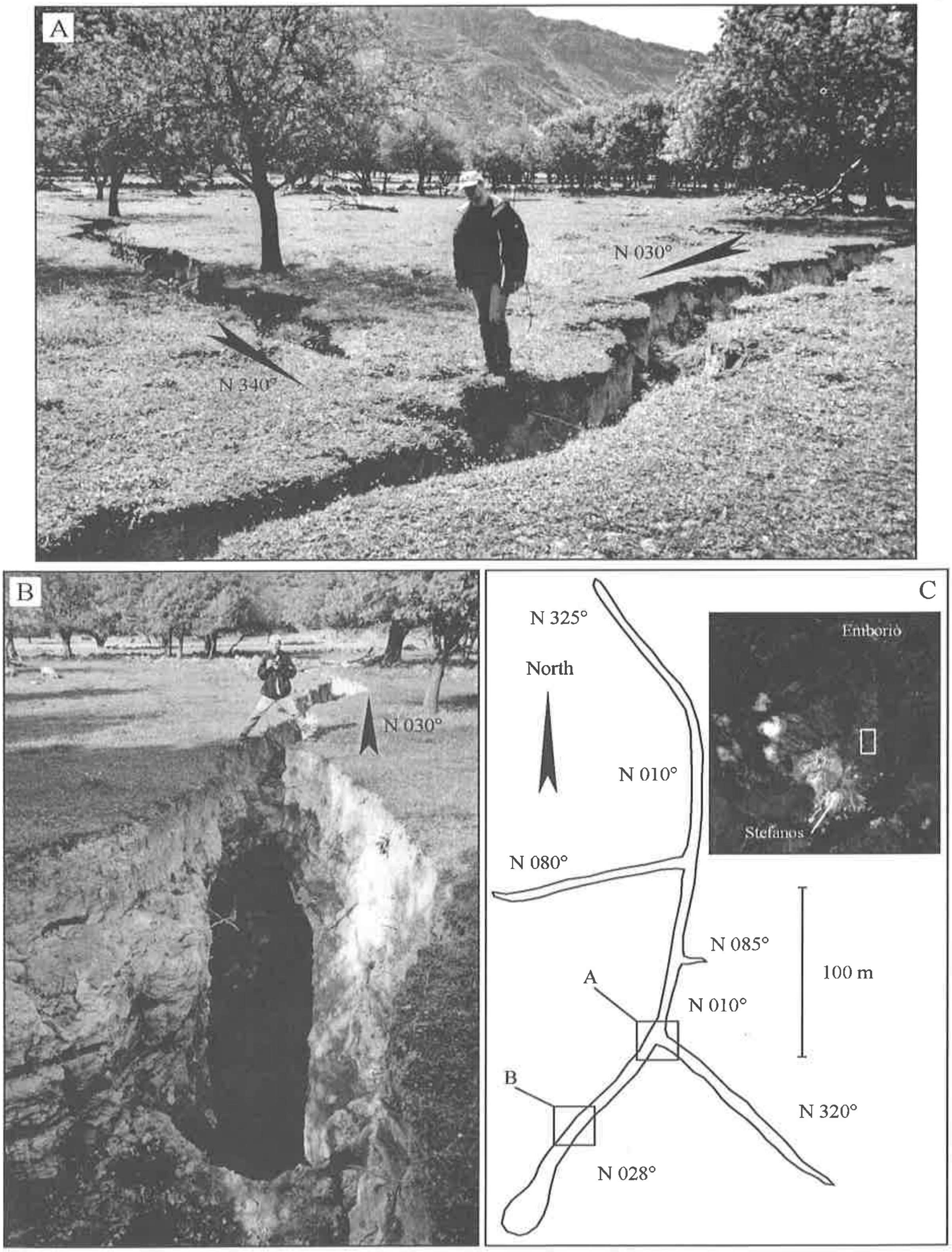

Fig. 4.8: Modern tectonic events in the Lakki plain. A & B:Photographs of the fractures, as revealed in December 2001, L. Vanderkluysen for scale. C: Simplified sketch of the fissure, with its orientation and localisation in the Lakki plain.

Fig. 4.9: Fumarolic holes within the crater of Stefanos; diameter of the holes is about 80 cm.

5. The petrology and geochemistry of lavas and tephras of Nisyros Volcano (Greece)

Loÿc Vanderkluysen(1), Alain Volentik(1), Jean Hernandez(1), Johannes C. Hunziker(1), François Bussy(1), Claudia Principe (2)

(1) Institut de Minéralogie et Géochimie, BFSH-2, Université, CH-1015 Lausanne, Switzerland.

(2) Istituto di Geoscienze e Georisorse, Area della Ricerca CNR-Pisa San Cataldo Via G. Moruzzi 1, I-56124 (Pisa), Italy.

Abstract - The products of Nisyros volcano belong to the calc-alkaline series and range in composition from basaltic andesites to rhyolites. A scarcity of samples with SiO_2 content between 61 and 63 wt% characterizes the dataset. Major and trace element trends can generally be explained by fractional crystallization processes, but most incompatible trace elements fail to be accurately modeled at the andesite-dacite transition zone. The presence of bimodal crystal populations, quenched mafic enclaves and reversely zoned crystals in some samples can be explained by crystal retention, removal and re-entrainment and by magma mixing and/or mingling processes. Some amount of crustal contamination is required to account for Sr, Nd, Pb and Hf isotopic variations in the rock suite. These processes, however, are insufficient to explain the peculiar behavior of incompatible trace elements in the dacites and rhyolites. Models of polybaric evolution can partly explain this behavior, although it remains unclear why the evolution from dacites to rhyolites takes place at greater depths than the transition from basaltic andesites to andesites. We recognize that our current state of knowledge is insufficient to offer an unambiguous model for the origin of rocks from Nisyros. Future work including Sr, Nd, Pb, O, Hf and U-Th isotopic analyses, mineral major and trace element and isotopic microanalyses and experimental data should help shed a new light on the origin of Nisyros' magmas.

5.1. Introduction

Previous studies of products of Nisyros volcano (e.g. Davis, 1967; Di Paola, 1974; Vougioukalakis, 1984; 1993; Bohla & Keller, 1987; Wyers & Barton, 1989; Lodise, 1987; Gansecki, 1991; Limburg & Varekamp, 1991; St. Seymour & Vlassopoulos, 1992; Francalanci et al., 1995; Innocenti et al., 2002; Volentik et al., 2002; Vanderkluysen & Volentik, 2002; Buettner et al., 2005) have highlighted that their petrological and geochemical characteristics mainly result from crystal fractionation, influenced by one or more of the following processes: magma mixing, polybaric evolution, crystal retention and re-entrainment, magma chamber replenishment and crustal assimilation.

Pe-Piper & Piper (2002) note that the low LIL (large ion lithophile elements) concentrations, together with the presence of a silica gap, are features that distinguish Nisyros from its South Aegean volcanic neighbors. Wyers & Barton (1989) proposed a polybaric evolution model to explain these features, and argue that more felsic products evolved separately from the basaltic andesites and andesites in a deeper magma chamber, whereas Vougioukalakis (1993) argues for the existence of a shallow storage system for the Nisyros rhyolitic magmas. The Wyers & Barton (1989) model, however, raises the issue of why two distinct and complete series (both from basaltic andesites to rhyolites, but formed at different depths) did not develop on the island.

The goals of this paper are to present a petrological and geochemical database of lava and tephra samples gathered on Nisyros volcano, review available data and discuss the magmatological processes that have been taking place throughout the geological history of the island.

5.2. Analytical methods

Approximately 140 samples were processed for major and trace element analysis and petrographic description. Of these, a set of 25 representative samples was selected for further trace and rare earth elements (REE) analysis.

Major element concentrations were measured on fused discs (obtained by mixing rock powders with lithium tetraborate) and trace elements on pressed pellets at the University of Lausanne X-Ray Fluorescence (XRF) facility. Rock powders were produced using agate and tungsten carbide mills. Results are presented in Table 5.1.

Additional REE and trace element measurements were obtained at the University of Lausanne LA-ICP-MS facility by laser-ablation of the same fused discs that had been used for XRF measurement. External standards were measured every three samples, and data reduction was realized using ^{42}Ca as internal standard; with this technique, relative uncertainties are expected to be of ± 10%. Because oxide interferences with Gd were not satisfactorily corrected for, the element was removed from the study. Results are presented in Table 5.2.

Microprobe analyses presented by Vanderkluysen & Volentik (2002) were realized on a CAMECA SX 50 device, and will not be repeated here. The dataset is available upon request to LV.

The stratigraphic position of each sample is identified in Tables 5.1 and 5.2, following the mapping and stratigraphic nomenclature of Volentik et al. (this volume), and a sample location map is presented in Fig. 5.1.

5.3. Results

5.3.1. Petrography

A summary of petrographic observations and parageneses is presented in Tables 5.3 and 5.4; petrographic observations for each sample are available upon request to LV.

The rocks from Nisyros range from basaltic andesites to rhyolites. In thin section, this succession is marked by an evolution of the phenocryst assemblage plagioclase + clinopyroxene ± olivine to plagioclase + clinopyroxene + orthopyroxene to plagioclase + clinopyroxene + orthopyroxene + amphibole + apatite + zircon.

Olivine is a frequently observed phase in rocks ranging from 50 to 59 wt% SiO_2. Olivine is also present as relics or ghosts and can be partly or entirely affected by iddingsitization. It ranges from Fo_{82} in basaltic andesites to Fo_{65} in the more silicic andesites, where it is rimmed by orthopyroxene.

Plagioclase (plag) is ubiquitous throughout the series, almost always zoned, with frequent resorbed cores and sieve textures. Its composition ranges from An_{90} in the most primitive samples to An_{25-30} in the rhyolites. Samples AV42c (**nlf**), AV9 (**xlf$_b$**) and AVN99-046 (**pfi**) show strongly bimodal plagioclase populations. Most plagioclases are normally zoned with superimposed oscillatory zoning. Reversely-zoned plagiclases have been identified in some enclave-bearing units such as **nlf**, **xlf$_b$**, **emb** and **pfi**.

An augitic clinopyroxene (cpx) appears in the most primitive rocks of the sequence and is still present in the rhyolites. A bronzite-type orthopyroxene (opx) appears in the andesites and evolves to more hypersthene-like compositions in the dacites and rhyolites. Some of the pyroxenes display rounded rims, reactions rims and resorbed cores. Reversely-zoned pyroxenes have been observed in enclave-bearing lavas.

Brown to green pleochroic hornblende occurs in the dacites and rhyolites. In the dacite, it often displays rounded or resorbed rims, or is present only as ghosts. In the rhyolites, it becomes more abundant and more stable. It should be noted here that amphibole is a prime constituent of the so-called "amphibole-bearing xenoliths" already described by Di Paola (1974) and Wyers & Barton (1989). Interestingly, amphiboles from enclaves of unit **nlf** have chemical compositions similar to hornblendes of the host rock. The Lakki pyroclastics (units **ka** and **kb**) are the only mafic unit containing amphibole.

Accessory phases include various sulfides and magnetite; apatite, zircon and ilmenite have been observed in more evolved samples.

Finally, biotite phenocrysts have been found in a single sample of unit **xlf$_b$**, and as an interstitial phase in the dacites of units **emb** and **vu$_J$**.

Texturally speaking, most rocks from Nisyros show phenocrysts a few millimetres in size within a microcrystalline groundmass. Groundmass crystals have a wide range of sizes, from 0.1 mm to 0.5 mm. In some andesites and basic andesites, as well as in some dykes and submarine lavas, hypocrystalline textures have developed. Glassy groundmass can also be observed in dacites and rhyolites. Rhyolitic glass often displays superimposed perlitic textures.

Amphibole-bearing enclaves, previously described by numerous authors (e.g. Di Paola, 1974; Wyers & Barton, 1989; St Seymour & Vlassopoulos, 1992; Francalanci et al., 1995; Gansecki, 1991; Limburg & Varekamp, 1991), have been found in units **xlf$_b$**, **emb**, **nlf**, **lp**, **up** and **pfi**. They typically display irregular curvy shapes, quenched rims and needle-like mineral textures (cpx and amphibole), and are basaltic andesitic or andesitic in composition. Acicular textures have been interpreted as resulting from undercooling, and quenched rims suggest that these enclaves are magmatic in origin, representing more mafic magmas that did not homogenize with their host prior to eruption.
Clinopyroxene and plagioclase-bearing glomeroporphyritic agglomerates are frequent in all types of deposits.

5.3.2. Geochemistry

Products of Nisyros' activity are sub-alkaline and range from basaltic andesites to rhyolites (Fig. 5.2), with a noticeable gap between 61 and 63 wt% of

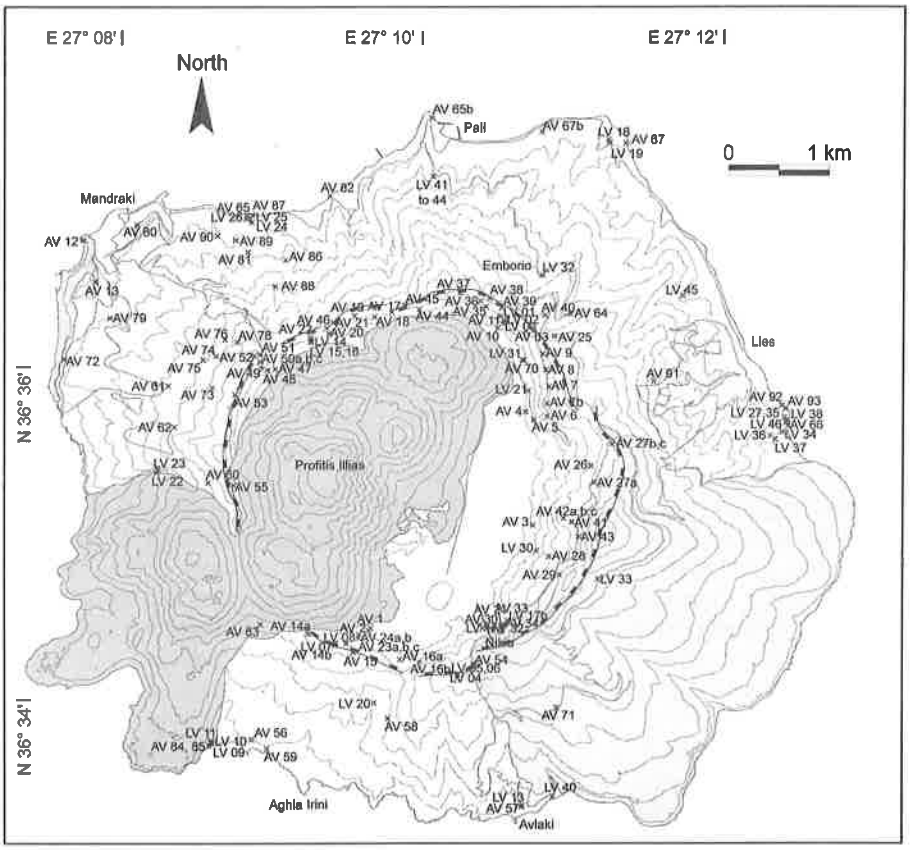

Figure 5.1. Sample location map.

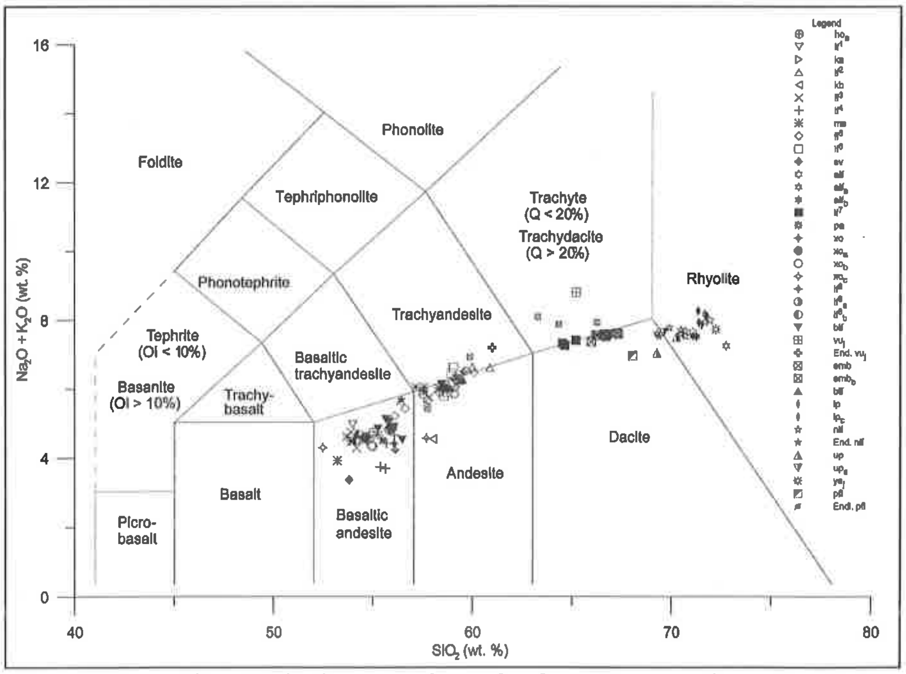

Figure 5.2. Total alkali (Na_2O + K_2O) vs. silica (TAS) diagram of samples from Nisyros volcano (Le Maitre, 1989). Data were recalculated on a water-free basis. Modified after Vanderkluysen & Volentik (2002).

SiO_2.

Major element trends (Fig. 5.3) are characterized by: (1) constant decrease of MgO, Al_2O_3 and CaO throughout the series, (2) constant increase of K_2O, (3) stable Fe_2O_3(t) for SiO_2 <60 wt%, followed by a decrease in Fe_2O_3(t) for SiO_2 >60 wt%, and (4) increasing amounts of Na_2O, TiO_2 and P_2O_5 for SiO_2 <60 wt%, after which concentrations of these elements begin to decrease. The discontinuity in Fe_2O_3(t), Na_2O, TiO_2 and P_2O_5 trends roughly coincides with the occurrence of the silica gap mentioned above.

Some trace element data (Fig. 5.4) display similar discontinuities in their evolution, such as for Nb, Zr, Y, Ce and La. Ni (not plotted) and Cr show rapidly decreasing concentrations, down to detection limits, while Ba shows a constant increase throughout the series. Sr decreases regularly, apart from an anomalous group of basaltic andesitic samples with high Sr concentration (>950 ppm). Trace element MORB-normalized diagrams (Fig. 5.5) typically show inclined patterns with steeper slopes in more evolved samples. As pointed out by Francalanci et al. (1995), Nisyros samples also display Nb-Ta-Ti anomalies typical of arc magmas. Vanderkluysen & Volentik (2002) used Nb and Zr as a tool to discriminate samples of different stratigraphic units with otherwise similar field and geochemical characteristics. Indeed, the pumices from the lower and upper pumice units (**lp** and **up**, respectively) and from the remobilised Yali fallout layer (**ya$_J$**) can be successfully differentiated on a Nb vs. Zr plot (Fig. 5.6).

Chondrite-normalized REE patterns are presented in Fig. 5.7. Light REE (LREE) are typically enriched relative to the heavy REE (HREE). LREE slopes tend to be steeper in more evolved samples (Ce/La ≈ 1.5 in rhyolites vs. 2.0 in basaltic andesites), whereas HREE slopes tend to be flat; some of the more evolved samples are also depleted in Dy, Ho, and Er. Nearly all REE (i.e. Pr, Nd, Sm, Eu, Tb, Dy, Ho, Er, Yb, Lu) show increasing concentrations from the basaltic andesites to the andesites, and a strong depletion in the rhyolites and dacites.

The study of stable and radiogenic isotope signature of Nisyros' volcanic products is still in its infancy (Wyers & Barton, 1989; Francalanci et al., 1995; Buettner et al., 2005), with approximately fifty $^{87}Sr/^{86}Sr$ analysis available in the literature, eleven of which also include $^{143}Nd/^{144}Nd$ and $^{176}Hf/^{177}Hf$ data. Not surprisingly, the most striking feature that emerges from these data is that, in the basaltic andesites, andesites and some dacites, $^{87}Sr/^{86}Sr$ is positively correlated with the degree of differentiation, ranging from 0.703384 in a basaltic andesite to 0.705120 in a dacite of the **pa** unit. Most dacites and all rhyolites do not follow this trend, however, with Sr isotope ratios between 0.7040 and 0.7045.

5.4. Discussion

5.4.1. Fractional crystallization

Previous authors (e.g. Di Paola, 1974, Wyers & Barton, 1989; St. Seymour & Vlassopoulos, 1992; Vougioukalakis, 1993; Francalanci et al., 1995) have described fractional crystallization (FC) as the dominant process of magmatic evolution on Nisyros.

Rayleigh fractionation calculations (Wyers & Barton, 1989; Vanderkluysen & Volentik, 2002) have shown that trace element and REE concentrations can be satisfactorily modeled between 51 and 60 wt% SiO_2 by removal of a cpx + plag ± olivine ± opx ± magnetite assemblage. Above 60 wt% SiO_2, decreasing contents of Fe_2O_3(t) and TiO_2 can be explained by ilmenite and Ti-magnetite fractionation, Zr and P_2O_5 decrease by apatite and zircon removal and Dy-Ho-Er depletion patterns by amphibole fractionation. Many moderately and highly incompatible elements fail to be satisfactorily reproduced by fractionation models, however. Elements such as La and Ce are particularly troublesome, as concentrations in the rhyolites would require fractionation of unrealistic amounts of accessory phases. The amount of fractionating ilmenite and apatite, in particular, would be inconsistent with estimates derived from TiO_2 and P_2O_5 variations. Wyers & Barton (1989) report similar problems with Rb, Zr, Cs, Ba, La, Ce, Sm, Yb, Hf and Th.

Previous authors (e.g. Wyers & Barton, 1989; St. Seymour & Vlassopoulos, 1993; Francalanci et al., 1995; Vanderkluysen & Volentik, 2002) have concluded that fractional crystallization cannot be the sole magmatic process involved in Nisyros' evolution, and that rhyolitic and, to a lesser degree, dacitic products are difficult to relate to the basaltic andesite-andesite series by simple crystal fractionation. These conclusion are based on the following considerations: (1) some trace and rare earth elements display unpredictable behaviors in felsic products, (2) a group of mafic samples display high (>950 ppm) Sr concentrations, which cannot be related to other samples by fractional crystallization, (3) a silica gap exists between 61 and 63 wt% SiO_2, (4) mafic enclaves and xenocrysts are frequently observed in evolved units, (5) crystals, and plagioclases in particular, sometimes display reverse zoning and signs of destabilization such as resorbed cores and sieve textures, (6) although $^{87}Sr/^{86}Sr$ isotope ratios increase from basaltic andesites to dacites, most dacites and rhyolites do not belong to this evolutive trend.

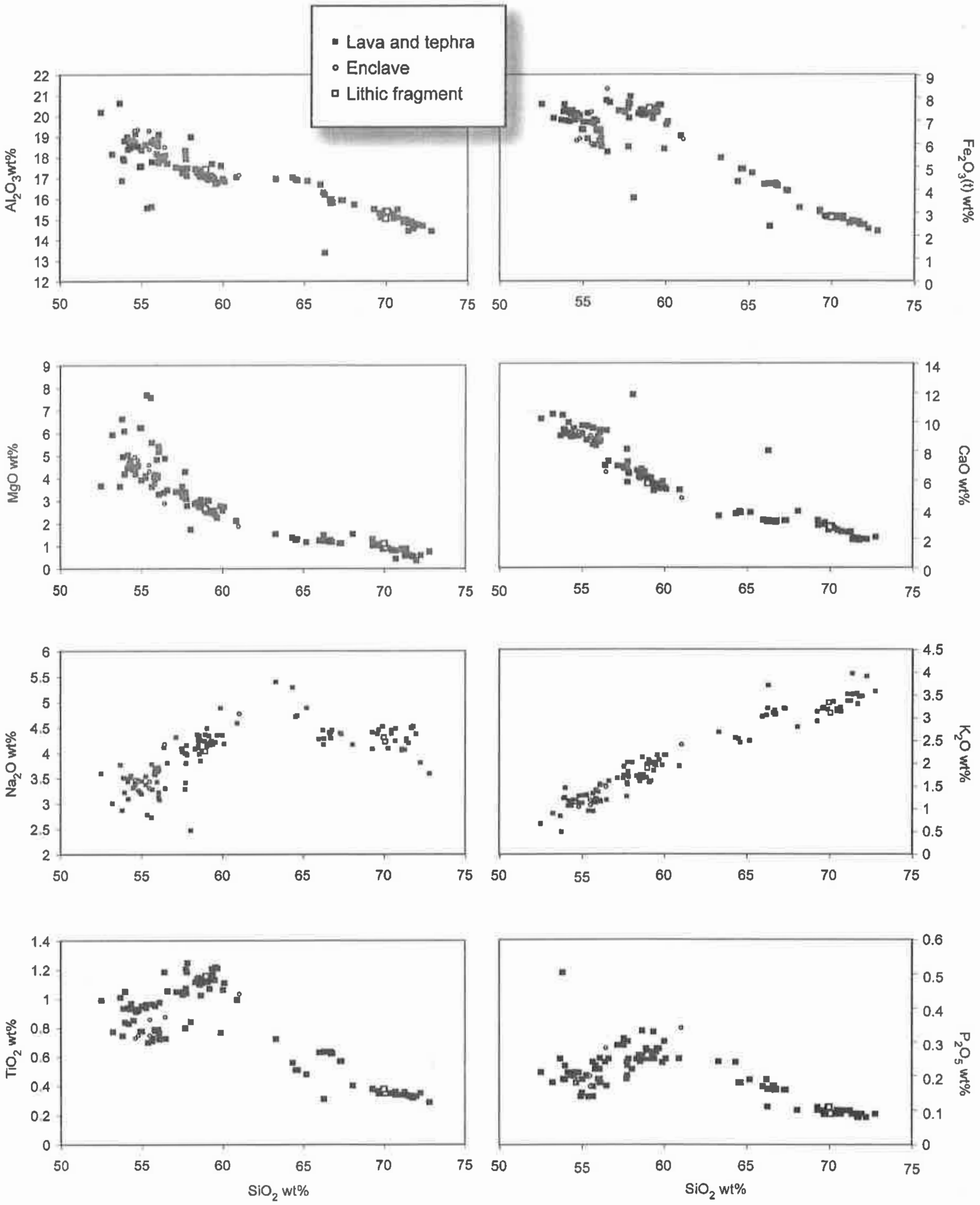

Figure 5.3. Summary of major element data.

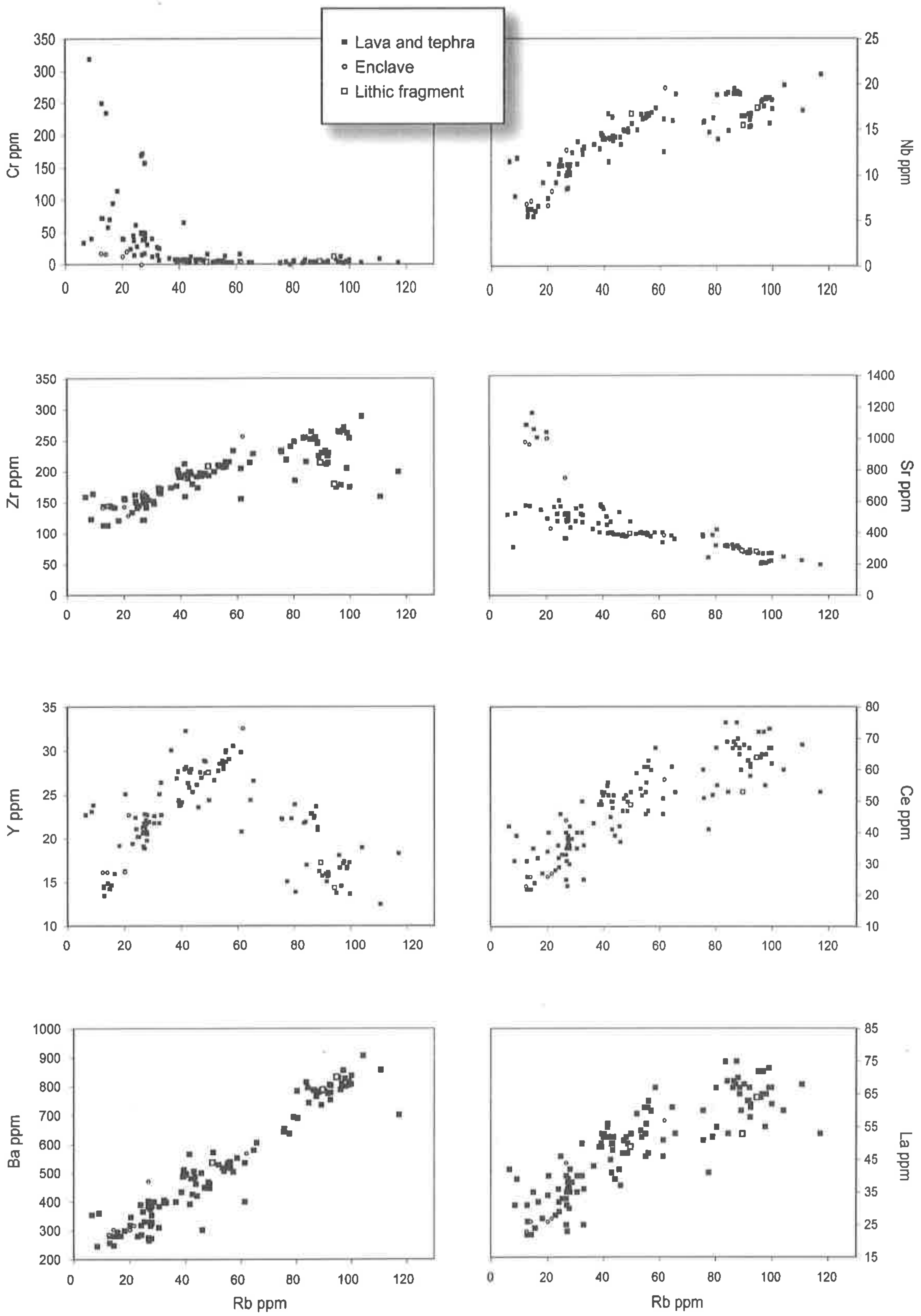

Figure 5.4. Summary of trace element data, using Rb as reference variable, as it shows the greatest variation and the most consistent behavior (Wyers & Barton, 1989).

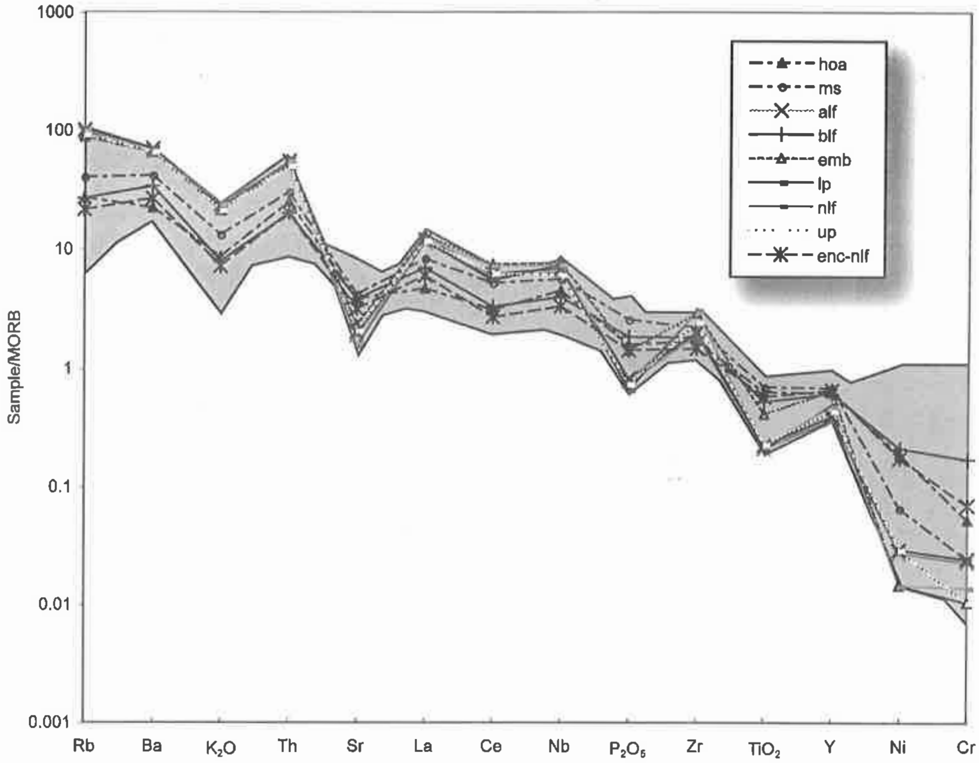

Figure 5.5. Trace element patterns of samples from Nisyros, using normalizing values of Bevins et al. (1984). The grey area highlights the entire range of observed values, while individual samples of representative units are shown by lines and symbols.

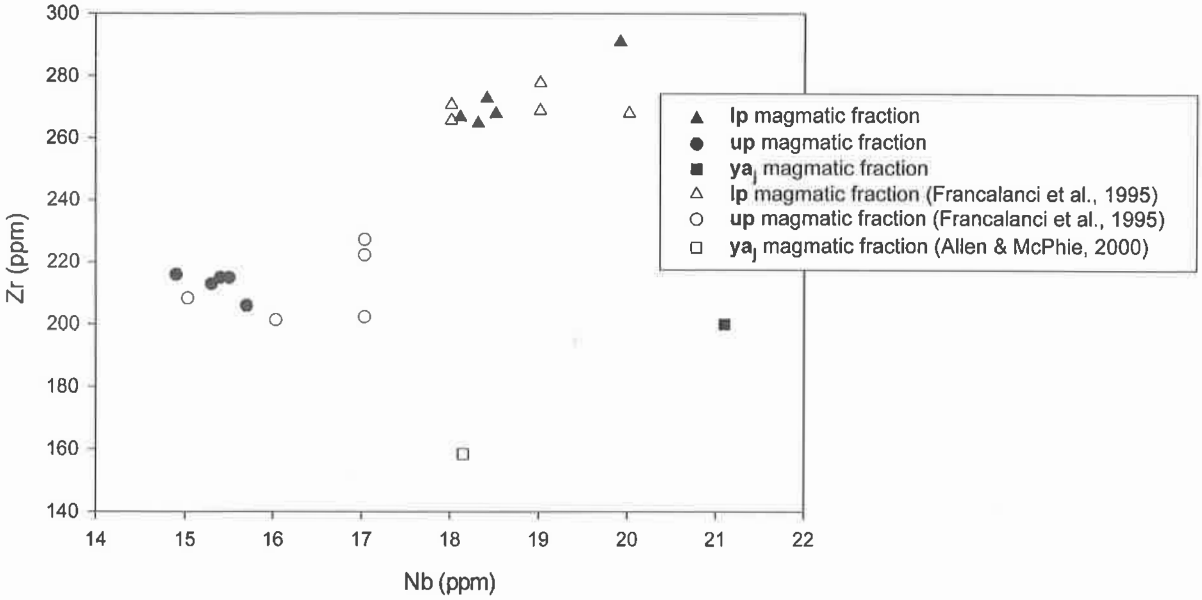

*Figure 5.6. Nb vs. Zr diagram of pumice samples from the **lp**, **up** and **ya$_j$** units.*

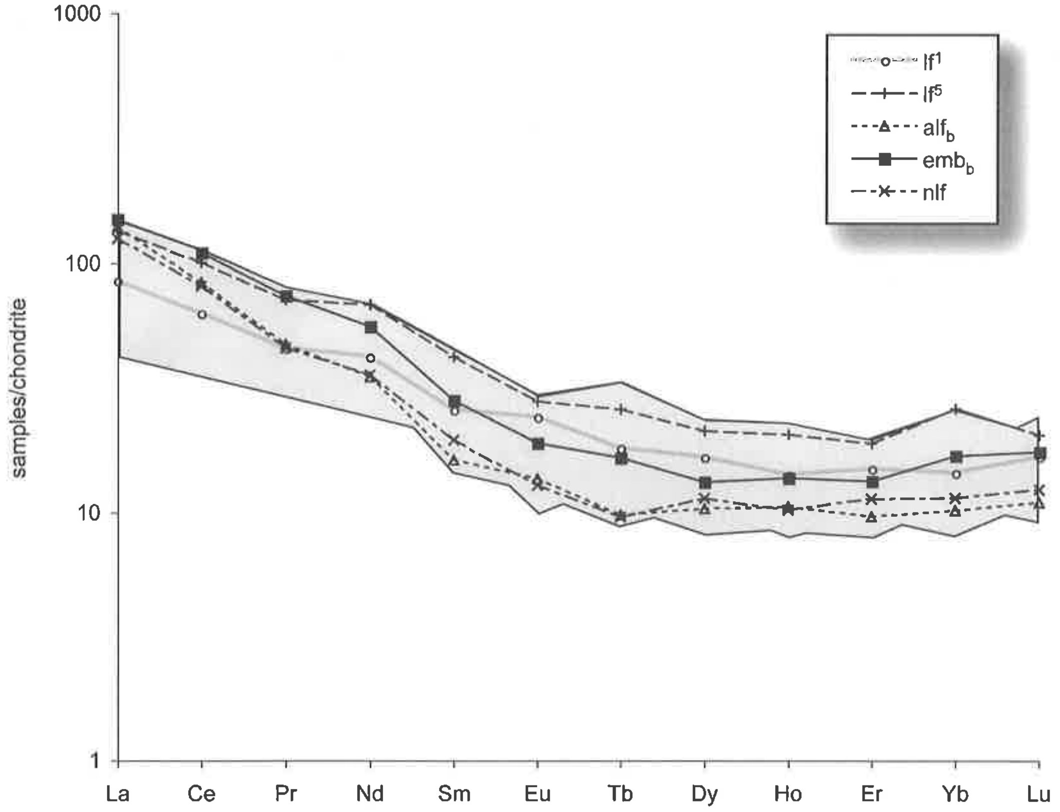

Figure 5.7: Chondrite-normalized REE patterns of selected samples from Nisyros, using normalizing values of Evensen et al. (1978). The grey area highlights the entire range of observed values, while individual samples of representative units are shown by lines and symbols.

5.4.2. Magma mixing

The magma mixing hypothesis (e.g. Gansecki, 1991; St. Seymour& Vlassopoulos, 1992) has been proposed based on the observation of xenocrysts and mafic enclaves in some dacitic and rhyolitic units, banded pumices, reversely zoned crystals, partly resorbed phenocrysts, bimodal plagioclase populations and some incompatible trace element characteristics (St. Seymour & Vlassopulos, 1992). Although mixing (or mingling) most likely occurred in enclave-bearing units (i.e. units **xlf**$_b$, **emb**, **lp**, **lp**, **nlf**, **up** and **pfi**) and can explain a number of petrographic observations, it does not in itself help resolve a number of geochemical features and other processes were likely involved. The absence of mixing lines in element vs. element diagrams, in particular, precludes that the process was dominant throughout the series.

5.4.3. Crustal and mantle contamination

Because of increasing $^{87}Sr/^{86}Sr$ from basaltic andesites to dacites, previous authors (e.g. Wyers & Barton, 1989; Francalanci et al., 1995) have generally concluded that a crustal component was assimilated during the magmatic evolution. On the other hand, Buettner et al. (2005) warn that the decoupling of the Sr, Pb, Nd and Hf isotopic systems require processes different from assimilation to account for their samples' isotopic variations. At any rate, it appears that the most primitive magmas were progressively contaminated by one (or more) lower and/or upper crustal components, and possibly by mantle-derived fluids (Buettner et al., 2005), as FC proceeded. In the absence of isotopic trends relating the rhyolites to other magma types, we infer that the rhyolites were either contaminated by different crustal components, or that they originated from a different source. In any case, crustal assimilation processes do not help explain the decoupling of the basaltic andesite to andesite series relative to the dacite to rhyolite sequence, as they do not account for the unpredictable trace element behaviors.

Mantle contamination, either through transference of fluids derived from subducted materials or involvement of altered oceanic crust, was also invoked to explain the difference between the $\delta^{34}S$ value estimated for the parent basaltic magma of Nisyros, +4‰, and the $\delta^{34}S$ value of pristine mantle, 0‰ (Marini et al., 2002; Marini & Fiebig, this volume).

5.4.4. Polybaric evolution

The polybaric evolution model of Wyers & Barton (1989) was designed to account for the difference in evolution trends between the basaltic andesite-andesite series and the dacite-rhyolite series. A polybaric evolution hypothesis implies varying partition coefficients (which are pressure-dependent), which helps to explain the varying behavior of incompatible trace elements, and allows introducing different crustal contaminants, which helps to explain the Sr isotopes observations. Wyers & Barton (1989) produced direct evidence of polybaric evolution in the form of geobarometric calculations, which showed, quite surprisingly, that the rhyolites evolved at depths *greater* than the basaltic andesites.

Vanderkluysen & Volentik (2002) tried to replicate Wyers & Barton's (1989) results using a different set of geobarometers (Hammarstrom & Zen, 1986; Hollister et al., 1987; Johnson & Rutherford, 1989; Thy, 1991a; 1991b; Nimis, 1996; 1999; Nimis & Ulmer, 1998), but noise in the data was such that they could neither confirm nor disprove the hypothesis. They concluded that (1) geobarometers were too sensitive to temperature of crystallization, which could not be determined with a sufficient degree of accuracy, (2) available geobarometers were not calibrated for compositions like those of Nisyros, and were particularly ill-suited for the silica-rich end of the spectrum, (3) in the absence of some mineral phases (such as sanidine and quartz in the rhyolites), the system can be considered to be thermodynamically underdetermined, thus leading to inaccurate results as a consequence of the added degrees of freedom and (4) these geobarometers require equilibrium conditions of crystallization, which has not been demonstrated (whereas petrographic evidence of disequilibrium are numerous, as shown in section 3). In addition, the reliability of some of these geobarometers has recently been questioned (e.g. Bachmann & Dungan, 2002).

In any case, basaltic andesitic or andesitic materials that show signs of having evolved at the same depth as the rhyolites are currently lacking. In addition, one might wonder why the basaltic andesites of the shallow chamber did not evolve all the way to the rhyolitic end of the spectrum, why the mafic parent magmas for the dacites and rhyolites did not reach the surface, and why the two magma series evolved independently from one another. Furthermore, it is unclear why the rhyolitic magmas remained at deeper depths without making their way to the shallower reservoir, but were then able (upon completion of their evolution) to ascend and discharge at the surface, a rather difficult task for a highly viscous rhyolitic magma.

5.4.5. Crystal retention, fractionation and crustal assimilation

The model developed by Francalanci et al. (1995), the most complete to date, involves a series of simultaneous or successive magmatic processes. Crystal retention, fractionation and re-entrainment in a dynamic magma chamber explain some petrographic observations (such as sieve textures and zoning in plagioclase) and geochemical data (such as high Sr concentrations in an anomalous group of basaltic andesites), while crustal assimilation accounts for a part of the $^{87}Sr/^{86}Sr$ variations. Francalanci et al. (1995) use the correlation of porphyritic index with some geochemical parameters as strong evidence that the evolution of Nisyros magmas is controlled by crystal removal, re-entrainment and accumulation processes. However, the model does not account for the unusual depletion of some incompatible trace elements in the silica-rich magmas from Nisyros.

5.4.6. The silica gap

The paucity of compositions between "60 and 66 wt% SiO_2" (Wyers & Barton, 1989) is a recurring observation on samples from Nisyros, and its origin is a matter of debate. The extent of the silica gap has varied over the years, from 61-65 wt% SiO_2 (Di Paola, 1974), to 60-66 (Wyers & Barton, 1989, St. Seymour & Vlassopoulos, 1992), to 57-59 (Francalanci et al., 1995); it was recently re-extended to 61-68 wt% SiO_2 by Buettner et al. (2005). In the dataset presented in Table 5.1, the gap extends from 61 to 63 wt% SiO_2 (recalculated on a water-free basis), which is significantly smaller than what has previously been reported in the literature. If all available analyses are taken into account, the "gap" virtually disappears. Not surprisingly, the smallest reported gaps come from studies (Francalanci et al., 1995; this paper) that take particular care in sampling all stratigraphic units. Careful sampling of the **pa** unit (*Kyra series* of Francalanci et al., 1995) is particularly critical, as the deposits straddle the andesite-dacite boundary.

As suggested by St. Seymour & Vlassopoulos (1992), it may very well be that the **pa** unit holds "the key to the eruptive history of Nisyros", since it ties the basaltic andesitic-andesitic series with the dacitic-rhyolitic series during a single eruptive period.

Even though the silica gap itself may be the result of undersampling, the scarcity of data between 61 and 64 wt% SiO_2 observed in over 500 geochemical analyses is undeniable, and should be considered as real.

5.4.7. The Nisyros melting pot

It is apparent from a review of the literature that no single process can account for the entire spectrum of geochemical and petrological observations of Nisyros samples. Although fractional crystallization is the dominant process involved (explaining major element compositions and most of the range of trace element compositions), a multitude of processes – presented in the literature as competing models - have been introduced. In order to explain all chemical, petrographic and isotopic features, however, it appears that nearly all processes need to be called upon. Crystal retention, fractionation and re-entrainment explain the anomalously Sr-rich group of samples, and correlations between porphyritic index and some geochemical parameters. Although basaltic andesitic and rhyolitic magmas are unlikely to have ever mixed to produce a set of hybrids, signs of magma mingling are numerous and mixing may have occurred at a small scale. Crustal assimilation was also invoked to account for some isotopic characteristics observed in Nisyros lavas and tephras. Rather than competing models, it appears more likely that multiple processes were important at various stages of the geological history of the island and acted together to produce the variety observed today in Nisyros' products.

The relative depletion of some incompatible elements (including some REE), however, remains largely unexplained. Although the polybaric evolution model of Wyers & Barton (1989) was an attempt to explain this feature, it does not fully resolve why the basaltic andesite-andesite series evolves separately from the dacite-rhyolite series, and why the mafic "parents" to the latter are missing from Nisyros' geochemical record. A model that has currently been overlooked to explain the origin of Nisyros' rhyolitic end-member is a formation by partial melting of a depleted lower crustal material (or re-melting of gabbroic or dioritic intrusives).

In conclusion, the current geochemical dataset of Nisyros volcanics does not yield an unambiguous picture of the magmatic processes at play on the island. The collection of Sr, Nd, Pb and Hf isotopic data by Buettner et al. (2005) offers a fresh viewpoint on the Nisyros problem, although the study does not cover pre-**lp**-caldera dacites and rhyolites (**emb**, **lf**^{7}, **alf**) thus leading to incomplete (and possibly erroneous) conclusions regarding the evolution of the volcano. Nevertheless, future geochemical work on the island should include (1) a Sr, Nd, Pb, O and Hf isotopic study of stratigraphy-anchored samples and (2) *in situ* major, trace and isotopic mineral analyses.

5.4.8. Variations with time

Claims that the pre- and post- **lp**-caldera magmas constitute two different series (Pe-Piper & Piper, 2002; Buettner et al., 2005) appear to be incorrect. When comparing rhyolites of the pre-**lp**-caldera (such as the Argos rhyolite, **alf**) and post-**lp**-caldera (e.g. the Nikia lava, **nlf**) sequences, no obvious geochemical difference arises. The same holds true for the dacites (**emb** and **pfi**, for instance). In absence of Hf, Pb and Nd isotopic data for pre-**lp**-caldera evolved rocks (Buettner et al., 2005), it is presumptuous to hypothesize that **lp**-caldera formation was a major break in the volcano's chemical evolution.

Geological events, however, do seem to have an effect on the island's magmatic system. Indeed, the comparative analysis shown in Fig. 5.8 demonstrates a correlation between the switches in the location of volcanic centres, changes in the dominant tectonic trends, and the synthematic subdivision applied to the stratigraphic record (Vanderkluysen et al., in review). These changes are also roughly correlated with variations in the geochemistry of products. These events, however, cannot be tied in with the major divide that separates andesites and basaltic andesites from dacites and rhyolites.

5.4.9. The potassium problem

The absence of K-bearing phases has been a long-standing problem for geochronologists working on Nisyros (for a review, see Hunziker, this volume). The rocks of Nisyros are by no means K-poor (typically between 1 and 3 wt% of K_2O, but as high as 4 wt% in some samples) but in the absence of any expressed K-bearing phase as phenocryst, scientists have wondered where the potassium is stocked.

Microprobe analyses (e.g. Wyers & Barton, 1989; St. Seymour & Vlassopoulos, 1992; Vanderkluysen & Volentik, 2002) have revealed that plagioclases are generally K-poor (typically in the 0.1-0.9 wt% K_2O range), as are amphiboles (0.3-0.7 wt% K_2O), although anomalously high values have been obtained for both (> 1 wt% in plagioclases from the **pfi** unit, and > 1 wt% in amphiboles from the **emb** and **vu**$_J$ units). Preliminary glass microprobe analyses from the post-**lp**-caldera dacite (**pfi**), the Argos (**alf**) and Nikia rhyolites (**nlf**), however, typically range from 3 to 4 wt% K_2O but reach 6 wt% in some analyses. Vanderkluysen & Volentik (2002) also report observing sanidine as an interstitial phase in some silica-rich samples, although it was too small to be effectively separated. This indicates that potassium is likely concentrated in the microcrystalline and glassy groundmass of Nisyros rocks (see also Hunziker, this volume).

5.5. Conclusions

Based on major and trace element patterns, isotopic characteristics and petrographic observations on the volcanic products of Nisyros, it is apparent that fractional crystallization is the dominant process of the island's magmatic evolution. It is clear, however, that to account for the range of observations, a number of processes must be invoked, such as (but not limited to) crystal retention, removal and re-entrainment, crustal assimilation and magma mingling (and possibly mixing).

In spite of the considerable number of petrographic observations and geochemical data gathered so far, the exact origin of Nisyros magmas, and in particular the origin of the more evolved rocks, currently remains uncertain. Another hypothesis that remains to be explored is the possibility that the felsic products result from the melting of crustal material, or re-melting of intrusives. In any case, the Nisyros dataset currently lacks in stratigraphically-anchored whole rock and mineral separate isotopic analyses, in experimental petrology data and in major and trace element and isotopic *in situ* microanalyses of minerals. Hopefully, these fields will provide the answers to our interrogations regarding the origin of Nisyros' magmas.

Acknowledgements - We would like to acknowledge the financial support of the Immanuel Friendlaender Foundation for Volcanology and of the Swiss Academy of Science (SANW/ASSN/SAS). We express our gratitude to Jean-Claude Lavanchy, Catherine Schlegel-Rey and Melissa Perret at the CAM in Lausanne for their help in the XRF lab, and to Philippe Monjoie at the microprobe. We are also in debt to Laurent Nicod for the preparation of our hundreds of thin sections. Luigi Marini is also thanked for his critical review of the manuscript.

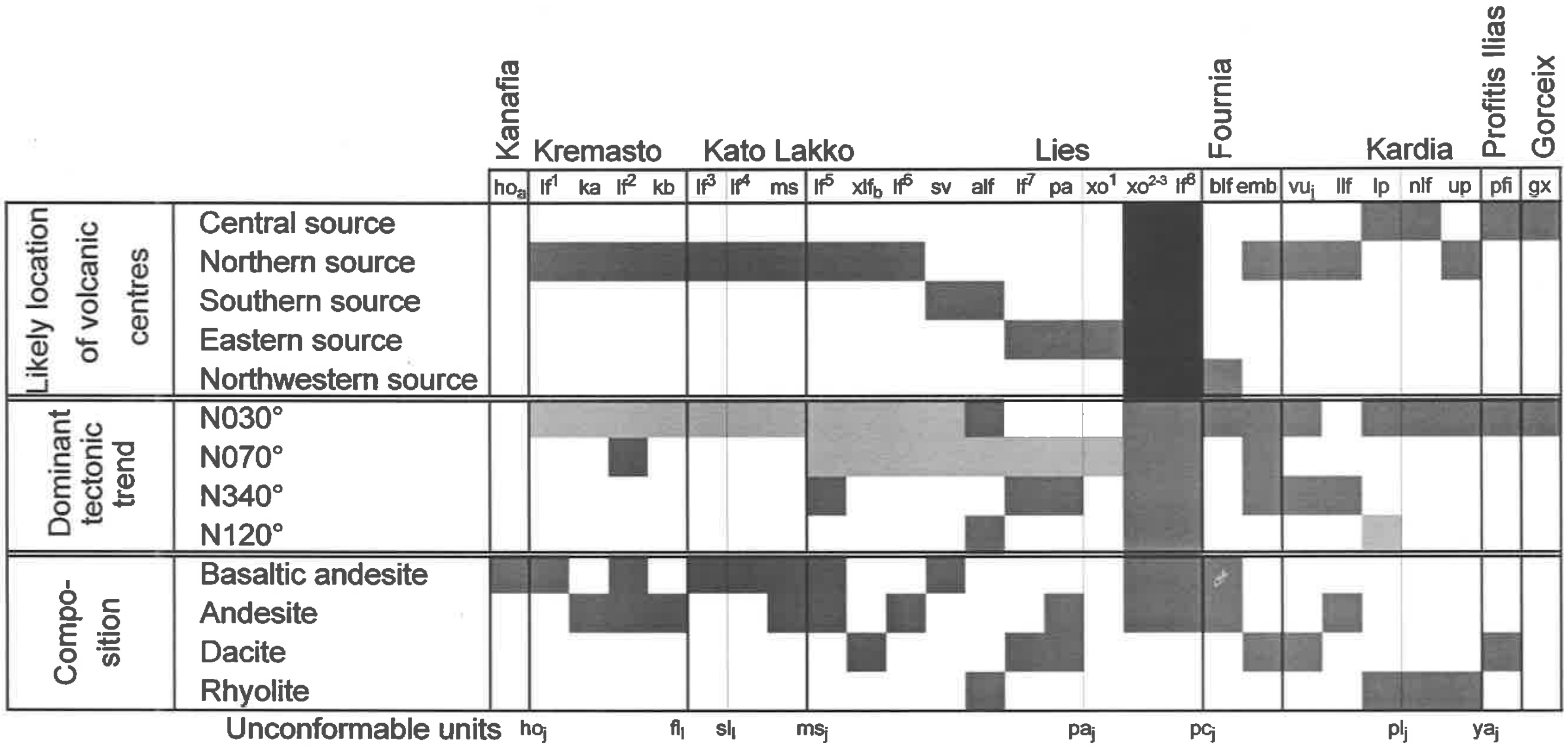

Figure 5.8. Vent location, composition and tectonic trends in effect at the time of each volcanic event on Nisyros. Light grey: evidence supported by single observations of dyke orientation or tectonic lineament measurement. Grey: evidence supported by multiple dyke orientation measurements and correlated with field observation of tectonic lineaments. Dark grey: strombolian event with vents scattered throughout the island. Black lines: synthematic boundaries; thin lines: sub-synthematic boundaries. After Vanderkluysen et al. (in review).

Sample		AV12	AV4	LV21	LV31	AV3	AV5	AV70	LV30	AV6	AV20	AV26	AV48	AV1	AV7B	AV10	AV18	AV47	LV1	LV2	LV3	LV15	LV16
unit		ho_a	lf^1	ka		lf^2			kb	lf^3	lf^3			lf^4					ms	ms			
SiO_2	wt-%	54.49	53.33	55.94	57.82	60.02	59.30	55.72	51.71	56.74	54.00	53.79	53.71	54.35	54.88	54.80	55.26	55.68	57.00	57.68	56.78	54.06	52.73
TiO_2	wt-%	0.94	1.05	1.17	1.18	0.99	1.05	1.17	0.76	1.23	0.83	0.84	0.93	0.74	0.69	0.70	0.78	0.73	1.04	1.01	1.02	0.85	0.77
Al_2O_3	wt-%	18.17	18.58	17.64	17.23	16.86	16.77	17.67	16.91	17.15	18.33	17.80	17.90	17.22	15.43	15.38	17.94	17.79	17.30	16.83	17.03	18.69	17.98
Fe_2O_3(t)	wt-%	6.88	7.36	7.55	7.15	6.41	6.74	7.80	3.24	7.90	6.94	6.99	7.69	5.85	6.86	6.77	6.06	5.95	7.35	7.23	7.26	6.97	7.05
MnO	wt-%	0.13	0.12	0.08	0.13	0.14	0.12	0.15	0.09	0.12	0.12	0.12	0.13	0.09	0.11	0.11	0.10	0.10	0.13	0.12	0.13	0.12	0.13
MgO	wt-%	3.90	4.15	3.27	2.44	2.13	2.55	3.33	1.56	2.74	5.03	6.08	4.95	5.02	7.67	7.52	4.78	5.60	3.17	2.71	3.60	4.38	5.89
CaO	wt-%	9.65	9.08	5.69	5.17	5.27	5.45	7.15	10.57	6.33	9.94	9.42	9.45	8.96	9.59	9.43	8.90	9.59	6.76	6.47	6.75	9.48	10.44
Na_2O	wt-%	3.42	3.47	3.34	4.16	4.53	4.33	4.09	2.21	3.92	3.09	3.22	3.51	3.04	2.78	2.72	3.39	3.29	4.01	3.81	4.06	3.29	3.01
K_2O	wt-%	1.29	1.45	2.02	1.87	1.99	2.23	1.50	1.86	1.74	1.19	1.25	1.23	1.48	0.95	0.94	1.36	1.14	1.98	2.17	1.78	1.19	0.90
P_2O_5	wt-%	0.19	0.23	0.19	0.32	0.25	0.30	0.24	0.20	0.25	0.21	0.19	0.19	0.19	0.14	0.14	0.19	0.17	0.31	0.33	0.29	0.20	0.18
LOI	wt-%	0.90	1.34	2.65	2.72	0.97	0.74	0.72	10.93	1.98	0.23	0.43	-0.25	2.25	0.95	1.48	0.49	0.09	0.91	1.01	1.40	0.51	0.36
Total	wt-%	99.96	100.15	99.55	100.18	99.55	99.58	99.54	100.03	100.11	99.90	100.13	99.44	99.19	100.06	99.97	99.24	100.14	99.96	99.36	100.09	99.75	99.44
Nb	ppm	11	14	13	16	15	17	13	13	13	12	10	11	7	6	6	8	6	14	14	14	11	9
Zr	ppm	150	148	174	200	200	234	165	156	174	141	142	150	142	113	113	157	144	194	191	191	145	121
Y	ppm	22	23	24	26	27	31	26	21	30	20	20	21	16	15	15	16	14	24	24	24	20	19
Sr	ppm	527	559	531	472	394	403	469	404	427	609	506	525	1008	577	574	1044	1088	568	553	570	572	549
Rb	ppm	27	31	46	43	52	59	33	61	37	25	28	24	17	13	14	20	13	40	40	40	25	18
Th	ppm	5	5	5	5	7	7	5	4	5	5	5	4	4	4	3	4	3	6	6	6	5	4
Pb	ppm	6	6	9	9	7	11	5	6	9	8	4	4	5	6	5	6	4	4	5	5	6	3
Ga	ppm	19	19	20	20	19	20	20	17	19	18	18	19	19	17	17	20	20	19	19	19	19	17
Zn	ppm	72	70	85	81	63	79	77	53	94	63	63	67	55	56	57	54	51	69	72	74	66	63
Ni	ppm	16	4	4	BDL	BDL	3	5	6	18	38	82	20	80	128	126	50	78	9	10	8	28	62
Cr	ppm	15	12	4	3	4	3	7	16	10	61	157	14	95	250	235	40	72	7	6	6	28	114
V	ppm	184	172	228	153	140	149	233	117	238	182	175	187	155	147	141	135	139	123	103	124	185	170
Ce	ppm	31	40	37	50	59	67	25	46	43	46	38	29	32	22	22	34	31	52	53	53	33	27
Ba	ppm	266	385	303	482	529	553	398	401	401	367	354	286	282	258	249	319	283	499	495	491	332	300
La	ppm	14	20	21	25	28	31	19	24	20	23	19	16	14	11	10	15	14	25	27	25	19	18

Table 5.1. Major and trace element data of samples from Nisyros. BDL = below detection limits. Unit names refer to the stratigraphy established by Volentik et al. (this volume) and Vanderkluysen et al. (in review).

Sample		LV17A	LV17B	LV20B	LV22	AV2	AV8	AV11	AV28	AV31	AV32	AV64	AV67A	AV67B	AV17	AV19	AV22	AV25	AV25	AV35	AV44	AV46
unit						lf^5	lf^5								lf^6	lf^6						
SiO$_2$	wt-%	52.64	53.98	53.46	57.14	54.06	59.71	56.31	59.50	54.25	53.97	57.58	58.51	58.10	59.22	59.12	59.13	58.81	58.58	58.54	58.55	58.70
TiO$_2$	wt-%	0.99	0.92	0.95	1.05	0.94	1.21	1.06	1.10	0.92	0.92	1.07	1.12	1.11	1.17	1.15	1.15	1.11	1.11	1.10	1.15	1.14
Al$_2$O$_3$	wt-%	20.24	18.20	18.16	17.53	18.41	16.82	17.62	16.69	18.58	18.45	17.21	17.50	17.13	17.01	17.11	17.12	17.32	17.40	17.40	16.95	17.17
Fe$_2$O$_3$(t)	wt-%	6.89	7.16	7.34	7.42	6.02	7.68	7.76	6.89	7.28	7.16	7.53	7.33	7.25	7.55	7.44	7.44	7.27	7.27	7.23	7.46	7.44
MnO	wt-%	0.07	0.09	0.13	0.13	0.11	0.13	0.12	0.14	0.13	0.12	0.13	0.13	0.13	0.14	0.13	0.13	0.13	0.13	0.13	0.14	0.13
MgO	wt-%	3.58	4.02	4.74	3.41	3.18	2.27	3.47	2.72	4.42	4.50	3.41	2.88	2.78	2.47	2.53	2.51	2.73	2.81	2.73	2.55	2.98
CaO	wt-%	8.88	8.57	8.85	6.98	8.40	5.43	7.49	5.33	9.00	9.04	6.95	6.69	6.56	5.64	5.77	5.76	6.60	6.59	6.77	5.88	6.25
Na$_2$O	wt-%	3.70	3.30	3.50	4.31	3.54	4.38	3.81	4.17	3.37	3.34	4.02	4.12	4.16	4.19	4.18	4.52	4.08	4.14	4.01	4.37	4.38
K$_2$O	wt-%	0.83	1.27	1.05	1.75	1.49	2.15	1.60	2.24	1.18	1.18	1.64	1.79	1.80	2.09	2.07	2.11	1.82	1.82	1.79	2.04	1.76
P$_2$O$_5$	wt-%	0.25	0.20	0.20	0.29	0.24	0.28	0.25	0.25	0.21	0.21	0.24	0.25	0.24	0.25	0.26	0.27	0.25	0.25	0.25	0.27	0.26
LOI	wt-%	1.86	1.41	0.82	0.20	2.96	-0.11	0.35	0.89	0.73	1.00	-0.22	-0.12	-0.14	0.24	0.27	-0.26	-0.13	-0.20	0.07	-0.14	-0.22
Total	wt-%	99.93	99.11	99.19	100.22	99.36	99.95	99.84	99.92	100.07	99.89	99.57	100.21	99.13	99.96	100.04	99.86	100.00	99.90	100.01	99.23	99.99
Nb	ppm	12	11	13	14	12	17	13	16	11	11	14	15	15	17	16	17	15	15	15	16	14
Zr	ppm	164	152	154	197	167	216	177	205	151	149	189	197	198	212	208	210	195	196	193	208	198
Y	ppm	24	21	22	24	25	30	27	30	22	22	26	28	28	29	29	29	29	29	27	29	28
Sr	ppm	527	477	435	582	571	387	461	340	475	473	401	382	382	393	397	401	379	381	388	405	405
Rb	ppm	9	24	29	39	32	56	39	61	28	27	43	49	47	56	55	55	48	49	47	54	43
Th	ppm	4	4	5	5	6	7	5	6	4	6	6	6	6	8	7	7	7	6	6	6	6
Pb	ppm	6	5	3	4	7	8	8	10	5	11	6	9	9	14	8	9	9	9	11	8	6
Ga	ppm	20	19	19	20	19	20	20	19	19	19	20	20	20	20	20	20	20	20	19	20	19
Zn	ppm	71	71	68	77	74	77	76	75	66	69	69	79	77	79	76	79	77	77	77	80	70
Ni	ppm	34	35	18	9	22	BDL	5	11	34	34	8	7	8	3	BDL	2	5	5	7	3	9
Cr	ppm	40	37	31	8	14	3	8	5	39	38	8	7	8	13	5	5	7	6	8	6	4
V	ppm	239	220	153	204	200	202	207	199	181	186	204	204	201	194	195	193	202	200	203	202	217
Ce	ppm	39	32	38	49	50	61	49	51	37	39	45	47	47	63	61	56	52	50	51	52	48
Ba	ppm	362	319	401	512	407	531	435	536	323	317	427	448	451	517	519	536	470	464	449	508	486
La	ppm	20	17	17	25	26	30	24	28	18	18	23	25	25	31	29	28	27	25	24	29	25

Table 5.1. (continued)

Sample		AV24B	AV58	AV23A	AV16A	AV16B	AV66	AV92	AV93	LV34	LV35	LV36	LV37	LV38	LV45	AV90	LV8	AV50A	LV4	LV7	LV13	LV23	LV5
unit		sv	alf	alf^a	alf^b		lf^7			pa			pa			xo	xo^1	xo^2				xo^2	xo^3
SiO_2	wt-%	50.79	69.37	70.49	69.54	71.00	63.54	63.76	65.23	55.22	58.91	54.43	60.01	59.41	57.50	55.50	58.24	54.23	54.66	58.17	54.26	56.73	50.34
TiO_2	wt-%	0.70	0.33	0.28	0.33	0.36	0.50	0.50	0.48	0.48	0.77	0.91	0.28	0.68	1.04	0.72	1.12	0.77	0.93	1.10	0.77	1.03	0.96
Al_2O_3	wt-%	15.95	14.51	13.99	14.69	14.93	16.72	16.72	16.89	14.66	17.32	19.08	12.13	15.98	17.85	17.56	16.95	17.34	18.48	16.69	17.35	17.24	19.36
Fe_2O_3(t)	wt-%	6.99	2.49	2.14	2.51	2.66	4.82	4.84	4.74	3.74	5.68	7.08	2.18	5.05	7.09	5.88	7.35	6.55	7.22	7.26	6.52	7.31	7.41
MnO	wt-%	0.12	0.07	0.06	0.07	0.05	0.13	0.13	0.13	0.12	0.13	0.12	0.06	0.13	0.13	0.09	0.13	0.12	0.12	0.13	0.12	0.13	0.13
MgO	wt-%	6.27	0.87	0.74	0.83	0.59	1.34	1.37	1.19	1.26	2.74	4.18	1.35	1.46	3.09	5.37	3.04	6.18	4.56	2.99	6.17	3.32	3.53
CaO	wt-%	9.89	2.39	2.06	2.38	2.47	4.04	3.99	3.80	3.39	5.81	9.01	7.27	3.35	7.24	9.33	6.19	9.10	9.03	6.10	9.06	6.84	9.81
Na_2O	wt-%	2.71	3.95	3.48	3.99	4.05	4.68	4.71	4.89	4.54	4.81	3.46	3.81	5.07	3.81	3.20	4.24	3.19	3.26	4.15	3.16	4.05	3.47
K_2O	wt-%	0.49	3.52	3.56	3.38	3.45	2.53	2.45	2.52	2.22	2.00	1.18	3.37	2.53	1.61	1.19	1.74	1.12	1.28	1.63	1.12	1.72	0.67
P_2O_5	wt-%	0.48	0.10	0.09	0.10	0.10	0.19	0.19	0.19	0.21	0.24	0.18	0.10	0.23	0.23	0.18	0.26	0.14	0.21	0.25	0.15	0.29	0.20
LOI	wt-%	4.81	2.10	3.01	1.88	0.46	1.34	1.25	-0.04	14.10	1.82	0.22	8.55	5.37	0.31	0.40	0.82	0.28	0.41	0.83	0.38	0.38	3.38
Total	wt-%	99.20	99.70	99.89	99.72	100.12	99.82	99.91	100.02	99.95	100.22	99.85	99.12	99.25	99.89	99.40	100.08	99.02	100.16	99.30	99.06	99.05	99.25
Nb	ppm	8	17	17	18	18	16	16	16	16	16	9	15	19	14	6	14	9	11	14	9	14	12
Zr	ppm	123	176	160	176	179	234	232	241	215	194	134	220	229	180	143	196	122	152	196	122	198	159
Y	ppm	23	14	13	14	15	22	22	22	24	24	19	15	27	25	15	28	19	22	28	19	24	23
Sr	ppm	312	272	224	271	269	388	379	385	383	473	568	242	361	391	1061	395	367	476	398	366	578	518
Rb	ppm	8	100	111	95	97	76	76	79	65	50	23	78	66	44	16	44	27	31	42	27	39	6
Th	ppm	5	11	13	12	12	7	8	7	6	6	4	8	7	6	4	6	4	4	6	4	6	5
Pb	ppm	6	10	12	11	19	11	11	13	10	8	6	10	11	8	6	8	5	8	6	4	5	4
Ga	ppm	17	16	15	15	16	19	19	19	17	18	19	13	19	19	19	19	17	19	19	17	20	20
Zn	ppm	69	35	31	34	38	70	71	67	75	74	69	36	83	78	55	75	59	70	75	60	74	74
Ni	ppm	143	4	5	3	7	BDL	BDL	BDL	BDL	12	26	BDL	BDL	10	74	11	87	31	9	89	9	33
Cr	ppm	319	7	9	8	12	3	2	BDL	3	16	24	4	3	12	70	5	172	40	6	169	8	34
V	ppm	160	34	27	33	30	41	45	32	42	96	169	12	27	195	135	208	168	173	197	174	207	42
Ce	ppm	31	62	68	72	72	60	51	52	61	53	28	41	53	39	24	52	23	35	52	25	50	42
Ba	ppm	246	838	859	831	856	645	655	696	581	573	281	639	606	422	296	463	274	312	482	277	508	355
La	ppm	15	36	36	36	38	31	31	33	29	32	13	27	30	23	14	26	12	17	26	14	26	20

Table 5.1. (continued)

Sample		LV40	AV50B	AV14A	AV14B	AV15	AV49	AV55A	AV55B	AV56	AV57	AV59	LV12	AV91	AV13	AV51	AV53	AV60	AV61	AV62	AV72	AV73	AV74
unit			lith-xo	lf[8]					lf[8]					Dike-lf[8]	blf			blf					
SiO_2	wt-%	58.56	69.79	55.76	55.58	54.06	58.30	55.74	56.03	54.36	54.84	54.37	59.00	57.39	53.03	58.55	55.92	55.83	55.63	56.15	55.42	55.56	55.38
TiO_2	wt-%	1.06	0.38	0.79	0.79	0.94	1.14	0.72	0.78	0.92	0.92	0.93	1.21	1.18	0.92	1.14	0.79	0.78	0.95	0.77	0.96	0.78	0.78
Al_2O_3	wt-%	16.90	15.01	18.74	18.78	18.96	16.94	17.93	17.79	18.50	18.55	18.77	16.58	17.00	17.86	17.31	18.88	18.59	18.60	18.59	18.67	18.60	18.69
Fe_2O_3(t)	wt-%	7.02	2.79	6.59	6.58	7.35	7.38	5.85	5.69	7.22	7.25	7.29	7.62	7.68	5.97	7.47	6.61	6.59	6.95	6.56	7.02	6.52	6.55
MnO	wt-%	0.13	0.07	0.12	0.12	0.13	0.13	0.09	0.11	0.13	0.12	0.13	0.14	0.13	0.12	0.12	0.12	0.12	0.12	0.12	0.12	0.12	0.12
MgO	wt-%	2.99	1.12	4.09	4.07	4.46	2.60	5.24	4.18	4.53	4.56	4.66	2.38	3.09	3.89	2.95	4.00	4.04	3.78	4.15	3.63	4.15	4.05
CaO	wt-%	6.08	2.78	8.77	8.71	9.23	5.79	9.38	7.88	9.10	9.08	9.12	5.44	6.52	9.34	6.25	8.67	8.71	8.36	8.71	8.44	8.75	8.68
Na_2O	wt-%	4.32	4.33	3.61	3.58	3.44	4.11	3.06	3.22	3.43	3.47	3.53	4.20	4.15	3.40	4.40	3.71	3.63	3.63	3.73	3.77	3.56	3.61
K_2O	wt-%	1.66	3.35	1.22	1.23	1.07	2.11	1.15	1.24	1.14	1.14	1.17	2.24	1.87	1.26	1.75	1.20	1.18	1.42	1.19	1.34	1.22	1.13
P_2O_5	wt-%	0.25	0.11	0.22	0.22	0.21	0.26	0.18	0.19	0.21	0.21	0.21	0.28	0.30	0.19	0.26	0.22	0.22	0.23	0.22	0.24	0.22	0.22
LOI	wt-%	0.91	0.35	0.09	0.40	0.05	0.35	0.53	1.91	0.02	-0.06	-0.19	0.89	0.28	3.83	-0.22	-0.13	-0.20	0.08	-0.06	0.01	0.29	-0.02
Total	wt-%	99.89	100.07	100.00	100.05	99.89	99.11	99.88	99.01	99.55	100.09	99.99	99.98	99.59	99.82	99.98	100.00	99.49	99.74	100.14	99.62	99.76	99.20
Nb	ppm	14	17	10	10	11	17	6	12	11	11	11	17	17	11	14	10	10	13	10	13	10	10
Zr	ppm	192	180	160	159	155	211	145	160	152	153	154	216	213	151	200	162	160	172	159	174	160	162
Y	ppm	26	14	21	21	25	28	14	32	22	23	23	29	28	21	28	21	21	23	21	22	21	22
Sr	ppm	391	284	518	516	493	402	1165	454	483	483	483	380	505	529	403	520	519	516	518	522	519	524
Rb	ppm	46	95	27	28	20	53	15	42	28	27	28	57	41	28	43	27	27	33	27	32	27	24
Th	ppm	6	12	4	5	5	7	4	5	4	5	5	7	7	4	6	4	4	5	5	4	4	4
Pb	ppm	4	10	6	6	8	10	5	7	8	54	6	10	9	6	8	6	6	7	7	6	6	6
Ga	ppm	18	16	19	19	19	20	20	18	19	19	19	20	20	19	20	19	19	19	19	20	19	19
Zn	ppm	72	37	64	64	72	80	56	71	67	108	69	84	83	70	73	62	62	70	66	66	65	62
Ni	ppm	10	6	29	29	31	5	66	40	31	32	35	BDL	9	13	8	30	29	21	29	18	31	32
Cr	ppm	8	12	50	49	39	5	58	65	38	38	41	3	8	17	5	48	49	25	48	27	50	45
V	ppm	190	44	161	161	179	199	131	146	164	169	174	199	228	186	210	160	155	170	159	182	160	152
Ce	ppm	42	64	40	42	40	54	35	56	36	36	35	60	55	30	50	40	33	36	35	40	38	36
Ba	ppm	501	833	384	386	348	519	281	393	331	332	329	506	566	274	488	382	404	400	402	398	375	390
La	ppm	24	36	22	20	23	27	16	28	18	18	18	27	34	14	26	19	21	20	20	19	20	21

Table 5.1. (continued)

Sample		AV75	AV76	AV79	AV80	AV65	AV82	AV81	AV21	AV36	AV37	AV39	AV45	AV52A	AV52B	AV63	AV78	AV86	AV88	AV89	LV11	LV18	LV25	LV24
unit					blf	vu_i	enc-vu_i	lith-vu_i	emb	emb^b				emb^b				llf			lp		lp	lp^a
SiO_2	wt-%	58.61	56.22	58.74	55.78	65.10	60.62	58.29	65.96	66.27	65.91	66.45	64.86	66.35	66.52	66.02	65.03	58.91	59.47	59.46	69.73	69.03	68.65	68.86
TiO_2	wt-%	1.15	0.79	1.13	0.72	0.62	1.04	1.15	0.61	0.62	0.63	0.63	0.62	0.56	0.56	0.63	0.62	1.12	1.13	1.13	0.31	0.33	0.33	0.32
Al_2O_3	wt-%	17.44	18.85	16.89	17.86	15.47	17.08	17.24	15.83	15.73	16.27	15.95	15.90	15.73	15.74	15.86	16.46	17.11	17.09	16.96	14.29	13.98	14.25	13.99
Fe_2O_3(t)	wt-%	7.49	6.56	7.38	5.58	4.21	6.32	7.47	4.18	4.18	4.28	4.25	4.19	3.92	3.90	4.25	4.22	7.39	7.43	7.38	2.41	2.53	2.53	2.50
MnO	wt-%	0.13	0.12	0.13	0.08	0.09	0.12	0.14	0.09	0.09	0.09	0.09	0.09	0.09	0.09	0.09	0.09	0.12	0.13	0.13	0.07	0.07	0.08	0.07
MgO	wt-%	2.96	4.09	2.57	4.82	1.24	1.92	2.65	1.21	1.19	1.25	1.19	1.21	1.13	1.13	1.19	1.24	2.83	2.59	2.59	0.53	0.85	0.62	0.56
CaO	wt-%	6.16	8.69	5.78	9.30	3.37	4.76	5.70	3.43	3.44	3.40	3.36	3.42	3.20	3.19	3.39	3.48	6.25	5.77	5.76	1.85	1.88	2.02	1.86
Na_2O	wt-%																							
		0.00	-0.18	-0.11	0.31	1.42	0.22	1.15	0.99	-0.02	0.28	0.45	1.36	1.31	1.25	0.10	1.40	0.02	-0.17	-0.12				
		100.17	100.19	99.03	99.10	99.09	99.56	100.02	99.89	99.22	99.83	100.05	99.21	99.96	100.03	99.22	99.97	100.05	99.97	99.84	99.83			
										3	3	BDL	3	2	2	4	4	9	BDL					

Sample		LV32	AV27	AV27B	AV29	AV34	AV42A	AV42B	AV54	AV71A	AV71B	AV95	LV33	LV42	LV19	LV26	LV47	AVN99-46	AV83A	AV83B	AV85	LV44
unit			nlf						nlf		enc-nlf	enc-nlf	up		up^a		ya$_i$	pfi	enc-pfi	enc-pfi	enc-pfi	lith
SiO_2	wt-%	68.76	70.39	69.22	68.85	71.53	69.40	67.91	69.48	70.56	55.34	55.53	68.76	67.24	68.23	67.95	68.42	67.08	55.04	54.72	53.99	67.82
TiO_2	wt-%	0.32	0.34	0.36	0.34	0.33	0.36	0.37	0.35	0.32	0.86	0.86	0.34	0.37	0.36	0.34	0.33	0.40	0.74	0.75	0.72	0.34
Al_2O_3	wt-%	14.32	15.04	15.28	14.71	14.67	15.19	15.20	15.01	14.57	18.34	18.21	14.99	15.05	15.01	14.75	13.93	15.52	19.15	19.33	19.10	14.90
Fe_2O_3(t)	wt-%	2.49	2.72	2.85	2.78	2.47	2.80	3.04	2.74	2.46	7.38	8.25	2.73	2.95	2.80	2.73	2.18	3.18	5.95	6.22	6.07	2.74
MnO	wt-%	0.08	0.07	0.08	0.07	0.04	0.04	0.08	0.07	0.07	0.13	0.15	0.07	0.07	0.07	0.07	0.07	0.07	0.10	0.11	0.11	0.07
MgO	wt-%	0.59	0.81	0.87	0.83	0.38	0.45	1.02	0.81	0.56	4.32	2.85	0.89	1.28	1.08	1.01	0.56	1.52	4.57	4.82	4.91	0.91
CaO	wt-%	1.96	2.47	2.57	2.50	1.97	2.45	2.84	2.58	2.00	8.69	6.68	2.67	3.17	2.90	3.04	1.85	3.83	8.99	9.30	9.27	2.77
Na_2O	wt-%	4.08	4.51	4.52	4.39	4.39	4.20	4.36	4.37	4.47	3.44	4.13	4.05	4.00	4.33	4.39	3.61	4.11	3.29	3.44	3.44	4.13
K_2O	wt-%	3.48	3.14	3.18	3.15	3.55	3.19	3.10	3.12	3.34	1.09	1.47	3.30	2.86	3.16	3.17	3.71	2.77	1.19	1.05	1.13	3.03
P_2O_5	wt-%	0.09	0.09	0.11	0.10	0.09	0.10	0.11	0.09	0.08	0.17	0.28	0.09	0.10	0.10	0.09	0.08	0.10	0.20	0.19	0.18	0.09
LOI	wt-%	3.68	0.49	1.07	1.64	0.60	0.94	1.99	1.22	0.75	0.32	0.92	1.98	2.29	2.20	2.73	4.78	0.47	0.83	0.05	0.80	2.29
Total	wt-%	99.84	100.06	100.10	99.35	100.01	99.11	100.02	99.83	99.18	100.07	99.33	99.87	99.37	100.24	100.26	99.51	99.05	100.06	99.97	99.72	99.08
Nb	ppm	18	16	17	17	19	17	17	17	18	8	13	16	15	15	15	21	14	7	7	7	16
Zr	ppm	264	226	231	234	263	226	226	231	255	129	167	206	216	215	213	200	186	145	142	143	215
Y	ppm	17	16	16	16	17	16	16	16	17	23	21	17	17	16	15	18	14	16	16	16	17
Sr	ppm	214	270	277	272	218	280	295	279	221	430	752	270	315	291	280	197	420	966	982	1004	287
Rb	ppm	96	92	92	91	99	92	89	90	100	22	27	99	84	92	92	117	81	14	13	20	90
Th	ppm	11	11	10	10	11	9	10	11	13	4	5	11	10	10	10	13	10	2	2	3	11
Pb	ppm	14	13	12	13	13	10	13	13	32	4	7	15	13	12	13	12	11	5	5	6	13
Ga	ppm	15	16	17	17	16	17	16	16	16	19	20	16	16	16	16	16	17	20	20	20	16
Zn	ppm	45	37	43	42	43	37	46	42	99	69	71	36	41	41	40	39	40	50	100	66	40
Ni	ppm	BDL	BDL	3	2	BDL	2	2	BDL	BDL	14	BDL	2	6	5	4	4	5	25	25	23	3
Cr	ppm	4	3	4	3	4	4	3	4	5	20	BDL	5	7	5	3	3	6	16	17	12	5
V	ppm	16	21	25	26	18	39	42	26	18	192	138	20	31	29	26	23	48	133	104	108	25
Ce	ppm	65	67	61	63	73	58	60	68	67	27	44	67	53	62	63	53	55	26	23	26	53
Ba	ppm	810	807	803	777	806	755	737	786	809	318	473	817	744	779	779	703	692	304	287	303	790
La	ppm	35	34	33	34	36	32	33	34	36	18	27	38	40	35	35	33	27	14	13	15	44

Table 5.1. (continued)

	AV12	AV4	LV31	AV5	AV6	AV7B	LV2	AV8	AV25	AV24B	AV16B	LV8	LV7	LV5	AV14B	AV15	AV13	AV53	AV39	LV24	AV54	AV71A	AV71B	LV26	AVN99-046
Unit	ho$_a$	lf^1	ka	lf^2	lf^3	lf^4	ms	lf^5	lf^6	sv	alf^b	xo^1	xo^2	xo^3	lf^8	lf^8	blf	blf	emb^b	lp^a	nlf	nlf	enc-nlf	up^a	pfi
La	19	21	27	36	22	11	25	33	29	20	34	34	28	19	21	30	16	21	36	35	31	35	17	29	29
Ce	40	40	53	71	43	23	48	64	57	41	53	65	50	41	39	55	33	43	70	54	52	57	31	50	53
Pr	5.3	4.4	6.0	7.6	4.9	3.0	5.1	6.8	6.1	4.8	4.5	7.2	5.6	5.2	4.2	6.6	4.3	4.7	7.1	4.9	4.4	4.9	3.9	4.3	5.0
Nd	21	20	29	32	24	13	23	32	28	20	17	32	24	20	19	28	17	20	26	19	17	19	18	16	18
Sm	4.9	4.0	5.4	6.7	5.0	3.2	4.9	6.5	5.3	4.0	2.5	7.0	5.0	3.8	3.9	5.6	3.5	3.7	4.3	3.4	3.0	2.9	3.9	2.6	3.1
Eu	1.2	1.4	1.4	1.6	1.3	0.9	1.3	1.6	1.6	1.1	0.8	1.7	1.4	1.2	1.2	1.6	1.1	1.3	1.1	0.7	0.7	0.8	1.2	0.7	0.7
Tb	0.88	0.68	0.73	1.2	0.74	0.52	0.64	0.97	0.94	0.82	0.37	1.3	0.90	0.62	0.65	1.1	0.68	0.60	0.62	0.47	0.36	0.53	0.60	0.40	0.43
Dy	4.9	4.2	4.4	5.8	4.8	2.9	3.9	5.4	5.1	4.8	2.6	6.1	5.8	4.0	3.8	5.3	3.9	3.7	3.4	2.7	2.9	2.5	3.7	2.8	2.3
Ho	1.0	0.80	0.87	1.2	0.99	0.66	0.75	1.2	1.2	1.0	0.60	1.3	1.2	0.82	0.86	1.2	0.86	0.70	0.78	0.75	0.58	0.72	0.73	0.49	0.52
Er	2.9	2.5	2.0	3.3	2.4	1.7	1.9	3.1	3.2	3.0	1.6	3.2	3.1	2.3	2.4	3.0	2.1	1.8	2.2	2.0	1.9	1.9	1.9	1.9	1.5
Yb	3.6	2.4	2.9	3.3	2.9	1.4	2.6	4.3	4.3	3.6	1.7	3.3	2.8	2.0	2.3	3.0	2.5	2.8	2.8	2.1	1.9	2.1	1.8	1.9	1.9
Lu	0.45	0.42	0.38	0.51	0.44	0.31	0.32	0.52	0.50	0.54	0.28	0.56	0.61	0.37	0.47	0.43	0.39	0.33	0.44	0.51	0.31	0.47	0.34	0.29	0.25
Co	39	27	38	27	28	42	29	31	42	35	16	46	32	29	31	38	31	35	26	25	23	29	52	17	65
Hf	4.4	3.2	3.4	5.2	3.2	2.7	3.2	5.5	4.5	3.8	3.9	5.3	4.3	3.0	3.3	4.0	3.4	3.3	6.5	5.3	4.5	4.7	2.5	4.4	4.5
Sc	25	22	13	16	17	26	16	12	13	32	4	22	22	23	21	20	24	12	7	3	3	2	20	3	6
Th	3.6	4.0	5.6	7.7	4.3	1.9	4.7	7.7	6.6	4.0	12.7	7.0	5.8	3.3	3.6	4.3	3.1	3.4	12	12	11	12	2.7	10	11

Table 5.2. REE data of selected samples from Nisyros. Data were collected by laser-ablation of fused glass discs.

Table 5.3. Brief summary of some petrographic observations of samples from Nisyros.

Synthem	Sub-synthem	Unit number	Comments	Chemical composition	Unit numbers of Volentik et al. (2002)
Profitis Ilias		pfi	*Post-caldera* lava domes: Ol-bearing mafic enclaves reach 30 cm in size	rhyodacitic	23
		ya$_j$	*Yali fallout* layer: aphyric	rhyolitic	22
Kàrdia	Pali	up	*Upper Pumice* pyroclastic deposits: contains amphibole-bearing enclaves	rhyodacitic	
		nlf	*Nikia* lava flows: amphibole-bearing mafic enclaves reach 1.5 m in size; presents glassy/perlitic facies	rhyolitic	21
	Loutrà	lp	*Lower Pumice* pyroclastic deposits: displays banded pumices	rhyolitic	20
		llf		andesitic	
		vu$_j$	*Vunari* debris avlanche deposit: same as **emb**		
Fournia		emb	*Emborio* lava: 1-2% of amphibole-bearing andesitic enclaves	dacitic	19
		blf	*Aghia Basilei* lava flows: glomeroporphyritic agglomerates	basalt-andesitic to andesitic	
Lies	Xolante	lf^8	Crustal xenoliths, glomeroporphyritic agglomerates and plag with resorbed cores	basalt-andesitic	17-18
		xo	Pyroclastic deposits: same as lf^8	basalt-andesitic	15-16
		21	Pyroclastic deposit: no data	basalt-andesitic	
Lies	Afionas	pa	*Pahia Ammos* pyroclastic deposits: no data	andesitic to dacitic	17
		lf^7		dacitic	
		alf	*Argos* lava: lava with reddish banding, perlitic textures, and resorbed plag	rhyolitic	14
		sv	*Stavros* pyroclastic deposits: highly altered; show olivine relics	basalt-andesitic	13
		lf^6	Displays glomeroporphyritic agglomerates and plag with resorbed cores	andesitic	12
		xlf$_b$	Lava flow with the peculiarity of incorporating up to 30% of enclaves (mainly andesitic blebs)	dacitic	11
		lf^5	Some plag display resorbed cores; relics of olivines	andesitic	10
Kato Lakki	Second lake	ms	*Melisserì* pyroclastic deposits: some plag display resorbed cores	andesitic	8
		lf^4	Some plag display resorbed cores	basalt-andesitic	7
	First lake	lf^3	Some plag display resorbed cores	basalt-andesitic	5
Kremasto		kb	*Lakkì B* pyroclastic deposits: same as **ka**	basalt-andesitic	
		lf^2	Lava flow with glomeroporphyritic agglomerates	andesitic	3
		ka	*Lakkì A* pyroclastic deposits: highly altered, poorly vesiculated and crystal-poor (cpx and fds).	basalt-andesitic	2
		lf^1	Plag displays resorbed cores	basalt-andesitic	1
Kanafià		ho$_a$	*Holaki* hyaloclastites and pillow lavas: plag displays resorbed cores	basalt-andesitic	

	pl	cpx	opx	ol	bt	amp	oxi	apa	zir
Encl pfi	◇ ×	◇ ×		◇		◇	◇ ×		
pfi	◈ ×	◇ ×	◇	✧		◇	◇ ×	◇	
ya$_j$	Aphyric								
up	◇		◇				◇	◇	◇
Encl nlf	◇ ×	×	×			◇and×	◇ ×		
nlf	◈	◇	◇			◇	◇	◇	◇
up	◇		◇				◇	◇	◇
llf	◇ ×	◇ ×		◇			◇ ×		
Encl vu$_j$	×					×	×		
vu$_j$	⟐to◈ ×	◇ ×	◇ ×			◇	◇ ×	◇	◇
emb	⟐to◈ ×	◇ ×	◇ ×			◇or✳	◇ ×	◇	◇
blf	◇to◈ ×	◇to⟐ ×	×	◇			◇ ×		
lf^8	◇to◈ ×	◇to⟐ ×		◇			◇ ×		
xo	◇to⟐ ×	◇to⟐ ×		◇			◇ ×		
pa	◇ ×	◇ ×					◇ ×		
lf^7	⟐ ×	◇ ×	◇ ×			◇	◇ ×	◇	◇
alf	◇to⟐ ×	◇ ×	◇ ×		×	◇	◇ ×	◇	◇
sv	⟐	◇		✳			◇		
lf^6	◇to⟐ ×	◇ ×		◇			◇ ×		
xlf$_b$	◈ ×	◇ ×		◇	✳		◇ ×		
lf^5	◇to◈ ×	◇to⟐ ×		◇or✳			◇ ×		
ms	⟐to◈ ×	◇ ×	×	◇or✳			◇ ×		
lf^4	◈to◆ ×	⟐to◈ ×		◇or✳			◇ ×		
lf^3	⟐to◈ ×	◇to◈ ×		◇to⟐			◇ ×		
kb	◇ ×	◇ ×		◇		◇	◇ ×		
lf^2	◇to◈ ×	◇to⟐ ×	◇	✳			◇ ×		
ka	◇ ×	◇ ×		◇			◇ ×		
lf^1	◈to◈ ×	⟐ ×		◇			◇ ×		
ho$_a$	◈to◈ ×	⟐					◇		

Table 5.4. Summary of observed phases in each stratigraphic unit (after Volentik et al., 2002; Vanderkluysen & Volentik, 2002; and Vanderkluysen et al., in review). pl = plagioclase, cpx = clinopyroxene, opx = orthopyroxene, ol = olivine, bt = biotite, amp = amphibole, oxi = oxides, apa = apatite, zir = zircon. Abundance of phenocryst phase: ◇ <5%, ⟐ 5-10%, ◈ 11-15%, ◈ 16-20%, ◆ > 20%. Mineral presents in groundmass: ×; Ghosts, remnants: ✳; Xenocrysts: ✧

6. Nisyros' volcanic evolution: the growth of a strato-volcano

Loÿc Vanderkluysen[(1)], Alain Volentik[(1)], Claudia Principe[(2)], Johannes C. Hunziker[(1)], Jean Hernandez[(1)]

[(1)] Institut de Minéralogie et Géochimie, BFSH-2, Université, CH-1015 Lausanne, Switzerland.

[(2)] Istituto di Geoscienze e Georisorse, Area della Ricerca CNR-Pisa San Cataldo Via G. Moruzzi 1, I-56124 (Pisa), Italy

Abstract - Field evidence clearly shows that both today's cone-like morphology is the result of the migration of volcanic centres along major tectonic trends and the volcano's morphology was periodically reorganized by collapse and faulting episodes. After the formation of a submarine paleo-edifice (which went through an immersion-and-emersion episode), a new subaerial cone was built eastwards by multiple effusive and explosive eruptions. These lead to the formation of a summit depression in which a lake settled. After the Melisserì eruption, activity drifted to the North-East, and the South of the island. After this stage, a widespread activity occurred throughout the island, giving birth to monogenetic vents scattered along Nisyros' main tectonic trends. Effusive activity followed in the North-West and North-East, and the formation of dacitic domes triggered the collapse of the northern volcano's flank. The Lower Pumice eruption lead to caldera collapse at the island's centre, whereas the Upper Pumice eruption was secluded to the flank collapse depression to the North. The caldera was later partly filled by dacitic domes, and it has been the main locus of hydrothermal activity in recent times.

6.1. Introduction

The geology of Nisyros has been described by previous authors (e.g. Davis, 1967; Keller, 1971; Di Paola, 1974; Vougioukalakis, 1984, 1993, 1998; Bohla & Keller, 1987; Keller et al., 1990; Limburg & Varekamp, 1991; Papanikolaou et al., 1991; St. Seymour & Vlassopoulos, 1992; Francalanci et al., 1995) as resulting from a succession of effusive and explosive volcanic eruptions, ranging in composition from basaltic andesites to rhyolites and emitted from a central vent. In the literature, the island's evolution has generally been divided in 4 major stages. Stage 1 is characterised by submarine activity, which likely pre-dates, at least partially, the eruption of the Kos Plateau Tuff (Keller, 1971; Rehren, 1988; Keller et al., 1990), which took place 161 ka B.P. (Smith et al., 1996). Stage 2 consists of the growth of the main andesitic strato-cone. The two eruptions of the Lower and Upper pumices and the effusion of large volumes of rhyolites (the Nikià lava) characterise stage 3 of Nisyros' activity. Finally, stage 4 comprises the caldera collapse, resulting from these pumice eruptions, and the subsequent emplacement of the dacitic domes of Prophitis Ilias, filling the western two thirds of the present day caldera.

Based on newly collected data and together with the findings of Volentik et al. (2002), the volcanic history that we draw differs with the general accepted view on various accounts. In the following reconstruction, we show that the present, perfectly conic shaped morphology of this "classical" strato-volcano topped by a summit caldera was caused by the migration of the eruptive vents along the main tectonic trends and by the occurrence of repeated collapses and faulting episodes.

6.2. Volcanic Evolution

The first volcanic events on Nisyros (Fig. 6.1-A and 6.2-A) gave birth to a submarine volcano. It consisted of lava pillows, now outcropping on the north-western shore of the island (Fig. 2.5 in Volentik et al. (a), this volume). There is full agreement in the literature that this pillow lava sequence lies at the base of the Nisyros volcanic stratigraphic succession. This submarine sequence is interrupted by an emersion stage testified by the erosion of the pillow lavas and their re-deposition in debris flow facies. The presence of reworked rounded pumices at the top of the submarine sequence, attributed by Keller (1971) to the KPT eruption that crops out in the nearby island of Kos (Allen & Cas, 2001), implies that the pillow lava sequence formed prior to 161 ka (the age of the KPT eruption; Smith et al., 1996). After this sub-aerial episode, an important tectonic event might have brought this edifice back below sea level, where submarine lava emission resumed. Alternatively, an inflation-deflation mechanism linked to the KPT magma chamber and the emission of this ignimbrite can be hypothesized. As a matter of fact, the occurrence of a sub-aerial debris flow between two submarine episodes implies that the emerged land was large enough to permit the development of a hydrographical system. If we consider the position of the KPT caldera as depicted by Allen & Cas (2001) (Fig. 6.3) and Pe-Piper et al. (2005) (Fig. 4.2-B in Volentik et al.(c), this volume), a fascinating hypothesis can be proposed, supported by the discovery by Keller (1971) of KPT pumices at the top of this stratigraphic sequence. In this hypothesis, the relict emerged portion of the volcanic edifice affected by the KPT collapse is represented on Nisyros by the pillow lavas of Holaki (**ho$_a$**). The re-immersion of the ancient submarine edifice (paleo-Nisyros), possibly due to ring-faults linked to the KPT collapse, might then explain the paucity of KPT deposits on Nisyros, although they reach thicknesses of several tens of meters (Fig. 6.4) on all surrounding emerged lands.

The first sub-aerial volcano (Figs. 6.1-B and 6.2-A), which grew eastward from the submarine edifice in the northern sector of the island, is a small cone. It collapsed as a consequence of the Lakkì explosive eruption and gave birth to the first recognisable caldera-like depression on the island, in which a lake settled. A similar succession of events repeated itself after volcanism resumed in the same area (Figs. 6.1-C & D and 6.2-B), with the building of a strato-cone before the explosive eruption of Melisserì, which possibly triggered another caldera collapse. Indeed, this eruption vented a great volume of material that was later reworked on the emerged part of the volcano (**ms$_j$** unit). The location and extension of the Kato Lakkì lacustrine deposits and the facies and thickness distribution of Melisserì deposits (see Volentik et al.(b), this volume, and the annexed geological map) supports a positioning of this constructive-destructive episodes on the Eastern corner of the present island morphology.

The subsequent activity mainly consists of the emission of Ellinikà lava flows (**lf^5**, **xlf$_b$**, **lf^6**) on the north-eastern sector of the island, followed by the migration of the volcanic activity to the south, resulting in the explosive volcanic eruption of Stàvros (**sv**) and in the emission of the Argos lava flows (**alf**). These three events contributed to depict a roughly rounded island morphology.

During the final stage of the Lies synthem, volcanic activity occurred from different polygenetic centres and from a number of monogenetic vents, all aligned along major faults (Fig. 4.2 in Volentik et al.(c), this volume). In contrast with previous stages, small effusive and explosive events (**lf^7, pa, xo,** and **lf^8**), took place from such scattered centres (Figs. 6.1-D and 6.2-B) rather than having large lava flows and important explosive events vented from a unique source. This paroxysm in volcanic activity was followed by a period of rest sufficiently long to allow both the reorganisation of the morphology of the island and the deposition of large volumes of epiclastites (**pc$_j$**) partly filling palaeovalleys.

After an undetermined gap of time, activity resumed on Nisyros with the building of a small basaltic andesitic to andesitic edifice (Figs. 6.1-E and 6.2-C). The remaining portion of this edifice is constituted by the Aghia Basilei lava flows (**blf**) that gently descend on the North-Western corner of Nisyros, topping the ancient submarine sequence (Fig. 3.8 in Volentik et al.(b), this volume).

Only at this point in the volcanic history of Nisyros did the emplacement of dacitic domes become prominent (**emb**). As a consequence, repeated episodes of minor block and ash flows took place, leading to the Vunàri sector collapse (**vu$_i$**), which dominates the present morphology along the northern coast of the island (Figs. 6.1-F). By that time, any remaining depression formed by earlier calderas had probably been filled.

Again, a large caldera was formed as a consequence of the explosive eruption that produced the deposits of the Lower Pumice (**lp**), (Figs. 6.1-F and 6.2-D) one of the three eruptions (along with those of Lakkì and Melisserì) displaying the typical explosive sequence of fallout and pyroclastic density currents that may link them to a shallow magma chamber. Remnants of this caldera collapse are constituted by the curved morphology in the northern half of the present caldera rim. The southern section of the present depression formed as the result of the enlargement of the former caldera by faults (Fig. 4.2 in Volentik et al.(c), this volume) linked to the major tectonics trends (i.e. N030°) at least after the effusion of the voluminous rhyolitic lava flow of Nikià (Fig. 6.2-D).

The last phase of explosive activity (Upper Pumice, **up**), which was tectonically controlled, built a tuff cone and pyroclastic flow deposits both linked to N030° fractures. The **up** tuff cone is located outside the **lp** caldera rim and inside the morphological depression previously induced by the Vunàri sector collapse.

The rhyodacitic domes of Profitis Ilias (**pfl**) constitute the youngest magmatic event on Nisyros (Figs. 6.1-G and 6.2-E), They filled the two thirds of the 4 km-caldera on its western side and partly outpoured towards the sea (Fig. 6.5).

The Ramos and Lakkì plain, which occupies the remaining third of the caldera floor, is the scene of hydrothermal activity that has been documented since the Antiquity. There hydrothermal explosions have been known to occur in historical times, most recently during the 19th century (Gorceix, 1873; Martelli, 1917).

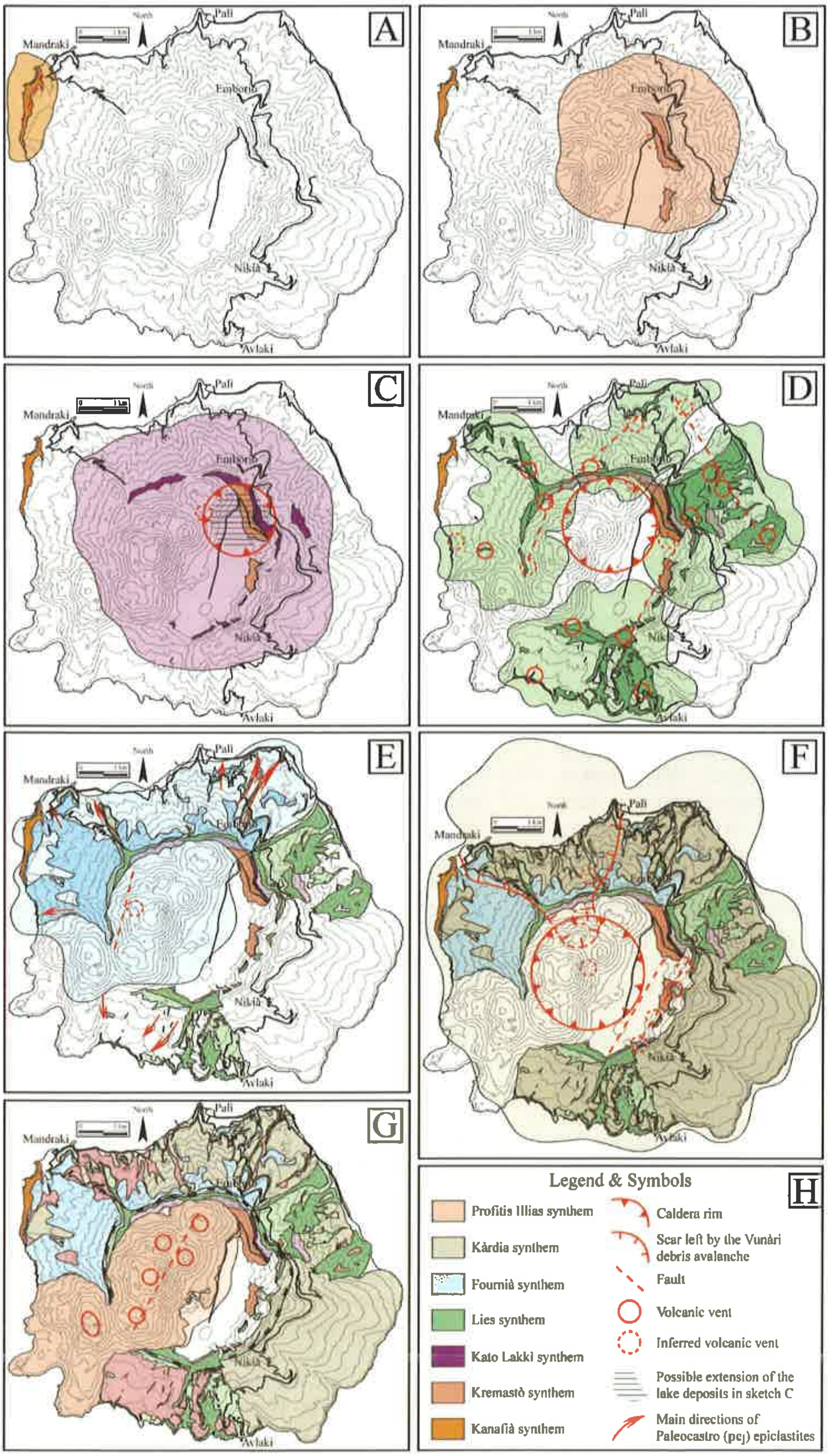

Fig. 6.1: Sketch maps of the evolution of Nisyros. Dark colours represent actual outcrops while light colours indicate the inferred extension of each synthem. Situation at the end of (A) the Kanafià synthem; (B) the Kremastò synthem; (C) the Katò Lakkì synthem; (D) the Lies synthem; (E) the Fournià synthem; (F) the Kàrdia synthem ; (G) the Profitis Ilias synthem; (H) Legend and symbols.

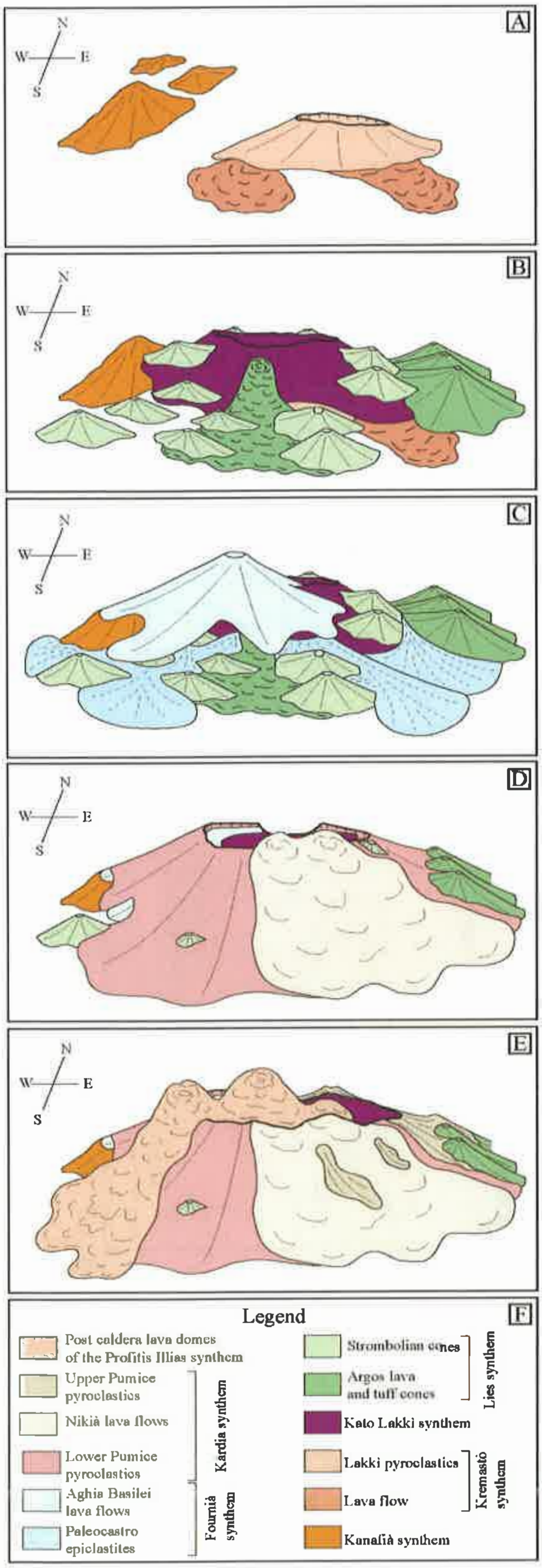

Fig. 6.2: The evolution of Nisyros in 3D, seen from the South. Situation after (A) the Kremastò synthem; (B) the Lies synthem; (C) the Fournià synthem; (D) the extrusion of the Nikià lava flows (nlf); (E) the Profitis Illias synthem. (F) Legend.

Fig. 6.3: A: Distribution of the KPT on the Dodecanese Island, Greece and western Turkey (Bodrum and Datça Peninsulas). From Allen & Cas (2001). B: Possible margin of the KPT caldera and present-day bathymetry of the Kos-Nisyros area (bathymetric contour interval, 100 m). From Allen (2001).

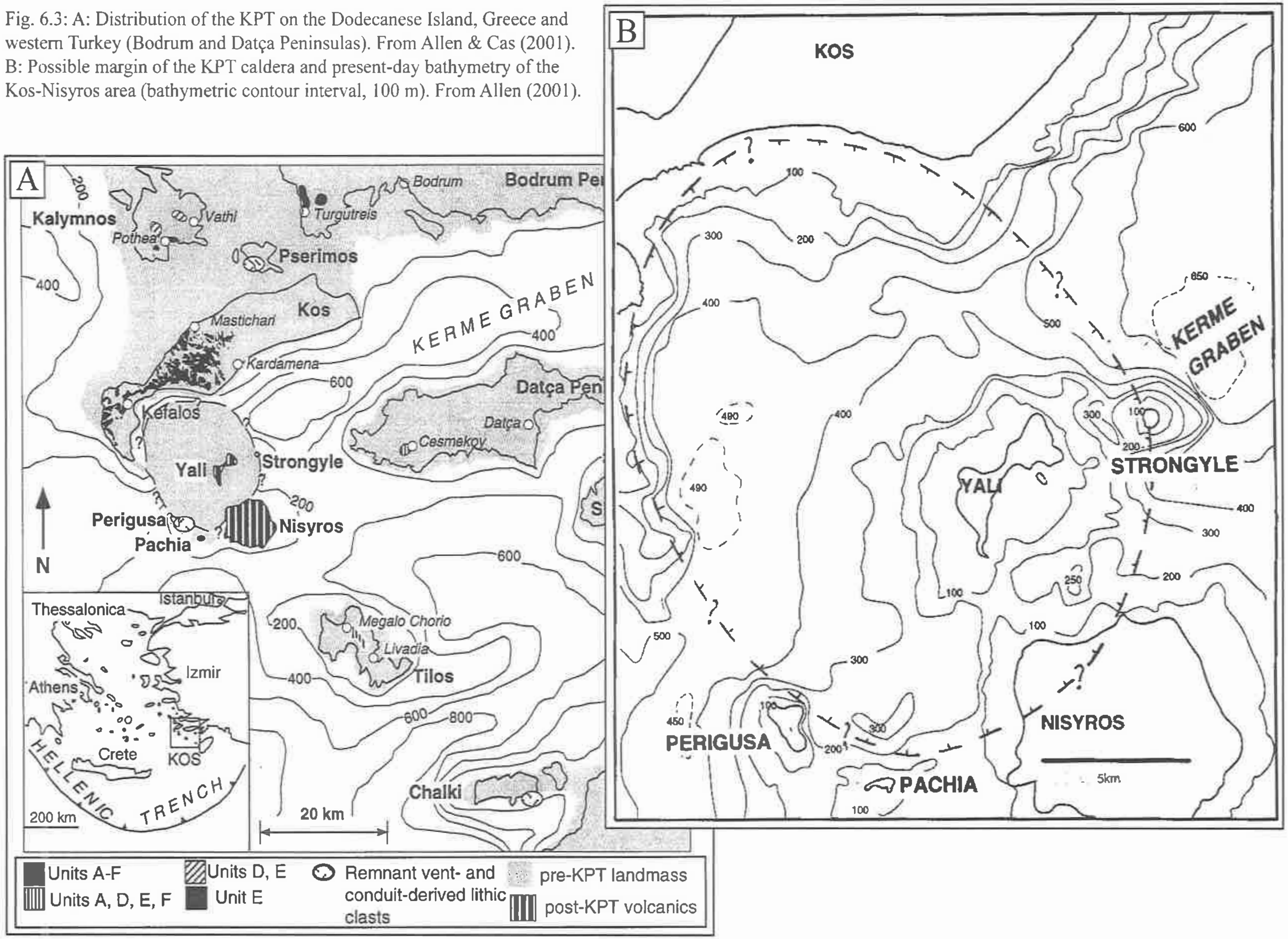

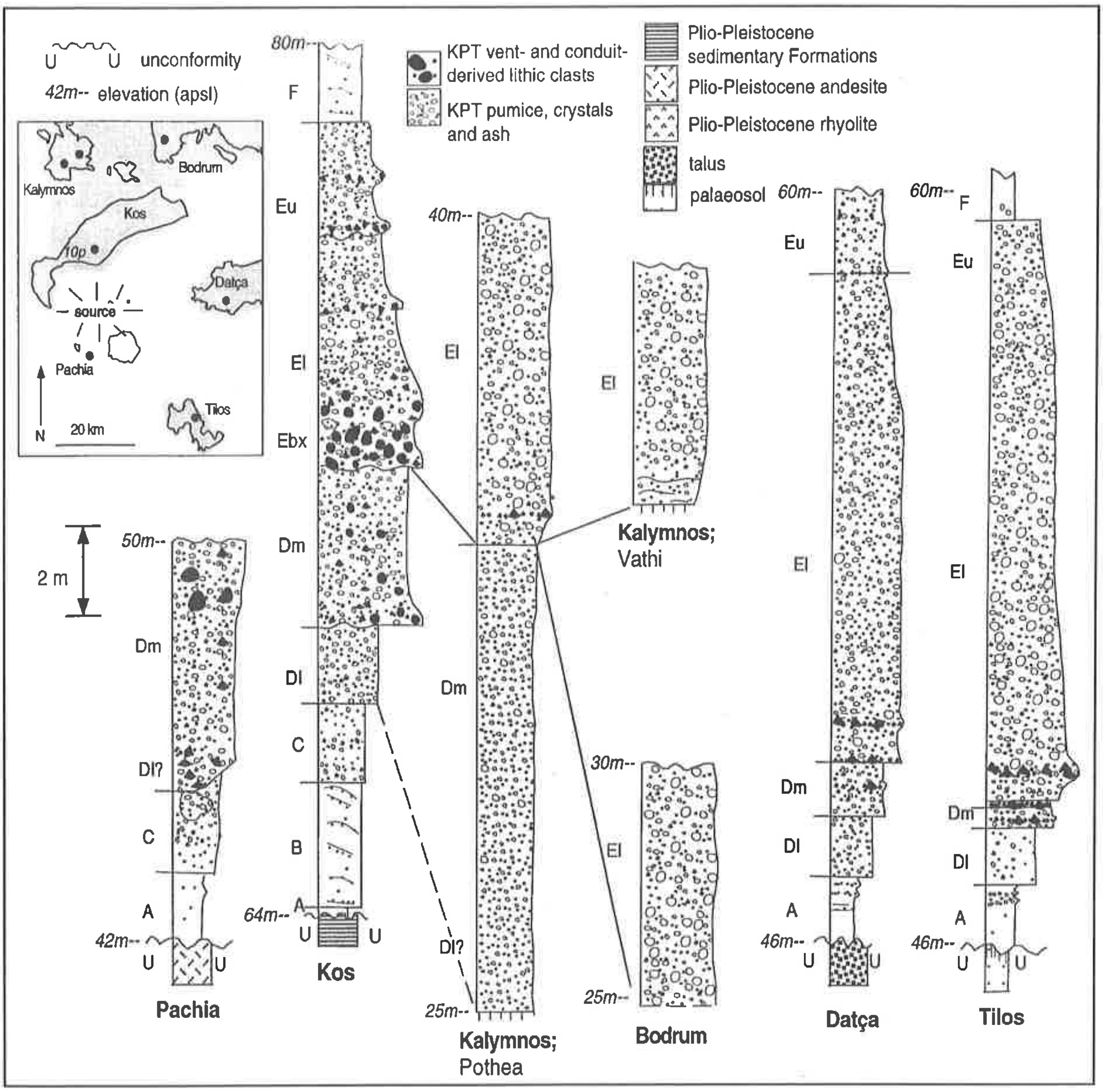

Fig. 6.4: Key stratigraphic section of the KPT, including elevations of the base and top of the sections. Distance from source is given at the base of each section. Section locations are shown in the inset map. From Allen & Cas (2001).

Fig. 6.5: View to the south from Nikià. Note the tectonic control of the southern caldera walls (area of the Monastery of Stàvros), the partial filling of the caldera by the Profitis Ilias rhyodacitic domes, their southwestern outpouring out of the caldera and the hydorthermal area.

7. A geophysical investigation of Nisyros' hydrothermal field using the self-potential and very low frequencies-tilt methods

Loÿc Vanderkluysen(1), **Pierre Gex**(2)

(1) Institut de Minéralogie et Géochimie, Université de Lausanne, BFSH2, Lausanne, CH-1015 Switzerland

(2) Institut de Géophysique, Université de Lausanne, CP-1, Lausanne, CH-1015 Switzerland.

Abstract - This contribution is aimed at studying fluid fluxes and fluid pathways in the Lakki plain and in Stephanos' hydrothermal crater using the self-potential (SP) and VLF-tilt (Very Low Frequencies) geophysical methods. Results show that N030° oriented lineaments occur in the Lakki plain, which are characterized by negative SP anomalies and electrically resistive materials; in Stephanos crater, these features typically show positive SP anomalies. In the field, these lineaments can be correlated with apparent superficial or subsuperficial fractures, which can also be shown to be correlated with high diffuse CO_2 fluxes from soils. As a result, we conclude that these fractures, which follow trends that have been active during various periods of Nisyros' activity, control the fluid pathways in the subsurface, such as zones of high CO_2 degassing, infiltration of meteoric waters in the Lakki plain, preferred fumarolic activity in hydrothermal craters and lateral and/or downwards migration of steam condensates in nearby areas. In addition, we suggest that a SP survey is a rapid way of obtaining a snapshot of Nisyros' hydrothermal activity, and that the method should be considered for future monitoring efforts of the island.

7.1. Introduction

Although the exact state of Nisyros volcano remains a matter of study, it appears that the island is seated above an active magmatic system (Papadopoulos et al., 1998; Chonia & Makris, 2000; Lagios et al., 2001; Marini et al., 2002; Sachpazi et al., 2002; Chiodini et al., 2002; Sykioti et al., 2003; Gottsmann et al., 2004), and therefore that the volcano can only be considered, at the present time, as dormant. Because hydrothermal explosions are known to have occurred in the recent past (between 1871 and 1873, Gorceix, 1873; and in 1887, Martelli, 1917), and because the Ramos area is the location of important touristic activity (Stephanos crater hosts 200-600 visitors a day between May and September), the area remains a matter of concern and of increased monitoring efforts.

The present study aims at studying the subsurface structure and fluid fluxes in the Lakki plain and Stephanos crater using the self-potential (SP) and VLF-tilt (very low frequencies) geophysical methods, and test their potential as monitoring tools of Nisyros' hydrothermal system.

7.2. Methods, setup and limitations

7.2.1. Methods

The self-potential method (SP) allows to measure electrical potentials naturally present in the ground between a measuring electrode and a reference electrode (which should be, if possible, located outside of the studied anomaly). These potentials are generally thought to be produced by electron fluxes, for instance in the vicinity of ore bodies (e.g. Sato & Mooney, 1960), or as fluids percolate through rocks, near water wells, springs, or fumarole fields (e.g. Rapolla, 1974; Massenet & Van Ngoc, 1985; Aubert & Lima, 1986; Gex, 1992; Apostolopoulos et al., 1997; Byrdina et al., 2003). In the latter case – called electrofiltration - upwards and downwards motion of fluids will result in positive and negative SP anomalies, respectively. Thanks to these properties, the SP method has become an integral part of volcano monitoring techniques, and permanent SP networks have been successfully set up at some volcanoes, such as the Piton de la Fournaise on Réunion Island (Michel & Zlotnicki, 1998; Zlotnicki et al., 2005).

The VLF method measures magnetic fields of very low frequencies (between 15 kHz and 30 kHz), produced by remote antennas used by the military to communicate with submarines. In a uniform terrain, the primary magnetic field produced by the antenna can be represented by a horizontal vector. In conductive bodies, a secondary magnetic field is produced, resulting in an inclined vector at the surface. The VLF-tilt method measures the inclination of the vector at the surface. As one approaches a conductive body, the vector begins to point upwards, while as one nears a resistive body, the vector begins to point downwards.

7.2.2. Instrumental setup

SP were measured with a millivoltmeter, custom-made at the University of Lausanne. We also used two unpolarisable electrodes, consisting of a copper bar dipped in solution saturated with copper sulfate, encased in a PVC tube with a wooden tip. Connection between the reference and measuring electrodes was made with a copper wire. While measuring profiles, the reference electrode was left static while the measurement electrode was carried along the profile, letting the copper wire unwind behind it. SP was set at zero at the reference electrode, and measurements were taken every 5 meters. In Stephanos crater, the reference point was set at zero at the northeastern corner of the 100 by 200 m grid. VLF-tilt measurements were made on a SCINTREX device, using a ~23.4 kHz frequency. Measurements were made every 10 meters.

Data for the present study were all collected in July and August of 2000.

7.2.3. Limitations

Soils in the Northern Lakki plain were entirely dry during the summer of 2000, as is generally the case in Greece during that season. As a result, good contact between the two SP electrodes could not be established and measurements could not be taken on a series of profiles north of Stephanos crater. Consequently, the present paper shows only one SP profile in the Ramos area. Future scientists should be aware of these adverse climate conditions and schedule surveys using electrical methods in the early months of the year (ideally between February and April). Thanks to fumarolic vapors and steam condensates, SP could be measured with ±3 mV accuracy in Stephanos crater. VLF-tilt measurements did not suffer from these conditions. However, available primary fields were poorly oriented compared to studied structures, and tilt angles were of relatively small amplitude (not exceeding 7°), yet remained significantly higher than measurement uncertainty (in the order of 0.5°).

7.3. Results

Data were collected along six profiles in the Lakki plain and a 5x10 m grid in the bottom of Stephanos crater (Fig. 7.1). Figure 7.2 displays VLF-tilt (all profiles) and SP (profile 5) measurements from West to East, while Fig. 7.3 shows the interpolated SP map of the bottom of Stephanos crater. VLF data on Fig. 7.2 have been filtered using a reversed Fraser filter (Fraser, 1969). The effect of this filter is to highlight zones of anomaly: in the present case, when the Fraser-filtered value is positive, there is an anomalously resistive zone in the subsurface. To counter the effects of noise, SP data on profile 5 have been filtered using a 5-point moving average.

VLF-tilt data shown for profile 4 (Fig. 7.2) displays a textbook example of a detected resistive anomaly, clearly highlighted by the Fraser filter. Although signals are sometimes superimposed, other profiles typically indicate the presence of three such anomalies. Interestingly, as shown on profile 5 (Fig. 7.2), these electrically resistive zones can be correlated with negative SP anomalies. Profiles 5 and 6 also seem to indicate that some of these anomalies are aligned with large cracks one can observe at the surface, in particular in the vicinity of Stephanos crater.

The SP map of Stephanos crater reveals strong positive anomalies, interpreted as zones of upwelling fluids, in the southern and eastern zones of the crater.

7.4. Discussion

The linear anomalies in the SP map of Stephanos crater have been highlighted in Fig. 7.4A. These anomalies correspond to lineaments detected with other methods, most notably by measuring CO_2 soil diffuse degassing and soil temperature (Brombach et al., 2001; Caliro et al., 2005). However, the spacing of the SP measurement grid is smaller than that of geochemical soil surveys and thus, linear features appear with improved resolution in Figs. 7.3 and 7.4A with respect to geochemical maps. These lineaments are also aligned with fractures that are apparent in the crater walls and in the crater's surroundings, yet do not have any surface expression at the crater's bottom. The linear arrangements typically have N350°, N040° and N070° orientations, which seem to be dominant tectonic orientations in the island's history (Papanikolaou et al., 1991; Marini et al., 1993; Lagios et al., 2001; Volentik et al., 2002).

Resistive anomalies detected by VLF-tilt along the 6 profiles in the Lakki plain seem to have similar broadness, spacing and amplitudes from profile to profile. We therefore interpret them as linear features as well, as shown in Fig. 7.4B. Interestingly, the easternmost of the inferred lineaments corresponds to a linear zone of high CO_2 degassing (Caliro et al., 2005). It also follows the track of an important fault located on the southern caldera wall (as seen on the map of Volentik et al., this volume). In profile 5, the VLF-tilt anomalies are exactly correlated with broad negative SP anomalies. This indicates downward fluid motion at these locations, whereas upwards CO_2 degassing at the same location does not seem to be detected by electrofiltration SP.

From these observations it can be inferred that faults and fractures, likely of tectonic or volcano-tectonic origin, control the pathways of fluid motion in the subsurface. Although they have little or no surface expression, these fractures or fractured zones influence the location of CO_2 degassing, infiltration of meteoric waters and lateral and/or downwards migration of steam condensates in the hydrothermal craters surroundings; in Stephanos crater, fumarolic activity occurs preferentially along the same fractured pathways. Intense hydrothermal activity and craters such as Stephanos and Polyvotis occur where the most prominent of these lineaments intersect, indicating that they played an important role in defining the location of past hydrothermal explosions and may do the same in the future.

7.4.1. The December 2001 fracture

On December 5th, 2001, a fracture appeared, without warning, in the middle of the Lakki plain during a period of intense rainfall on the island (Vanderkluysen & Volentik, 2002). In the absence of any anomalous seismicity, and because of the uncharacteristic weather conditions, local geologists concluded that the fracture was a pre-existing zone of weakness covered by a soil layer that was washed away by rain. In this respect, chemical weathering promoted by the acidic steam condensates moving away from the hydrothermal crater area (1420 t/d, Caliro et al., 2005) should not be underestimated (see also Principe et al., this volume). The fracture, some 250 m in length and reaching 10 m in depth, follows a N030°-N010° orientation. Although we did not have the proper instruments to measure the fracture's location with precision, on first approach it appears to coincide with the central anomalous trend of profiles 4 to 6 (Fig. 7.4B). If this were confirmed, it would mean that the VLF-tilt data successfully detected the fracture as a zone of higher electrical resistance, and SP detected it as a zone of fluid circulation. It would also mean that there might be other such fractures below the surface of the Lakki plain, which may present a hazard for farmers and grazing animals. This hazard could be mitigated by carefully mapping these features using a combination of geophysical methods.

7.4.2. Geophysical monitoring

The monitoring of Nisyros' geothermal activity has so far focused on measuring CO_2 soil degassing and chemical and isotopic composition of fumarolic gases (Chiodini et al., 1993; 2002; Marini et al., 1993; 2002; Kavouridis et al., 1999; Dotsika & Michelot, 1993; Brombach et al., 2001; 2003; Cardellini et al., 2003; Caliro et al., 2005; Fiebig et al., 2004). While these methods provide useful information on the state of the hydrothermal system, such as the contribution of magmatic gases and the aquifer's temperature (both useful indicators of impending eruptions), they are ill suited for continuous monitoring, because of the relatively long time needed for mapping the CO_2 flux from soil and the very long time required for fumarole sampling and analysis. A SP survey, on the other hand, can be realized and interpolated in a day, the drawback being that SP anomalies are ambiguous to interpret (for they are not directly related to either temperature, chemistry, and mass flux of fumarolic fluids). Although continuously recording SP networks have been installed at other volcanoes, it remains unlikely on Nisyros: inside Stephanos and Polyvotis crater, high ground temperatures and corrosive gases would lead to rapid degradation of the instruments; in the Lakki plain, the absence of hydrothermal activity and dryness of soils during the summer and fall would not yield meaningful results. However, regular SP monitoring of Polyvotis and Stephanos craters (weekly or biweekly) would yield useful insight into the spatial and temporal variations of the island's geothermal field. This could serve as indicator of periods of anomalous activity, on which more time-demanding geochemical techniques could be focused.

7.5. Conclusions

The VLF-tilt and SP survey has revealed the existence on Nisyros of linear features that control the pathways of fluid motion in the subsurface, whether as zones of meteoric infiltration in the Lakki plain, or of fumarolic fluid upwelling in areas of intense hydrothermal activity, such as Stephanos crater, or of lateral and/or downwards movements of steam condensates near the hydrothermal craters.

These features are associated with higher electrical resistivities than their surrounding, and often with high soil CO_2 fluxes. In December of 2001, a crack (approximately 250 m in length, a few meters in width, and up to 10 m in depth) was revealed where one such lineament had been detected by VLF-tilt in the summer of 2000. Finally, these lineaments have orientations consistent with major tectonic trends active on the island. This seems to indicate that:

1) faults and fractures, some pre-dating the formation of the hydrothermal craters, are the preferred loci of CO_2 degassing, hydrothermal activity and infiltration of meteoric waters

2) areas of intense geothermal activity such as Stephanos and Polyvotis craters occur where these fractures intersect

3) there may be cracks below the surface along these zones of weakness, covered by a thin layer of soil and alluvial deposits, as appears to have been the case for the December 2001 crack. These cracks can be a hazard for Nisyros' inhabitants, but have been shown to be detectable with VLF-tilt, and thus likely with other electrical methods as well.

In addition, SP data collection is faster than gas flux measurements and much faster than fumarole sampling and analysis, allowing tighter measurement grids and thus, greater resolution on spatial features and temporal variations. This might prove to be an extremely useful feature as a potential monitoring tool of Nisyros' hydrothermal activity if used in conjunction with more time-demanding geochemical surveys.

Acknowledgements - We would like to acknowledge the financial support of the Immanuel Friendlaender Foundation for Volcanology. The GEOWARN group is thanked for their logistical help and in particular Evangelos Lagios and Radu Gogu for sharing their experience with geophysics. We are grateful to Francine Gass for her positive insight and for computational support. We also express our utmost gratitude to those who have contributed to this work, in the field or otherwise, and have offered critical reviews of the manuscript, in particular, Alain Volentik, Prof. Luigi Marini, Prof. Johannes Hunziker, Claudia Principe and Prof. Jean Hernandez.

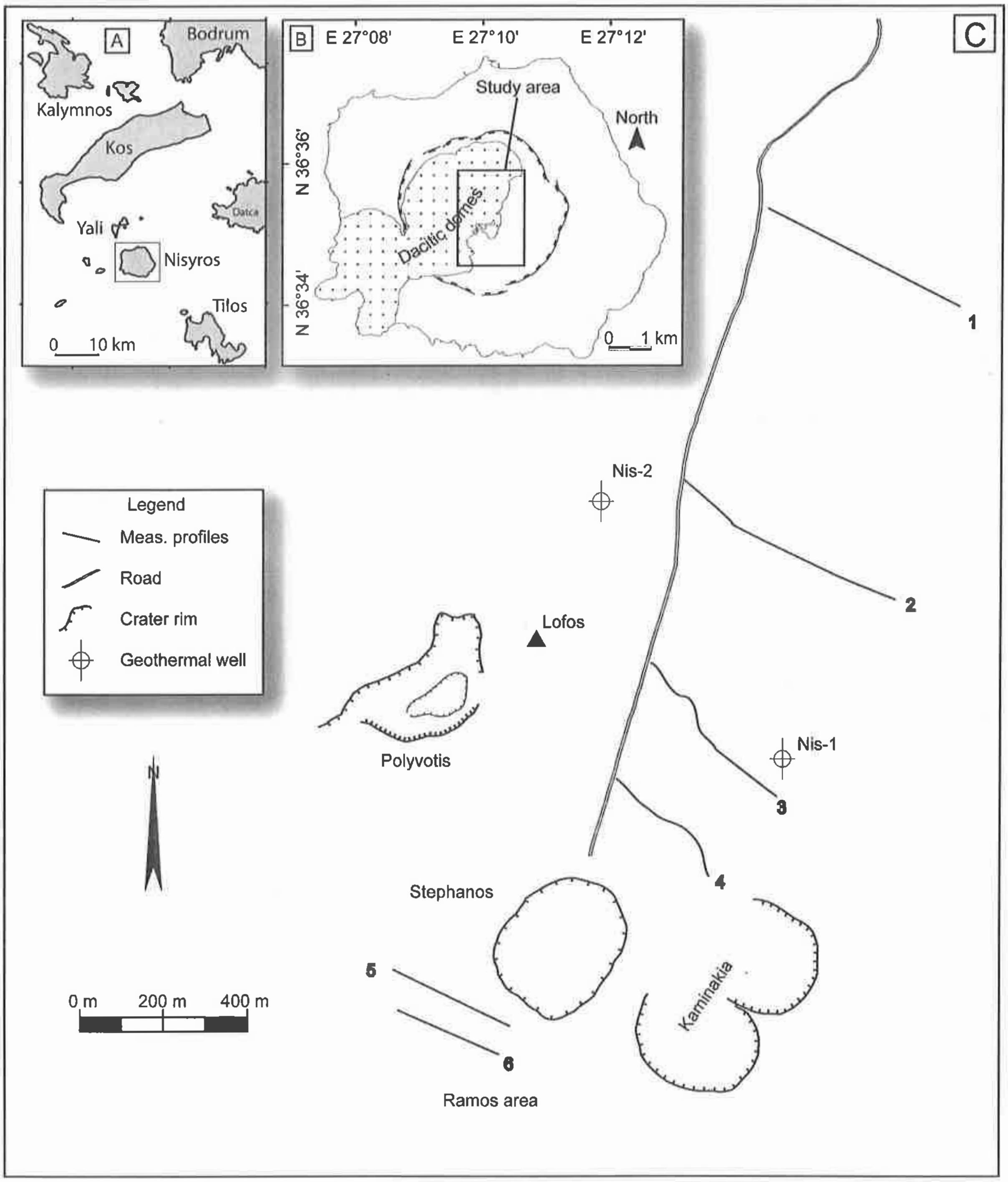

Figure 7.1. A. Geographical location of Nisyros in the Dodecanese (Aegean Sea, Greece). B. Map of Nisyros showing the study area, the morphological caldera rim and the location of the caldera-filling domes. C. Location of the 6 studied profiles in the Lakki plain, the craters of Stephanos, Polyvotis and Kaminakia, the two abandoned geothermal wells Nis-1 and Nis-2 (Geotermica Italiana, 1983; 1984) and the small dome of Lofos.

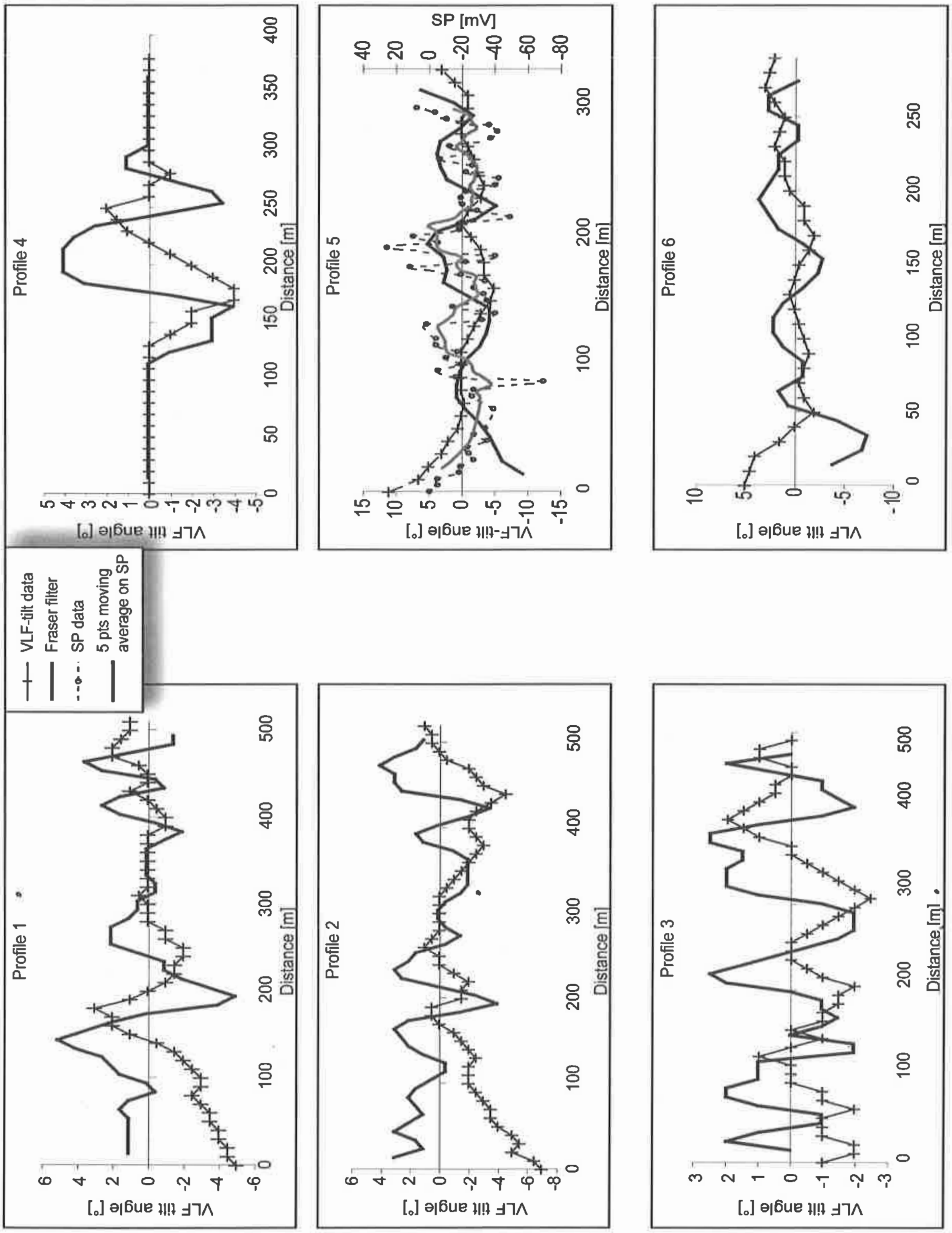

Figure 7.2. Profiles measured (from West to East) with VLF-tilt (1 to 6) and SP (5). VLF-tilt data have been filtered with a reversed Fraser filter (Fraser, 1969); see section 3 for details. Filtered data are shown with a thick black line. SP data have been filtered with a 5-point moving average (thick grey line).

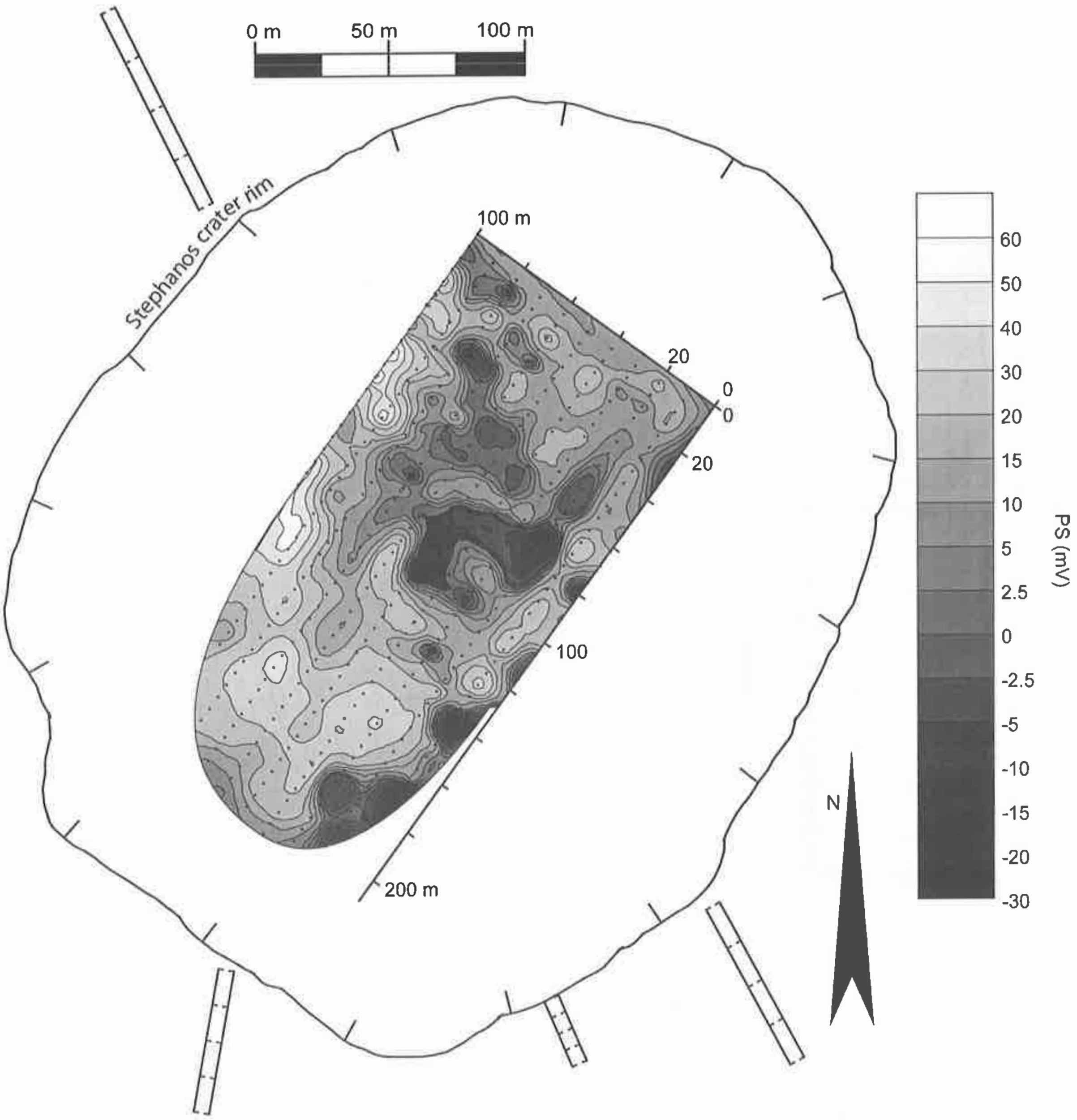

Figure 7.3. Self-potential map of Nisyros volcano. Dots represent measurement points on a 5x10 m grid. Interpolation between measurements was done by kriging.

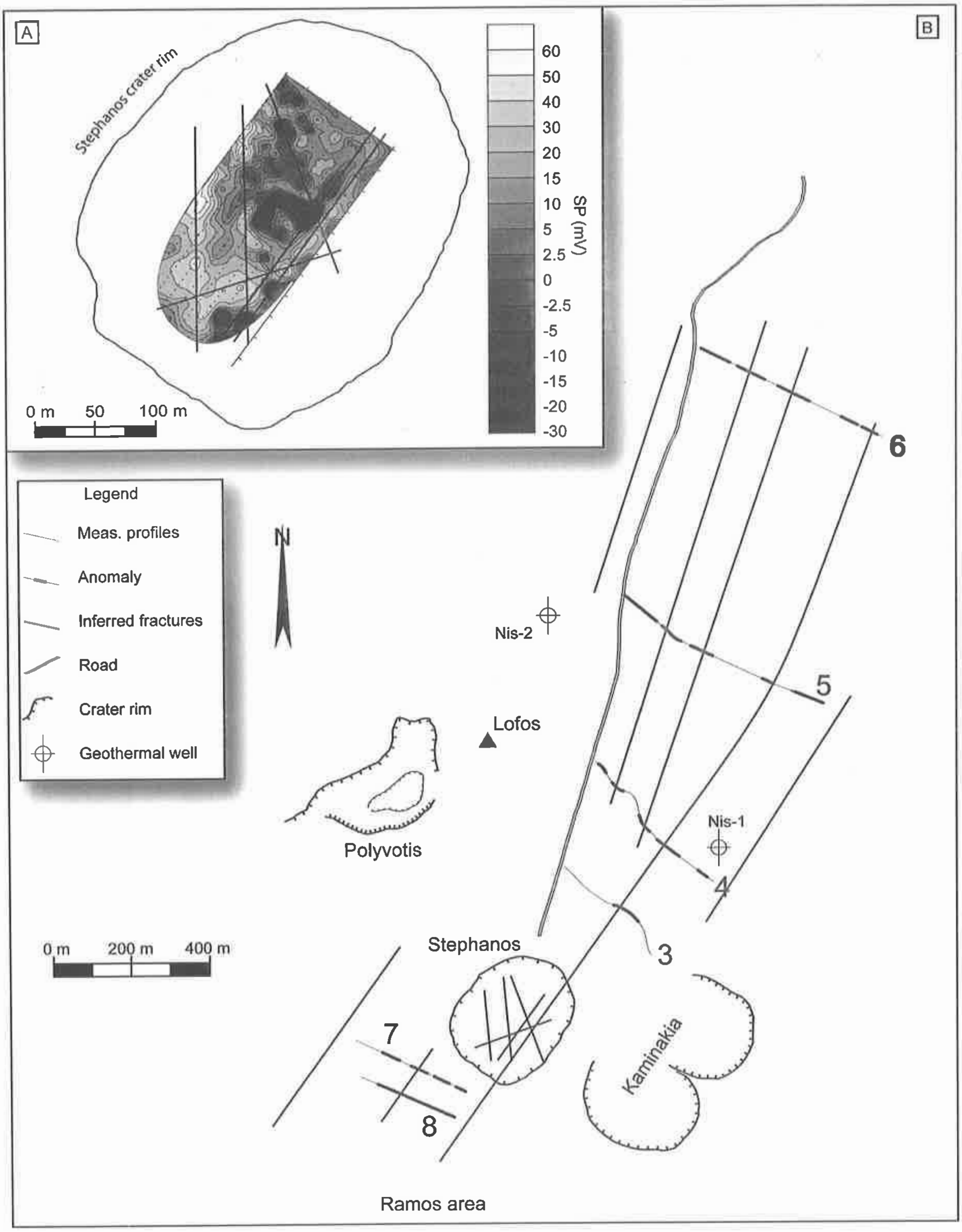

Figure 7.4. A. Lineaments interpreted from SP data in Stephanos crater. B. Lineaments interpreted from VLF-tilt and SP anomalies in the Lakki plain and Stephanos crater.

8. The need for the stochastic approach in the evaluation of the fluxes and total output of CO_2 emissions from soil

Marino Vetuschi Zuccolini$^{(1)}$, **Luigi Marini**$^{(1)}$

$^{(1)}$ Laboratorio di Geochimica, Dip.Te.Ris., Università di Genova, Corso Europa 26, I-16132 Genova, Italy

Abstract - This paper focuses on the comparison among interpolation and extrapolation algorithms of possible use for mapping the diffuse CO_2 flux from soil and quantifying total CO_2 output, including a procedure based on stochastic simulations. The limits of applicability and flexibility of these techniques are discussed. The dataset related to the hydrothermal explosion craters of Stephanos and Kaminakia (Nisyros) by Brombach et al. (2001) is used to test these procedures. Carbon dioxide fluxes and total output of CO_2 obtained by means of different methods range from 63.7 to 116 g $d^{-1}m^{-2}$ and from 25.4 to 46.2 Mg d^{-1}, respectively, from an area of 0.35 km^2. The sequential Gaussian simulations technique is the most powerful among the considered procedures since it permits the best visualization of local and regional uncertainties and the best investigation of spatial anisotropy.

8.1. Introduction

Carbon dioxide plays a fundamental role in many processes taking place in the biosphere, lithosphere, hydrosphere and atmosphere and concurring to the global carbon cycle (e.g., Berner et al., 1983). Terrestrial CO_2, i.e., the CO_2 released by spontaneous outgassing through the Earth surface from both active volcanic areas (e.g., Williams et al., 1992; Baubron et al. 1991; Seward and Kerrick, 1996) and non-volcanic geothermal areas (e.g., Chiodini et al. 1999), represents a poorly known, probably important component of the total budget of terrestrial CO_2.

Different techniques are used to quantify CO_2 degassing. In active volcanic areas the CO_2/SO_2 ratio directly measured in the volcanic plume by COSPEC is commonly used to compute the CO_2 flux, with errors attaining 75% (Williams et al, 1992). In geodynamic settings where SO_2 is virtually absent, e.g., where volatiles released from the magmatic system are totally absorbed by the overlying geothermal system, the outputs of CO_2 have been evaluated based on the thermal characteristics of the geothermal system and on the CO_2 concentrations in the reservoir (Kerrick et al., 1995; Seward and Kerrick, 1996). Temperature and CO_2 concentrations in the reservoir, are adopted as key parameters to compute the expected CO_2 output for areas geodynamically similar to test areas. Errors close to 50% are usual (Kerrick et al., 1995).

Direct measurements are required to improve the evaluation of the diffuse CO_2 flux from geothermal and volcanic areas. Among the different analytical techniques, the accumulation chamber method (Parkinson, 1981) is usually preferred as it allows one to carry out measurements within a wide concentration range (0.2-10000 g m^{-2} d^{-1}), with errors lower than 15% and reproducibility close to 10% (Chiodini et al., 1998). In order to survey the area of interest, CO_2 flux measurements are usually carried out in several stations situated at the nodes of a more or less regular grid. Some statistical tools, interpolation algorithms, and mapping procedures are then needed to obtain the total CO_2 output from the area of interest.

In other terms, processing of analytical data is largely based on the determination of a variable in an unknown site, a problem which can be solved through either deterministic or stochastic methods. In a deterministic model we know (or we suppose to know) the variability law that governs the distribution of the variable in space. Knowledge of the processes controlling the distribution of the variable in the investigated domain is in this case, therefore, implicit.

In a probabilistic approach, the genetic model governing the natural distribution of the variable is unknown but it is assumed "a priori" that the data distribution is governed by random processes. Contrary to the deterministic approach, in the probabilistic methods we use the data set to switch from the data space to the model space through inverse-technique methods (Tarantola, 1987; Ottonello, 2001). The results of several popular deterministic algorithms are here compared with the results of stochastic procedures in the investigation of CO_2 fluxes and CO_2 total budget. It is shown that probabilistic procedures are an important tool in deciphering and quantifying the effect of structural heterogeneity whenever associated to a proper description of regionalized variables.

Some CO_2 sources and sinks related to human activities (landfill, wastes and re-injected reservoirs) can be surveyed as well by this methodology, providing a reliable estimate of the bulk transfer of this gaseous component to the atmosphere.

8.2. Case study

The used dataset refers to a sampling survey performed on Nisyros Island (Greece), in the area of Stephanos and Kaminakia hydrothermal explosion craters (Brombach et al., 2001). It comprises 566 measurement points regularly distributed over an area of 0.35 km^2 following a 25 m × 25 m survey grid, which is made up of 29 × 22 cells. Data were acquired following the procedure of Chiodini et al. (1998), and span the range 0.26 - 6175 g m^{-2} d^{-1}. Descriptive statistics is given in Figure 8.1a.

The total CO_2 output from the study area was already calculated by Brombach et al. (2001) following the simple approach of Sinclair (1974). This represents a statistical evaluation of the CO_2 flux variable without considering spatial techniques. In synthesis, the statistical characteristics (mean and variance) and the relative proportions of each population constituting a multi-component population are obtained based on the inflection points of the cumulative curve in the log-normal probability plot. The CO_2 output relative to each population is computed by multiplying its mean CO_2 flux times the pertinent area, and the total CO_2 output is the sum of the contributions of each population. For the entire area, Brombach et al. (2001) obtained a total CO_2 output of 27.5 Mg d^{-1}, with a confidence interval (2σ) of 23.0-35.2 Mg d^{-1}.

8.3. Stochastic approach

Geostatistics, which has its roots in the concept of "regionalized variable" (Matheron, 1965), provides the fundamental tools to approach spatial problems. Any regionalized variable is basically the result of the linear combination of two terms, one related to regional variations and the other to local changes. Any dataset of direct measurements, e.g., the CO_2 flux from soil, is considered a set of outcomes of a random variable, RV, (or a random function, RF) which is generated by a probabilistic process.

Kriging, a linear and unbiased algorithm, is the most used tool to predict the value of a RV in a site where it is unknown. Kriging is an exact interpolator since it respects the dataset value if this is situated exactly on a computation node. Similar to the low-pass filters, Kriging underestimates the high values and overestimates the low values. It smooths the variability and truncates the local information related to high-frequency signals, depending on the local density of points: the smoothing is small near the datum but it increases moving away from it. Solving a Kriging matrix defines a variance that is relative only to the patterns of spatial data and uncorrelated to the variance of dataset.

Actually the term Kriging is used to define a wide series of algorithms. Common to all of them is the minimization of the variance of the error through the minimization of the residuals between true values and estimated values. Simple Kriging (SK) and Ordinary Kriging (OK) are the two types of Kriging most frequently implemented in software packages (Deutsch and Journel, 1992). In SK the mean is assumed to be constant throughout the study area. The OK is more flexible, robust, and less computational demanding and could be considered a SK with a "local" constant mean.

Most geochemical variables, including the flux of CO_2 from soil, approximate a log-normal distribution. Therefore, it is common practice to operate on the logarithm of the variable, for a correct use of a linear operator as the Kriging is. Alternatively, to avoid bias due to the non-gaussianity of the original distribution of a given variable, its transformation to the normal space can be performed by calculating the so called "normal scores". This procedure corresponds to the conversion of the percentiles of a distribution in the percentiles of a gaussian distribution. A backtransforming is then done at the end of the computation.

A crucial point in the computation of a result based on a partial set of data is the quantification of the uncertainty. In particular, a source of great uncertainty is the extrapolation of a point-like determination (i.e., related to a very small area) to an area much larger than that directly investigated. This operation is usually called "change of support". The dataset of Stephanos - Kaminakia (Brombach et al., 2001) is based on CO_2 flux measurements whose 'support' (the base of the accumulation chamber) is ~300 cm^2, whereas the grid surveyed in the field and used afterwards in mapping and related computations is made up of cells of 25 × 25 m^2, i.e., ~21,000 times larger. Straightforward application of Kriging to measurements with this type of aggregation leads to estimates with the same aggregation state, again areas of 300 cm^2. Several procedures can be used to compute CO_2 flux values related to a 'support' which is different from that of sampling, including the affine correction, the direct

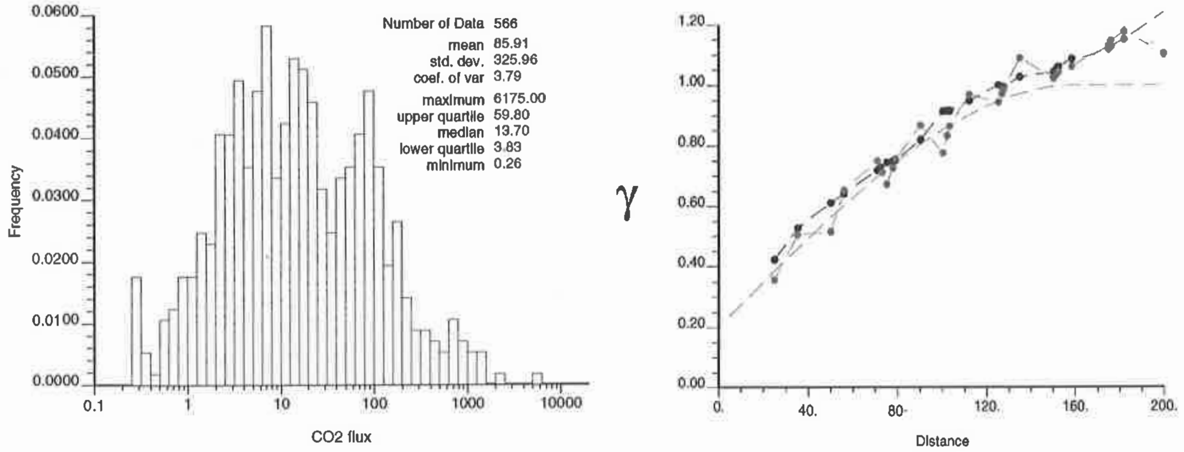

Figure 8.1. (a, left) *Descriptive statistics (in log space) of the CO_2 fluxes (g m^{-2} d^{-1}) from soil in the Stephanos - Kaminakia area (modified from Brombach et al., 2001).* ***(b, right)*** *experimental and model variograms of the dataset.*

log-normal correction, and the indirect log-normal correction (Isaaks and Srivastava, 1989). An alternative approach, usually leading to similar results, is Block Kriging (BK), which basically consists in averaging the results of the Kriging matrix solution for discrete areas.

Kriging-like algorithms define a list or a mosaic of discrete values which can be used for mapping. A unique solution, i.e., a unique map is thus produced.

A more complete approach to the investigation of the regional variability of a continue variable with normal distribution is taken by means of the so-called 'sequential Gaussian simulation' (sGs). In this technique, the regional variability of the variable of interest is assumed to be conditioned by both the original data and the simulated data. The peculiarity of sGs is the computation not only of one realization, as in the Kriging procedures considered so far, but of l high-resolution, alternative realizations (l is chosen by the user), each one with the same probability of the other ones. In other words, sGs leads to the generation of l equiprobable maps. The variability of the statistical parameters of each realization is mainly due to the random path followed in the estimation of grid nodes, which is based on the Monte Carlo procedure. In each realization, the visit path of the computational nodes is modified and, consequently, is also modified the set of original and simulated data. These made up the set of conditioning data used for the computation of an unknown value by means of the Kriging algorithm. The higher is the similarity between realizations (ergodic condition) the lower is the number of realizations to be computed. The expected mean of the l equiprobable realizations respect both data statistics (mean and variance) and the spatial model representing the original data. Therefore, they can be used as extrapolators, with some care, outside the minimal polygon encompassing the original data.

8.4. Discussion

Returning to the Stephanos - Kaminakia example, analytical data have not been declustered, because they were sampled along a regular grid. However, each cell has been subdivided in 4 sub-cells with side of 12.5 m. This means that the smallest considered area is of 12.5 × 12.5 m^2. For comparison purposes, we have started our investigation by using one of the simplest interpolation algorithms, the Inverse Distance Weighted (IDW) with 2 as exponent of the inverse distance. The obtained map (Figure 8.2a) clearly shows zones of maximum flux inside the Stephanos crater, with a low-flux ring around it. This "bull-eyes" of low values might be an artifact due, at least in part, to IDW, which frequently generates circular and often symmetrical structures of decreasing values around local maxima. The total CO_2 output computed through IDW is 35.7 Mg d^{-1}.

The two probabilistic methods here presented (BK and sGs) share the spatial analysis of data. To this purpose, experimental, normalized variograms have been calculated for the two orthogonal directions N-S and E-W (Figure 8.1b). The spatial distribution of CO_2 flux appears to be isotropic, as it exhibits the same spatial continuity along any direction. Therefore, the omni-directional variogram model can be used. This has a 'nugget' of 0.2, indicating that the small-scale variability is 20% of the total (consequently, the regional variability is 0.8), and a range close to 160 m. In carrying out

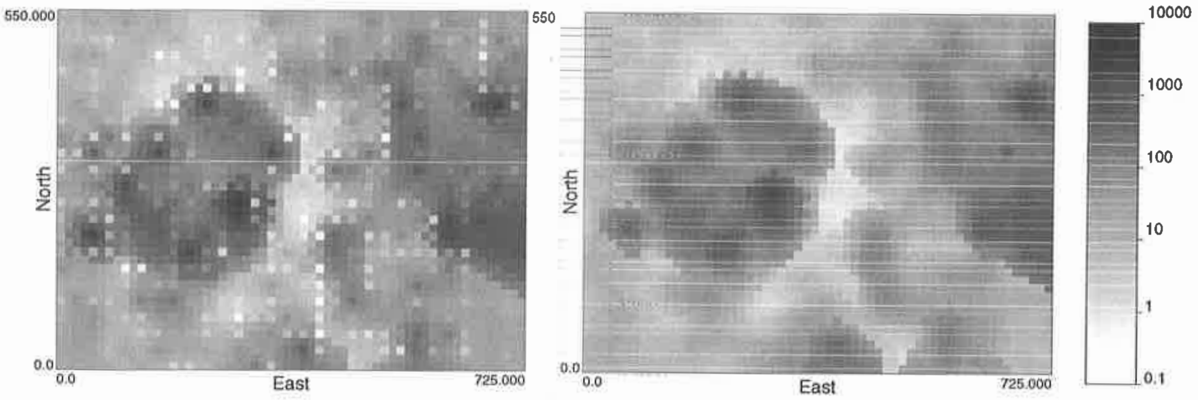

Figure 8.2. *Distribution maps of the CO_2 flux from soil (g d^{-1} m^{-2}) in the Stephanos - Kaminakia area generated through **(a, left)** IDW and **(b, right)** BK.*

these exercises, it is advisable to use simple, easy-to-interpret variogram models, rather than complex variogram models, which overfit the experimental variogram and can bring about both difficulties in the interpretation and mathematical instability.

The CO_2 flux computation by BK is done by further discretization of the cells of 12.5 × 12.5 m^2 in 64 sub-cells and by computing the intra-block mean of these 64 points. The obtained value is referred to the center of the cell, but it represents the average value of the cell and not the value related to that particular point. The map of CO_2 fluxes based on BK shows the typical smoothing of Kriging (Figure 8.2b). In this case, however, smoothing is partly due to the averaging procedure carried out within each cell. The total CO_2 output computed by BK is 34.1 Mg d^{-1}.

In sGs the total output of CO_2 is based on 50 equiprobable realizations. The calculation grid is the same as in BK and results have been re-computed on the initial 'support' to made them comparable with those of the other procedures. The sGs gives total CO_2 outputs ranging between a minimum value of 25.4 Mg d^{-1} (lowest cost realization, #28) and a maximum value of 46.2 Mg d^{-1} (highest cost realization, #13, Figure 8.3a). The mean value of the total CO_2 output, obtained for the E-estimate, i.e., through linear averaging of all the realizations, is 32.8 Mg d^{-1}. The correspondent distribution map of the CO_2 flux from soil is given in Figure 8.3b. Remarkable oscillations are present between the first and the last realizations. The statistical parameters of the realizations are not numerically equal, but equiprobable. The frequency distribution of the total CO_2 output (Mg d^{-1}) obtained for 50 equiprobable realizations is given in (Figure 8.4a). The data generated by sGs can be used to evaluate and visualize the uncertainty, since 50 realizations are now available for each point (block) and it is possible to compute its variability. Figure 8.4b shows the cumulative distribution function of the CO_2 flux for a randomly chosen block and the pertinent statistic moments defining how the CO_2 flux from that block varies during the simulations.

8.5. Conclusions

The value of a variable in a given point of the investigated surface area can be computed by means of different approaches. The choice of the most suitable procedure is usually dictated by the characteristics of the variable as well as by data availability and spatial distribution.

IDW is totally driven by the algorithm, irrespective of data features. This method is particularly sensitive to the extreme values, thus an erratic datum can lead to either overestimate or underestimate the computed value, mainly depending on the distance of the nearby point data. In the case of the Stephanos- Kaminakia example, the total CO_2 output and mean CO_2 flux computed by IDW are indeed maximum values and their uncertainty is unknown (Table 8.1).

BK computes the average value for a discrete area (change of support). Local variability is eliminated but, thanks to OK, the errors are minimized. Therefore, a control on the result is possible. This procedure produces only one realization. BK decreases the variance without changing the total mean, which does not depend on the size of the 'support'.

The sGs are totally based on the available data and on their spatial distribution. All the significant features of the RV of interest are captured and converted into models by means of sGs. The flexibility of the sGs tools allows one to visualize the uncertainty (both local and regional), to

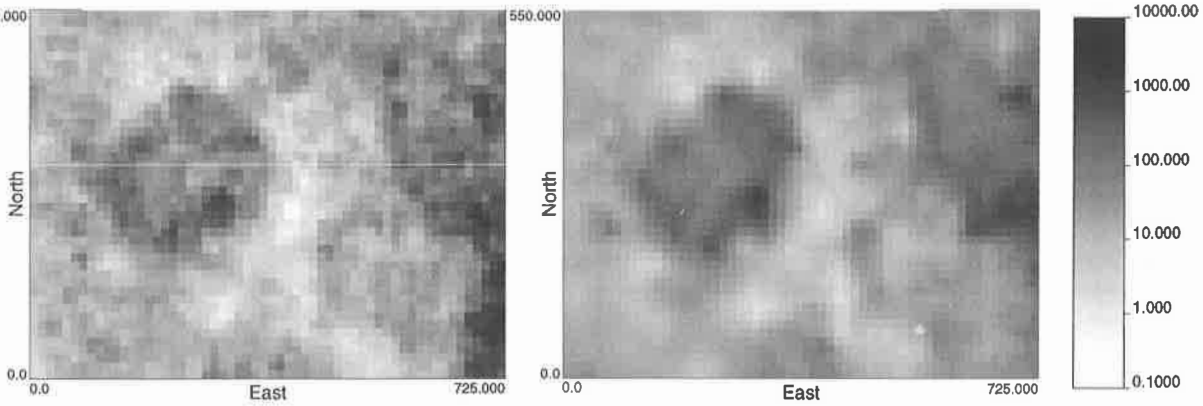

*Figure 8.3. Distribution maps of the CO_2 flux from soil (g d^{-1} m^{-2}) in the Stephanos - Kaminakia area obtained through sGs (**a, left**) realization #13; (**b, right**) mean distribution based on 50 realizations.*

investigate spatial anisotropy, thus helping to infer the possible relations between the distribution of the considered RV and the controlling physical processes. Although the average value of the total CO_2 output obtained for the Stephanos - Kaminakia example (area 0.35 km^2) by sGs (32.3 Mg d^{-1}) is similar to the estimate of the rather crude Sinclair's method, 27.5 Mg d^{-1} (Brombach et al., 2001), much more insights into this matter have been acquired through application of the sGs procedure. This is especially important for the mitigation of the risk of hydrothermal explosions and volcanic eruption, which is the ultimate purpose of geochemical surveillance of Nisyros island.

In addition to volcanic and geothermal areas, CO_2 sink-sources related to human activities (landfills, geological reservoirs for CO_2 confinement and sequestration) can also be surveyed by means of the accumulation chamber method. In all these applications, a correct evaluation of the amount of CO_2 transferred to the atmosphere through the soil is needed and related uncertainties have also to be carefully estimated. Sequential Gaussian simulations is the best methodology fulfilling these expectations.

Recently, Cardellini et al. (2003) and Caliro et al. (2005) acquired further data on the diffuse CO_2 flux from soil over the whole hydrothermal craters' area of Nisyros and elaborated maps of CO_2 fluxes from soil using a sGs algorithm. In particular, Cardellini et al. (2003) wrote that in their work "*Conditional sequential Gaussian simulations (sGs) have been applied for the first time to the study of soil diffuse degassing from different volcanic and nonvolcanic systems.*" This is incorrect, as the sGs algorithm was used earlier by Vetuschi Zuccolini (2002), whose contribution was completely ignored by Cardellini et al. (2003), although they (at least the senior author G.C.) knew it very well. Leaving this question out of consideration, we must admit that the two contributions by Cardellini et al. (2003) and Caliro et al. (2005) greatly improved the knowledge of diffuse degassing and related processes from the hydrothermal craters' area of Nisyros, as summarised in Table 8.2.

Table 8.1. Total CO_2 output and mean CO_2 flux computed for the Stephanos – Kaminakia example by means of different procedures from Brombach et al. (2001) and this work.

Method	Total CO_2 output (Mg d^{-1})	Mean CO_2 flux (g d^{-1} m^{-2})
Sinclair	27.5	85.9
IDW	35.7	89.6
BK	34.1	85.5
SGs mean	32.3	81.1
SGs max	46.2	116.0
Sgs min	25.4	63.7

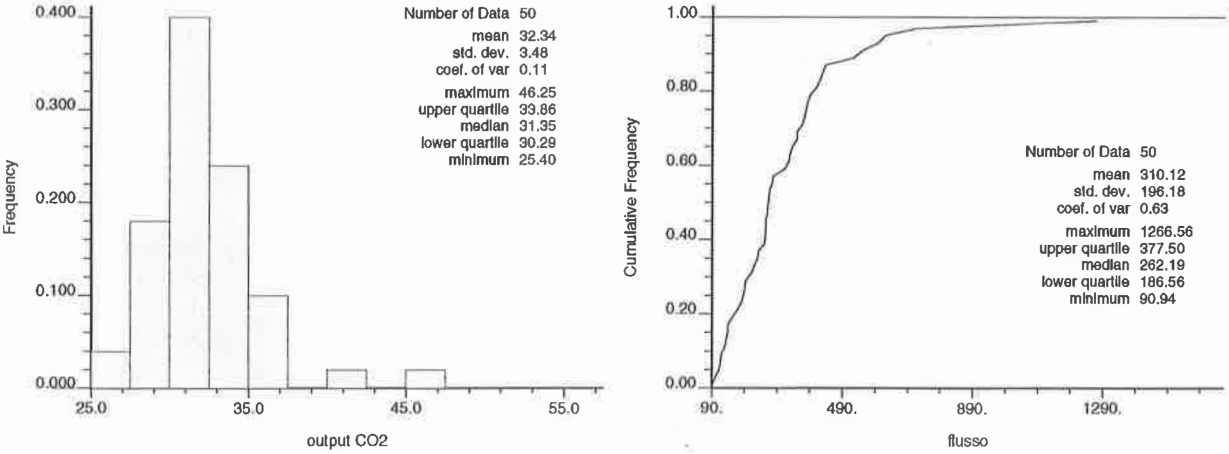

Figure 8.4. (a, left) *Histogram of the total CO_2 output (Mg d^{-1}) from the Stephanos - Kaminakia area computed for the 50 realizations;* ***(b, right)*** *Cumulative distribution function of the CO_2 flux for a randomly chosen block and pertinent statistical moments.*

Table 8.2. Total- and hydrothermal-CO_2- output, total flux of condensed steam, and related release of thermal energy from the whole hydrothermal craters' area and different sectors of it (from Caliro et al., 2005, modified). These figures were obtained following the approach of Brombach et al. (2001).

Zone	Area (km2)	Total CO_2 output (t/d)	Hydrothermal CO_2 output (t/d)	H_2O/CO_2 wt. ratio of fumarolic fluids (a)	Total flux of condensed steam (t/d)	Thermal energy release (MW)
Lofos dome	0.4	26.4	23.2	29.4	681	20.4
Stephanos	0.08	11.8	11.2	36	403	12.1
Kaminakia	0.28	28.2	25.9	6.1	158	4.7
Other areas	1.34	18.2	7.5	*23.8* (b)	178	5.3
Whole area	2.1	84.6	67.8	-	1420	42.5

(a) Note that this is the H_2O/CO_2 weight ratio and not the CO_2/H_2O ratio as erroneously indicated by Caliro et al. (2005)

(b) Average value of all the fumaroles of the hydrothermal craters' area.

9. Fluid geochemistry of the magmatic-hydrothermal system of Nisyros (Greece)

Luigi Marini(1), **Jens Fiebig**(2)

(1) Laboratorio di Geochimica, Dip.Te.Ris., Università di Genova, Corso Europa 26, I-16132 Genova, Italy

(2) Geologisch-Paläontologisches Institut, Goethe Universität, Senckenberganlage 32, D-60325 Frankfurt am Main, Germany

Abstract - All the available geochemical data on deep geothermal wells, fumaroles, thermal springs, and cold waters of Nisyros Island have been compiled and reviewed for the period 1990-2002. This holistic approach has prompted the need for new interpretations, including the contribution of radiogenic Ar to the deep hydrothermal aqueous solution, the extrapolation of CO-H_2 equilibrium temperatures by using restored $\log(X_{H_2}/X_{H_2O})$ and $\log(X_{CO}/X_{CO_2})$ ratios, the kinetics of CO re-equilibration, the occurrence of Rayleigh steam condensation, the temperature of saturation with anhydrite for thermal waters. Fumarolic gases emitted at the surface of the Lakki Plain are mainly fed by an aquifer occurring at 1-2 km depth with temperatures of 320-360°C. Under the central parts of the area of the hydrothermal craters, the liquid phase hosted in the deep aquifer is a mixture of 75% andesitic-magmatic water with 25% seawater. The contribution of seawater increases moving towards peripheral locations, such as Kaminakia and Phlegeton. Physicochemical conditions of the deep aquifer are best reflected by the CH_4-CO_2 redox pair. In contrast, the CO-CO_2 system is able to re-equilibrate at lower temperatures and bears physicochemical information on the ascent of the liquids from the deep aquifer to the vapor separation zone. The depth at which vapor separation occurs varies in space and, possibly, in time. The presence of a very hot aquifer at 1-2 km depth only, ongoing seismic activity, and concurrent movements of the vapor separation zone towards the deep aquifer are all indicators that hydrothermal explosion activity on Nisyros island might resume.

9.1. Introduction

The geochemistry of fluids related to the magmatic-hydrothermal system of Nisyros has been the subject of several investigations in the last fifteen years (Chiodini et al., 1993a; Minissale et al., 1997; Dietrich et al., 1998; Kavouridis et al., 1999; Brombach, 2000; Panichi et al., 2000; Brombach et al., 2001; Panichi and La Ruffa, 2001; Chiodini et al., 2002; Marini et al., 2002; Cardellini et al., 2003; Brombach et al., 2003; Fiebig et al., 2004; Shimizu et al., 2005; Caliro et al., 2005). Most of these studies were carried out during and after the increase in activity that took place in 1995-1998 comprising intense seismicity and ground deformations, as well as changes in the chemistry of fumarolic effluents (Chiodini et al., 2002; Shimizu et al., 2005; Caliro et al., 2005).

In spite of the considerable efforts aimed at understanding the magmatic-hydrothermal system of Nisyros, the geochemical data acquired so far (Tables 9.1, 9.2, and 9.3) were often interpreted without taking into account those collected by other authors and a thorough review and synthesis of the existing information is still lacking. The main aim of this paper is to fill this gap and to provide an updated conceptual model of the magmatic-hydrothermal system of Nisyros.

9.2. Subsurface information

Present knowledge of the Nisyros subsurface is based almost entirely on data acquired by the two geothermal wells Nisyros-1 and Nisyros-2, which were drilled in the southern part of the Lakki plain (Figure 9.1) to total depths of 1816 m and 1547 m, respectively, by the Greek Energy Authority, PPC, in the '80s (Geotermica Italiana, 1983, 1984; Marinelli et al., 1983; Koutroupis, 1983; Vrouzi, 1985; Orkustofnun-Virkir, 1986).

Well Nisyros-1 passed into the carbonate sedimentary rocks underlying the volcanic sequence, whereas well Nisyros-2 passed into a thicker volcanic sequence and did not meet the carbonate rocks (Figure 9.2). This suggests that the caldera collapse was larger in the central sector than in the peripheral sectors of the caldera. The deepest sections of both geothermal wells penetrated quartz-dioritic subintrusive rocks and thermo-metamorphic rocks.

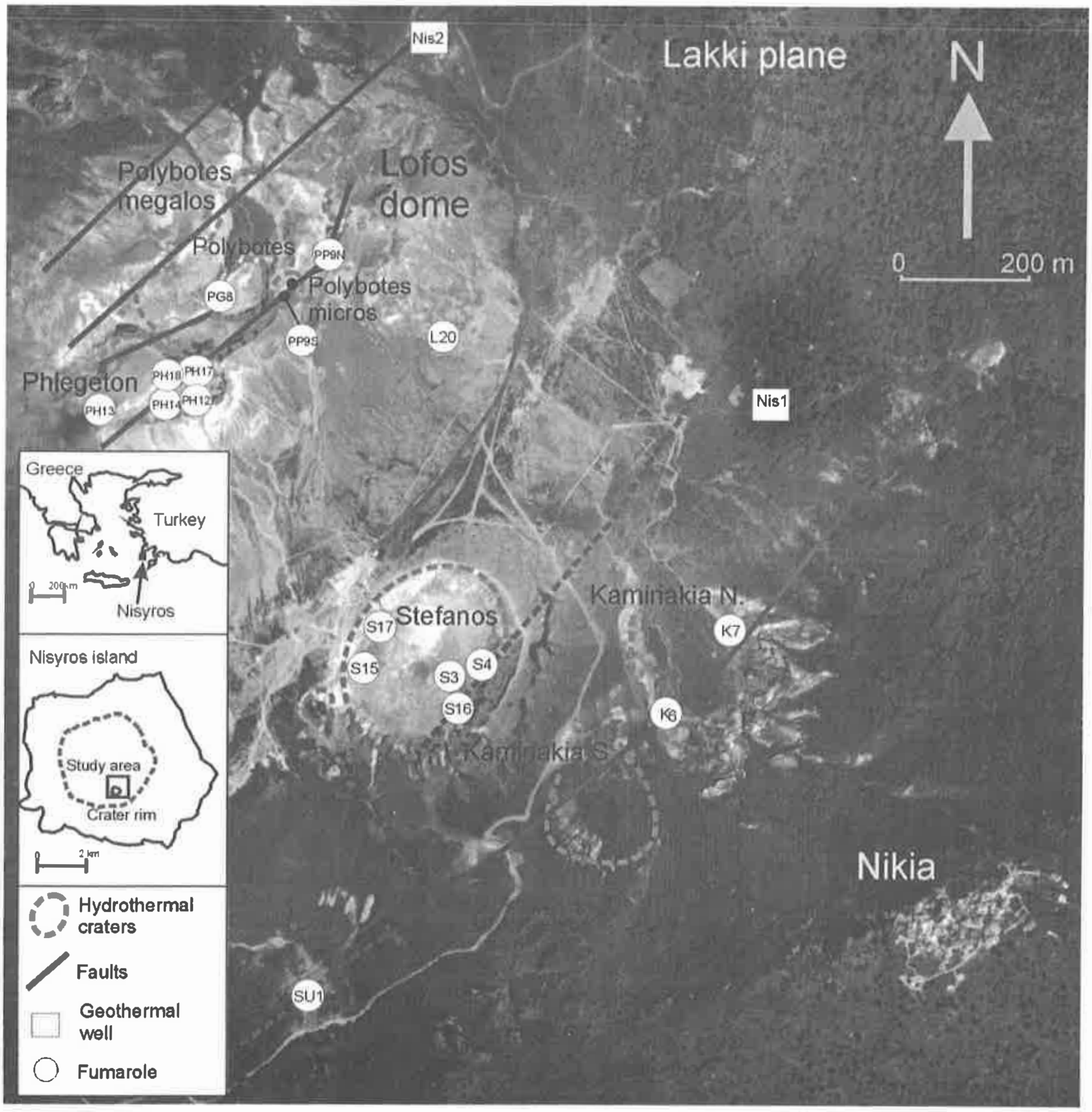

Figure 9.1. Location map of hydrothermal craters, fumaroles, and the deep geothermal wells Nisyros-1 and Nisyros-2 (from Chiodini et al., 2002, modified).

Both wells crossed a shallow permeable zone and a deep permeable zone. The shallow permeable zone occurs from 400 to 700 m depth in well Nisyros-1 and from 250 to 350 m depth in well Nisyros-2. The most abundant hydrothermal minerals of this zone are chlorite in well Nisyros-1 and sericite in well Nisyros-2. Less frequent quartz, zeolites, pyrite, anhydrite, and carbonates were also identified. These hydrothermal minerals are typical of the phyllitic-zeolitic paragenesis, which develops at temperatures of 120-180°C.The deep permeable zone extends from 1400 m to well-bottom in Nisyros-1 and from 1000 to 1350 m in Nisyros-2. Propylitic hydrothermal minerals, formed at temperatures > 250°C, are present in this zone. Typical minerals, such as epidote, adularia, and albite, are associated with quartz, pyrite, anhydrite, stilpnomelane, wairakite, garnet, tremolite, and pyroxene. Some hydrothermal minerals (scapolite, pyrrhotite, and arsenopyrite) were recognised in well Nisyros-1 only, whereas chlorite and sericite-muscovite occur in well Nisyros-2 only. Approaching the well-bottom in Nisyros-1,

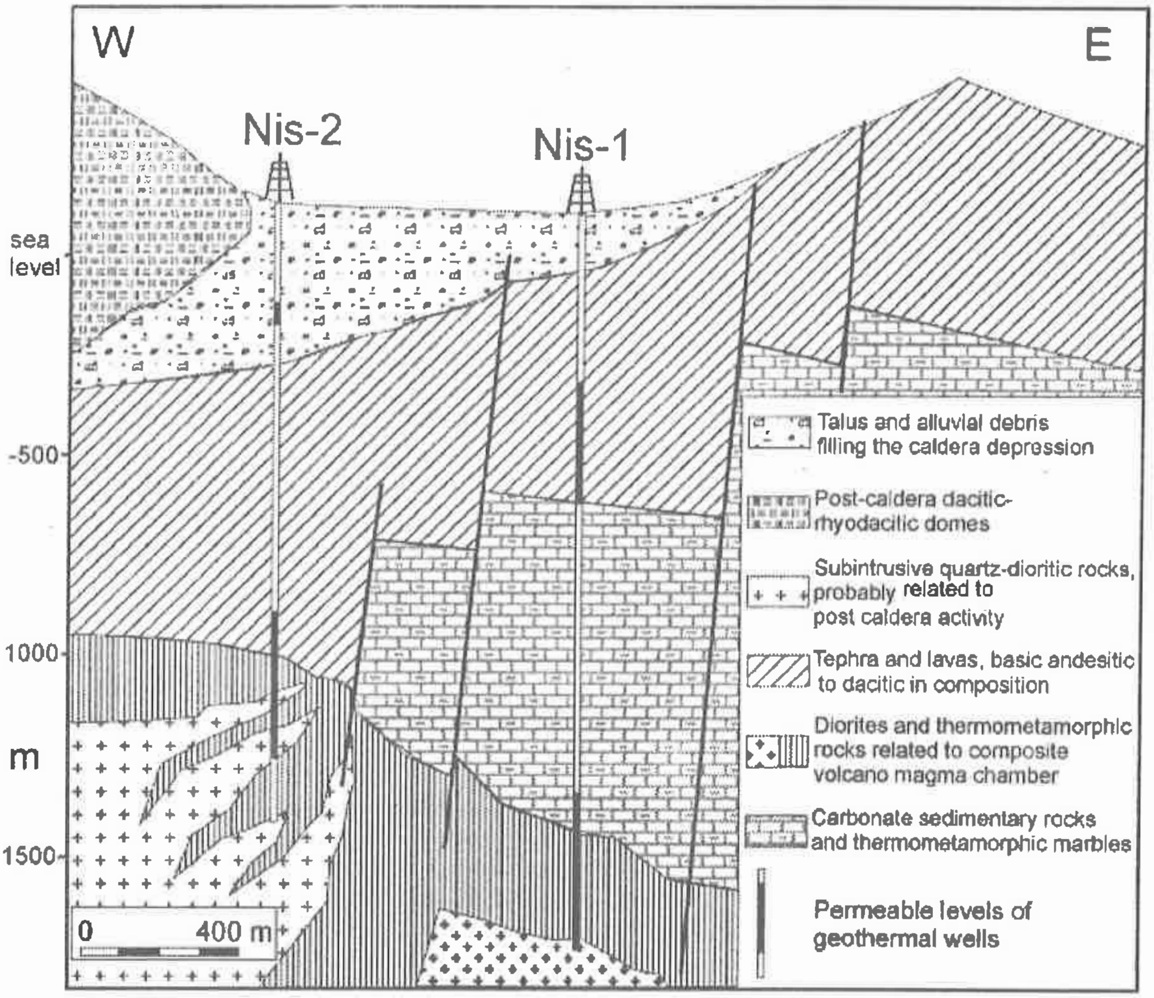

Figure 9.2. *Geological cross-section through the two deep geothermal wells Nisyros-1 and Nisyros-2 (from Geotermica Italiana, 1984).*

appearance of biotite and disappearance of epidote and tremolite suggests temperatures >350°C.

The maximum measured temperatures, close to well-bottom, are about 340°C in well Nisyros-1 and near 320°C in well Nisyros-2.

Only short-term production tests were carried out for well Nisyros-1 and acquisition of reliable data was complicated by precipitation of Na-Ca-K chlorides. In addition, brines separated at atmospheric pressure had high Mg^{2+} and SO_4^{2-} concentrations and low dissolved SiO_2 concentrations indicating that they were still mixed with seawater, which was used to make up the drilling mud. Total discharge enthalpy, 2340 - 2360 J/g approximately, is significantly higher than the enthalpy of liquid water at reservoir temperature (330-335°C), 1525 - 1559 J/g. This suggests occurrence of steam separation in the reservoir and preferential entrainment of steam in the two-phase mixture tapped by the well.

In contrast, well Nisyros-2 was the subject of both short- and long-term production tests and, consequently, the physical and chemical characteristics of the reservoir fluid tapped by this well are known with enough accuracy. Total discharge enthalpy, 1375 ± 25 J/g, is slightly higher than the enthalpy of liquid water at reservoir temperature (290°C), 1289 J/g. It seems likely that a single liquid phase is present in the reservoir, under static conditions, but it becomes a two-phase system with a small excess enthalpy (86 J/g) under dynamic conditions.

9.3. The surface manifestations of hydrothermal activity

The fumarolic field of the southern sector of the Lakki plain and the thermal springs situated along the northern and southern coasts of Nisyros represent the surface manifestations of deep hydrothermal activity.

A large fumarolic field is located in the southern part of the Lakki plain, between the small dome of Lofos and the foot of the southeastern caldera escarpment (Figure 9.3). This area is affected by fracturing along the main NE-trending tectonic system and, in historical times, was devastated by several hydrothermal eruptions, the last of which took place in 1871-1873 and 1888. A detailed description of these events was given by the French scientist M. H. Gorceix and the Italian geologist A. Martelli (see Marini et al., 1993 and references therein). Many hydrothermal craters, such as those of Stephanos, Polybotes Micros, Polybotes Megalos, Phlegethon, and Kaminakia are still well preserved and host the most important fumarolic vents. All these vents have outlet temperature close to 100°C. Before 1990, steam was also discharged from a shallow borehole situated about 150 m west of Nisyros-1 (sample 1 of Chiodini et al., 1993a), but it does not exist anymore. The area of the hydrothermal craters is also characterized by high CO_2 fluxes from soil and elevated soil temperatures (see below).

Owing to the morphology of the stratovolcano, the thermal springs are obviously found along the coasts, the only places where the water table intersects the topographic surface. Water circulation is also controlled, at least partly, by the active NE-trending tectonic system. The hottest thermal springs are situated at Avlaki (58-50°C), Pali Spa (49-33.5°C), Levkos (48-46°C), Loutra (47-33°C), Katsouni (44°C), and Aghia Irini (39°C). Thermal waters (35-40°C) were also found in two shallow wells drilled near Pali (Figure 9.3).

9.4. Previous investigations

The first conceptual geochemical model of the magmatic-hydrothermal system of Nisyros was proposed by Chiodini et al. (1993a) based on the subsurface geological, physical and chemical data acquired by the deep geothermal wells Nisyros-1 and Nisyros -2 and the chemical composition of both the nearby fumaroles and the thermal waters discharging along the coasts of the island. According to this conceptual geochemical model, two distinct hydrothermal aquifers are present below the Lakki plain: (i) a deep aquifer with temperatures of 290-340°C and (ii) a shallow aquifer with temperatures of 170-255°C. The geothermal vapors separated from the shallow aquifer feed the fumarolic vents of the southern Lakki plain, whereas the liquid phase flows towards the northern and southern coasts of the island, thus contributing to the thermal springs.

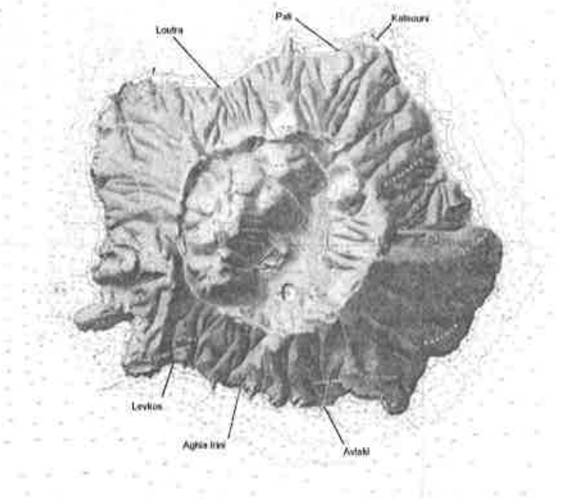

Figure 9.3. Location map of the thermal springs of Nisyros Island.

It must be underscored that no isotope data were available at that time. The D/H and $^{18}O/^{16}O$ isotope ratios of fumarolic steam condensates, thermal waters, and local groundwaters determined by Kavouridis et al. (1999), Panichi et al. (2000), Brombach (2000), Panichi and La Ruffa (2001), and Brombach et al. (2003) provided new insights into the magmatic-hydrothermal system of Nisyros, although they were interpreted in different ways (see below).

In addition to the isotope composition of water, other available isotope data include: (i) $^3He/^4He$ isotope ratio of fumarolic effluents (Dietrich et al., 1998; Fiebig et al., 2004; Shimizu et al., 2005); (ii) concentrations of noble gases and the $^{20}Ne/^{22}Ne$, $^{21}Ne/^{22}Ne$, $^{38}Ar/^{36}Ar$, and $^{40}Ar/^{36}Ar$ isotope ratios of fumarolic fluids (Shimizu et al., 2005); (iii) $\delta^{13}C$ values of fumarolic CO_2 (Kavouridis et al., 1999; Brombach, 2000; Panichi et al., 2000; Brombach et al., 2003; Fiebig et al., 2004); (iv) $\delta^{13}C$ values of fumarolic CH_4 (Kavouridis et al., 1999; Panichi et al., 2000; Fiebig et al., 2004); (v) $\delta^{34}S$ values of fumarolic H_2S, dissolved SO_4 in thermal waters, elemental sulfur deposited by fumarolic fluids, and gypsum crystals from hydrothermal debris flows and limnic deposits (Brombach, 2000; Marini et al., 2002; Brombach et al., 2003); (vi) δD values of fumarolic H_2 (Kavouridis et al., 1999; Panichi et al., 2000); (vii) tritium activity for two groundwaters, one thermal water, and local seawater (Kavouridis et al., 1999). All these data provide new insights (already discussed in the quoted papers and reconsidered below) that either fit in the existing conceptual model thus adding new details or call for amendments of the model itself. This check of the conceptual geochemical model is of utmost importance for volcanic surveillance.

Finally, several surveys of CO_2 fluxes from soil and soil temperatures were carried out in the area of the hydrothermal craters and adjacent parts of the Lakki plain (Brombach, 2000; Brombach et al., 2001; Cardellini et al., 2003; Caliro et al., 2005). It turned out that these high CO_2 fluxes from soil and elevated soil temperatures are the surface expression of a remarkable flux of ascending hot hydrothermal vapors. Steam mostly condenses close to the surface, while both CO_2 and heat are released to the atmosphere. In particular, Cardellini et al. (2003) and Caliro et al. (2005) elaborated maps of CO_2 fluxes from soil using a sequential Gaussian simulation algorithm. Further details on this matter are given in Vetuschi Zuccolini & Marini (this volume).

9.5. Origin of fumarolic gases

The origin of N_2, He, Ar, CO_2, CH_4, and H_2S is presented in this section, whereas the origin of fumarolic H_2O will be discussed in a separate section (chapter 9.7), for reasons of clarity. Since fumarolic H_2O is prone to significant isotopic fractionations in two-phase hydrothermal systems, the temperatures at which vapor separation occurs (have to be identified first, if isotopic data are used to trace the origin of H_2O. Knowledge of both separation temperature and initial temperature enables the computation of the fractions of separated vapor and liquid phases, adopting an isoenthalpic model.

Before discussing the chemical and isotopic characteristics of fumarolic gases to infer their origin, it must be recalled that the average outlet temperature is 99.7 ± 0.9 (1σ) °C at all sites apart from the Kaminakia craters, where an average outlet temperatures of 98.0 ± 0.9 °C was recorded.

Considering that the dependence of the average atmospheric pressure, P_{atm} (bar) on the elevation (E in m) is described by the following linear equation:

$$P_{atm} = 1.013 - 0.000111 \times E, \qquad (1)$$

(which applies at least in the first 2 km above the Earth surface) and that the fumarolic field is situated at ~100 m above sea level, the local average atmospheric pressure is expected to be 1002 mbar. At this pressure, the vapor-liquid equilibrium temperature for pure water is 99.662°C (Lemmon et al., 2003). Although steam condensation is possible at all sites, it appears to be more likely at Kaminakia craters, where the concentration of H_2O in fumarolic gases, 934 ± 27 (1σ) mmol/mol is significantly lower than at other sites, 983 ± 6 mmol/mol.

9.5.1. Origin of N_2

The N_2-Ar-He triangular plot (Figure 9.4) was proposed by Werner F. Giggenbach, one of the most brilliant geochemists who ever studied magmatic and hydrothermal systems, (e.g., Giggenbach, 1996 and references therein) as an effective tool to discriminate the N_2-rich gases typically discharged along convergent plate boundaries from the He-rich gases of crustal origin or mantle provenance, including mid-ocean ridges and oceanic islands locations. Also shown in this plot are the points representative of atmospheric air and air-saturated groundwater (ASW), both characterised by low relative contents of He.

Quite surprisingly, the fumarolic effluents of Nisyros plot along the lines joining the He-rich compositions typical of mantle and crustal gases and the two He-poor atmospheric endmembers, as already noticed by Kavouridis et al. (1999) and Brombach et al. (2003). Interestingly, also the gases from other locations along the Aegean Island arc, such as Milos (Giggenbach, 1997) and Kos (La Ruffa et al., 1999), not shown in Figure 9.4, have comparatively low N_2/He and N_2/Ar ratios and plot along the same mixing lines (see Figure 2 in Brombach, 2003). These peculiar characteristics of the gases from the Aegean Island arc can be attributed to both lack of N-rich sedimentary materials in the subducted slab and occurrence of N-poor rocks above the mantle wedge, including the rocks hosting the hydrothermal system. Consequently, N_2 contained in fumarolic gases appears to be totally (or almost so) of atmospheric origin. An independent proof of this hypothesis could be given by isotopic analysis of gaseous N_2 which, unfortunately, has never been performed on Nisyros discharges.

9.5.2. Origin of He

The provenance of He cannot be resolved by means of the N_2-Ar-He triangular plot, but must rely on the isotopic composition of He. The $^3He/^4He$ ratio in fumarolic effluents was measured by Dietrich et al. (1998), Fiebig et al. (2004), and Shimizu et al. (2005). The measured ratio, R, is usually divided by the He isotope ratio in the atmosphere (Ra = 1.39×10^{-6}, Ozima and Podosek, 2002) thus obtaining the

R/Ra value. This is costumarily corrected for air contamination based on the measured He/Ne ratio, as suggested by Sano and Wakita (1985).

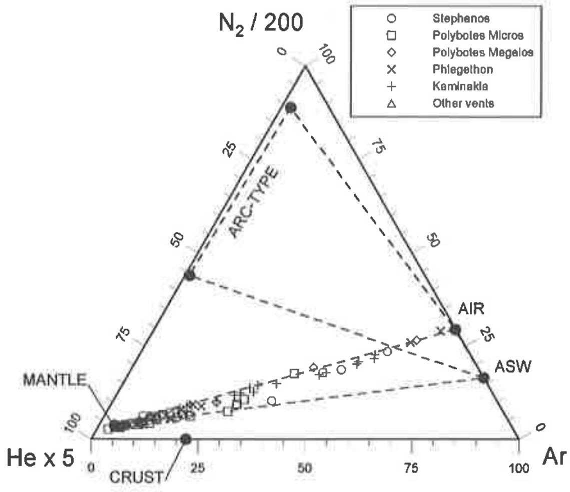

Figure 9.4. Triangular diagram N_2-Ar-He, also showing the endmember compositions of crustal, mantle, and arc-type gases (after Giggenbach, 1996, modified).

Before dealing with the interpretation of these data, it must be underscored that if the He/Ne ratios are relatively low, corrected He isotope ratios are significantly higher than the uncorrected counterparts. For instance, three of the four samples analysed by Dietrich et al. (1998), have low He/Ne ratios, from 3.2 to 4.2, and differences between corrected and uncorrected R/Ra values from 0.4 to 0.5; the other sample, coming from one of the Kaminakia craters, has a very low He/Ne ratio, 0.87, and an uncorrected value of 4.28 Ra, which is the lowest measured value at Nisyros, whereas the corresponding corrected value is 6.19 Ra, which represents one of the highest data. It is clear that all the data by Dietrich et al. (1998) are affected by strong uncertainties.

Uncorrected He isotope ratios and He/Ne ratios were not reported by Fiebig et al. (2004) and, therefore, it is impossible to evaluate the quality of their data. In contrast, He/Ne ratios are generally in the range 250 to 1000 for the samples of Shimizu et al. (2005), thus making the correction for air contamination virtually unnecessary. Only for one sample, with He/Ne ratio of 11, the corrected ratio, 6.11 Ra, deviates significantly from the uncorrected value, 5.96 Ra.

As already noticed by previous authors, Nisyros gases have the highest ^{3}He/^{4}He ratios of the Aegean island arc, which was attributed to the inherent characteristics of the subcontinental lithospheric mantle beneath the Aegean arc (Shimizu et al., 2005). Since the He isotope ratio can be affected by several processes along the migration of gases from the subducted slab to the Earth surface, the reliability of these inferences is uncertain.

In contrast, it is very important, in our opinion, to underscore the time changes in the He isotope ratio of fumarolic effluents from 1993 to 2002 (Figure 9.5a), that is before and after the seismic crisis which affected the island of Nisyros from the end of 1995 to 1998, with the largest episode, $M_S = 5.3$, on August 1997 (Papadopoulos et al., 1998; Stavrakakis and Papoulia, 1998).

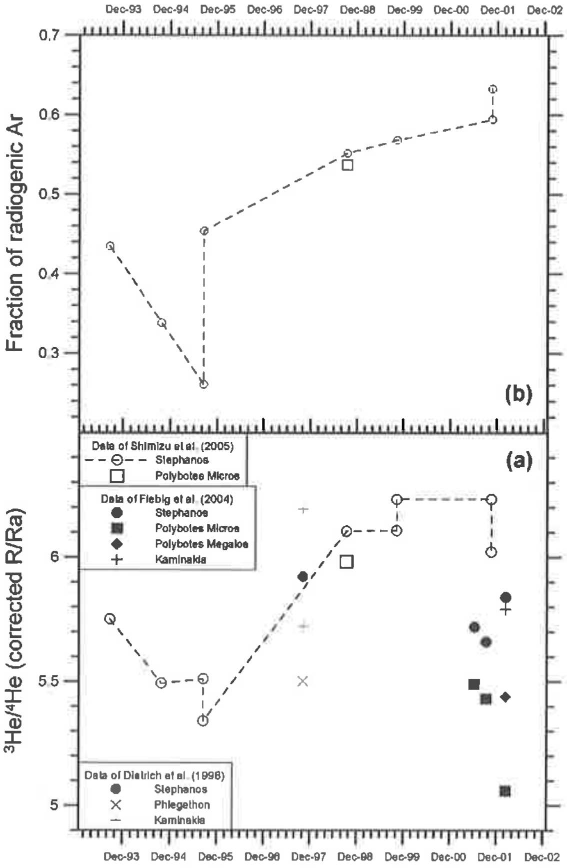

Figure 9.5. Time changes of (a) the ^{3}He/^{4}He ratio, expressed as R/Ra value corrected for air contamination according to Giggenbach et al. (1993), and (b) the fraction of radiogenic argon.

Indeed, the samples of Shimizu et al. (2005), all of which except one were collected from the fumaroles of Stephanos crater, record a significant change in the ^{3}He/^{4}He ratio, from values ≤ 5.7 Ra in 1993-1995 to values > 6.0 Ra in 1998-2001. The sample collected by these authors from "Polybotes crater" (most likely Polybotes Micros) in September 1998 has a ^{3}He/^{4}He ratio in substantial agreement with that of the corresponding sample from Stephanos crater. In contrast, the gas samples of Dietrich et al. (1998) and Fiebig et al. (2004), especially those collected in February 2002, show considerable changes from vent to vent. For the samples of Dietrich et al. (1998), these differences can be due to analytical uncertainties because of the strong air contamination, whereas nothing can be said for the samples of Fiebig et al. (2004), owing to the lack of uncorrected He isotope ratios and He/Ne ratios. All in all, it is a pity that the interesting time changes observed by Shimizu et al. (2005) cannot be confirmed by means of data of other workers. According to Shimizu et al. (2005), these time changes in He isotopes suggest that the seismic crisis was caused by the upward movement of magma, which triggered an increased contribution of mantle He. Alternatively, the greater contribution of deep (mantle) He can be caused by the opening of new deep-reaching fractures, as a consequence of the seismic crisis, similar to what was observed at Vulcano island after the 1978 earthquakes (e.g., Chiodini et al., 1992a).

9.5.3. Origin of Ar

Among the noble gas concentrations and isotope ratios reported by Shimizu et al. (2005), the isotopic ratio of Ar and the concentration of ^{40}Ar are of special interest, because Ar is the partner of H_2 in the H_2-Ar geothermometer, which was proposed by Giggenbach (1991, see below). This geothermometric technique is based on the hypothesis that the Ar concentration of the hydrothermal fluids is equal to that of the air-saturated groundwater feeding the system. The N_2-Ar-He triangular plot supports this assumption, but this evidence is not conclusive. The availability of data on the isotopic ratios of Ar and the concentration of ^{40}Ar allows a further, independent evaluation.

Argon has three stable isotopes with masses 36, 38, and 40, of which ^{36}Ar and ^{38}Ar are entirely of atmospheric origin, whereas ^{40}Ar is partly atmospheric and partly radiogenic, i.e., produced through radioactive decay of ^{40}K (Faure, 1986). The ^{40}Ar/^{36}Ar and ^{38}Ar/^{36}Ar ratios of atmospheric air are 295.5 and 0.1880, respectively (Ozima and Podosek, 2002). The ^{40}Ar/^{36}Ar ratio measured in some fumarolic gases from Nisyros (Shimizu et al., 2005) is somewhat higher than the atmospheric ratio, indicating addition of a non-atmospheric component of mantle or crustal origin.

The ^{36}Ar/^{40}Ar ratio of these gases (the inverse of the ratio mentioned above) can be used to calculate the fraction of air present in these gas mixtures by means of the general binary mixing equation (Langmuir et al., 1978; Faure, 1986):

$$\begin{aligned} R_M \cdot C_M &= R_A \cdot C_A \cdot f_A \\ &\quad + R_N \cdot C_N \cdot (1 - f_A), \end{aligned} \qquad (2)$$

where R identifies the isotope ratio of the considered element, C is its concentration, and f represents the fraction of component A in the binary mixture. Equation (2) is based on the assumption that fumarolic gases are binary mixtures (subscript M) of a non-atmospheric (radiogenic) component (subscript N) and an atmospheric component (subscript A). Assuming that ^{36}Ar is present only in the atmospheric component (i.e., setting $[^{36}\mathrm{Ar}/^{40}\mathrm{Ar}]_N = 0$), the term referring to the non-atmospheric component cancels from this equation and the fraction of air present in the mixture, f_A, can be readily computed. Then f_A can be inserted into the mass balance:

$$^{40}\mathrm{Ar}_M = {}^{40}\mathrm{Ar}_A \cdot f_A + {}^{40}\mathrm{Ar}_N \cdot (1 - f_A) \qquad (3)$$

to calculate the concentration of ^{40}Ar in the non-atmospheric component, $^{40}\mathrm{Ar}_N$. Computed values of $^{40}\mathrm{Ar}_N$ range between 0.5 and 1.3 ppm, apart from one sample highly contaminated with air. The corresponding fractions of radiogenic Ar, computed dividing $^{40}\mathrm{Ar}_N$ by $^{40}\mathrm{Ar}_M$, range between 0.001 and 0.055.

Alternatively, the contribution of non-atmospheric ^{40}Ar in fumarolic gases can be obtained by means of the relation:

$$^{40}\mathrm{Ar}_N = {}^{40}\mathrm{Ar}_M - \left(\frac{^{40}\mathrm{Ar}}{^{20}\mathrm{Ne}}\right)_A \cdot {}^{20}\mathrm{Ne}_M \qquad (4)$$

which is based on the same assumption used for correcting ^{3}He/^{4}He ratios, i.e., that ^{20}Ne is entirely of atmospheric origin; the atmospheric ratio $[^{40}\mathrm{Ar}/^{20}\mathrm{Ne}]_A$ is equal to 566.6 (Ozima and Podosek, 2002). Obtained values of $^{40}\mathrm{Ar}_N$ range between 6.8 and 43 ppm, again excluding the sample highly contaminated with atmospheric air. The corresponding fractions of radiogenic Ar range between 0.26 and 0.59.

We ended up with two different series of $^{40}\mathrm{Ar}_N$ concentrations, which are negatively correlated (r = -0.738). Interestingly, the fraction of non-atmospheric (radiogenic) Ar based on equation (4) are positively correlated with both the corrected and uncorrected ^{3}He/^{4}He ratios, with correlation coefficients of +0.81. In principle, the correlation with the corrected ^{3}He/^{4}He ratios could be biased by the correction procedures, since both involve ^{20}Ne, but this possible bias does not apply to the correlation between the fraction of non-atmospheric (radiogenic) Ar and the uncorrected ^{3}He/^{4}He ratios. In contrast, the fraction of non-atmospheric (radiogenic) Ar based on equations (2) and (3) bears no relation with the He isotope ratios. The assumption that ^{36}Ar is present only in the atmospheric component, which was introduced in equation (2), is probably false. The second series of $^{40}\mathrm{Ar}_N$ concentrations seems instead more reasonable.

The reliability of these possible contributions of radiogenic ^{40}Ar can be checked taking into account the decay of ^{40}K. Let us refer to 1 kg of water circulating into the hydrothermal reservoir, which is in contact with R kg of reservoir rocks, containing 4% K_2O (the average concentration of dacites reported by Reed, 1997), corresponding to 3.3% K. Considering that the natural abundance of ^{40}K is 0.012%, the amount of ^{40}K in R kg of reservoir rocks is:

$$\left(\frac{3.3}{100}\cdot \mathrm{R}\right)\cdot\frac{0.012}{100} = \mathrm{R}\cdot 4\cdot 10^{-6}\,\mathrm{kg} \qquad (5)$$

or R · 10^{-4} moles of ^{40}K. The moles of ^{40}Ar radiogenic produced through radioactive decay of this amount of ^{40}K are readily computed by means of the relation (Faure, 1986):

$$^{40}\mathrm{Ar}_N = \frac{\lambda_{EC}}{\lambda_{tot}}\cdot \mathrm{R}\cdot 10^{-4}\left[\exp(\lambda_{tot}\cdot t)-1\right] \qquad (6)$$

where λ_{EC} is the electron-capture decay constant (0.581×10^{-10} a^{-1}), λ_{tot} is the total ^{40}K decay constant (5.543×10^{-10} a^{-1}), and t is time in years (Faure, 1986). Upon boiling of the reservoir water, this ^{40}Ar enters almost entirely in the steam produced through boiling from the average CO-re-equilibration temperatures T_O, 239 and 287°C, to the average separation temperatures T_S, 234 and 271°C, for the fumarolic gases from Stephanos and Polybotes Micros craters, respectively (see below), that is in 13 – 51 g of steam or 0.73 – 2.8 moles ($n_{H_2O(g)}$). Therefore, the molar concentration of radiogenic Ar in fumarolic steam (in µmoles/moles) is:

$$^{40}\mathrm{Ar}_{N,\mathrm{steam}} = \frac{^{40}\mathrm{Ar}_N}{n_{H_2O(g)}}\cdot 10^6 . \qquad (7)$$

Results are presented in Figure 9.6, also showing the measured range of radiogenic Ar in fumarolic steam; measured data were reported in µmoles/moles of total fluid, based on the average total Ar concentrations of fumarolic effluents from Stephanos and Polybotes Micros craters, 0.3 µmoles/moles.

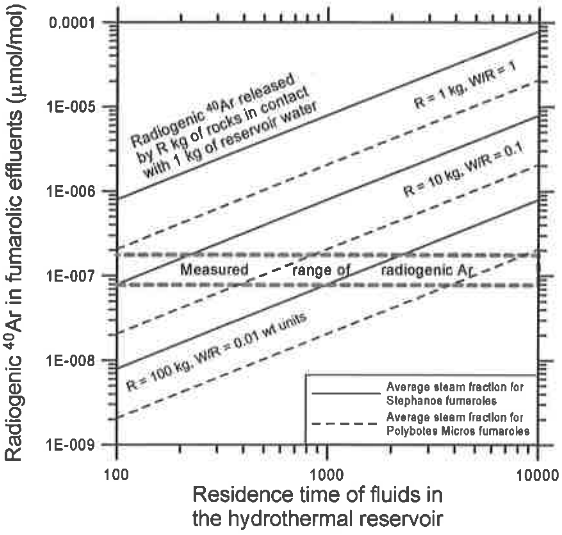

***Figure 9.6**. Computed ^{40}Ar concentrations in fumarolic steam based on different residence times of fluids in the hydrothermal reservoir and different water/rock ratios. The analytical range of ^{40}Ar concentrations in fumarolic effluents of Stephanos and Polybotes Micros is shown for comparison.*

R was taken equal to 1, 10, and 100 kg, corresponding to water/rock weight ratios of 1, 0.1, and 0.01, respectively, which are reasonable values for hydrothermal systems. Figure 9.6 shows that the data of Shimizu et al. (2005) are consistent with the expected supply of radiogenic Ar for reasonable values of water/rock ratios and residence time of fluids in the hydrothermal reservoir of Nisyros.

The fraction of radiogenic Ar computed by means of equation (4), therefore, can be considered reliable and its changes with time corroborate the temporal variations of ^{3}He/^{4}He ratios (Figure 9.5).

9.5.4. Origin of CO_2

The δ^{13}C value of carbon dioxide (Table 9.4) was analysed for the first time on 4 fumarolic gas samples collected in October 1991 from Stephanos, Polybotes, and Kaminakia craters, obtaining an average value of –2.3 ± 0.4 (1σ) ‰ (Kavouridis et al., 1999; Panichi et al., 2000).

A second series of measurements was carried out on 10 fumarolic gas samples taken in November 1997 from Stephanos, Polybotes Micros, Polybotes Megalos, Phlegethon, and Kaminakia craters and an average $\delta^{13}C_{CO2}$ value of –2.4 ± 1.0 ‰ was obtained (Brombach, 2000; Brombach et al., 2003). Finally, Fiebig (unpublished data) and Fiebig et al. (2004) performed a series of determinations on 55 gas samples collected in September 2000, February

2001, June 2001, September 2001, and February 2002 from Stephanos, Polybotes Micros, Polybotes Megalos, Phlegethon, Lofos, and Kaminakia craters. The samples taken in September 2000 gave an average $\delta^{13}C_{CO2}$ value of –0.6 ± 0.5 ‰, whereas the averages of the subsequents datasets were –1.2 to –1.3 ‰ with deviations of 0.2 to 0.3 ‰.

It is possible that the $\delta^{13}C$ value of fumarolic CO_2 increased with time from 1991 to 2002, perhaps because of the seismic crisis of 1995-1998, but this possibility is far from certain owing to the large deviations of the 1997 data, which could be caused by either shallow processes or analytical uncertainties or other unknown reasons. In contrast to possible changes with time, the variations from vent to vent are relatively limited (Table 9.4), suggesting that relatively shallow processes, such as steam separation and condensation, have negligible effects on the $\delta^{13}C$ value of fumarolic CO_2. Assuming that the increase in the $\delta^{13}C$ value of fumarolic CO_2 with time is not an analytical artifact, it would indicate an increase in F_{CO2} (the fraction of CO_2 remaining dissolved in the degassing magma batch which is present below the hydrothermal system), based on the closed- and –open systems degassing models of Holloway and Blank (1994), indicating that ^{13}C is partitioned preferentially into the gas phase during magma degassing. Since an increase in F_{CO2} is impossible, due to the irreversible nature of magma degassing, the involvement of a less-degassed magma batch must necessarily be invoked. The changes with time in the isotope ratios of He and Ar could be attributed to the same process.

In contrast with this interpretation, the variations monitored for the $\delta^{13}C_{CO2}$ value before the year 2000 could be an analytical artifact. Since 2000, CO_2 has been directly taken from dry gas samples for carbon isotope analyses (Fiebig, unpublished data, and Fiebig et al., 2004). Prior to 2000, the carbon isotopic composition of CO_2 was instead determined by other authors (Kavouridis et al., 1999; Panichi et al., 2000; Brombach, 2000; Brombach et al., 2003) on the CO_3^{2-} ion which is generated by the interaction of CO_2 with NaOH in Giggenbach's bottles. It is important to underscore that 4M NaOH acts as a sink for atmospheric CO_2 if the solution is exposed to air in the laboratory. Atmospheric CO_2 exhibits $\delta^{13}C$ values of -7 to -8‰. Entrainment of atmospheric CO_2 during either the preparation of 4M NaOH or the precipitation of $SrCO_3$ might, therefore, explain many of the relatively low $\delta^{13}C_{CO2}$ values measured prior to 2000.

As shown by Sano and Marty (1995), the plot of $\delta^{13}C_{CO2}$ vs. $CO_2/^3He$ ratio (Figure 9.7) is an effective graphical tool to estimate the contributions of the three major sources which are considered to be involved in the production of CO_2 along convergent plate margins, i.e., mantle, organic sediments, and marine limestones. Only the Nisyros gases collected and analysed by Fiebig et al. (2004) are reported on this plot, since the He isotope ratio and the $\delta^{13}C_{CO2}$ value were both measured on the same samples in this study only. These fumarolic gases plot along the mixing trend between the mantle source and the marine limestone source, suggesting that the contribution of CO_2 through thermal degradation of sedimentary organic matter is virtually nil. As already recognised by Brombach (2000) and Brombach et al. (2003), this finding is consistent with the origin of fumarolic nitrogen, which is entirely explained by mixing of atmospheric gases and mantle gases without any contribution of organic-derived N_2.

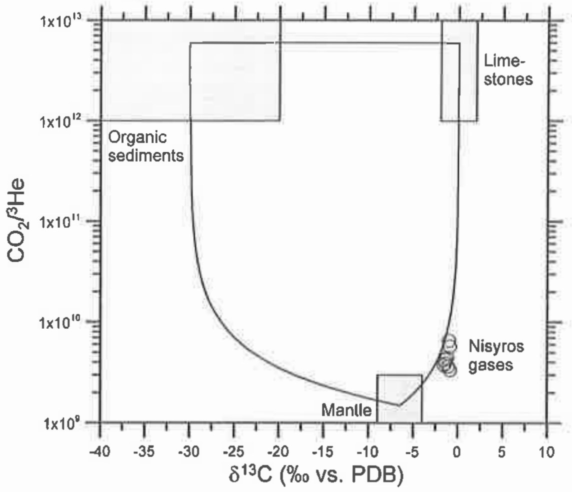

Figure 9.7. Plot of $\delta^{13}C_{CO2}$ values vs. $CO_2/^3He$ ratio (from Sano and Marty, 1995), showing the characteristics of the three main CO_2 sources present in subduction zones (mantle, organic sediments, and marine limestones) and their contribution to the fumarolic fluids of Nisyros.

9.5.5. Origin of CH_4

The $\delta^{13}C$ value of methane was first determined on 4 fumarolic gases sampled in October 1991 from different vents, obtaining an average value of –22.2 ± 0.5 ‰ (Kavouridis et al., 1999; Panichi et al., 2000). Very precise determinations of the $\delta^{13}C$ values of methane were carried out by Fiebig et al. (2004) on 35 gas samples collected in 2001-2002 from several vents. These data, which vary from –22 to –25 ‰, and the average data by Kavouridis et al. (1999) and Panichi et al. (2000) are represented in the plot of $\delta^{13}C_{CH4}$ vs. $\delta^{13}C_{CO2}$ (Figure 9.8). Also shown are the isotherms computed by means of the equilibrium isotope fractionation factors of both

Bottinga (1969) and Horita (2001), which differ by 0.3 to 0.4 ‰ units at temperatures between 300 and 600°C.

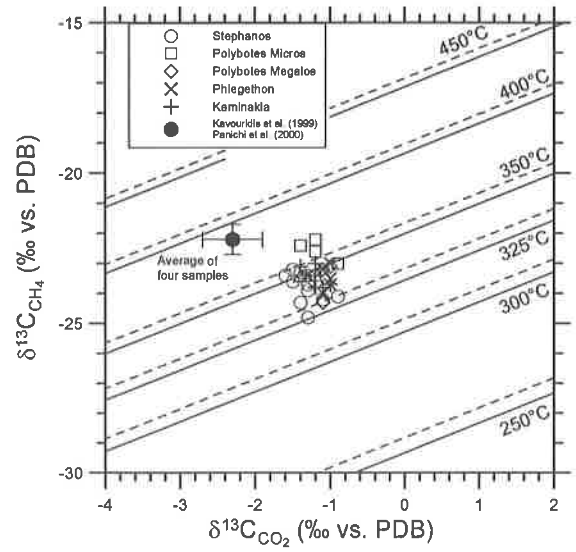

***Figure 9.8**. Plot of $\delta^{13}C_{CH4}$ vs. $\delta^{13}C_{CO2}$ values for the fumarolic gases of Nisyros, also showing the isotherms computed by means of the equilibrium isotope fractionation factors of both Bottinga (1969, dashed lines) and Horita (2001, solid lines).*

Most data by Fiebig et al. (2004) indicate CO_2-CH_4 isotope equilibrium temperatures of 325-350°C, apart from three samples from Polybotes Micros crater, which point to temperatures slightly above 350°C. These geothermometric evaluations virtually coincide with the maximum temperature measured in well Nisyros-1 close to well bottom, 340°C approximately. In contrast, C isotope partitioning between CO_2 and CH_4 yields a temperature close to 370°C for the average data of Kavouridis et al. (1999) and Panichi et al. (2000); this is somewhat higher than the maximum temperature of well Nisyros-1. However, comparison of the $\delta^{13}C_{CH4}$ and $\delta^{13}C_{CO2}$ of Kavouridis et al. (1999) with those of Fiebig et al. (2004) shows that the $\delta^{13}C_{CO2}$ values of Kavouridis et al. (1999) are 1.0-1.5‰ lower than those of Fiebig et al. (2004), whereas the $\delta^{13}C_{CH4}$ values of both studies are indistinguishable. Lower $\delta^{13}C_{CO2}$ values (up to -5‰) have also been monitored in the years before 2000, when isotopic measurements of CO_2 were not undertaken on dry gas samples, but on Giggenbach's bottles (see above). Since Kavouridis et al. (1999) performed their isotopic CO_2 analyses on Giggenbach's bottles, atmospheric contamination is probably the reason for their lower $\delta^{13}C_{CO2}$ values and their higher apparent C isotope fractionation temperatures.

Based on their apparent C isotope fractionation temperatures that are somewhat higher than aquifer temperature, Kavouridis et al. (1999) concluded that CH_4 is not in equilibrium with CO_2. They argued that the carbon isotopic composition of CH_4 is characteristic of worldwide occurring thermogenic CH_4 that generally is not co-genetic with CO_2. If so, the apparent C isotope fractionation temperatures derived by Fiebig et al. (2004) would be fortuitous. This seems, however, not to be the case. Fiebig et al. (2004) investigated another volcanic-hydrothermal system, that of Vesuvio, Italy, and again found apparent C isotope fractionation temperatures to be in agreement with independently determined aquifer temperatures, although the temperature of the Vesuvian hydrothermal system is 130°C higher than that of Nisyros. Furthermore, CH_4/CO_2 ratios from both locations closely correspond to equilibrium values. These findings imply that CO_2 and CH_4 are able to respond to temperature, both chemically and isotopically. Based on this background, the highest apparent C isotope fractionation temperatures evaluated for the gases emitted in 2001-2002 from the Polybotes Micros crater (where the last hydrothermal explosion occurred) acquire particular relevance.

All in all, it can be concluded that methane and carbon dioxide are in isotopic and chemical equilibrium, in the deep hydrothermal reservoir of Nisyros, and that this equilibrium condition remains quenched during the relatively quick uprise of fumarolic gases towards the surface discharge, as already underscored by Fiebig et al. (2004). This interpretation requires a quick kinetics for CO_2 - CH_4 conversion at reservoir temperature and an important decrease in the rate of this process upon cooling of the fumarolic fluids. An attempt to quantify the kinetics of chemical equilibration between CO_2 and CH_4 was presented by Giggenbach (1997). Assuming that the conversion of CO_2 to CH_4 may be described by a pseudo-first order reaction, the reaction half-time would be less than 4 years at 340°C, 45 years at 260°C, and 160,000 at 100°C. Chemical equilibrium can, therefore, be attained in less than 25 years (considering that equilibrium is approximated within 6-7 reaction half-times). However, following the hypothesis of Giggenbach (1997) in that the rate of isotopic re-equilibration is 400 times slower than that of chemical equilibration, the system CO_2-CH_4 would have required approximately 10,000 years for the attainment of isotopic equilibrium. Considering that Nisyros was the site of hydrothermal eruptions only 120 years ago, which may have disturbed chemically and isotopically the CO_2-CH_4 system, these very long isotopic equilibration times seem to be unreasonable. So far, there exists only limited experimental data for the equilibration rates of the CO_2-CH_4 system under hydrothermal conditions and hence the topic cannot be clarified any further.

9.5.6. Origin of H_2S

The $\delta^{34}S$ value of H_2S was first measured in 9 samples collected in November 1997 and in 10 samples taken in September 1998 from different fumarolic vents of Nisyros (Brombach, 2000; Marini et al., 2002; Brombach et al., 2003). The first batch of samples has a mean $\delta^{34}S$ value of +4.1 ± 0.5 (1σ) ‰, whereas the average $\delta^{34}S$ value of the second batch is +3.3 ± 0.3 ‰.

Afterwards, Fiebig (unpublished data) performed new measurements on 54 gas samples collected in September 2000, February 2001, June 2001, September 2001, and February 2002 from Stephanos, Polybotes Micros, Polybotes Megalos, Phlegethon, Lofos, and Kaminakia craters. Average $\delta^{34}S$ values were found to fluctuate between +4.4 and +3.1 ‰, with standard deviations of 0.2 to 0.5 ‰ units (Table 9.4). These changes with time are apparently meaningful, at least within ± 1σ, but their oscillating nature casts some doubts on their significance.

The involvement of a less-degassed magma batch was considered above as a possible (though unlikely) hypothesis to explain the changes with time in the $\delta^{13}C$ value of CO_2. One might ask why this process does not bring about concurrent variations in the $\delta^{34}S$ value of H_2S. However, the occurrence of changes in both C and S isotopes is not a necessary condition, owing to both the very different solubilities of CO_2 and S gases in magmas (e.g., Giggenbach, 1996) and the influence of different parameters on the gas-melt fractionation for S (Marini et al., 1998 and references therein).

In contrast with changes with time, the changes from vent to vent are small (Table 9.4), indicating that shallow and relatively shallow processes, such as steam separation and condensation, have virtually no effect on the $\delta^{34}S$ value of fumarolic H_2S.

Let us now recall the main results of the investigation by Marini et al. (2002). These authors started from the assumption that fumarolic H_2S is produced through single-step steam separation of a parent geothermal liquid, which is a mixture of local seawater and arc-type magmatic water (as indicated by water isotopes, see below), and reconstructed the evolution of the concentrations and $\delta^{34}S$ values of S-bearing solutes and minerals during the processes originating the parent geothermal liquid, by reaction path modelling. In this way it was possible to constrain the isotopic composition of sulfur in the magmatic gases entering the hydrothermal system from below. Leaving out of consideration all the details of this modelling exercise for obvious space reasons and coming to the final result, the S isotope ratio of magmatic S gases turned out to be +3.2 ± 0.6 ‰, under closed-system conditions.

The $\delta^{34}S$ values of the rhyodacitic degassing magma presumably present below the hydrothermal system was then estimated to be +6.3 ± 1.5 ‰, following the approach of Marini et al. (1998) and assuming closed-system degassing at 850°C, f_{H2O} of 1 kbar, redox conditions fixed by the magmatic gas buffer of Giggenbach (1987), and a fraction of S remaining in the silicate melt of 0.5. Then, the S isotope ratio of the rhyodacitic melt was shown to be consistent with fractional crystallization of a parent basaltic magma with an initial $\delta^{34}S$ value of +4 (± at least 1.5 ‰). Four sequential, isothermal-isobaric steps of closed-system degassing were considered to accompany magma evolution from basalt to rhyodacite. Interestingly, the results of these calculations compare nicely with the $\delta^{34}S$ values and S concentrations of some volcanic rocks from Nisyros and Yali, which were recently obtained (Figure 9.9).

Accepting that the parent basaltic magma of Nisyros has a $\delta^{34}S$ value of +4‰, mantle contamination, through either transference of fluids derived from subducted materials or involvement of altered oceanic crust, can be invoked to explain the difference between this value and the $\delta^{34}S$ value of pristine mantle, 0‰ (Marini et al., 1998 and references therein). In contrast, contribution of biogenic sulfides from subducted sediments appears to be negligible or nil. This conclusion can be probably extended to the whole Aegean island arc and is in line with the absence in Nisyros gases of organic-derived N_2 and CO_2 (see above).

9.6. Geothermometry and geospeedo-metry of fumarolic gases

As already stated in section 9.2, two geothermal boreholes were drilled near the margins of the area of the hydrothermal craters in the early 80's and temperatures up to 320-340°C were encountered at 1.5 – 1.8 km depth in both wells (Geotermica Italiana, 1983, 1984). The deep hydrothermal aquifer met in both boreholes seems to play a dominant role in governing the chemical composition of the gases originally rising from the underlying magmatic system, because highly soluble, typically magmatic gases such as SO_2, HCl, and HF are practically absent in the fumarolic fluids discharged at the surface (e.g., Chiodini et al., 1993a). This circumstance, combined with the underground information available from the two boreholes, makes Nisyros an ideal site to study the re-equilibration of magmatic gases under bi-phase hydrothermal conditions.

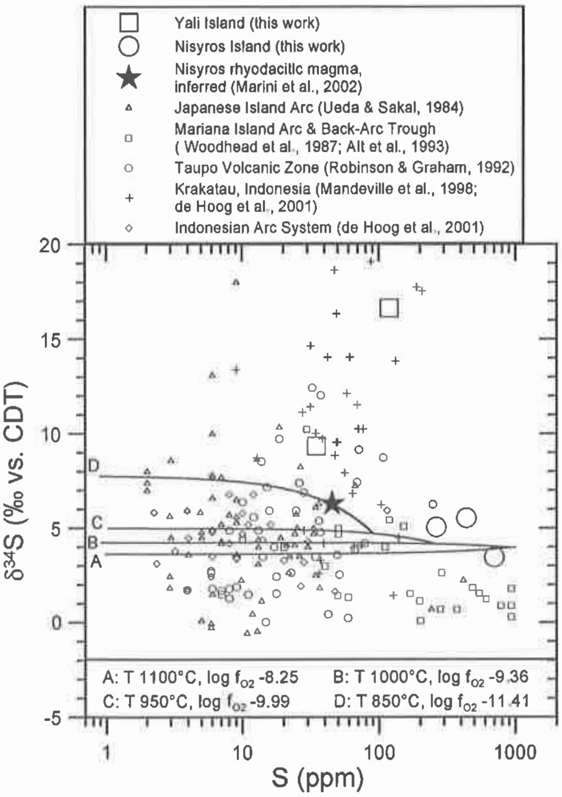

Figure 9.9. *Plot of $\delta^{34}S$ values vs. S concentrations for volcanic rocks from island arcs. Lines A, B, C, and D describe the theoretical changes caused by closed-system degassing which accompany magma evolution from basalt to rhyodacite (from Marini et al., 2002, modified).*

9.6.1. Geothermometry

9.6.1.1. Gas equilibria in the H_2-H_2O-CO-CO_2-CH_4 system

Gas equilibria in the Nisyros hydrothermal system were investigated by several authors (Chiodini et al., 1993a; Chiodini and Marini, 1998; Kavouridis et al., 1999; Panichi et al., 2000; Chiodini et al., 2002; Brombach et al., 2003; Fiebig et al., 2004). These studies brought forth similar results in that apparent temperatures derived from the H_2-H_2O-CO-CO_2-CH_4 geothermometers were always lower (170 - 320°C) than those measured directly in the deep hydrothermal aquifer. In contrast, carbon isotope partitioning between CO_2 and CH_4 yields apparent isotopic temperatures that reflect deep aquifer temperatures (Fiebig et al., 2004, see section 9.5.5). In other words, though CH_4 is involved in both geothermometers, the inferred temperatures are not consistent. What are the reasons for this inconsistency? Could it be that the distinct redox pairs involved in the H_2-H_2O-CO-CO_2-CH_4 system do not reflect overall equilibrium at deep aquifer temperatures, but re-equilibrated to different extents, as already established for the medium-high-temperature magmatic-hydrothermal gases of White Island (Giggenbach, 1987) and Vulcano Island (Chiodini et al., 1993b)? In order to answer these questions we have to go through the fundamentals of the H_2-H_2O-CO-CO_2-CH_4 system.

The attainment of equilibrium in the H_2-H_2O-CO-CO_2-CH_4 system can be checked through the graphical comparison of the log-ratios X_{CO}/X_{CO_2}, X_{CH_4}/X_{CO_2}, and X_{H_2}/X_{H_2O}, which are based on the reactions:

$$CO + ½\, O_2 = CO_2 \qquad (8)$$

$$CH_4 + 2\, O_2 = CO_2 + 2\, H_2O \qquad (9)$$

$$H_2 + ½\, O_2 = H_2O, \qquad (10)$$

respectively. All these reactions depend on oxygen fugacity and, therefore, on the redox conditions in the environments of gas equilibration. As long as oxygen fugacity is known at any temperature, theoretical values of the log-ratios X_{CO}/X_{CO_2}, X_{CH_4}/X_{CO_2}, and X_{H_2}/X_{H_2O} , can be computed for equilibration both in the single vapor phase and, under consideration of corresponding vapor-liquid distribution coefficients, in the single liquid phase (Chiodini and Marini, 1998). Fiebig et al. (2004, their Figure 7) observed that the $\log(X_{CH_4}/X_{CO_2})$ values of fumarolic gases from Polybotes Micros and Stephanos agree with the theoretical values predicted, at deep aquifer temperatures, for oxygen fugacities fixed by the FeO-$FeO_{1.5}$ buffer of Giggenbach (1987). Equilibrium values for $\log(X_{H_2}/X_{H_2O})$, $\log(X_{CH_4}/X_{CO_2})$ and $\log(X_{CO}/X_{CO_2})$ were, therefore, computed under the assumption that the FeO-$FeO_{1.5}$ buffer of Giggenbach (1987) correctly describes the redox conditions in the deep hydrothermal aquifer of Nisyros. The two plots of Figure 9.10 present a comparison between measured and computed values. Both diagrams also contain contour lines that show the chemical composition of vapors separated iso-enthalpically at temperature T_S from a liquid, whose gaseous constituents were in chemical equilibrium at temperature T_O prior to boiling. In order to calculate these theoretical compositions at any separation temperature, T_S, we start to write the following mass balance:

$$X_{i,O} = X_{i,V}\, s + X_{i,L}\, (1 - s) \qquad (11)$$

where s is the steam fraction and subscripts O, V and L identifies the original liquid of temperature T_O, the separated vapor and the boiled liquid, respectively. The steam fraction is given by:

$$s = \frac{h_O - h_L}{h_V - h_L} \qquad (12)$$

where h's stand for the specific enthalpies of the subscripted phases under saturation conditions, i.e., coexistence of vapor and liquid (Lemmon et al., 2003).

Taking into account the definition of the vapor-liquid distribution coefficient, B_i:

$$B_i = \frac{\left(n_i/n_{H_2O}\right)_V}{\left(n_i/n_{H_2O}\right)_L} \cong \frac{X_{i,V}}{X_{i,L}} \qquad (13)$$

and rearranging equation (11), one obtains:

$$X_{i,V} = \frac{X_{i,O} \cdot B_i}{1 - s + s \cdot B_i}, \qquad (14)$$

which is the equation of interest.

In the diagram of $\log\left(X_{CH_4}/X_{CO_2}\right)$ vs. $\log\left(X_{H_2}/X_{H_2O}\right)$ (Figure 9.10a) most fumarolic samples (especially those released from Polybotes Micros and Stephanos) and the gases discharged from the geothermal well Nisyros-1 plot close to the liquid line at temperatures of ~350°C ± 50°C. These temperatures are in close agreement with the temperature of 340°C, which was directly measured at the bottom of well Nisyros-1, and the temperatures inferred from carbon isotope thermometry. In contrast, the diagram of $\log\left(X_{CO}/X_{CO_2}\right)$ vs. $\log\left(X_{H_2}/X_{H_2O}\right)$ (Figure 9.10b) shows a completely different spread of points. Most fumarolic gases (especially those from Stephanos crater) distribute along a horizontal trend (indicated by an arrow) that is characterized by nearly constant X_{H_2}/X_{H_2O} ratios and variable X_{CO}/X_{CO_2} ratios.

The disagreement in the equilibration temperatures indicated by Figures 9.10a and 9.10b provides evidence that CO, in contrast to CH_4, continues to be converted to CO_2 during the ascent of the fluids from the deep hydrothermal aquifer towards the surface. As a consequence, the CO/CO_2 ratio reflects lower temperatures of equilibration than the CH_4/CO_2 ratio, which is nearly kept frozen during the upflow of fumarolic fluids.

Apart from the Kaminakia gases, which are discussed below, H_2 seems to be also involved in re-equilibration reactions during the uprising of fumarolic fluids, although the extent of H_2-re-equilibration is certainly much lower than that of CO re-equilibration.

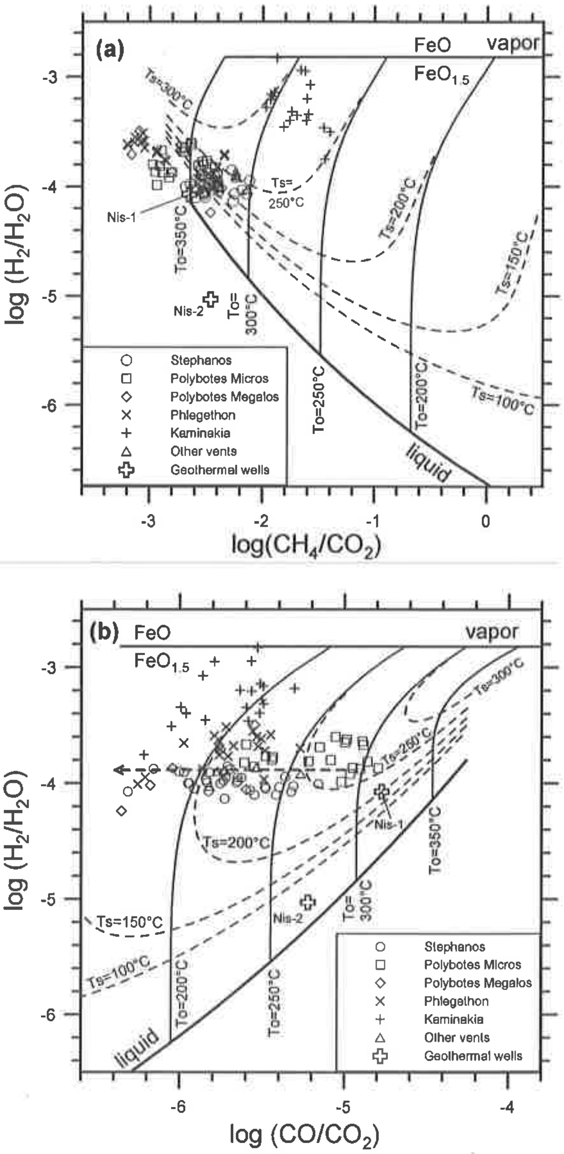

Figure 9.10. *Plots of (a)* $\log\left(X_{CH_4}/X_{CO_2}\right)$ *vs.* $\log\left(X_{H_2}/X_{H_2O}\right)$ *and (b)* $\log\left(X_{CO}/X_{CO_2}\right)$ *vs.* $\log\left(X_{H_2}/X_{H_2O}\right)$ *for the fumarolic gases and the geothermal wells of Nisyros, also showing the theoretical compositions for gas equilibration both in a single vapor phase and in a single liquid phase, as well as the effects of steam separation at temperature* T_S *on liquids initially equilibrated at temperature* $T_O > T_S$ *(see Chiodini and Marini, 1998). Redox conditions are considered to be fixed by the FeO-FeO*$_{1.5}$ *hydrothermal buffer of Giggenbach (1987).*

In addition to these general trends, Figures 9.10a and 9.10b also display some other interesting features. For instance, the gases from well Nisyros-2 have a X_{CH_4}/X_{CO_2} ratio comparable with that of most fumarolic gases, but a much lower X_{H_2}/X_{H_2O} ratio. Possibly, this liquid derives from the deep hydrothermal reservoir of Nisyros too, but significant amounts of H_2 were oxidized to H_2O upon cooling. The gases from the Kaminakia craters have both X_{CH_4}/X_{CO_2} and X_{H_2}/X_{H_2O} ratios significantly higher than those of the other fumarolic vents and cluster in a different zone, both in Figures 9.10a and 9.10b. Higher X_{H_2}/X_{H_2O} ratios could be due to water loss caused by steam condensation, a process which is very likely because outlet temperatures of Kaminakia fumaroles are below 100°C (see beginning of section 9.5). The higher X_{CH_4}/X_{CO_2} ratios are more difficult to explain. Fiebig et al. (2004, their Figure 7) demonstrated that the X_{CH_4}/X_{CO_2} ratios of Kaminakia and Phlegeton fumaroles are higher and lower, respectively, than equilibrium values defined by the deep aquifer temperature and oxygen fugacities fixed by the FeO-$FeO_{1.5}$ buffer of Giggenbach (1987). Possibly, redox conditions underneath Kaminakia and Phlegeton differ from those existing beneath Polybotes Micros and Stephanos.

Summing up, it seems likely that the X_{CH_4}/X_{CO_2} remains quenched at the pressure and temperature conditions of the deep hydrothermal reservoir, whereas the X_{CO}/X_{CO_2} ratio re-equilibrates relatively fast upon cooling during the uprising of fumarolic fluids towards the surface. However, it remains open whether re-equilibration of CO to CO_2 occurs in the single vapor phase, i.e., after boiling, or in the single liquid phase, i.e. , prior to boiling. Further, there might be local variations in the redox characteristics of the deep aquifer. Also, the redox conditions of CO re-equilibration remain unidentified. These matters cannot be elucidated from Figure 9.10b because, next to re-equilibration, the molar ratios of the gases were affected by vapor separation and vapor condensation processes.

If re-equilibration of CO occurs in the single liquid phase prior to vapor separation, the corresponding redox conditions can be identified provided that the contributions of vapor separation and condensation on the log(X_{H_2}/X_{H_2O}) and log(X_{CO}/X_{CO_2}) ratios are adequately computed and eliminated. To this purpose, Chiodini and Marini (1998) suggested the use of a correlation plot between $3\cdot\log(X_{CO}/X_{CO_2})+\log(X_{CO}/X_{CH_4})$ and $\log(X_{CO}/X_{CO_2})-\log(X_{H_2}/X_{H_2O})$, since the sums of these log-ratios are independent of redox conditions. The temperature of last equilibration in a single liquid phase (T_O), the temperature of liquid/vapor separation (T_S), and either the corresponding fraction of separated steam (s) or the fraction of condensed steam at fumarolic outlet temperature (c) can be evaluated by comparison of theoretical and measured sums of log-ratios under the following assumptions: (1) all five gas constituents are in overall equilibrium prior to boiling; (2) the process of vapor separation occurs in a single, iso-enthalpic step; (3) the process of vapor condensation occurs in a single step too; (4) to compute c, s is assumed equal to zero; (5) during and after vapor separation, gases are not involved in reactions anymore; if, however, reactions in the vapor phase still occur, the computed T_O, T_S and s (or c) would be erroneous.

Strictly, hypothesis (1) is not fulfilled for Nisyros discharges, because CO and CH_4 are not in equilibrium anymore. However, the highest weight on the sums of log-ratios $3\cdot\log(X_{CO}/X_{CO_2})+\log(X_{CO}/X_{CH_4})$ and $\log(X_{CO}/X_{CO_2})-\log(X_{H_2}/X_{H_2O})$ is made by CO. In that sense, any temperature information displayed by the two sums of log-ratios chiefly reflects CO-CO_2 equilibration temperatures, whereas the weight of CH_4 is low and deviations from overall equilibrium relatively small. The approach of Chiodini and Marini (1998) is, therefore, still usable to compute meaningful c or s, T_O and T_S values.

Figure 9.11 presents the comparison between theoretical and measured sums of log-ratios. The spread of points is similar to that of Figure 9.10a. Polybotes Micros fumaroles exhibit the highest CO-based equilibration temperatures T_O and fractions of separated steam s. However, CO re-equilibration temperatures are always lower than apparent carbon isotopic temperatures. This is in agreement with what has been inferred from Figure 9.10, in that CO re-equilibrates to lower temperatures than CH_4. CO re-equilibration is even more pronounced in Stephanos and Phlegeton discharges. Kaminakia fumaroles experienced nearly the same extent of CO re-equilibration as Stephanos and Phlegeton discharges, but were additionally affected by water vapor condensation, partly shifting the Kaminakia group to the left of the single vapor equilibrium line.

The equations necessary for the calculation of s (or c), T_O and T_S as well as for the restoration of log(X_{H_2}/X_{H_2O}) and log(X_{CO}/X_{CO_2}) values prior to boiling are given in Chiodini and Marini (1998). Computed values for s, c, T_O, T_S and restored ratios of log(X_{H_2}/X_{H_2O}) and log(X_{CO}/X_{CO_2}) prior to boiling are listed in Table 9.1.

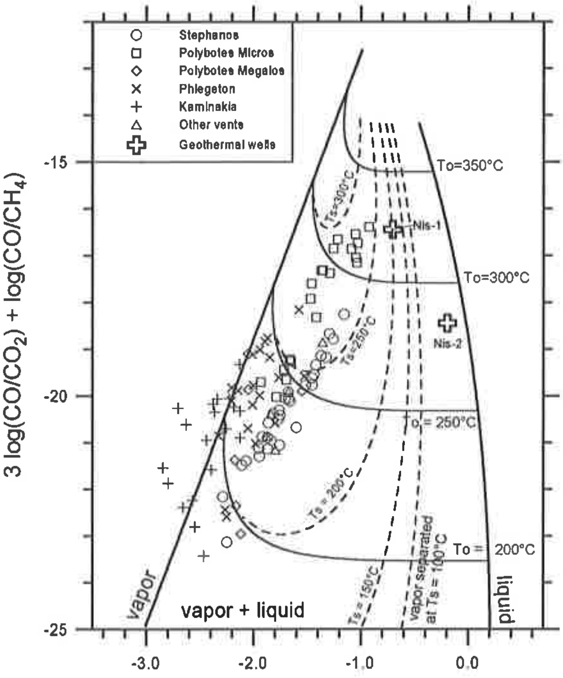

Figure 9.11. Diagram of $3 \cdot \log\left(X_{CO}/X_{CO_2}\right) + \log\left(X_{CO}/X_{CH_4}\right)$ *versus* $\log\left(X_{CO}/X_{CO_2}\right) - \log\left(X_{H_2}/X_{H_2O}\right)$ *for the fumarolic gases and the geothermal wells of Nisyros, also showing the theoretical compositions for gas equilibration either in a single vapor phase or in a single liquid phase, as well as the effects of steam separation at temperature T_S on liquids initially equilibrated at temperature $T_O > T_S$ (see Chiodini and Marini, 1998).*

Note that restored $\log(X_{H_2}/X_{H_2O})$ and $\log(X_{CO}/X_{CO_2})$ values do not refer to the single liquid phase which is present prior to boiling, but to the hypothetical single vapor phase in equilibrium with it. The reason for this choice is the obvious involvement of gaseous species, rather than dissolved species, in gas buffers. Figure 9.12 presents the correlation plot of restored $\log(X_{H_2}/X_{H_2O})$ versus restored $\log(X_{CO}/X_{CO_2})$ values. Only the samples collected since May 2000 have been considered (see discussion below). In contrast to Figure 9.10b and 9.11, data points from each location follow tight alignments in Figure 9.12. The highest $\log(X_{H_2}/X_{H_2O})$ and $\log(X_{CO}/X_{CO_2})$ values are always lower than those expected for equilibration in the deep hydrothermal reservoir, under redox conditions fixed by the FeO-FeO$_{1.5}$ buffer. For each location, the alignments can be extrapolated to intersect the FeO-FeO$_{1.5}$ buffer-line.

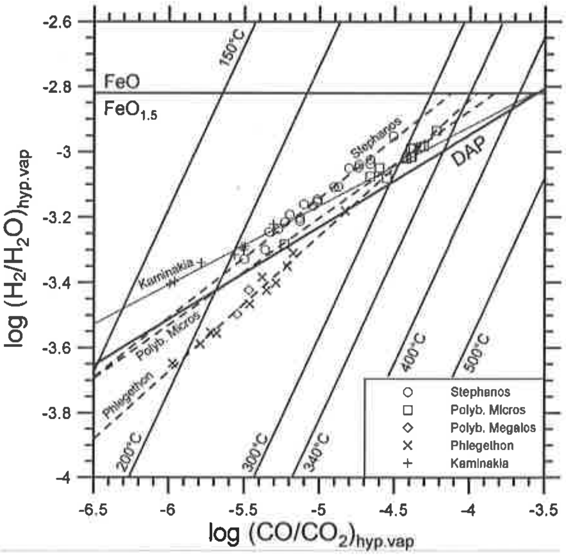

Figure 9.12. Diagram of restored $\log\left(X_{CO}/X_{CO_2}\right)$ *vs.* $\log\left(X_{H_2}/X_{H_2O}\right)$*. Restored ratios are referred to the hypothetical single vapor phase. Each set of data has been extrapolated back to the redox buffer line of Giggenbach (1987). The redox buffer of D'Amore and Panichi (1980) is also shown (DAP line). See text for discussion.*

The apparent CO-H$_2$ temperatures displayed by the intersections are then compared with the mean temperatures inferred from carbon isotope partitioning between CO$_2$ and CH$_4$ (Table 9.5). For Polybotes Micros and Stephanos extrapolated CO-H$_2$ temperatures (369°C and 320°C, respectively) are consistent with isotopic temperatures (352°C and 337°C, respectively). Considering that also CH$_4$ and CO$_2$, for Polybotes Micros and Stephanos fumaroles, attain chemical and isotopic equilibrium in the deep aquifer, under redox conditions controlled by the FeO-FeO$_{1.5}$ buffer (see Figure 7 of Fiebig et al. 2004 and Figure 9.10a), a coherent picture is now obtained for these two locations: CH$_4$, CO, CO$_2$, H$_2$ and H$_2$O attain overall primary equilibrium in the deep aquifer. Again, redox conditions in the deep aquifer underneath these craters are correctly described by the FeO-FeO$_{1.5}$ buffer. From this zone, ascent of fluids as a single liquid phase occurs, at least initially. CH$_4$ is not able to re-equilibrate at the decreasing temperature and varying redox conditions met by uprising fluids, whereas CO and to a lesser extent H$_2$ experience re-equilibration, as long as the fluids reach depths and pressure conditions under which boiling (steam separation) takes place. In other words, CO and H$_2$ re-equilibration ends at the temperature of vapor/liquid separation. Since this temperature and the fraction of separated vapor (or condensed steam) are accurately displayed in the correlation plot of $3 \cdot \log\left(X_{CO}/X_{CO_2}\right)$

$+\log(X_{CO}/X_{CH_4})$ versus $\log(X_{CO}/X_{CO_2}) - \log(X_{H_2}/X_{H_2O})$, any significant re-equilibration of CO and H_2 in the vapor phase can be excluded. Otherwise, the computed values of s, T_O, and T_S for these locations would be erroneous and, consequently, temperatures inconsistent with apparent isotopic temperatures would have been extrapolated. The alignments for these locations closely fit the oxygen buffer of D'Amore and Panichi (1980). Likewise this buffer may be representative for the redox conditions of the environment that is encompassed by the fluids during their ascent from the deep aquifer prior to boiling.

For Phlegeton fumaroles, the CO-H_2 temperature extrapolated from Figure 9.12 (339°C) also coincides with the mean value given by carbon isotope thermometry (342°C), although CH_4/CO_2 ratios at these temperatures are lower than dictated by the FeO-$FeO_{1.5}$ buffer under equilibrium conditions (Figure 7 of Fiebig et al., 2004). CH_4, therefore, might have been removed after overall equilibrium with respect to the FeO-$FeO_{1.5}$ buffer was attained (see also discussion in section 9.8). However, other explanations are possible. Overall equilibrium might have been attained under slightly more oxidizing conditions than represented by the FeO-$FeO_{1.5}$ buffer, and extrapolation to a $\log(X_{H_2}/X_{H_2O})$ value of -2.82, therefore, may be not correct. Alternatively, the deep hydrothermal aquifer underneath Phlegeton might be thinner than beneath Polybotes Micros and Stephanos. This could cause either limited conversion of magmatic CO_2 to CH_4, in the hydrothermal system under redox conditions reflected by the FeO-$FeO_{1.5}$ buffer, or mixing of magmatic gases, which are virtually free of CH_4, with CH_4-rich hydrothermal gases.

This scenario is in agreement with the observation that CO_2 contents are the highest of all locations, excluding Kaminakia, where CO_2 is enriched by water vapor condensation. Disagreement between extrapolated CO-H_2 temperatures (416°C) and mean isotopic temperature (340°C) is obtained for Kaminakia fumaroles. These fumaroles are subject to significant condensation of fumarolic water vapor. It seems that condensation of water vapor represents a Rayleigh process (see section 9.7 and Figure 9.16) rather than a single-step (batch) process as it is assumed for the computation of c. Rayleigh-type condensation might also be responsible for the significant enrichment in CH_4 over the more soluble CO_2 in Kaminakia fumaroles. However, as for Phlegeton, deviations from the redox-buffering of the FeO-$FeO_{1.5}$ pair cannot be excluded. In contrast, addition of CH_4 after overall re-equilibration in the deep aquifer can be ruled out, because then the carbon isotopic composition of Kaminakia-CH_4 should differ from that of other locations, which is evidently not the case.

9.6.1.2. The H_2-Ar and H_2- N_2 geothermometers

The X_{H_2}/X_{Ar} log-ratios of fumarolic gases are compared with corresponding X_{H_2}/X_{H_2O} log-ratios in the plot of Figure 9.13, also showing the theoretical compositions for gas equilibration in a single vapor phase and in a single liquid phase (Giggenbach, 1991; Brombach et al., 2003), as well as the effects of steam separation at temperature T_S on liquids initially equilibrated at temperature $T_O > T_S$.

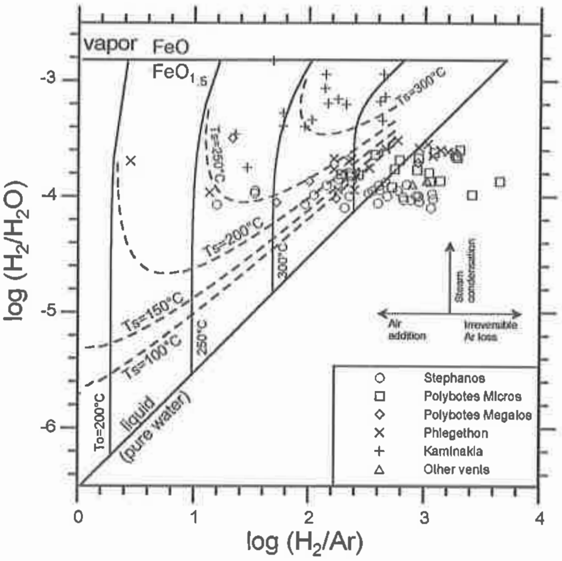

Figure 9.13*. Diagram of* $\log(X_{H_2}/X_{Ar})$ *versus* $\log(X_{H_2}/X_{H_2O})$ *for the fumarolic gases of Nisyros, also showing the theoretical compositions for gas equilibration in a single vapor phase and in a single liquid phase, as well as the effects of steam separation at temperature* T_S *on liquids initially equilibrated at temperature* $T_O > T_S$ *(modified from Giggenbach, 1991 and Brombach et al., 2003). Redox conditions are considered to be fixed by the FeO-*$FeO_{1.5}$ *hydrothermal buffer of Giggenbach (1987).*

These theoretical compositions are based on the assumptions that (1) redox conditions are fixed by the FeO-$FeO_{1.5}$ hydrothermal buffer of Giggenbach (1987) and (2) Ar concentrations of the hydrothermal reservoir liquids are equal to that of air-saturated groundwater at room temperature, although it was shown above that a significant amount of dissolved Ar (~ 50 % on average) originates from radioactive decay of ^{40}K (see section 9.5.3). Consideration of these amounts of non-atmospheric Ar in the hydrothermal liquid phase would shift the liquid line to the left, in Figure 9.13, of 0.3 log-units approximately.

Most fumarolic gas compositions cluster to the right of the liquid line and indicate equilibration temperatures of 350-370°C assuming attainment of chemical equilibrium in the liquid phase. Other gas samples, mostly coming from Phlegethon, plot to the left of the liquid line, likely due to either trivial air contamination or air entrainment in the fumarolic conduits upstream of the surface discharge, which determine a decrease in the H_2/Ar ratio. In contrast, steam condensation brings about an increase in the H_2/H_2O ratio, shifting the sample points towards the vapor line, as is the case of Kaminakia fumaroles (see above). Assuming equilibration in the liquid phase, the H_2/Ar ratio indicates temperatures of 300-360°C for these gases.

The plot of $\log(X_{H_2}/X_{N_2})$ vs. $\log(X_{H_2}/X_{H_2O})$ is given in Figure 9.14. Again, the theoretical grid was computed assuming that N_2 concentrations of the hydrothermal reservoir liquids are equal to that of air-saturated groundwater at room temperature (Arnórsson, 1987; Brombach et al., 2003). This appears to be a reasonable hypothesis in the case of Nisyros, owing to the virtual absence of non-atmospheric N_2 as suggested by the N_2-Ar-He triangular diagram (see section 9.5.1).

The spread of sample points in Figure 9.14 is similar to that observed in Figure 9.13, in that most fumarolic gas samples from Stephanos and Polybotes Micros plot close to the liquid line at temperatures of 350-360°C. Again: (1) samples affected by air entrainment/contamination are shifted towards lower H_2/N_2 ratios but maintain their H_2/H_2O ratios, as is the case for many gas samples collected from the Phlegethon fumaroles, and (2) the fumarolic effluents affected by steam condensation (e.g., those of Kaminakia craters) are displaced towards the vapor line but maintain their H_2/N_2 ratios, which suggest equilibrium temperatures of 300-350°C, assuming equilibration in a liquid phase.

The average gas compositions of the geothermal wells Nisyros-1 and Nisyros-2 are also shown in Figure 9.14. Assuming gas equilibration in a single liquid phase, temperatures of 355-310°C and 290-270°C are estimated for wells Nisyros-1 and Nisyros-2, respectively. The H_2-H_2O temperatures are close to measured values, whereas the H_2-N_2 temperatures are somewhat lower (20 - 30°C) than measured values. These uncertainties could be partly due to the presence, in the natural system, of a redox buffer somewhat different from the FeO-$FeO_{1.5}$ hydrothermal redox buffer of Giggenbach (1987).

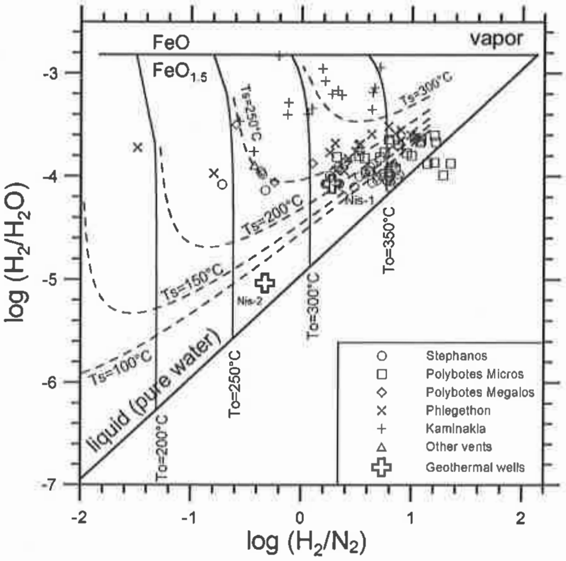

***Figure 9.14**. Diagram of $\log(X_{H_2}/X_{N_2})$ vs. $\log(X_{H_2}/X_{H_2O})$ for the fumarolic gases and the geothermal wells of Nisyros, also showing the theoretical compositions for gas equilibration in a single vapor phase and in a single liquid phase, as well as the effects of steam separation at temperature T_S on liquids initially equilibrated at temperature $T_O > T_S$ (modified from Giggenbach, 1991, and Brombach et al., 2003). Redox conditions were considered to be governed by the FeO-$FeO_{1.5}$ hydrothermal f_{O2} buffer of Giggenbach (1987).*

Further uncertainties in the H_2-Ar and H_2-N_2 geothermometers are caused by gas losses from the hydrothermal reservoir and subsequent gas re-equilibration, as noticed by Chiodini et al. (2002) and Brombach et al. (2003). Gas losses do not vary appreciably the H_2/Ar and H_2/N_2 ratios, owing to the similar solubilities in aqueous solutions of these sparingly soluble gases. Nevertheless, addition of atmospheric Ar and N_2 and of radiogenic Ar are unlikely to re-establish the initial (before gas losses) concentrations of these gases, whereas H_2 is likely to be generated through fast reactions, such as molecular dissociation of water. Therefore, the H_2/Ar and H_2/N_2 ratios are expected to increase upon gas losses from the hydrothermal reservoir.

9.6.1.3. Geothermometry of fumarolic gases: a synthesis

In spite of the limitations and uncertainties of geothermometric techniques, for all the fumarolic gases (apart from those of Kaminakia), the H_2-H_2O, CH_4-CO_2, H_2-Ar, and H_2-N_2 chemical geothermometers and the partitioning of C isotopes between CH_4 and CO_2 consistently indicate equilibrium temperatures close to the maximum temperature physically measured at depth in well Nisyros-1, that is about 340°C. This suggests that all these fumarolic effluents derive from a liquid phase with this initial temperature. In addition, CO-based geothermometers [chiefly the diagram of $3 \cdot \log(X_{CO}/X_{CO_2}) + \log(X_{CO}/X_{CH_4})$ versus $\log(X_{CO}/X_{CO_2}) - \log(X_{H_2}/X_{H_2O})$, which is independent of redox conditions] suggest that this liquid phase experiences conductive cooling from about 340°C to the temperature of CO re-equilibration, T_O, whose average values are indicated in Table 9.6. Indeed CO re-equilibration is a relatively fast process at relatively high temperatures and in a liquid phase, where several dissolved constituents act as catalysts for the water-gas shift reaction. Cooling is followed by liquid-vapor separation at temperatures T_S, whose average values are also listed in Table 9.6. Corresponding steam fractions are relatively small, ≤ 0.05.

The gases emitted by the Kaminakia fumaroles experience steam condensation which hinders the use of the H_2-H_2O geothermometer and complicates the use of the plot of $3 \cdot \log(X_{CO}/X_{CO_2}) + \log(X_{CO}/X_{CH_4})$ versus $\log(X_{CO}/X_{CO_2}) - \log(X_{H_2}/X_{H_2O})$. However, the $\Delta^{13}C(CH_4\text{-}CO_2)$ isotope geothermometer and the CH_4-CO_2, H_2-Ar, and H_2-N_2 chemical geothermometers suggest that also these gases derive from a liquid of high initial temperature, similar to those estimated for the other fumaroles. Again, this liquid phase undergoes cooling to an average temperature T_O of 195°C, followed by both separation of very small amounts of vapor at an average temperature T_S, which is very close to T_O, and extensive steam condensation.

9.6.2. Geospeedometry: the kinetics of CO re-equilibration

The fast rate of the water-gas shift reaction (15) in high-temperature aqueous solutions (but well below the critical point of pure water) is consistent with several experimental observations (e.g., Elliott and Sealock, 1983; Elliott et al., 1983, 1986; Yoshida et al., 2004). However, kinetic data for the water-gas shift reaction are only available, so far, for the supercritical phase and not for liquid water, in which re-equilibration of CO most likely takes place at Nisyros (see above). Assuming that: (1) CO re-equilibration is governed by the water-gas shift reaction in the deep hydrothermal aqueous solution, before vapor/liquid separation:

$$CO_{(aq)} + H_2O_{(aq)} = CO_{2(aq)} + H_{2(aq)} \qquad (15)$$

and (2) the concentrations of H_2O, CO_2, and H_2 remain nearly constant (which certainly holds true for the major components H_2O and CO_2), it can be concluded that reaction (15) follows a pseudo-first order kinetics.

In order to derive time constraints concerning the re-equilibration of CO, we decided to refer to the hypothetical single vapor phase. The CO concentration in the hypothetical vapor X_{CO,T_O} at the temperature of CO-re-equilibration T_O is related to the initial CO concentration in the hypothetical vapor phase under reservoir conditions, X_{CO,T_R} (i.e., the CO-H_2 temperature extrapolated from Figure 9.12), by the following equation:

$$\ln X_{CO,T_O} = \ln X_{CO,T_R} - k \cdot \tau\,, \qquad (16)$$

where k is the pseudo-first order rate constant and τ is the travel time of the liquid phase between the deep hydrothermal reservoir and the zone where vapor/liquid separation takes place. For each fumarolic sample, X_{CO,T_O} can easily be computed considering the measured fraction of CO in the vapor phase, the corresponding temperatures of vapor separation T_S and liquid-phase re-equilibration T_O, the fraction of condensed water vapor c or separated vapor s, and equations (47) or (41) given by Chiodini and Marini (1998), neglecting their j-terms. X_{CO,T_R} can generally be approximated by multiplying extrapolated, local-specific CO/CO_2 ratios times fumarolic-specific X_{CO_2,T_O} (which, in turn, can be calculated the same way as X_{CO,T_O}, this time neglecting the i-terms of equations [47] or [41] by Chiodini and Marini [1998]). Because CO_2 is a major gas constituent, X_{CO_2,T_O} does not significantly deviate from X_{CO_2,T_R}.Owing to the large cooling experienced by the liquid phase and the possible presence of unknown catalysts in the natural system, k cannot be readily constrained. Therefore, the X_{CO,T_O} for the maximum CO-re-equilibration temperature, T_O = 322°C (sample PP9N from Polybotes Micros collected in February 2002), and the X_{CO,T_R} for Polybotes Micros were used to estimate k, imposing a time of 1 arbitrary unit. The obtained k value of 0.8886, was then used to compute the pre-exponential factor A of the Arrhenius-type equation:

$$k = A \cdot \exp\left(\frac{-Ea}{RT}\right), \qquad (17)$$

setting the activation energy Ea equal to 95 (±3) kJ/mol (Holgate et al., 1992) and T equal to the average between T_O and T_R. The A value 9.286×10^7 [mol/arbitrary time unit] was thus obtained. Based on this value of A, equations (17) and (16) were then used to compute τ for each fumarolic gas sample, using the values of X_{CO,T_R} and T_R estimated for each fumarole and, again, taking T equal to the average between T_O and T_R in equation (17).

The computed travel times for the fumarolic gas samples collected since May 2000 from Polybotes Micros, Stephanos, and Phlegethon are correlated with the corresponding temperatures of CO- re-equilibration T_O in Figure 9.15, where a marked inverse dependence is evident.

Interestingly, in spite of the assumptions involved in the calculation of τ, the average travel times are 3 ± 4 (1 σ) for Polybotes Micros, 23 ± 14 for Stephanos, and 30 ± 18 for Phlegethon, indicating that, on the average, the liquid below Polybotes Micros travel much faster than underneath the other two areas which have similar values of τ. Calculations were not carried out for Kaminakia, due to the possible occurrence of Rayleigh condensation instead of batch condensation.

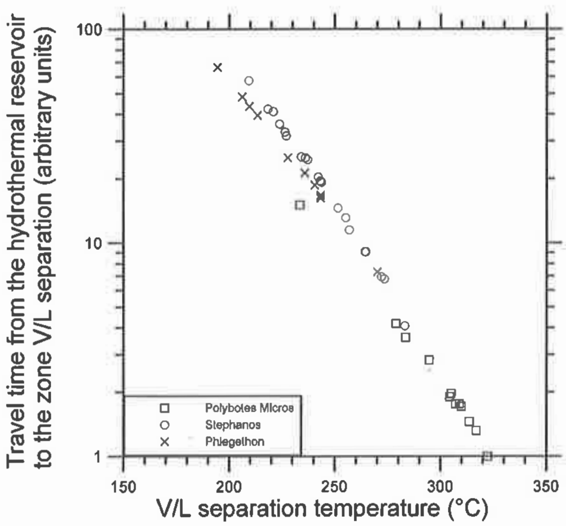

Figure 9.15. Correlation plot between the transit time from the deep hydrothermal reservoir to the zone of vapor/liquid separation and the vapor/liquid separation temperature for the fumarolic gas samples collected since May 2000 from Polybotes Micros, Stephanos, and Phlegethon.

9.7. Origin of fumarolic H_2O

The results of gas geothermometry, namely the temperature of CO re-equilibration, T_O, assumed to be representative of the temperature at which the geothermal liquid cools conductively before boiling and the temperature of liquid/vapor separation, T_S, are of fundamental importance for a correct interpretation of the δD and $\delta^{18}O$ values of the fumarolic steam condensates, as already underscored by Brombach et al. (2003). However, our interpretation is somewhat different from that of Brombach et al. (2003), who assumed occurrence of boiling from the initial reservoir temperature of 345°C to a constant separation temperature of 280 ± 30°C.

First, the $\delta^{18}O$ values of steam condensates were corrected for exchange of oxygen isotopes between $H_2O_{(g)}$ and $CO_{2(g)}$, following the approach of Chiodini et al. (2000). Owing to the comparatively small concentrations of CO_2, most measured values are modified to a relatively small extent (0.4 to 1.1 ‰), apart from the fumarolic gases of Kaminakia, with CO_2 concentrations higher than other fumaroles, which cause ^{18}O-corrections of 1.5 to 4.4 ‰.

In the plot of δD versus $\delta^{18}O$ (Figure 9.16), 40 of the 45 gas samples from Stephanos and Polybotes Micros cluster in a single group with an average δD value of −11.5 ± 3.0 ‰ and an average $\delta^{18}O$ value of +3.8 ± 0.6 ‰. In contrast, the gas samples from Phlegethon, Polybotes Megalos, and Kaminakia distribute along an alignment roughly parallel to the meteoric water line, but shifted 3 to 4 ‰ units to its right. In order to explain this second spread of points, it is convenient to recall the isotopic composition of the reservoir liquid tapped by the geothermal well Nisyros-2. The δD and $\delta^{18}O$ values of the vapor and liquid phases discharged from this well were measured by Dotsika (1992). Based on these data, Brombach et al. (2003) computed a δD of −1.9 ‰ and a $\delta^{18}O$ of +3.7 ‰ for the single liquid phase presumably present in the hydrothermal reservoir at 290°C.

The δD and $\delta^{18}O$ values (both indicated as δ_V) of the vapors separated at temperature T_S, in a single-step, from a reservoir liquid of incipient boiling temperature T_O and isotopic composition δ_O are constrained by the following relation (Giggenbach and Stewart, 1982):

$$\delta_V = \delta_O - 1000 \ln\alpha_{L\text{-}V} (1 - s) \qquad (18)$$

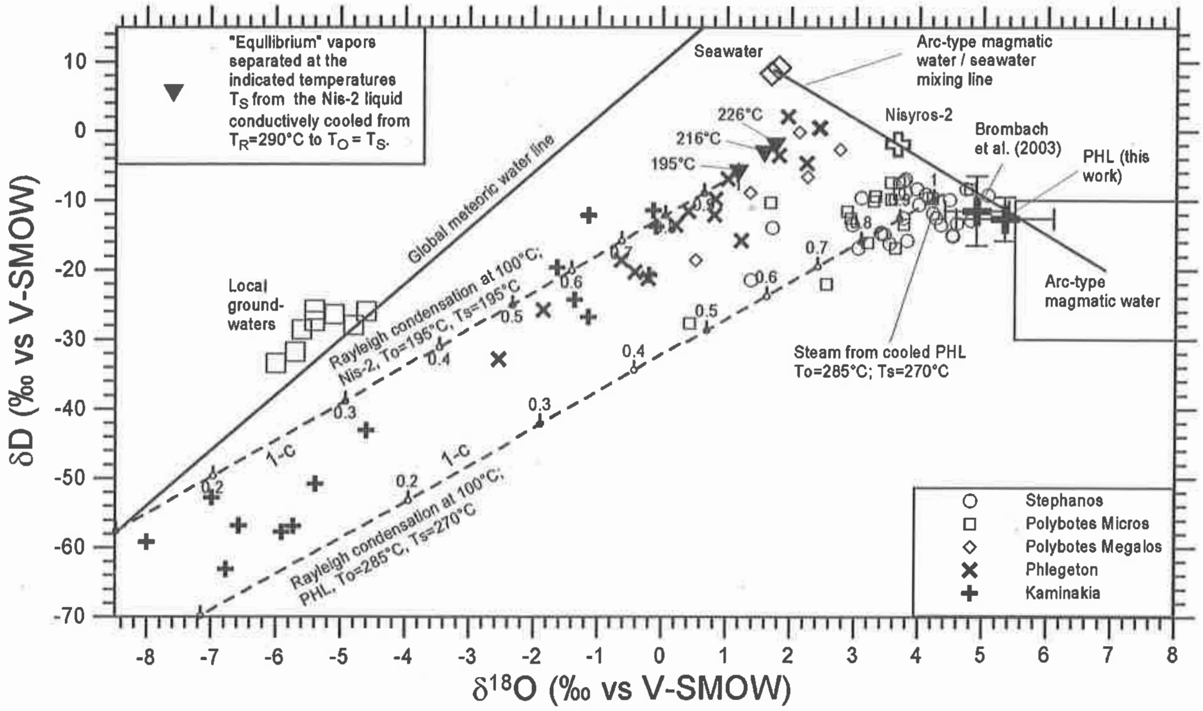

Figure 9.16. *δD versus δ18O diagram for the steam condensates from different fumaroles of Nisyros (see legend). Also shown are the global meteoric water line, the isotopic composition of local groundwaters and local seawater (from Kavouridis et al., 1999 and Brombach et al., 2003), the reservoir liquid tapped by the geothermal well Nisyros-2 (Dotsika, 1992; Brombach et al., 2003), arc-type magmatic water (Giggenbach, 1992), as well as the theoretical isotopic composition of steam formed through single-step separation from both the parent hydrothermal liquid PHL for T_O = 285°C, T_S = 270°C and from the Nisyros-2 liquid conductively cooled from the reservoir temperature (T_R = 290°C) to T_O=T_S temperatures of 195, 216, and 226°C. The overwhelming effects of Rayleigh steam condensation at 100°C on the vapors separated from the parent hydrothermal liquid PHL (for T_O = 285°C and T_S = 270°C) and the Nisyros-2 reservoir liquid (for T_O = T_S = 195°C), both cooled conductively at 100°C, are also displayed (c is the fraction of condensed steam).*

where s is the steam fraction, which is computed by means of equation (12) for isoenthalpic steam separation, and 1000 $\ln\alpha_{L\text{-}V}$ is the liquid/vapor equilibrium fractionation factor at T_S. In other words, it is assumed that water vapor and the remaining liquid attain isotopic equilibrium at the vapor separation temperature T_S. Liquid-vapor fractionation factors of O and H isotopes for pure water from 0°C to the critical temperature are given by the following relationships (Horita and Wesolowski, 1994, T in K):

$$1000\cdot\ln\alpha_{L-V(D)} = 1158.8\frac{T^3}{10^9} - 1620.1\frac{T^2}{10^6} + 794.84\frac{T}{10^3} - 161.04 + 2.9992\frac{10^9}{T^3} \qquad (19)$$

$$1000\cdot\ln\alpha_{L-V(^{18}O)} = -7.685 + 6.7123\frac{10^3}{T} - 1.6664\frac{10^6}{T^2} + 0.35041\frac{10^9}{T^3}. \qquad (20)$$

Using equation (18) and the fractionation factors given by equations (19) and (20), the δD and $\delta^{18}O$ values for the vapor phases separated in a single step at temperatures T_S of 226, 216, and 195°C from the Nisyros-2 liquid, cooled conductively from the reservoir temperature (T_R = 290°C) to temperatures T_O = T_S, were readily computed. These temperatures were chosen as they closely reflect the average T_O and T_S values indicated by the H_2-H_2O-CO-CO_2-CH_4 geoindicator for Phlegethon, Polybotes Megalos, and Kaminakia fumaroles (see Table 9.6). The obtained theoretical isotope compositions are similar to the heaviest values measured for the steam condensates from Phlegethon, Polybotes Megalos, and Kaminakia (Figure 9.16). The vapors discharged from the same fumaroles, but enriched in light isotopes, could have experienced conductive cooling from T_S to 100°C followed by Rayleigh steam condensation at 100°C. The isotopic effects of the latter process, also indicated by theoretical lines in Figure 9.16, are computed by means of the equation (e.g., Ohmoto and Goldhaber, 1997):

$$\delta_V = (\delta_{V,O} + 1000) \cdot (1 - c)^{(\alpha_{L-V} - 1)} - 1000 \tag{21}$$

where the subscripts V,O and V refer to the steam before condensation and after condensation, respectively, and c is the fraction of condensed steam. Separation of secondary steam through boiling of steam condensates, re-heated upon percolation at depth and possibly mixed with local groundwater, might also explain the lightest isotope compositions, but the former explanation is more straightforward.

To evaluate the δD and $\delta^{18}O$ values of the reservoir liquid originating the vapors discharged from the fumarolic vents of Stephanos and Polybotes Micros craters, again it was assumed isoenthalpic boiling from T_O (the temperature at which the geothermal liquid cools conductively) to T_S (the liquid/vapor separation temperature). The corresponding steam fraction provided by the CO-based geothermometers and the δD and $\delta^{18}O$ values of each steam condensate were inserted in equation (18), which was solved for δ_O. Results were then averaged, obtaining a δD of –12.7 ± 3.2 ‰ and a $\delta^{18}O$ of +5.3 ± 0.8 ‰ for the parent hydrothermal liquid (PHL). These isotope values are very similar to those proposed by Brombach et al. (2003), in spite of the different interpretations of available data. Thus, the liquid tapped by the geothermal well Nisyros-2 can be considered to be a mixture made up of ~50 % of PHL and ~50 % of local seawater.

What is the origin of PHL? Craig (1961) suggested that hydrothermal liquids originate from local meteoric precipitations. The often observed enrichment of ^{18}O in thermal waters relative to corresponding meteoric waters was attributed to exchange of O isotopes with the surrounding rocks at low water-rock ratios. Instead, the δD value of the exchanging meteoric waters remains almost unaffected because the abundance of hydrogen in rocks is much lower than that of oxygen. However, in the case of Nisyros, the δD value of the PHL is 10 to 15‰ higher than that of local meteoric waters. Significant D-enrichments relative to local meteoric waters seem to be common for hydrothermal systems that are located along convergent-plate margins. Giggenbach (1992), therefore, postulated the existence of a new andesitic (or arc-type) magmatic endmember. In this respect, the PHL seems to be a mixture of andesitic-magmatic water with local Mediterranean seawater. Two peculiarities arise from the mixing trend displayed in Figure 9.16:

(1) Accepting that the δD values of arc-type magmatic water is –20 ‰ (in spite of the large uncertainty of ± 10 ‰ units), the fraction of magmatic water contributing to PHL would be ~75%. This is a very large value, compared to the typical contributions of magmatic waters for most geothermal systems, 10-35 %, although few values close to 60 % are also reported (Giggenbach, 1992). However, a parent brine with a δD close to –20 ‰ and a $\delta^{18}O$ close to +5 ‰ was identified at Montserrat in 1991-1992 (Chiodini et al., 1996), few years before the magmatic eruption which started in September 1995. These values indicates a fraction of magmatic water close to 70 %.

(2) In the case of Nisyros, mixing of arc-type magmatic water occurs with seawater, in contrast to what was recognised in most (if not all) geothermal systems situated along convergent plate margins, where arc-type magmatic water mixes with local groundwaters of meteoric origin. Besides, the contribution of seawater increases drastically for peripheral locations such as Phlegeton and Kaminakia.

Accepting the mixed magmatic-marine origin of PHL and extrapolating the seawater/ Nisyros-2 mixing line (i.e., following the approach of Brombach et al., 2003), the Cl concentration of PHL can be estimated to be either 78,920 mg/kg, based on the δD-Cl diagram (not shown), or 75,480 mg/kg, based on the $\delta^{18}O$-Cl plot (not shown). Extrapolation of the seawater/Nisyros-2 mixing line in the δD-Cl diagram indicates a Cl concentration of 98,340 mg/kg, corresponding to a Cl/H_2O molar ratio of 0.05, for the magmatic water, whose $\delta^{18}O$ results to be close to +6.9 ‰. The δD and $\delta^{18}O$ values and the Cl content of PHL and the magmatic water of Nisyros are comparable to those estimated by Brombach et al. (2003).

A very different interpretation of water isotopes was instead proposed by Kavouridis et al. (1999), Panichi et al. (2000), and Panichi and La Ruffa (2001). Kavouridis et al. (1999) suggested the presence of (i) a deep geothermal brine (DGB) of marine origin, that experienced an oxygen shift of +3.5 ‰ owing to prolonged circulation in high-temperature environments and (ii) a shallow geothermal water (SGW) produced through mixing of local groundwaters and steam condensates of deep derivation.

The isotopically heavy vapors emitted from the fumaroles of Stephanos and Polybotes Micros are considered to be separated at 100°C, i.e., to be originated through maximum steam loss from the DGB. In contrast, the isotopically light vapors discharged from the Kaminakia fumaroles are considered to be the product of maximum steam loss from the SGW. However, the hypothesis of maximum steam loss is consistent with the presence at the surface, or very close to it, not only of the separated vapors but also of the separated liquids. In contrast with this interpretation, no such liquids reach the surface in Nisyros island ! Even the thermal waters discharging along the coasts of the island do not contain any trace of boiled geothermal liquids (see section 9.9).

The model proposed by Kavouridis et al. (1999) was slightly modified by Panichi and La Ruffa (2001), who recognised that the 6‰ depletion in δD of the deep geothermal brine with respect to local seawater may be explained by addition of andesitic magmatic water to the isotopically modified seawater. The isotopic composition of well Nisyros-2 (Dotsika, 1992) was invoked to support this hypothesis. Partial involvement of andesitic magmatic water was also evoked for the shallow geothermal water. However, the magmatic contributions postulated by Panichi and La Ruffa (2001) are minor and their conceptual model is very different from that of Brombach et al. (2003), which was revisited above.

Concerning the shallow geothermal reservoir, it must be noted that it was met by the deep geothermal wells Nisyros-1 and Nisyros-2 and its presence under the fumarolic field was initially suggested by Chiodini et al. (1993a), based on the geochemistry and geothermometry of the gas samples collected during the 1990 survey. Apparent equilibrium temperature of 170-255°C were derived for the corresponding liquid using the H_2-H_2O-CO-CO_2-CH_4 geoindicator (Chiodini et al., 1993a). However, accepting that the H_2-H_2O-CO-CO_2-CH_4 geoindicator monitors, in the case of Nisyros, the temperature of last gas re-equilibration prior to vapor separation, as discussed above, it follows that the "shallow aquifer" of Chiodini et al. (1993a) does not exist at all below the hydrothermal crater area. In constrast, the liquids coming from the deep aquifer ascend locally, along faults and fractures, at relatively shallow depths. These depths vary from location to location and appear to be largest underneath Polybotes Micros, since here the temperatures derived from the H_2-H_2O-CO-CO_2-CH_4 geoindicator are closest to deep aquifer temperature.

9.8. Changes in fumarolic gas chemistry with time

Chiodini et al. (2002) found decreasing CH_4/CO_2 ratios, accompanied by increasing H_2S/CO_2 ratios, for the period 1997-2001. Simultaneously, the CO content rose.

Changes in the chemical composition of Nisyros fumarolic gases are suitably investigated using the ternary plots of H_2O-CO_2-H_2S (Figure 9.17) and H_2-CH_4-CO (Figure 9.18). The observed shift in chemical composition is most pronounced for Phlegeton fumaroles. For this location, three groups can be identified: group 1 comprises the data measured from 1990 to 1997, group 2 includes the samples taken in 1998 and 1999, and group 3 refers to the period 2000-2002. Compared to group 1, group 3 is 5-6 fold depleted in CH_4 and up to 2 fold enriched in H_2S, whereas group 2 is intermediate between groups 1 and 3. For the central locations of Polybotes Micros and Stephanos both the depletion in CH_4 and the enrichment in H_2S are not as pronounced as for Phlegeton. The time-dependent depletion in CH_4 is not visible at all for Kaminakia fumaroles.

The observation that the depletion in CH_4 goes along with an increase in H_2S seems to provide evidence for a possible change in the redox regime of the deep aquifer towards more oxidizing conditions owing to an increased input of magmatic SO_2.

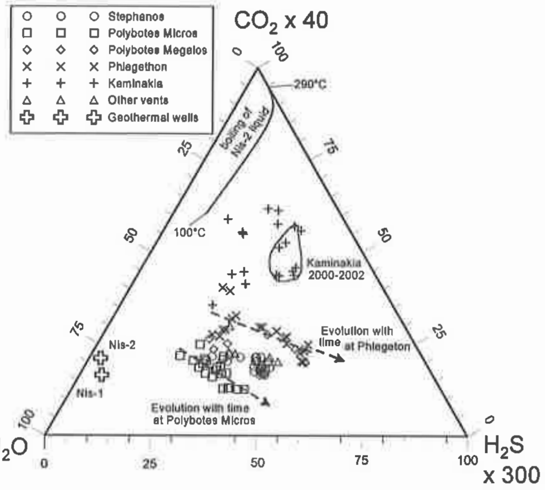

Figure 9.17. Triangular diagram H_2O-CO_2-H_2S for the fumaroles and geothermal wells of Nisyros. The composition of the gases separated through single-step boiling from the liquid tapped by well Nisyros-2 is also shown.

Since enrichment and depletion trends of gas species are not unique for all locations, one may conclude that the input of magmatic SO_2 into the deep aquifer varied locally. If a magmatic gas pulse occurred, it seems that it did not cause any detectable increase in aquifer temperature relative to the 80's, because temperatures inferred from carbon isotope thermometry and from extrapolation of restored CO/CO_2 and H_2/H_2O values virtually coincide with those measured 20 years ago. Further, the magmatic SO_2 pulse must have been of relatively low intensity, so that the redox conditions of the aquifer were not significantly affected: present aquifer temperatures have been extrapolated from restored CO/CO_2 and H_2/H_2O values under the assumption that the strongly reducing hydrothermal FeO-$FeO_{1.5}$ buffer governs the redox conditions of the deep aquifer since the year 2000. If SO_2 injection occurred, the Nisyros hydrothermal system must have been somewhat more reducing than predicted by the FeO-$FeO_{1.5}$ buffer before the period of seismic unrest, because SO_2 is an oxidizer. Hydrothermal redox conditions more reducing than expressed by the FeO-$FeO_{1.5}$ buffer could be produced by the dominance of the mineral assemblage fayalite-magnetite-quartz (FMQ). However, the FMQ redox buffer is typical of basaltic environments (e.g., Taran et al., 2002), but not of subduction zone settings.

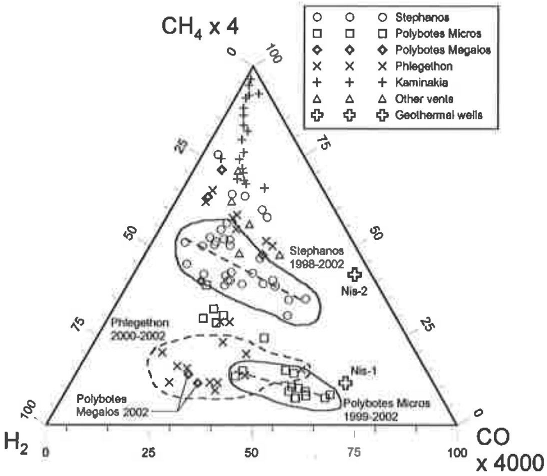

Figure 9.18. *Triangular diagram H_2-CH_4-CO.*

Secondary processes that may affect the chemical composition of fumarolic vapor are condensation, vapor-liquid separation and re-equilibration in the single liquid phase. In the previous chapter we provided evidence that negligible to no condensation occurred at Polybotes Micros, Stephanos and Phlegeton. Underneath these locations, the process of vapor separation was assumed to take place in a single-step. However, single-step vapor separation cannot cause the compositional variations that are observed for these locations in Figure 9.18, because the water solubilities of CO, H_2, and CH_4 vary within less than one order of magnitude. Re-equilibration processes can only be responsible for the observed compositional shifts if any change in physicochemical conditions lead to significant removal of CH_4. In this context, it is interesting to note that the seismic crisis also went along with a significant increase in CO content for Polybotes Micros and, to a lesser extent, for Stephanos discharges. Accepting that the CO content reliably reflects biphase-hydrothermal parameters, the increase in CO corresponds to an increase in vapor separation temperatures of up to 50°C underneath Polybotes Micros and up to 10°C underneath Stephanos, respectively. This possibly implies that the biphase hydrothermal zone moved downwards, i.e., towards the deep aquifer underneath these locations.

In Figure 9.18, Kaminakia fumaroles plot closest to the CH_4 vertex, although the solubility in liquid water at temperatures < 100°C decreases in the order $CH_4 > H_2 > CO$. During Rayleigh-type condensation, CH_4, therefore, should have been removed most effectively from the residual vapor phase and Kaminakia data should plot much closer to the CO vertex. However, Kaminakia discharges also experienced the highest degrees of CO and H_2-re-equilibration, because the temperatures of re-equilibration inferred from Figure 9.11 are much lower than the temperature of the deep aquifer as reflected by carbon isotopes. In this respect, CO and H_2 had already been removed in significant amounts, before enrichment due to Rayleigh condensation occurred. As there is no trend visible, it seems that both effects are of equal importance for Kaminakia discharges.

Summing up, there is no simple mechanism that can explain all the compositional variations

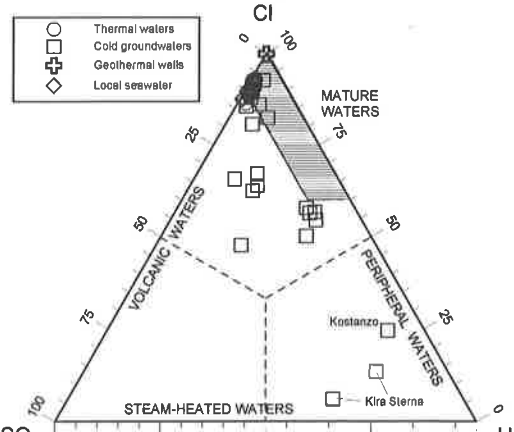

Figure 9.19. *Cl^--SO_4^{2-}-HCO_3^- triangular plot for the waters of Nisyros Island (from Giggenbach, 1991).*

observed for all the locations of fumarolic gas discharge. Rather, it seems that coupled primary effects (injection of magmatic SO_2) and secondary effects (changes in redox conditions of liquid-phase re-equilibration) are responsible for the compositional variations that occurred after the seismic crisis.

9.9. Chemistry, isotope chemistry, and geothermometry of thermal waters

9.9.1 Water chemistry

The relative ratios between main anions (Cl^-, SO_4^{2-}, and HCO_3^-) and main cations [(Na^++K^+), Ca^{2+}, and Mg^{2+}] are displayed in the triangular plots of Figures 9.19 and 9.20, respectively, for the thermal waters (outlet temperature ≥ 33°C), cold groundwaters (outlet temperature ≤ 28°C), local seawater, and the liquids discharged from the deep geothermal wells Nisyros-1 and Nisyros-2.

The two triangular plots clearly show that: (i) cold groundwaters have variable composition, from Ca^{2+}-HCO_3^- to Na^+-Cl^-, (ii) thermal waters have Na^+-Cl^- composition and are situated very close to the samples of local seawater in both diagrams; thermal waters are therefore compositionally similar to local seawater, at least on the basis of the relative ratios between main anions and main cations.

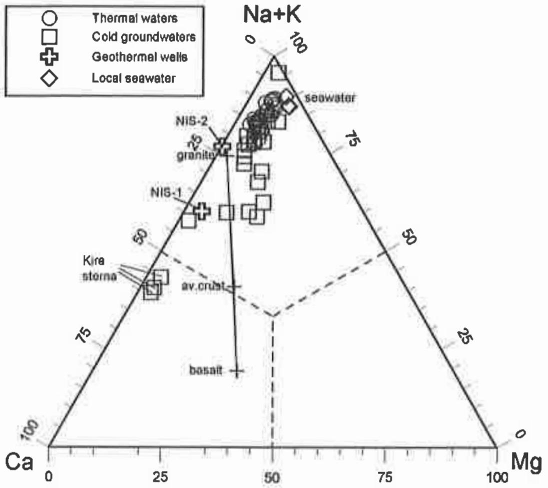

Figure 9.20. (Na^++K^+)-Ca^{2+}-Mg^{2+} triangular plot for the waters of Nisyros Island, also showing the average composition of granite, basalts, and of the average crust.

9.9.2. Isotope chemistry of waters

9.9.2.1. The δD and $\delta^{18}O$ values of H_2O

Further indications are provided by the δD and $\delta^{18}O$ values of H_2O, which are reported against chloride concentration in the plots of Figure 9.21.

Among the cold groundwaters, the samples from the stagnant pool of Thermiani are of little interest as their isotopic characteristics are strongly affected by kinetic effects during surface evaporation. The same process seems to influence also the water from Peroulis well. All the other groundwaters define the possible δD and $\delta^{18}O$ values and chloride concentrations expected upon dilution of seawater, i.e., addition of local groundwaters to local marine waters.

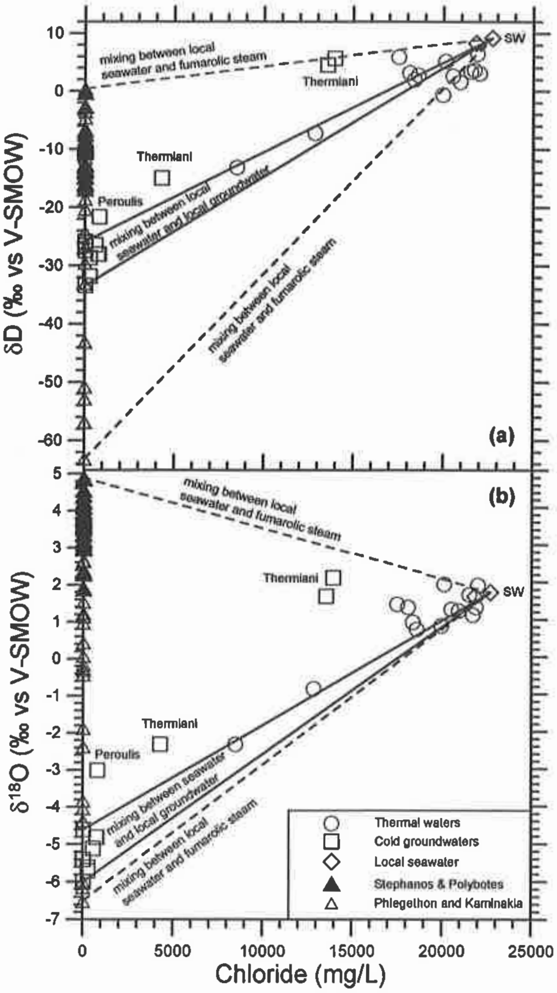

Figure 9.21. Plots of (a) δD and (b) $\delta^{18}O$ values of H_2O versus chloride concentrations for the waters of Nisyros Island. Fumarolic steam samples are shown for comparison.

Also shown in these diagrams are the isotope compositions and chloride concentrations controlled by mixing of seawater with fumarolic steam. Owing to the large variations in the D/H and $^{18}O/^{16}O$ isotope ratios of fumarolic steam (section 9.7), its addition to local seawater determines a very large spread in isotope composition, much larger than that caused by seawater dilution and encompassing it. These findings are different from those of Kavouridis et al. (1999), which were based on a limited number of fumarolic steam samples.

In spite of the overlapping of the fields of seawater-groundwater mixing and seawater-fumarolic steam mixing, comparison of the δD vs. chloride and $\delta^{18}O$ vs. chloride diagrams allows to distinguish the two processes. Not surprisingly, the thermal waters are found close to the seawater point and their spread is ascribable to addition of fumarolic steam (or steam condensates) of variable isotope composition rather than to seawater-groundwater mixing.

Of course, the involvement of steam rather than steam condensate cannot be distinguished by means of the chloride-isotope plots of Figure 9.21, whereas the enthalpy-chloride plot can be used to this purpose (see section 9.9.3.4).

9.9.2.2. The $\delta^{34}S$ values of dissolved sulfate

The few available $\delta^{34}S$ values of dissolved sulfate in thermal waters and local seawater (Brombach et al., 2003) are plotted against sulfate concentration in Figure 9.22. For comparison, the $\delta^{34}S$ values of H_2S in fumarolic gases (see section 9.5.6) are also represented in this plot. To this purpose, the H_2S concentration of fumarolic gases has been converted to mg/L of sulfate. Also shown in Figure 9.22 are the mixing lines between marine sulfate and fumarolic sulfur, considering the two fumarolic gases with the highest and lowest H_2S concentration. The isotopic ratios of binary mixtures were computed by means of the general binary mixing equation (Langmuir et al., 1978; Faure, 1986) reported above (equation 2).

Thermal waters are situated to the left of the mixing lines between marine sulfate and fumarolic sulfur and close to the seawater endmember, as they have $\delta^{34}S$ values of SO_4^{2-} similar to or somewhat lower than those of marine sulfate and SO_4^{2-} concentration somewhat lower than those of local seawater. To explain this shift with respect to these mixing lines, it is necessary to admit that the marine endmember has lost some sulfate, contrary to what is suggested by Brombach et al. (2003). Among the possible processes for this loss of sulfate, the precipitation of anhydrite and the bacteria-mediated reduction of dissolved SO_4^{2-} appear to be the most likely candidates.

Precipitation of anhydrite appears to be a possible explanation for the sulfate loss experienced by thermal waters, assuming that they come from environments with temperatures close to 100°C (see section 9.9.3.3). It must be underscored that precipitation of anhydrite brings about a negligible fractionation of the S isotopes of dissolved sulfate.

Bacterial sulfate reduction produces either H_2S or HS^- or S^{2-} depending on pH, which are expected to separate from thermal waters either as solid sulfides, mainly pyrite, or as gaseous H_2S. The $\delta^{34}S$ value of the remaining sulfate (i.e., not involved in the reductive process) is expected to increase significantly owing to bacterial sulfate reduction (e.g., Marini et al., 2000b), although the extent of this increase depends on several factors, such as the extent of reduction, the separation mechanism (open- or closed-system), the type of fractionation (kinetic or equilibrium), etc. (Ohmoto and Goldhaber, 1997).

Considering that both $\delta^{34}S$ values and SO_4^{2-} concentrations of thermal waters are similar to those of local seawater, anhydrite precipitation seems to be much more important than bacteria-mediated reduction of dissolved SO_4^{2-}.

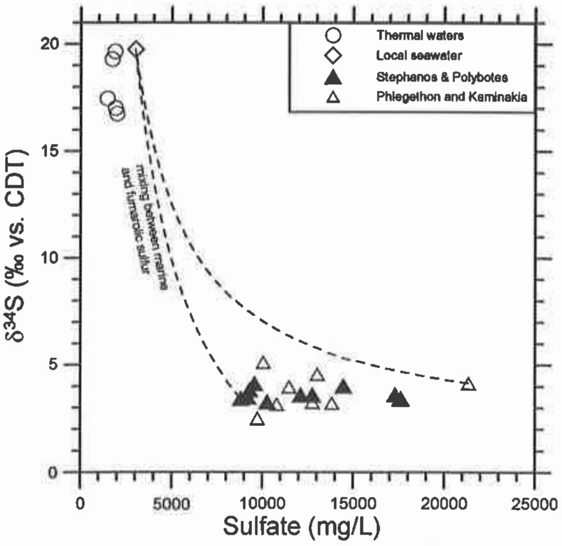

Figure 9.22. Plot of $\delta^{34}S$ values of dissolved sulfate vs. sulfate concentration, for the waters of Nisyros Island. Also shown are the samples of fumarolic gases, whose H_2S concentration has been expressed as mg/L of sulfate, and the mixing lines between marine and fumarolic sulfur.

9.9.3. Geothermometry of thermal waters

9.9.3.1. The Na-K-$Mg^{0.5}$ triangular diagram of Giggenbach (1988)

The Na-K-$Mg^{0.5}$ triangular diagram of Giggenbach (1988) is one of the most powerful graphical tools for the chemical thermometry of geothermal liquids. In this diagram (Figure 9.23), only the reservoir liquid tapped from well Nisyros-2 plots relatively close to the full equilibrium line, albeit indicating a Na-K temperature of 256 °C and a K-Mg temperature of 218 °C, both of which are significantly lower than the temperature measured in the productive interval of the well (~290 °C) and the equilibrium temperature suggested by gas equilibria (270-320 °C, see above).

Also in this plot, thermal waters are situated close to the samples of local seawater, suggesting again their partial marine origin. These thermal waters are found near the boundary line separating the field of partially equilibrated waters from that of immature waters. Their Na-K temperatures, 200 ± 14 (1σ) °C, have no physical meaning, owing to the long time required for the re-equilibration of the Na-K ratio, especially at low temperatures. In contrast, K-Mg temperatures, 119 ± 9 °C, could still be realistic, due to the higher speed with which the K-Mg geothermometer adjusts to temperature variations with respect to the Na-K system.

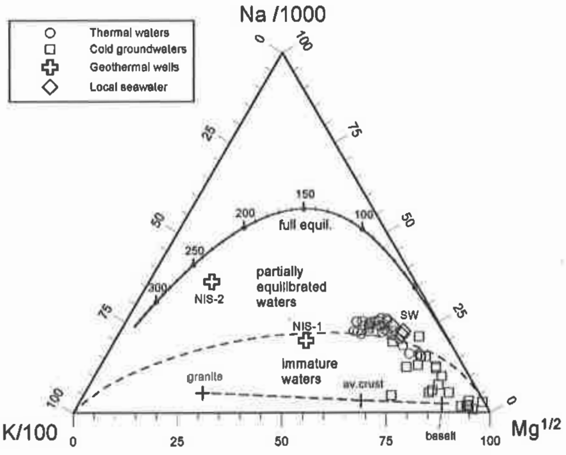

Figure 9.23. *The Na-K-$Mg^{0.5}$ triangular diagram of Giggenbach (1988) for the waters of Nisyros.*

9.9.3.2. The plot of log(K^2/Mg) vs. log(SiO_2)

Another useful graphical technique is obtained by combining the two chemical subsystems responding most quickly and with comparable speed to changes in temperatures, that is those based on dissolved silica and on the K^2/Mg ratio (Giggenbach, et al., 1994). In this plot (Figure 9.24a), the thermal waters of Nisyros indicate silica temperatures of 142 ± 25 °C, assuming that they cool conductively, as already underscored by Kavouridis et al. (1999). However, the reliability of these silica temperatures is undermined by the achievement of saturation with respect to either amorphous silica or opal-CT at outlet temperatures, not only for the thermal waters, but also for the cold groundwaters (Figure 9.24b). The almost ubiquitous attainment of these conditions for all the waters of Nisyros Island, apart from few samples affected by mixing with silica-poor seawater, prevents the use of silica geothermometers.

9.9.3.3. The saturation temperature with anhydrite

The temperature of anhydrite saturation (equilibrium) represents another possible geothermometric technique of interest for the thermal waters of Nisyros Island. The calculation of this temperature is not straightforward but requires use of geochemical modeling codes. First, the chemical speciation of the aqueous solution have to be reconstructed at outlet temperature. Then, the progressive heating of the considered aqueous solution have to be simulated.

In this contribution, the first step was carried out by using the code EQ3NR (Wolery, 1992), whereas the second step was performed by means of the program EQ6 (Wolery and Daveler, 1992). Reference was made to the COM thermodynamic database, which includes a large number of solid, aqueous, and gaseous species, whose thermodynamic properties are mostly derived from Johnson et al. (1992). In particular, the standard state thermodynamic properties of anhydrite are from Helgeson et al. (1978). Activity coefficients of ionic species were computed by means of the modified (B-dot) Debye- Hückel equation, although the stoichiometric ionic strength of the thermal waters of Nisyros is 0.62 ± 0.14 mol/kg. Calculations were carried out not only for all the thermal waters but also for the local seawater samples and average seawater, for comparison.Seawater attains saturation with respect to anhydrite at 141 ± 12 (1σ) °C, upon heating along the vapor-liquid P-T curve for water, whereas thermal waters saturate with anhydrite at 101 ± 12 °C upon heating, with most samples equilibrating with anhydrite between 90 and 110 °C, apart from three samples from the thermal spring of Pali (with low chloride concentration and equilibrium temperature close to 120°C), one sample from Loutra (with the highest Ca concentration and equilibrium temperature of 82°C), and a sample from Katsouni (with the highest SO_4^{2-} concentration and equilibrium temperature of 59°C), as shown in the plot of Figure 9.25.

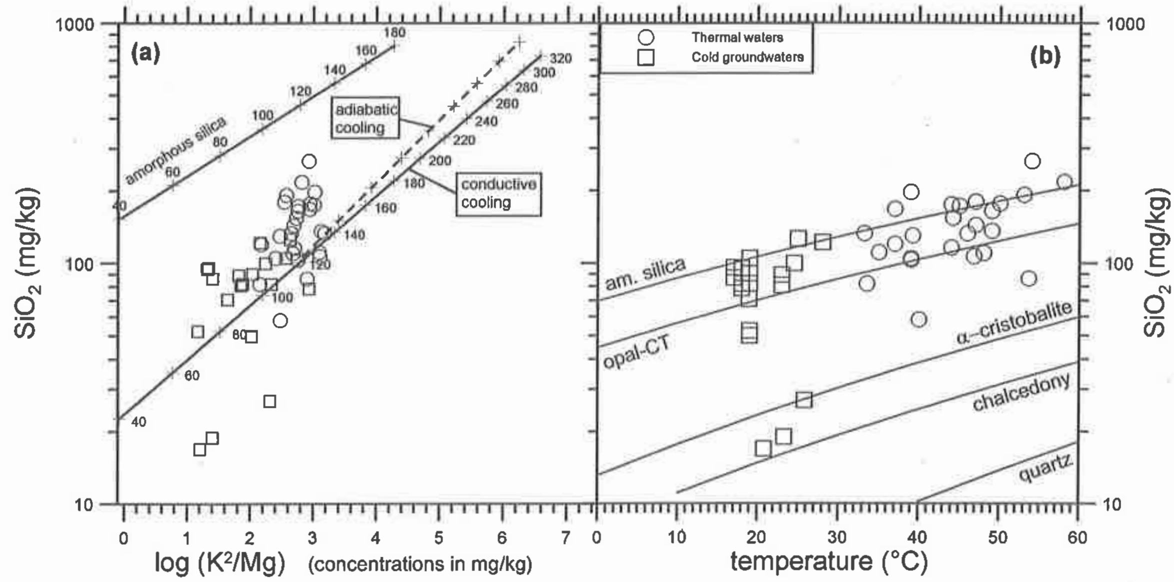

Figure 9.24. Plots of (a) log(SiO_2) vs. log(K^2/Mg) (from Giggenbach et al., 1994) and (b) log(SiO_2) vs. outlet temperature for the waters of Nisyros Island.

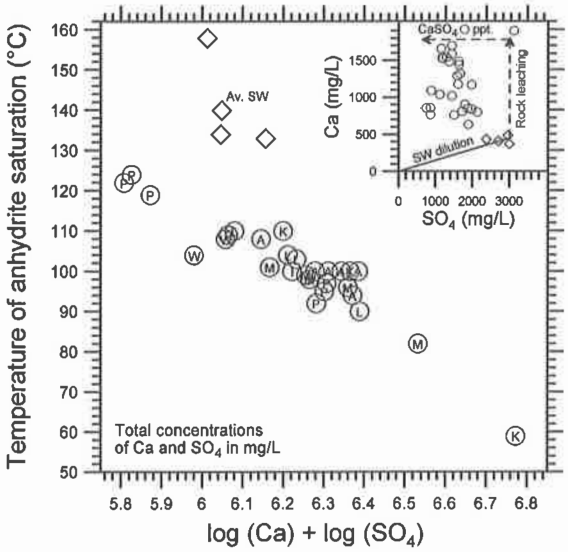

Figure 9.25. The temperature of saturation with respect to anhydrite for the thermal waters of Nisyros Island (A = Avlaki spring, I = Irini spring, K = Katsouni spring, L = Levkos spring, M = Loutra spring, P = Pali spring, W = Pali shallow well) is compared with the sum of the logarithms of total Ca and total SO_4 concentrations, both in mg/L. The correlation diagram between total Ca and total SO_4 concentrations is shown in the inset.

Not surprisingly, anhydrite saturation temperatures are linearly, negatively correlated with the sum of the logarithms of total Ca and total SO_4^{2-} concentrations (R = -0.930). The lower temperature of saturation with anhydrite of thermal waters, with respect to seawater, is probably regulated by acquisition of Ca through interaction of thermal waters with volcanic rocks, also causing sulfate loss through anhydrite precipitation, as suggested by the Ca vs. SO_4^{2-} plot (see inset in Figure 9.25). Indeed, although thermal waters originate through dilution of seawater (by addition of fumarolic steam or steam condensate, see section 9.9.2.1 and 9.9.3.4), their Ca concentrations are significantly higher (up to a factor 4) than those of local seawater samples.

All in all, it seems reasonable to accept the attainment of temperatures close to 100°C, during the heating and dilution of seawater, leading to the generation of Nisyros thermal waters.

9.9.3.4. The enthalpy-chloride plot

As mentioned in section 9.9.2.1, the enthalpy-chloride plot (Fournier, 1979) can be used, in principle, to identify the fluid involved in the heating and dilution of seawater, either fumarolic steam or steam condensate, originating the thermal waters discharging along the coast of the island. Although both fumarolic (saturated) steam and steam condensate have negligible to nil Cl concentration, their enthalpy is very different, 2676-2804 J/g for the former against 419 J/g, at 100°C, 1 bar for the latter. Consequently they are situated far apart in the enthalpy-chloride plot (Figure 9.26).

Accepting that seawater attains temperatures close to 100°C (see previous section), addition of fumarolic steam rather than steam condensate has to be invoked necessarily, followed by conductive cooling at outlet temperature.

Alternatively, addition of both fumarolic steam and steam condensate, in varying proportions could explain the outlet enthalpies and chloride concentrations of most thermal waters, with Cl > 17,000 mg/L. Conductive cooling after addition of steam condensate have to be hypothesised for the thermal springs with Cl < 15,000 mg/L.

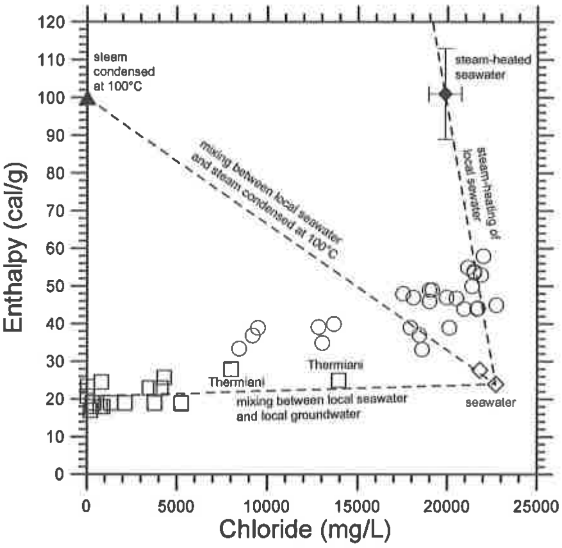

Figure 9.26. Enthalpy-chloride plot for the waters of Nisyros Island (from Fournier, 1979).

9.9.3.5. Geothermometry of thermal waters: a synthesis

Although the use of SiO_2 geothermometers is prevented because thermal waters attain saturation with either amorphous silica or opal-CT and the Na-K geothermometer gives unrealistic results, average equilibrium temperatures of 100 or 120°C have been estimated based on anhydrite saturation or the K-Mg geothermometer, respectively.

Accepting the attainment of temperatures close to 100°C, heating of seawater requires direct involvement of fumarolic steam, whereas addition of both fumarolic steam and steam condensate, is consistent with the outlet characteristics of most thermal waters.

9.10. The updated conceptual geochemical model of the magmatic-hydrothermal system of Nisyros

Based on previous discussion, the conceptual geochemical model of the magmatic-hydrothermal system of Nisyros, first proposed by Chiodini et al. (1993a, see section 9.4), is updated as follows.

A degassing magma body, possibly a rhyodacitic melt produced through fractional crystallization from a parent basaltic magma, is present at unknown depth below the caldera of Nisyros. The parent basaltic magma has a $\delta^{34}S$ value of +4‰, as suggested by Marini et al. (2002), chiefly based on the $\delta^{34}S$ of fumarolic H_2S, and confirmed, in this work, by newly acquired $\delta^{34}S$ values and S concentrations of volcanic rocks from Nisyros and Yali. The $\delta^{34}S$ value of the parent basaltic magma of +4‰ is significantly higher than that of pristine mantle, 0‰, probably due to mantle contamination, through either transference of fluids derived from subducted materials or involvement of altered oceanic crust. In contrast, the contribution of biogenic sulfides from subducted sediments appears to be small or absent.

The gases released by the degassing magma body contains H_2O with a δD value close to –20 ‰, as is typically observed along convergent plate margins. Besides, these gases are characterised by relatively high $^3He/^4He$ ratios (close to 6.2 Ra or higher), which is also typical of this type of geodynamic framework, and contain a significant fraction of radiogenic Ar (close to 0.6 or higher).

In contrast to the magmatic gases from other island arc systems, the gases of Nisyros have low N_2/Ar and N_2/He ratios, likely due to lack of N-rich sedimentary materials in the subducted slab. Consistent with this indication and that given by S isotopes, the $\delta^{13}C$ values of CO_2 suggest that the contribution of CO_2 through thermal degradation of sedimentary organic matter is virtually absent or undetectable. These peculiar characteristics of Nisyros can be probably extended to the whole Aegean island arc.

The gases released from the degassing magma body enter the overlying hydrothermal aquifer from below, supplying matter and heat. Under the central parts of the area of the hydrothermal craters, the contribution of arc-type magmatic water is close to 75 %, whereas the remaining 25 % of water is of marine provenance. However, the contribution of seawater increases moving towards peripheral locations, such as Kaminakia and Phlegeton. The involvement of seawater is a peculiarity of the magmatic-hydrothermal system of Nisyros, as in most (if not all) such systems situated along convergent plate margins, arc-type magmatic water mixes with groundwater rather than with seawater, as at Nisyros.

The deep hydrothermal aquifer has temperatures up to 340°C or somewhat higher (as indicated by partition of C isotopes between CO_2 and CH_4 and chemical geothermometry of fumarolic effluents) and host high-salinity aqueous solutions with Cl concentrations up to 75,500-78,900 mg/kg (as shown by water isotopes-chloride relationships).

Indeed, a reservoir liquid with 50,400 mg/kg Cl and a temperature close to 290°C was tapped by the deep geothermal well Nisyros-2.

Below the area of the hydrothermal craters, the deep hydrothermal liquids rise towards the surface, along faults and fractures, and cool conductively from the initial reservoir temperatures to average temperatures of 195 to 284°C (see T_O values in Table 9.6). Then boiling sets in and vapors separate completely from the conductively cooled deep hydrothermal liquids at average temperatures of 195 to 271°C (as suggested by CO-based geothermometers, see T_S values in Table 9.6) and are finally discharged at the surface either experiencing negligible condensation (e.g., from the Stephanos and Polybotes Micros craters, as shown by water isotopes) or significant condensation, a process which is especially important for the fumaroles of Kaminakia.

Assuming a vapor-static regime from the zone where the vapor phase is completely separated from the liquid phase (at temperature T_S) to the surface discharge (at temperature close to 100°C), the depth of the vapor/liquid separation zone can be evaluated to be close to 490 m for T_S = 195°C and 765 m for T_S = 271°C.

In addition to these hydrothermal vapors discharged by the fumarolic vents, another even more important flux of vapors ascends towards the surface in the area of the hydrothermal craters and adjacent parts of the Lakki plain, as testified to by the high CO_2 fluxes from soil and elevated soil temperatures measured in this area. Steam mostly condenses close to the surface, while both CO_2 and heat are released to the atmosphere. A total hydrothermal CO_2 output of 67.8 t/d, accompanied by a condensed steam flux of 1420 t/d (16 kg/s) and a heat flux of 42.5 MW occur from a total area of 2.1 km^2 (Caliro et al., 2005).

This remarkable flux of vapors occupies a sort of central irregular column, whose shape is locally controlled by the presence of faults and fractures, situated above the deep hydrothermal aquifer. Consequently, the shallow aquifer is not present in this area, contrary to previous conclusions by Chiodini et al. (1993a). However, the shallow aquifer, with temperatures up to 120-180°C, is present in nearby areas, as proven by the deep geothermal wells (see section 9.2).

It is likely that the condensed steam flows from the area of the hydrothermal craters and adjacent parts of the Lakki plain towards the coasts of the island, thus contributing to feed the thermal springs, although its partial recycle (i.e., infiltration at depth and re-entrainment in the ascending vapor flow) cannot be ruled out. These thermal waters have chemical compositions similar to that of seawater and originate through addition of fumarolic steam and/or steam condensate to local seawater infiltrating inland and interacting with volcanic rocks. The average equilibrium temperature of these waters is close to 100°C (based on anhydrite saturation) – 120°C (based on the K-Mg geothermometer).

We hope that this work may be of help for the volcanic surveillance of this Earthly Paradise, locally resembling hell.

Acknowledgements – We are indebted to Annett Buettner and Barbara Gambardella for providing sulfur contents and isotope data on volcanic rock samples from Nisyros and Yali. Helpful comments on the manuscript were provided by Torsten Vennemann.

Table 9.1. Chemical and isotopic data of fumarolic gas samples from Nisyros Island and average total discharge from the deep geothermal wells Nisyros-1 and Nisyros-2 .

Sample	date	T (°C)	H_2O ppmv	CO_2 ppmv	H_2S ppmv	H_2 ppmv	N_2 ppmv	CH_4 ppmv	CO ppmv	He ppmv	Ar ppmv	O_2 ppmv	δD_{H2O} ‰	$\delta^{18}O_{H2O}$ ‰	$\delta^{18}O_{H2O,CORR}$ ‰	$\delta^{18}O_{CO2}$ ‰
S3	Sep-1990	nd	987000	10730	2330	73.1	157	58.4	0.02	nd	nd	nd	nd	nd	nd	nd
S4	Sep-1990	nd	987000	10710	2190	84.9	39	59.9	0.016	nd	nd	nd	nd	nd	nd	nd
S	Oct-1991	nd	987000	10725	1911	84.5	52	76.7	0.0052	0.26	0.923	nd	-14	+1.4	+2.0	nd
S4	Nov-1997	nd	985000	12220	2710	112	27	92.9	0.053	0.363	0.275	nd	-13	+4.3	+4.9	nd
S16	Nov-1997	nd	985000	11960	2390	91.7	19	78	0.039	0.26	0.14	nd	-10	+4.0	+4.6	nd
S4	Sep-1998	104	983000	13240	3240	139	55.6	69.9	0.026	0.650	0.776	0	-11	+3.5	+4.1	nd
S15	Sep-1998	99.0	984000	12500	3290	133	55.2	41.4	0.009	0.595	0.567	7.400	-9	+3.4	+4.0	nd
S16	Sep-1998	99.6	984000	12660	3300	123	58.1	47.3	0.019	0.652	0.864	0.905	-8	+3.5	+4.1	nd
S4	Sep-1999	99.5	983000	13240	3780	111	261	33.1	0.031	0.533	3.290	0	-10	+3.7	+4.2	+39.2
S15	Sep-1999	99.6	983000	13320	3760	123	29.7	41.2	0.014	0.564	0.306	0	-14	+2.5	+3.1	nd
S16	Sep-1999	99.3	983000	13800	3460	131	30.0	54.1	0.028	0.569	0.287	0	-8	+4.2	+4.9	nd
S16	May 2000	nd	983000	13400	3300	105	28.1	44.1	0.019	0.421	0.322	0	nd	nd	nd	nd
S4	Sep-2000	99.8	985000	11100	3490	78.8	26.5	28.2	0.031	0.339	0.386	0	-14	+3.9	+4.4	nd
S15	Sep-2000	99.3	984000	12070	3840	105	239	27.5	0.022	0.407	3.128	0	-15	+3.0	+3.5	nd
S16	Sep-2000	99.6	984000	11850	3450	101	57.0	45.0	nd	0.384	0.922	0	nd	nd	nd	nd
S17	Sep-2000	99.3	984000	12340	3240	99.0	29.8	25.7	0.014	0.397	0.443	0	-17	+2.6	+3.2	nd
S4	Feb-2001	100	985291	11137	3435	89.0	15.0	33.0	0.014	0.377	0.099	0.020	-16	+3.4	+3.9	nd
S15	Feb-2001	99.8	984847	11463	3528	111	18.1	32.0	0.026	0.406	0.190	0.058	-13	+3.3	+3.9	nd
S16	Feb-2001	99.2	985402	11235	3202	100	15.9	44.8	0.016	0.362	0.113	0	-16	+3.1	+3.7	nd
S17	Feb-2001	99.7	984404	11792	3660	98.6	15.8	28.9	0.021	0.388	0.113	0	-15	+3.0	+3.5	nd
S4	Jun-2001	99.3	986000	10900	3440	86.6	20.0	32.0	0.029	0.340	0.220	0.000	nd	nd	nd	nd
S15	Jun-2001	99.3	985000	11400	3490	99.3	20.9	38	0.013	0.38	0.21	0.000	nd	nd	nd	nd
S16	Jun-2001	100.3	984000	12100	3500	110	27.2	48	0.023	0.4	0.31	0.000	nd	nd	nd	nd
S17	Jun-2001	101.7	985000	11100	3660	125	19.1	32.3	0.011	0.42	0.18	0.000	nd	nd	nd	nd
S4	Sep-2001	99.8	986000	10400	3490	84	440	31.1	0.049	0.35	5.37	0.000	nd	nd	nd	nd

Table 9.1. (continued)

Sample	date	T (°C)	H_2O ppmv	CO_2 ppmv	H_2S ppmv	H_2 ppmv	N_2 ppmv	CH_4 ppmv	CO ppmv	He ppmv	Ar ppmv	O_2 ppmv	δD_{H2O} ‰	$\delta^{18}O_{H2O}$ ‰	$\delta^{18}O_{H2O,CORR}$ ‰	$\delta^{18}O_{CO2}$ ‰
S15	Sep-2001	101.4	986000	10800	3510	91.8	15.5	37.5	0.043	0.35	0.12	0.000	nd	nd	nd	nd
S16	Sep-2001	100.2	985000	11000	3400	97.5	18	44.3	0.076	0.37	0.15	0.000	nd	nd	nd	nd
S17	Sep-2001	101.4	986000	10700	3570	94	12.8	27.6	0.052	0.35	0.08	0.000	nd	nd	nd	nd
S4	Feb-2002	98.6	986000	10000	3430	79.1	12.6	30.6	0.038	0.32	0.07	0.000	nd	nd	nd	nd
S15	Feb-2002	98.8	986000	10400	3570	99.6	16.5	31.4	0.023	0.38	0.12	0.000	nd	nd	nd	nd
S16	Feb-2002	98.8	986000	10300	3220	89	14.1	41.6	0.034	0.32	0.1	0.000	nd	nd	nd	nd
S17	Feb-2002	99.2	986000	10300	3620	104	13.6	29.2	0.023	0.34	0.09	0.000	nd	nd	nd	nd
PP9N	Sep-1990	nd	989000	9250	1500	138	47.6	25.9	0.026	nd	nd	nd	nd	nd	nd	nd
PP	Oct-1991	nd	989000	9427	1221	149.6	40.7	35.2	0.0231	0.264	0.638	nd	-7	+3.2	+3.7	nd
PP9N	Nov-1997	nd	988000	9730	1790	159	16.1	29.1	0.035	0.216	0.146	nd	-10	+2.9	+3.4	nd
PP9S	Nov-1997	nd	988000	10000	1740	154	74.8	26.9	0.060	0.183	0.818	nd	-13	+2.5	+3.0	nd
PP9N	Sep-1998	99.0	990000	8490	1650	171	30.6	27.0	0.028	0.368	0.310	0.085	-10	+3.2	+3.6	nd
PP9S	Sep-1998	99.0	989000	9230	1720	167	18.8	26.8	0.034	0.358	0.195	0.061	-9	+3.0	+3.4	nd
PP9N	Sep-1999	99.8	986000	11330	2210	237	22.7	26.6	0.117	0.571	0.196	0	-7	+3.2	+3.7	+38.7
PP9S	Sep-1999	99.8	986000	12030	1570	223	18.4	24.9	0.121	0.535	0.120	0	-9	+3.2	+3.7	nd
PP9N	May-2000	nd	989000	8700	2050	204	27.3	17.5	0.061	0.431	0.336	0	nd	nd	nd	nd
PP9S	May-2000	nd	988000	9600	2160	158	48.2	10.2	0.079	0.265	0.688	0	nd	nd	nd	nd
PP9N	Sep-2000	100	988000	9190	2070	228	37.2	17.5	0.118	0.447	0.611	0	-16	+2.8	+3.2	nd
PP9S	Sep-2000	100	989000	8340	2210	153	30.1	10.3	0.115	0.259	0.571	0	-13	+3.4	+3.8	nd
PP9N	Feb-2001	nd	990202	7564	1990	214	13.1	15.1	0.0190	0.388	0.112	0.026	-10	+1.4	+1.7	nd
PP9S	Feb-2001	99.9	990030	7867	1819	250	15.7	18.2	0.069	0.462	0.124	0	-10	+3.9	+4.3	nd
PP9N	Jun-2001	98.7	989000	8700	2340	212	18	11.1	0.113	0.35	0.24	0.000	nd	nd	nd	nd
PP9S	Jun-2001	101.3	991000	6200	2300	120	17	9.2	0.067	0.19	0.23	0.000	nd	nd	nd	nd
PP9N	Sep-2001	101.1	991000	6410	2450	133	9.7	8.3	0.08	0.2	0.12	0.000	nd	nd	nd	nd
PP9S	Sep-2001	100.5	991000	6440	2420	136	8.6	7.2	0.072	0.19	0.1	0.000	nd	nd	nd	nd

Table 9.1. (continued)

Sample	date	T (°C)	H_2O ppmv	CO_2 ppmv	H_2S ppmv	H_2 ppmv	N_2 ppmv	CH_4 ppmv	CO ppmv	He ppmv	Ar ppmv	O_2 ppmv	δD_{H2O} ‰	$\delta^{18}O_{H2O}$ ‰	$\delta^{18}O_{H2O,CORR}$ ‰	$\delta^{18}O_{CO2}$ ‰
PP9N	Feb-2002	99.2	990000	6740	2900	134	6	10.6	0.108	0.21	0.03	0.000	nd	nd	nd	nd
PP9S	Feb-2002	99.4	991000	6510	2710	103	5.4	7.5	0.062	0.16	0.04	0.000	nd	nd	nd	nd
A12	Sep-1990	nd	981000	16200	2070	97.4	38.4	58.9	0.009	nd	nd	nd	nd	nd	nd	nd
A13	Sep-1990	nd	971000	25200	2150	192	1660	115	0.044	nd	nd	nd	nd	nd	nd	nd
A14	Sep-1990	nd	978000	19610	2320	130	57.9	72.1	0.027	nd	nd	nd	nd	nd	nd	nd
A12	Nov-1997	nd	977000	20760	2440	147	56.3	81.6	nd	0.435	0.582	nd	-30	-2.8	-1.9	nd
A13	Nov-1997	nd	967000	24800	1880	184	5690	113	0.081	0.74	65.9	nd	-19	-1.6	-0.7	nd
A14	Nov-1997	nd	980000	16470	2150	107	668	66.4	0.053	0.31	7.9	nd	-4	+1.2	+1.8	nd
A17	Sep-1998	99.5	983000	14740	2020	112	46.3	57.4	0.009	0.651	0.455	0.053	1	+2.0	+2.7	nd
A18	Sep-1998	101	983000	14500	1820	113	55.8	57.8	0.026	0.698	0.629	0.085	-10	+0.3	+1.0	nd
A17	Sep-1999	nd	975000	20890	3400	168	94.3	29.3	0.041	0.893	1.018	0	0	+1.7	+2.6	nd
A18	Sep-1999	99.5	975000	21310	3530	172	56.7	28.7	0.037	0.933	0.520	0	-14	-0.5	+0.5	+35.2
A18	May-2000	nd	973000	22380	4250	206	103	26.2	0.047	0.818	1.258	0	nd	nd	nd	nd
A17	Sep-2000	100	974000	21350	4650	204	60.8	24.5	0.063	0.871	0.872	0	-5	+1.5	+2.4	nd
A18	Sep-2000	100	973000	22160	4800	197	60.8	25.5	0.118	0.879	0.899	0	-20	-1.3	-0.3	nd
A17	Feb-2001	99.5	974817	20118	4799	219	27.9	18.0	0.021	0.769	0.187	0.018	-16	+0.6	+1.6	nd
A18	Feb-2001	99.2	972577	22280	4830	256	36.4	19.9	0.079	0.933	0.284	0	-33	-3.4	-2.3	nd
A17	Jun-2001	98.6	974000	20500	5620	252	59	17.3	0.033	0.78	0.55	0.000	nd	nd	nd	nd
A18	Jun-2001	98.6	970000	23700	6350	298	49	20.5	0.045	0.93	0.51	0.000	nd	nd	nd	nd
A17	Sep-2001	99.7	975000	19300	5630	247	25.6	14	0.056	0.76	0.18	0.000	nd	nd	nd	nd
A18	Sep-2001	100.5	973000	20700	5970	275	34.7	15.2	0.057	0.84	0.26	0.000	nd	nd	nd	nd
A17	Feb-2002	98.6	977000	17000	5650	233	19.9	10.8	0.029	0.61	0.13	0.000	nd	nd	nd	nd
A18	Feb-2002	98.6	977000	17100	5790	238	21.9	10.7	0.053	0.62	0.15	0.000	nd	nd	nd	nd
PG8	Sep-1990	nd	985000	13560	1760	57.5	37.9	46.6	0.006	nd	nd	nd	nd	nd	nd	nd

Table 9.1. (continued)

Sample	date	T (°C)	H_2O ppmv	CO_2 ppmv	H_2S ppmv	H_2 ppmv	N_2 ppmv	CH_4 ppmv	CO ppmv	He ppmv	Ar ppmv	O_2 ppmv	δD_{H2O} ‰	$\delta^{18}O_{H2O}$ ‰	$\delta^{18}O_{H2O,CORR}$ ‰	$\delta^{18}O_{CO2}$ ‰
PG8	Nov-1997	nd	983000	13920	2270	87.2	154	43.5	0.035	0.303	1.685	nd	-7	+1.7	+2.3	nd
PG8	Sep-1998	99.0	986000	12050	1920	95.7	52.8	52.2	0.008	0.536	0.555	0.117	0	+1.8	+2.3	nd
PG8	Sep-2000	98.7	976000	19950	3760	132	106	31.3	0.018	0.707	1.319	0	-3	+2.1	+3.0	nd
PG8	Jun-2001	98.6	973000	19800	5310	312	1230	15.9	0.056	0.48	14.5	117	nd	nd	nd	nd
PG8	Sep-2001	99.7	nd	nd	nd	nd	nd	nd	nd	nd	nd	nd	-3	+1.2	nd	nd
PG8	Feb-2002	98.2	977000	17100	5920	192	26	11.7	0.03	0.62	0.22	0.000	nd	nd	nd	nd
K6	Sep-1990	nd	946000	49310	1610	297	828	1940	0.044	nd	nd	nd	nd	nd	nd	nd
K7	Sep-1990	nd	966000	30040	2710	472	104	540	0.096	nd	nd	nd	nd	nd	nd	nd
road	Sep-1990	nd	977000	20380	1670	346	58.6	312	0.029	nd	nd	nd	nd	nd	nd	nd
Kb	Oct-1991	nd	966000	30294	2131.8	391	343.4	523.6	0.0918	0.442	4.284	nd	nd	nd	nd	nd
Ka	Oct-1991	nd	946000	49194	2338.2	604.8	324	1209.6	0.1134	0.648	4.158	nd	-43	-6.0	-2.4	nd
K6	Nov-1997	nd	906000	85110	4000	313	1150	2940	0.220	1.110	13.82	nd	-27	-3.8	-0.5	nd
K7	Nov-1997	nd	896000	95880	5100	1030	203	2060	0.260	0.962	2.354	nd	-51	-8.1	-4.0	nd
K6	Sep-1998	97.5	947000	48660	2390	169	459	1730	0.030	0.995	5.885	0	-12	-2.4	-0.5	nd
K7	Sep-1998	98.0	962000	33680	2590	436	101	676	0.085	0.915	1.020	0	-53	-8.0	-6.5	nd
K6	Sep-1999	98.3	911000	80940	4900	785	484	2130	0.112	3.096	5.747	0	-24	-3.4	+0.0	+32.6
K7	Sep-1999	97.1	881000	105470	8200	1310	2130	1400	0.310	2.235	27.11	0	-57	-8.8	-4.6	+28.1
K6	Sep-2000	99.3	920000	71700	5570	374	504	1740	0.078	2.222	6.339	0	-12	-1.9	+1.1	nd
K7	Sep-2000	98.7	949000	44480	4440	502	663	470	0.139	0.899	8.475	0	-57	-8.0	-6.1	nd
K6	Feb-2001	97.9	930393	62406	4821	429	349	1595	0.063	1.780	4.076	0	-14	-1.6	+1.1	nd
K7	Feb-2001	98.8	948932	45057	4634	593	258	522	0.122	0.958	2.837	0	-63	-8.1	-6.1	nd
K6	Jun-2001	97.8	888000	101000	7190	1010	660	2380	0.164	2.69	7.26	0.000	nd	nd	nd	nd
K7	Jun-2001	98.4	937000	55200	5940	681	150	697	0.168	1.23	1.51	0.000	nd	nd	nd	nd
K6	Sep-2001	97.8	nd	nd	nd	nd	nd	nd	nd	nd	nd	nd	nd	nd	nd	nd

Table 9.1. (continued)

Sample	date	T (°C)	H_2O ppmv	CO_2 ppmv	H_2S ppmv	H_2 ppmv	N_2 ppmv	CH_4 ppmv	CO ppmv	He ppmv	Ar ppmv	O_2 ppmv	δD_{H2O} ‰	$\delta^{18}O_{H2O}$ ‰	$\delta^{18}O_{H2O,CORR}$ ‰	$\delta^{18}O_{CO2}$ ‰
K7	Sep-2001	97.7	932000	59800	6330	618	141	727	0.294	1.14	1.51	0.000	nd	nd	nd	nd
K6	Feb-2002	nd	nd	nd	nd	nd	nd	nd	nd	nd	nd	nd	nd	nd	nd	nd
K7	Feb-2002	96.1	939000	53100	5970	653	308	619	0.169	1	3.68	0.000	nd	nd	nd	nd
L20	Sep-1990	nd	985000	12580	2530	93	27.9	91.5	0.019	nd	nd	nd	nd	nd	nd	nd
L20	Sep-2001	nd	981000	14500	3850	135	19.5	83.3	0.042	0.47	0.13	0.000	nd	nd	nd	nd
L20	Feb-2002	99.2	981000	14200	4240	125	21	81.6	0.024	0.44	0.16	0.000	nd	nd	nd	nd
nearW1	Sep-1990	nd	985000	12460	2340	120	54.1	72.7	0.067	nd	nd	nd	nd	nd	nd	nd
LG10	Sep-1990	nd	979000	17630	2270	127	344	52.2	0.033	nd	nd	nd	nd	nd	nd	nd
Nis-1	Dec-1982	340	994250	5246	223.3	84.8	45.3	11.7	0.089	nd	nd	9.73	nd	nd	nd	nd
Nis-2	Oct-1984	290	993250	6858	118.8	9.38	20.0	23.9	0.041	nd	nd	nd	-2	+3.7	nd	nd

Table 9.1. (continued)

Sample	date	$\delta^{13}C_{CO2}$ ‰	$\delta^{13}C_{CH4}$ ‰	$\delta^{34}S_{H2S}$ ‰	$^3He/^4He$ R/Ra	$T(\Delta CH_4-CO_2)$ (°C)	To (°C)	Ts (°C)	s	c	log (CO/CO_2) hyp. vap.	log (H_2/H_2O) hyp. vap.	$\delta D_{H2O,L0}$ ‰	$\delta^{18}O_{H2O,L0}$ ‰
S3	Sep-1990	nd	nd	nd	nd	nd	237.1	232.3	0.0126	0	nd	-3.09	nd	nd
S4	Sep-1990	nd	nd	nd	nd	nd	228.1	225.3	0.0071	0	nd	-3.14	nd	nd
S	Oct-1991	nd	nd	nd	nd	nd	191	190.4	0.0014	0	nd	-3.29	-9	+4.3
S4	Nov-1997	-3.34	nd	+4.0	nd	nd	260.1	252.1	0.0229	0	nd	-2.97	-15	+6.2
S16	Nov-1997	-1.94	nd	+3.6	nd	nd	252.8	245.6	0.0202	0	nd	-3.01	-11	+6.0
S4	Sep-1998	nd	nd	+3.6	nd	nd	230.2	228.6	0.0040	0	nd	-3.16	-11	+5.9
S15	Sep-1998	nd	nd	+3.4	nd	nd	195.7	195.4	0.0007	0	nd	-3.38	-5	+6.3
S16	Sep-1998	nd	nd	+3.4	nd	nd	224.6	223.3	0.0033	0	nd	-3.21	-8	+6.0
S4	Sep-1999	nd	nd	nd	nd	nd	244.7	241.6	0.0083	0	nd	-3.17	-11	+5.9
S15	Sep-1999	nd	nd	nd	nd	nd	213.0	212.3	0.0017	0	nd	-3.31	-12	+5.2
S16	Sep-1999	nd	nd	nd	nd	nd	234.0	232.3	0.0047	0	nd	-3.17	-9	+6.6
S16	May 2000	nd	nd	nd	nd	nd	226.4	224.8	0.0042	0	-5.23	-3.22	nd	nd
S4	Sep-2000	+0.14	nd	+5.3	nd	nd	255.2	248.0	0.0203	0	-4.88	-3.11	-15	+5.8
S15	Sep-2000	-1.24	nd	+4.4	nd	nd	237.1	234.7	0.0061	0	-5.13	-3.21	-15	+5.2
S16	Sep-2000	nd	nd	nd	nd	nd	nd	nd	nd	nd	nd	nd	nd	nd
S17	Sep-2000	+0.13	nd	+4.9	nd	nd	220.9	219.7	0.0030	0	-5.36	-3.30	-16	+5.0
S4	Feb-2001	-1.23	nd	+3.1	nd	nd	223.9	222.0	0.0045	0	-5.27	-3.24	-15	+5.8
S15	Feb-2001	-1.32	nd	+3.0	nd	nd	242.1	239.4	0.0076	0	-5.04	-3.16	-13	+5.4
S16	Feb-2001	-1.40	nd	+3.2	nd	nd	227.0	225.1	0.0049	0	-5.20	-3.19	-16	+5.4
S17	Feb-2001	-1.35	nd	+3.1	nd	nd	236.1	233.6	0.0065	0	-5.13	-3.20	-15	+5.2
S4	Jun-2001	-1.2	-23.6	+3.4	nd	338	251.6	245.8	0.0162	0	-4.91	-3.11	-16	+4.9
S15	Jun-2001	-1.6	-23.4	+3.7	5.72	348	218.3	217.0	0.0032	0	-5.34	-3.24	-14	+6.6
S16	Jun-2001	-1.4	-23.3	+3.4	nd	346	234.1	231.9	0.0060	0	-5.11	-3.16	-15	+6.3
S17	Jun-2001	-1.3	-23.9	+3.4	nd	335	209.3	208.7	0.0014	0	-5.50	-3.33	-10	+6.5
S4	Sep-2001	-1.3	-23.7	+3.7	nd	338	272.0	258.6	0.0407	0	-4.66	-3.02	-11	+5.4
S15	Sep-2001	-1.4	-24.3	+3.3	5.66	331	264.1	254.7	0.0274	0	-4.74	-3.04	-9	+5.2

Table 9.1. (continued)

Sample	date	$\delta^{13}C_{CO2}$	$\delta^{13}C_{CH4}$	$\delta^{34}S_{H2S}$	$^3He/^4He$	$T(\Delta CH_4\text{-}CO_2)$	To	Ts	s	c	log (CO/CO_2) hyp. vap.	log (H_2/H_2O) hyp. vap.	$\delta D_{H2O,L0}$	$\delta^{18}O_{H2O,L0}$
		‰	‰	‰	R/Ra	(°C)	(°C)	(°C)					‰	‰
S16	Sep-2001	-1.5	-23.6	+3.5	nd	342	283.0	264.1	0.0597	0	-4.51	-2.95	-10	+5.0
S17	Sep-2001	-1.3	-24.8	+3.5	nd	321	273.5	261.6	0.0365	0	-4.66	-3.04	-12	+4.4
S4	Feb-2002	-1.5	-23.2	+4.5	nd	350	264.6	253.5	0.0321	0	-4.74	-3.05	-15	+6.0
S15	Feb-2002	-0.9	-24.1	+4.2	5.84	327	243.0	239.6	0.0094	0	-5.02	-3.15	-22	+3.0
S16	Feb-2002	-1.3	-23.4	+4.7	nd	343	256.9	249.3	0.0217	0	-4.80	-3.05	-11	+6.6
S17	Feb-2002	-1.1	-24.2	nd	nd	327	243.7	240.4	0.0090	0	-5.02	-3.15	-13	+5.9
PP9N	Sep-1990	nd	nd	nd	nd	nd	247.2	244.7	0.0072	0	nd	-3.15	nd	nd
PP	Oct-1991	nd	nd	nd	nd	nd	239.1	237.3	0.0049	0	nd	-3.16	-8	+5.2
PP9N	Nov-1997	-2.47	nd	+4.1	nd	nd	253.9	251.1	0.0082	0	nd	-3.12	-12	+4.8
PP9S	Nov-1997	-2.32	nd	+3.8	nd	nd	275.4	268.6	0.0219	0	nd	-3.04	-15	+4.1
PP9N	Sep-1998	nd	nd	+3.4	nd	nd	248.7	246.7	0.0060	0	nd	-3.14	-11	+5.2
PP9S	Sep-1998	nd	nd	+3.5	nd	nd	253.6	251.1	0.0075	0	nd	-3.13	-11	+4.9
PP9N	Sep-1999	nd	nd	nd	nd	nd	291.9	285.2	0.0241	0	nd	-3.01	-11	+4.7
PP9S	Sep-1999	nd	nd	nd	nd	nd	292.9	285.4	0.0263	0	nd	-3.02	-12	+4.7
PP9N	May-2000	nd	nd	nd	nd	nd	278.8	274	0.0156	0	-4.66	-3.08	nd	nd
PP9S	May-2000	nd	nd	nd	nd	nd	294.6	284.4	0.0363	0	-4.55	-3.08	nd	nd
PP9N	Sep-2000	-0.48	nd	+3.8	nd	nd	304.3	293.4	0.0416	0	-4.40	-2.99	-19	+4.1
PP9S	Sep-2000	-0.52	nd	+4.1	nd	nd	316.8	289.6	0.1049	0	-4.31	-2.98	-17	+4.6
PP9N	Feb-2001	-0.78	nd	+2.8	nd	nd	233.4	232.8	0.0016	0	-5.23	-3.28	-11	+3.5
PP9S	Feb-2001	-0.93	nd	+2.7	nd	nd	283.4	279.0	0.0151	0	-4.60	-3.05	-13	+5.3
PP9N	Jun-2001	-1.2	-22.6	+3.0	nd	354	308.9	296.4	0.0493	0	-4.39	-3.02	-20	+4.4
PP9S	Jun-2001	-1.4	-22.4	+2.9	5.49	362	307.0	279.5	0.0976	0	-4.38	-2.99	-25	+3.5
PP9N	Sep-2001	-1	nd	+3.0	nd	nd	313.5	283.8	0.1096	0	-4.33	-2.98	-12	+4.2
PP9S	Sep-2001	-1.2	-22.2	+3.2	5.43	361	309.8	286.2	0.0870	0	-4.39	-3.01	-15	+3.8
PP9N	Feb-2002	-1.2	-23.4	+3.5	nd	340	322.3	276.3	0.1660	0	-4.22	-2.93	-11	+5.7

Table 9.1. (continued)

Sample	date	$\delta^{13}C_{CO2}$ ‰	$\delta^{13}C_{CH4}$ ‰	$\delta^{34}S_{H2S}$ ‰	$^3He/^4He$ R/Ra	T(ΔCH_4-CO_2) (°C)	To (°C)	Ts (°C)	s	c	log (CO/CO_2) hyp. vap.	log (H_2/H_2O) hyp. vap.	$\delta D_{H2O,L0}$ ‰	$\delta^{18}O_{H2O,L0}$ ‰
PP9S	Feb-2002	-0.9	-23	+3.5	5.06	345	305.0	276.4	0.0993	0	-4.42	-3.02	-31	+1.4
A12	Sep-1990	nd	nd	nd	nd	nd	194.9	194.5	0.0011	0	nd	-3.36	nd	nd
A13	Sep-1990	nd	nd	nd	nd	nd	219.2	218.6	0.0013	0	nd	-3.25	nd	nd
A14	Sep-1990	nd	nd	nd	nd	nd	220.5	219.6	0.0024	0	nd	-3.25	nd	nd
A12	Nov-1997	-1.44	nd	+4.6	nd	nd	nd	nd	nd	0	nd		nd	nd
A13	Nov-1997	-3.21	nd	+5.1	nd	nd	244.7	242.8	0.0049	0	nd	-3.12	-20	+1.0
A14	Nov-1997	-4.08	nd	+4.0	nd	nd	253.8	248.4	0.0151	0	nd	-3.07	-5	+3.3
A17	Sep-1998	nd	nd	+3.2	nd	nd	195.4	195.1	0.0009	0	nd	-3.37	+5	+5.0
A18	Sep-1998	nd	nd	+2.5	nd	nd	232.5	230.4	0.0054	0	nd	-3.17	-10	+2.7
A17	Sep-1999	-0.52	nd	nd	nd	nd	230.9	230.1	0.0019	0	nd	-3.31	+0	+4.4
A18	Sep-1999	nd	nd	nd	nd	nd	225.2	224.7	0.0012	0	nd	-3.37	-13	+2.3
A18	May-2000	nd	nd	nd	nd	nd	227.8	227.4	0.0009	0	-5.38	-3.38	nd	nd
A17	Sep-2000	nd	nd	+5.0	nd	nd	243.3	242.5	0.0021	0	-5.18	-3.31	-6	+3.9
A18	Sep-2000	-0.73	nd	+4.6	nd	nd	270.1	267.5	0.0086	0	-4.83	-3.18	-23	+0.8
A17	Feb-2001	-0.96	nd	+3.4	nd	nd	194.4	194.4	0.0000	0	-5.98	-3.65	-12	+3.7
A18	Feb-2001	-1.00	nd	+3.3	nd	nd	243.4	243.0	0.0011	0	-5.22	-3.35	-34	-0.9
A17	Jun-2001	-1.3	-23.4	+4.1	nd	344	206.1	206.1	0.0000	0	-5.79	-3.59	-10	+3.1
A18	Jun-2001	-1	-23.7	+3.5	nd	334	209.5	209.5	0.0000	0.087	-5.72	-3.55	-17	+2.3
A17	Sep-2001	-1	-23.5	+4.0	nd	338	235.8	235.5	0.0006	0	-5.35	-3.42	+2	+3.7
A18	Sep-2001	-1.1	-24	+3.6	nd	330	227.7	227.6	0.0002	0	-5.47	-3.47	-7	+2.9
A17	Feb-2002	-1	-23	+4.6	nd	345	213.5	213.4	0.0001	0	-5.68	-3.56	-10	+2.5
A18	Feb-2002	-1.1	-23.2	+4.6	nd	343	240.5	240.2	0.0009	0	-5.29	-3.40	-27	-0.2
PG8	Sep-1990	nd	nd	nd	nd	nd	196.7	195.7	0.0023	0	nd	-3.35	nd	nd
PG8	Nov-1997	-2.09	nd	+3.6	nd	nd	248.8	243.8	0.0144	0	nd	-3.11	-8	+3.8

Table 9.1. (continued)

Sample	date	$\delta^{13}C_{CO2}$ ‰	$\delta^{13}C_{CH4}$ ‰	$\delta^{34}S_{H2S}$ ‰	$^3He/^4He$ R/Ra	$T(\Delta CH_4\text{-}CO_2)$ (°C)	To (°C)	Ts (°C)	s	c	log (CO/CO_2) hyp. vap.	log (H_2/H_2O) hyp. vap.	$\delta D_{H2O,L0}$ ‰	$\delta^{18}O_{H2O,L0}$ ‰
PG8	Sep-1998	nd	nd	+3.3	nd	nd	200.7	200.1	0.0016	0	nd	-3.30	+3	+4.6
PG8	Sep-2000	-0.61	nd	+4.3	nd	nd	207.3	206.9	0.0009	0	nd	-3.41	+0	+5.0
PG8	Jun-2001	-1	-23.1	+3.7	nd	343	222.4	222.4	0.0000	0.005	-5.55	-3.50	-18	+2.5
PG8	Sep-2001	-1.1	-24.3	+3.8	nd	327	nd	nd	nd	nd	nd	nd	nd	nd
PG8	Feb-2002	-1.1	-23.2	+4.2	5.44	343	221.0	220.7	0.0007	0	-5.47	-3.42	-8	+3.4
K6	Sep-1990	nd	nd	nd	nd	nd	173.6	173.5	0.0001	0	nd	-3.29	nd	nd
K7	Sep-1990	nd	nd	nd	nd	nd	208.8	208.7	0.0002	0	nd	-3.17	nd	nd
road	Sep-1990	nd	nd	nd	nd	nd	188.2	188.2	0.0001	0	-5.69	-3.31	nd	nd
Kb	Oct-1991	nd	nd	nd	nd	nd	215.2	215	0.0005	0	nd	-3.14	nd	nd
Ka	Oct-1991	nd	nd	nd	nd	nd	191.4	191.4	0.0000	0.186	nd	-3.28	-33	-1.6
K6	Nov-1997	-2.46	nd	+4.1	nd	nd	213.2	212.8	0.0009	0	nd	-3.06	-25	+1.6
K7	Nov-1997	-0.4	nd	nd	nd	nd	196.9	196.9	0.0000	0.532	nd	-3.27	-32	-2.3
K6	Sep-1998	nd	nd	+3.3	nd	nd	178.7	178.6	0.0004	0	nd	-3.26	-6	+1.8
K7	Sep-1998	nd	nd	+3.2	nd	nd	201.6	201.5	0.0001	0	nd	-3.25	-50	-4.5
K6	Sep-1999	nd	nd	nd	nd	nd	177.4	177.4	0.0000	0.489	nd	-3.36	-4	+2.6
K7	Sep-1999	nd	nd	nd	nd	nd	202.5	202.5	0.0000	0.656	nd	-3.29	-36	-2.6
K6	Sep-2000	-1.38	nd	+4.1	nd	nd	172.0	172.0	0.0000	0.011	-5.96	-3.40	-3	+2.9
K7	Sep-2000	-1.09	nd	+4.1	nd	nd	206.0	206.0	0.0000	0.050	-5.51	-3.30	-53	-4.2
K6	Feb-2001	-1.81	nd	+3.2	nd	nd	169.8	169.8	0.0000	0.145	-5.99	-3.40	-1	+3.3
K7	Feb-2001	-1.25	nd	+3.0	nd	nd	201.1	201.1	0.0000	0.222	-5.57	-3.31	-54	-3.8
K6	Jun-2001	-1.2	-23	+4.5	nd	347	182.4	182.4	0.0000	0.598	-5.79	-3.34	+2	+3.5
K7	Jun-2001	-1.2	-23.8	+3.4	nd	335	203.9	203.9	0.0000	0.294	-5.52	-3.29	-48	-5.0
K6	Sep-2001	-1.1	-23.8	+3.6	nd	334	nd	nd	nd	nd	nd	nd	nd	nd

Table 9.1. (continued)

K7	Sep-2001	-1.2	-23.4	+4.3	nd	340	218.5	218.5	0.0000	0.092	-5.31	-3.22	-16	+0.6
K6	Feb-2002	-1.4	-23.1	+5.0	nd	350	nd	nd	nd	nd	nd	nd	nd	nd
K7	Feb-2002	-1	-23.7	+4.5	5.79	334	205.8	205.8	0.0000	0.260	-5.50	-3.29	-48	-3.0
L20	Sep-1990	nd	nd	nd	nd	nd	245.9	242.2	0.0100	0	nd	nd	-37	-1.3
L20	Sep-2001	-1.4	-23.4	+3.5	nd	343	244.8	241.6	0.0084	0	-4.93	-3.07	nd	nd
L20	Feb-2002	-1.4	-23.4	+4.0	nd	345	227.0	225.4	0.0041	0	-5.16	-3.16	-35	-0.6
nearW1	Sep-1990	nd	nd	nd	nd	nd	269.1	259.6	0.0287	0	-4.63	-2.97	nd	nd
LG10	Sep-1990	nd	nd	nd	nd	nd	233.1	231.4	0.0042	0	-5.16	-3.21	nd	nd
Nis-1	Dec-1982	nd	nd	nd	nd	nd	nd	nd	nd	nd	nd	nd	nd	nd
Nis-2	Oct-1984	nd	nd	nd	nd	nd	nd	nd	nd	nd	nd	nd	-2	+3.7

<u>**References:**</u>
Sep-1990: Chiodini et al. (1993a);
Oct-1991: Kavouridis et al. (1999);
Nov-1997, Sep-1998, Sep-1999, May-2000, Sep-2000, Feb-2001: Brombach et al. (2003), Fiebig, unpublished $\delta^{13}C_{CO2}$ and $\delta^{34}S_{H2S}$ data;
Jun-2001, Sep-2001, Feb-2002: Fiebig et al. (2004), Fiebig, unpublished $\delta^{13}C_{CO2}$ and $\delta^{34}S_{H2S}$ data.
Nis-1, Nis-2: Chiodini et al. (1993a), Dotsika (1992), Brombach et al. (2003).

Table 9.2. Chemical and isotopic data of waters samples from Nisyros Island. Concentrations in mg/kg.

Sample	Type	Date	T(°C)	pH	Cl	Br	SO_4	HCO_3	Ctot (HCO_3)	Li	Na	K	Mg	Ca	SiO_2	B	NO_3	NH_4	δD (‰)	$\delta^{18}O$ (‰)	$\delta^{34}S$ (‰)	^3H (TU)	Code	Ref
Nisyros-1	geot. well	Dec-82	340.0	5.16	48230	nd	88.2	79.3	17526	8.2	14967	2545	1154	10439	7.81	160	nd	nd	nd	nd	nd	nd	1443	(a)
Nisyros-2	geot. well	Oct-84	290.0	4.87	50390	nd	24.7	64.3	7021	7.59	21610	2870	78.1	7340	639	41.8	nd	nd	nd	nd	nd	nd	2001	(a)
Avlaki	spring	nr	55.0	6.36	21130	nd	1670	137	195	1.08	10540	850	778	1320	nd	nd	nd	nd	nd	nd	nd	nd	8-II	(a)
Avlaki	spring	nr	50.0	6.70	21370	nd	1610	145	173	1.68	11380	821	773	1180	177	13.6	nd	nd	nd	nd	nd	nd	8-I	(a)
Avlaki	spring	nr	54.0	6.40	21480	nd	1632	189	261	0.79	11100	764	697	1440	267	12.5	nd	8.87	nd	nd	nd	nd	M-18	(b)
Avlaki	spring	1991	53	6.40	21870	nd	1634	153	210	nd	12879	589	948	1484	192	nd	22.8	nd	+7	+1.4	nd	nd	N11	(c)
Avlaki	spring	Oct-92	58	6.30	21990	nd	1585	139	205	nd	11960	716	795	1291	218	9.3	37.2	nd	+3	+2.0	nd	nd	N11	(c)
Avlaki	spring	Sep-98	53.6	6.36	21500	63.7	1720	144	207	nd	11400	742	705	812	86.5	nd	nd	nd	+3	+1.7	+19.3	nd	Av	(d)
Irini	spring	Sep-98	39.0	6.39	20100	60.9	1980	258	370	nd	11000	622	689	842	103	nd	nd	nd	+5	+2.0	+16.8	nd	Ir	(d)
Katsouni	spring	nr	44.0	6.25	21650	nd	1980	453	706	0.935	11500	704	1010	1170	116	9.45	nd	nd	nd	nd	nd	nd	15	(a)
Katsouni	spring	Sep-98	44.2	5.77	21700	65.0	1870	384	1050	nd	11600	690	900	847	154	nd	nd	nd	+4	+1.2	+19.7	nd	Ka	(d)
Katsouni(?)	spring	nr	45.0	6.50	22720	nd	3120	500	649	0.73	11700	714	887	1900	173	9.29	nd	5.65	nd	nd	nd	nd	M-19	(b)
Levkos	spring	Sep-98	48.0	6.00	17500	55.0	1890	381	780	nd	10100	555	666	636	110	nd	nd	nd	+6	+1.5	+17.0	nd	Le	(d)
Levkos	spring	Oct-92	47	6.75	18090	nd	1796	419	495	nd	9890	528	817	906	180	5.2	15.5	nd	+3	+1.4	nd	nd	N12	(c)
Levkos	spring	nr	46.0	6.60	18990	nd	2130	398	500	1.03	10520	626	895	802	133	6.3	nd	nd	nd	nd	nd	nd	12	(a)
Levkos(?)	spring	nr	49.0	6.70	18990	nd	1440	378	451	0.79	9099	612	668	1700	165	8.97	nd	3.6	nd	nd	nd	nd	M-21	(b)
Loutra	spring	May-91	nr	7.20	18368	nd	1177	179	202	nd	9499	456	550	1531	nd	7.6	12.4	nd	+2	+1.0	nd	0	N2	(c)
Loutra	spring	Oct-91	33.2	7.28	18581	nd	1201	201	212	nd	9407	899	541	1533	133	8.1	1.9	nd	+3	+0.8	nd	nd	N2	(c)
Loutra	spring	1991	47	6.60	19952	nd	1780	220	271	nd	12251	625	809	1916	144	nd	41.9	nd	-1	+0.9	nd	nd	N2	(c)
Loutra	spring	Sep-98	46.8	6.94	20500	60.7	1440	186	207	nd	10700	830	550	1020	107	nd	nd	nd	+3	+1.3	+17.5	nd	Lu	(d)
Loutra	spring	Oct-92	44	6.50	20921	nd	1441	259	339	nd	11040	841	700	1587	175	8	12.4	nd	+2	+1.3	nd	nd	N2	(c)
Pali	spring	Oct-91	33.5	7.20	8475	nd	749	186	200	nd	4080	235	394	858	82	4.1	12.4	nd	-13	-2.3	nd	nd	N4	(c)
Pali	spring	nr	37.0	6.49	9210	nd	865	195	270	0.611	4600	258	450	862	120	5.09	nd	nd	nd	nd	nd	nd	11-II	(a)
Pali	spring	nr	39.0	7.00	9500	nd	870	212	236	0.84	4760	332	447	770	105	5.85	nd	nd	nd	nd	nd	nd	11-I	(a)
Pali	spring	Oct-92	39.2	6.35	12837	nd	1114	281	420	nd	6440	414	589	1042	130	5.6	43.4	nd	-7	-0.8	nd	nd	N4	(c)
Pali	spring	nr	37.0	6.56	18430	nd	1300	183	236	1.53	9430	704	572	1540	168	9.85	nd	nd	nd	nd	nd	nd	19-II	(a)
Pali	spring	nr	49.0	6.90	19140	nd	1370	188	211	1.53	9770	899	613	1480	136	9	nd	nd	nd	nd	nd	nd	19-I	(a)
Pali(?)	spring	nr	39.0	6.50	17930	nd	1152	226	300	1.32	9099	655	413	1660	198	8.75	nd	1.67	nd	nd	nd	nd	M-17	(b)

Table 9.2. (continued)

Sample	Type	Date	T(°C)	pH	Cl	Br	SO_4	HCO_3	Ctot (HCO_3)	Li	Na	K	Mg	Ca	SiO_2	B	NO_3	NH_4	δD (‰)	$\delta^{18}O$ (‰)	$\delta^{34}S$ (‰)	^3H (TU)	Code	Ref
Pali-well	shallow well	nr	35.0	7.10	13040	nd	877	142	155	1.31	6710	626	321	1090	111	8.55	nd	nd	nd	nd	nd	nd	20	(a)
Pali-well	shallow well	nr	40.0	6.20	13680	nd	1500	106	181	0.73	7360	430	618	762	58.3	6.98	nd	nd	nd	nd	nd	nd	10	(a)
Kira sterna	spring	Oct-91	nr	8.08	5	nd	26	53	54	nd	9	4	1	19	3	0.1	0	nd	-26	-5.4	nd	nd	N8	(c)
Kira sterna	spring	May-91	nr	7.70	11	nd	14	57	61	nd	9	4	1	16	nd	0.1	0	nd	-27	-5.4	nd	nd	N8	(c)
Kira sterna	spring	Oct-92	20.8	8.05	11	nd	14	57	58	nd	9	4	1	18	17	0.1	3.1	nd	-33	-6.0	nd	nd	N8	(c)
Kostanzo	pool	Oct-92	23.3	8.03	28	nd	10	76	77	nd	21	5	1	18	19	0.3	3.1	nd	-26	-4.6	nd	nd	N6	(c)
Panaghias Kiras	dug well	nr	17.0	6.56	184	nd	36.5	97.6	158	nd	89.7	21.1	20.7	32.1	96.1	1.08	nd	nd	nd	nd	nd	nd	7-II	(a)
Panaghias Kiras	dug well	nr	17.0	7.40	202	nd	40.8	115	125	0.044	103	23.5	21.9	31.3	87	nd	nd	nd	nd	nd	nd	nd	7-I	(a)
Kira	spring	Oct-92	18	7.90	266	nd	53	169	173	nd	115	28	38	48	95	0.2	27.9	nd	-32	-5.7	nd	nd	N9	(c)
Kira	spring	Oct-91	18.9	7.44	269	nd	82	185	199	nd	120	41	39	68	71	0.1	18.6	nd	-29	-5.6	nd	nd	N9	(c)
Mandraki	shallow well	nr	19.0	7.10	386	nd	259	164	190	0.043	214	23.5	38.2	121	52.4	0.4	nd	nd	nd	nd	nd	nd	22	(a)
Kira	spring	May-91	nr	7.40	574	nd	101	336	378	nd	255	4	75	107	nd	0.2	0	nd	-26	-5.1	nd	nd	N9	(c)
Peroulis	pool	Oct-91	18	7.64	738	nd	259	185	193	nd	465	102	49	148	82	2.3	310	nd	-28	-4.8	nd	nd	N1	(c)
Peroulis	pool	May-91	nr	7.30	777	nd	245	196	226	nd	449	59	51	143	nd	2.4	143	nd	-28	-4.8	nd	5	N1	(c)
Peroulis	pool	Oct-92	24.5	7.15	798	nd	221	171	192	nd	483	86	43	140	100	1.9	198	nd	-22	-3.0	nd	nd	N1	(c)
Mandraki	spring	nr	18.0	6.95	886	nd	332	132	161	0.075	529	235	65.7	152	78.6	nd	nd	nd	nd	nd	nd	nd	17	(a)
Mandraki	shallow well	nr	19.0	7.10	1320	nd	212	105	121	0.158	690	78.2	57.2	168	90.5	1.08	nd	nd	nd	nd	nd	nd	18	(a)
NW-coast	spring	nr	19.0	7.05	2110	nd	296	61.6	72	0.03	1380	70.4	47.4	18	50	nd	nd	nd	nd	nd	nd	nd	16	(a)
East coast	spring	nr	23.0	6.90	3490	nd	356	391	470	0.3	1760	117	212	317	89.3	2.65	nd	nd	nd	nd	nd	nd	13	(a)
Mira Mare	spring	nr	19.0	6.80	3770	nd	179	122	155	0.354	1770	196	107	401	105	1.5	nd	nd	nd	nd	nd	nd	23	(a)
Kethros	spring	nr	23.0	7.20	4110	nd	410	255	280	0.34	2210	117	195	269	81	2.5	nd	nd	nd	nd	nd	nd	9	(a)
Thermiani	spring	Oct-91	25.8	7.26	4291	nd	327	67	73	nd	2171	180	158	361	27	2	37.2	nd	-15	-2.3	nd	nd	N3	(c)
NE-coast	spring	nr	19.0	7.00	5260	nd	579	149	174	0.138	2730	156	326	257	82.2	1.49	nd	nd	nd	nd	nd	nd	21	(a)
nr	spring	nr	28.0	6.90	8023	nd	768	177	207	0.52	3749	215	328	760	122	5.83	nd	1.03	nd	nd	nd	nd	M-20	(b)
Thermiani	spring	May-91	nr	7.95	13546	nd	1109	165	168	nd	6836	218	559	1146	nd	6	55.8	nd	+5	+1.7	nd	1	N3	(c)
Thermiani	spring	Oct-92	25	7.95	13936	nd	1028	165	165	nd	7130	500	593	1118	126	6.1	46.5	nd	+6	+2.2	nd	nd	N3	(c)

References: (a) = Chiodini et al. (1993a); (b) = Minissale et al. (1997); (c) = Kavouridis et al. (1999); (d) = Brombach et al. (2003).

Table 9.3. $\delta^{34}S$ values and S concentrations of volcanic rocks from Nisyros and Yali (courtesy of Annette Buettner and Barbara Gambardella).

Code	**S** ppm	**$\delta^{34}S$** ‰
NIS11C	443	+5.6
NIS11	265	+5.1
NIS14	696	+3.5
YALI2A	118	+16.7
YALI2A+	35.4	+9.4

Table 9.4. Variations from vent to vent and in time of the $\delta^{13}C$ values of fumarolic CO_2 and $\delta^{34}S$ values of fumarolic H_2S

Vent	**$\delta^{13}C$** ‰	**$\delta^{34}S$** ‰
Stephanos	-1.3 ± 0.7 (n=21)	+3.7 ± 0.6 (n=23)
Polybotes Micros	-1.2 ± 0.6 (n=12)	+3.4 ± 0.5 (n=14)
Phlegethon	-1.4 ± 1.0 (n=13)	+4.0 ± 0.8 (n=15)
Polybotes Megalos	-1.2 ± 0.5 (n= 5)	+3.8 ± 0.4 (n= 6)
Kaminakia	-1.3 ± 0.5 (n=12)	+3.9 ± 0.6 (n=13)

Date	**$\delta^{13}C$** ‰	**$\delta^{34}S$** ‰
October 1991	-2.3 ± 0.4 (n= 4)	nd
November 1997	-2.4 ± 1.0 (n=10)	+4.1 ± 0.5 (n= 9)
September 1998	nd	+3.3 ± 0.3 (n=10)
September 2000	-0.6 ± 0.5 (n=10)	+4.4 ± 0.5 (n=10)
February 2001	-1.2 ± 0.3 (n=10)	+3.1 ± 0.2 (n=10)
June 2001	-1.3 ± 0.2 (n=11)	+3.5 ± 0.5 (n=11)
September 2001	-1.2 ± 0.2 (n=12)	+3.6 ± 0.3 (n=12)
February 2002	-1.2 ± 0.2 (n=12)	+4.3 ± 0.5 (n=11)

Table 9.5. Comparison between the CO-H_2 temperature extrapolated from Figure 12 and the temperature given by partition of C isotopes between CO_2 and CH_4. R^2 is the square of the correlation coefficient between restored $\log(X_{H_2}/X_{H_2O})$ and $\log(X_{CO}/X_{CO_2})$ in Figure 12.

Period	Location	$T_{extr.}$ (°C)	R^2	T_{carbon} (°C)
05/2000-06/2002	**Polybotes Micros**	369	0.97	352 ± 9
	Stephanos	320	0.98	337 ± 9
	Phlegethon	347	0.98	339 ± 8
	Kaminakia	416	0.97	340 ± 6
1997-06/2002	**Polybotes Micros**	378	0.95	
	Stephanos	313	0.97	
	Phlegethon	334	0.83	
	Kaminakia	316	0.76	

Table 9.6. Average temperatures of CO re-equilibration in the liquid phase (T_O), average temperatures of steam separation (T_S), and corresponding steam fractions (s) for the fumaroles of different hydrothermal craters (standard deviations are also reported). The average fraction of condensed steam, c, is also given for the Kaminakia vents.

Hydrothermal craters	**T_O (°C)**	**T_S (°C)**	**s**	**c**
Polybotes Micros (n = 20)	284 ± 29	271 ± 20	0.0465 ± 0.0471	no cases
Stephanos (n = 31)	239 ± 22	234 ± 18	0.0131 ± 0.0139	no cases
Phlegethon (n = 20)	226 ± 20	226 ± 20	0.0024 ± 0.0037	one case
Polybotes Megalos (n = 6)	216 ± 19	215 ± 18	0.0033 ± 0.0055	one case
Kaminakia (n = 19)	195 ± 16	195 ± 16	0.0001 ± 0.0002	0.295 ± 0.221 (n=12)
Lofos (n = 3)	239 ± 11	236 ± 10	0.0075 ± 0.0031	no cases

10. Reaction path modeling of argillic alteration (AA) and advanced argillic alteration (AAA): consequences for debris avalanches induced by flank collapse and hydrothermal eruptions.

Claudia Principe (1), **Luigi Marini** (2)

(1) Istituto di Geoscienze e Georisorse, Area della Ricerca CNR, Via Moruzzi 1, 56124 Pisa, Italy

(2) Laboratorio di Geochimica, Dip.Te.Ris., Università di Genova, Corso Europa 26, I-16132 Genova, Italy

Abstract - The progressive dissolution of a local andesite both in a rainwater-diluted degassed fumarolic steam condensate and in an undiluted conductively-cooled steam condensate was simulated in two reaction path modeling experiments by using the EQ3/6 Software Package. In spite of the simulation uncertainties, which are mainly due to the difficulties in constraining the reactive surface area of primary minerals, it was shown that very short time intervals are needed to produce the clay minerals typical of AAA (kaolinite) and AA (smectites) in amounts sufficient to lubricate flank-collapse-induced debris avalanches and hydrothermal debris flow deposits.

Today, all the other boundary conditions needed to generate debris avalanches induced by flank collapse and to trigger hydrothermal eruptions are locally present at Nisyros. Therefore, the risks related to these two volcanic phenomena must to be taken in serious consideration.

10.1. Introduction

Both hydrothermal eruptions and flank-collapse-induced debris avalanches took place at Nisyros Island in the past and will certainly occurr in the future. Hydrothermal eruptions devastated the southern part of the Lakki plain and the small Lofos dome in a recent past, as testified by several hydrothermal craters which are still well preserved today (Marini et al., 1993). A newly discovered flank-collapse-induced debris avalanche is the Vunàri deposits, cropping out along the northern flank of the volcano near Loutra (Vanderkluysen et al., 2005; Volentik et al., this volume).

One might wonder which are the relations, if any, between these two kinds of volcanic events. The link is represented by the pivotal role played by clay minerals in the emplacement mechanisms of both kinds of deposit. These clay minerals are produced by hydrothermal alteration, either argillic alteration (AA) or advanced argillic alteration (AAA), which represents the central subject of this communication.

10.2. Shallow hydrothermal alteration

Hydrothermal alteration minerals are present within the cuttings and the less frequent cores collected during geothermal drilling and have been the subject of many investigations. Although the sequence of alteration minerals varies from system to system, a general relationship between hydrothermal alteration minerals and temperature range was recognised, as summarized by Henley and Ellis (1983). The same mineral parageneses were also found in hydrothermal ore deposits, which are the fossil analogues of active geothermal systems.

In near-surface steam-heated zones, acid-sulfate waters are produced through absorption of H_2S-bearing vapors in shallow groundwaters or surface waters, followed by oxidation, driven by atmospheric oxygen, of H_2S to sulfuric acid (e.g., Ellis and Mahon, 1977; Henley et al., 1984; Giggenbach, 1988). Interaction of these strongly acidic solutions with rocks removes mobile chemical constituents, adds sulfate, and breaks down framework silicates, determining the formation of silica minerals, e.g., opal and cristobalite, clay minerals, chiefly kaolinite, sulfate minerals, such as alunite, jurbanite, jarosite, and gypsum, and hydrous ferric oxides. These are the typical phases of the AAA.

In places where acid-sulfate leaching does not take place, AA occurs near the surface and at shallow depths. AA is characterized by the abundant development of clay minerals of the smectite group, including montmorillonite, beidellite, saponite, and nontronite, eventually accompanied by illite, chlorites, and low-temperature zeolites, such as heulandite and stilbite. This hydrothermal alteration originates up to temperatures of 150-160°C, above which smectites become unstable.

At Nisyros, abundant clay minerals associated with less frequent iron oxides and pyrite were found above 150-160 m depth in geothermal well Nisyros-1 (Geotermica Italiana, 1983). This AA zone is followed by the argillic-phyllitic zone, between 150-160 m and 370-380 m depths, where clay minerals are accompanied by illite, carbonate minerals, silica minerals, pyrite, and locally by anhydrite and zeolites. In well Nisyros-2, the AA zone occurs above 140-150 m depth, whereas the argillic-phyllitic zone extends between 140-150 m and 250-270 m depths. Both are characterised by development of clay minerals, carbonate minerals, silica minerals, pyrite, and anhydrite accompanied by less frequent illite and chlorites and locally by zeolites (Geotermica Italiana, 1984).

Summing up, AA and argillic-phyllitic alteration were recognised at shallow depths in both geothermal wells. AAA is instead present in the area of the hydrothermal craters, where strongly acidic fumarolic steam condensates are responsible of acid-sulfate leaching and deposition of silica minerals, clay minerals, sulfate minerals, and hydrous ferric oxides. Which are the reasons for the lateral transition from AAA to AA ? The supply of atmospheric O_2 is a very important factor, in that a continuous replenishment of O_2 brings about total conversion of dissolved sulfide to sulfate, whereas H_2S may persists stably under reducing conditions. It is also possible that moving away from the area of the hydrothermal craters, fumarolic steam condensates mix with rain waters. Although the annual precipitation on Nisyros is rather limited, with ~ 500 mm, most of the rain falling within the caldera rim ultimately collects in the southern part of the Lakki plain, nearby the area of the hydrothermal craters. Dilution increases the pH of the fumarolic steam condensate and decreases its sulfate concentration causing a different path of water-rock interaction, that ultimately leads to development of AA instead of AAA.

In order to verify these hypotheses and evaluate the time needed for the development of clay minerals, we decided to simulate andesite dissolution both in a rainwater-diluted degassed fumarolic steam condensate (model A) and in an undiluted degassed fumarolic steam condensate (model B) by means of two separate computer experiments.

10.3. Reaction path modeling of andesite dissolution

Reaction path modeling has received considerable attention in geochemistry. The thermodynamic relationships describing irreversible water-rock mass transfers were established by Helgeson (1968, 1979) and PATHI, the first software code for reaction path modeling, was developed by Helgeson and coworkers.

Among the other codes inplemented afterwards, the EQ3/6 Software Package (Wolery, 1979) is one of the most reliable and known. Version 7.2b of EQ3/6 (Wolery, 1992; Wolery and Daveler, 1992) was used here to simulate the irreversible mass exchanges during the progressive dissolution of a local andesite both in a rainwater-diluted degassed fumarolic steam condensate (model A) and in an undiluted conductively-cooled steam condensate (model B). Reference was made to the thermodynamic database COM, which includes the thermodynamic properties of several solids, aqueous species, and gases, mostly derived from SUPCRT92 (Johnson et al., 1992).

Reaction path modeling was performed in titration mode, that is by adding at each step of the reaction progress variable, ξ (Helgeson, 1979 and references therein), suitable amounts of the solid reactants to the system, and equilibrating at each step the aqueous solution with the possible product solid phases (Wolery and Daveler, 1992). These are kept in partial equilibrium with the aqueous solution throughout the simulation and may eventually re-dissolve for increasing values of ξ. In this respect, the system is considered closed.

Calculations were carried out in time frame, taking into account the dissolution rates and surface areas of primary solid phases, whereas product minerals were assumed to attain instantaneous equilibrium.

Both rock dissolution experiments were carried out at constant temperature of 50°C and 1 bar total pressure. In model A a constant f_{CO_2} of $10^{-1.4}$ bar was imposed with no constraint on f_{O_2}, whereas in model B both f_{CO_2} and f_{O_2} were kept constant at $10^{-0.16}$ and $10^{-0.678}$ bar, respectively. This f_{O_2}, which is the average atmospheric value, was chosen to reproduce a continuous supply of O_2 from the atmosphere to the system. Besides, in both models, the system is assumed to be replenished continuously with CO_2, and the imposed f_{CO_2} values are those of the initial aqueous solution.

10.3.1. The initial aqueous solutions

10.3.1.1. The initial aqueous solution in model A

As already recalled, the rainwater-diluted, degassed fumarolic steam condensate from the Stephanos crater was taken to be representative of the initial aqueous solution in model A.

The composition of the undiluted steam condensate was calculated based on the average

H_2O, CO_2, and H_2S concentrations of Stephanos fumarolic fluids (see Marini and Fiebig, this volume). A negligible total concentration, 10^{-20} mol/kg, was assumed for dissolved Cl, Na, K, Mg, Ca, Al, Fe, and SiO_2 to activate these chemical components. Temperature was set at 100°C and f_{O2} at $10^{-57.4}$ bar, which is the value fixed by the FeO-$FeO_{1.5}$ hydrothermal redox buffer of Giggenbach (1987). The electroneutrality condition was imposed to calculate pH.

From a first EQ3 run, it turned out that computed total fluid pressure exceeds 1 bar. If external pressure is assumed to be 1 bar, the aqueous solution must experience gas exsolution (degassing) until total fluid pressure attains 1 bar. Single-step degassing was, therefore, modeled starting from the composition of the aqueous phase computed by the first EQ3 run, referring to the following mass balance:

$$\left(\frac{n_j}{n_{H_2O}}\right)_O = \left(\frac{n_j}{n_{H_2O}}\right)_G x + \left(\frac{n_j}{n_{H_2O}}\right)_L (1-x) \tag{1}$$

and assuming equilibrium gas-liquid partitioning of gas species, i.e.:

$$B_j = \left(\frac{n_j}{n_{H_2O}}\right)_G \Bigg/ \left(\frac{n_j}{n_{H_2O}}\right)_L , \tag{2}$$

where the subscripts O, G, and L indicate the initial undegassed liquid, the separated gas, and the degassed liquid phase, respectively, and x is the fraction of separated gas. Water fugacity was assumed to be fixed by temperature. The partition coefficients B_j of CO_2 and H_2S were computed from gas solubility data (Henry's constants) reported in the COM thermodynamic database of EQ3/6, $K_{H,j}$, and f_{H_2O}, by means of the equation:

$$B_j = \frac{K_{H,j}}{f_{H_2O}} . \tag{3}$$

To compute degassing effects, x was tentatively varied until total fluid pressure equalled 1 bar. At this point it was necessary to recompute the composition of the degassed liquid phase, by means of a second EQ3 run. The pH of the undiluted, degassed steam condensate resulted to be 4.5 (Table 10.1). This value is constrained by dissociation of aqueous CO_2 and H_2S, by far the two prevailing solutes, with molalities of 1.43×10^{-3} and 1.24×10^{-3}, respectively. The products of their first dissociation, HCO_3^- and HS^- ions, have molalities of 1.87×10^{-5} and 1.30×10^{-5}, respectively. Therefore, this aqueous solution has a certain pH-buffering capacity.

In the absence of chemical data on local rainwater, its composition was obtained through dilution of seawater assuming a Cl concentration of 16.2 mg/L, which is a reasonable value for coastal rains (e.g., Appelo and Postma, 1996; Berner and Berner, 1996). The fugacities of CO_2 and O_2 were fixed at the average atmospheric values, $10^{-3.5}$ and $10^{-0.678}$ bar, respectively. Temperature was set to 15°C. Again, the electroneutrality condition was imposed to compute pH, which turned out to be 7.70, a rather high but still plausible value for a rain (Table 10.1).

Then, the degassed steam condensate and the rain water were mixed by running EQ6. Assuming a temperature of 50°C for the mixture, the fractions of the two components were computed by means of a simple enthalpic balance, obtaining values of 0.41 for the degassed steam condensate and 0.59 for the rain water. The computed f_{O2} and pH resulted to be $10^{-61.6}$ bar and 4.49, respectively (Table 10.1). This pH value is not appreciably different from that of the undiluted, degassed steam condensate, 4.5, due to its pH-buffering capacity (see above). The aqueous speciation of the diluted steam condensate is dominated by dissolved CO_2 and H_2S, with molalities of 7.61×10^{-4} and 4.17×10^{-4}, respectively. However, also SO_4^{2-} ion has a significant molality of 1.10×10^{-4}.

10.3.1.2. The initial aqueous solution in model B

In model B, the average fumarolic fluid of Stephanos crater was cooled conductively from 100 to 50°C imposing an f_{O2} of $10^{-0.678}$ bar, i.e., the average atmospheric value. Again, in a first EQ3 run, total fluid pressure exceeded 1 bar. Since P_{H2S} has a negligible value of 10^{-115} bar under these highly oxidising conditions, total fluid pressure corresponds to the sum of P_{H2O} plus P_{CO2} plus P_{O2}. Since P_{H2O} and P_{O2} are known, P_{CO2} was adjusted straightforwardly to $10^{-0.16}$ bar, which is the difference between 1 bar and $P_{H2O} + P_{O2}$.

The composition of the undiluted conductively-cooled steam condensate was then computed by means of a second EQ3 run. The pH of this fluid was found to be 0.81 (Table 10.1). This very low value is constrained by the dissociation of HSO_4^- ion and total sulfate molality, 0.186, which is mainly explained by HSO_4^- ion (91.74 %) and subordinately by SO_4^{2-} ion (8.25 %). Therefore, the pH-buffering capacity of this aqueous solution is due to the HSO_4^- / SO_4^{2-} pair. Of course, at this very low pH, aqueous CO_2 accounts for all the dissolved carbonates.

10.3.2. The solid reactants

The minerals forming a local andesite (Table 10.2a) as phenocrysts, groundmass crystals, and microlites in glass have been considered as solid reactants in reaction path modeling. Based on petrographic observations (Francalanci et al., 1995; Vanderkluysen et al., this volume), these selected minerals are plagioclase, sanidine (although it is virtually absent in Nisyros rocks, at least as phenocryst), a SiO_2-glass, clinopyroxene, olivine, magnetite, ilmenite, and apatite. Their molar fractions (Table 10.2b) were estimated by means of simple mass balances. Sanidine, magnetite, ilmenite, and apatite were taken as pure phases. Plagioclase was assumed to be a solid mixture of albite (X_{Ab} = 0.64) and anorthite (X_{An} = 0.36), clinopyroxene was considered to be a solid mixture of clinoenstatite (X_{En} = 0.50) and wollastonite (X_{Wo} = 0.40) with a subordinate contribution of ferrosilite (X_{Fs} = 0.10), and olivine was hypothesized to be a solid mixture of forsterite (X_{Fo} = 0.75) and fayalite (X_{Fa} = 0.25).

Incidentally, the term "solid solution" is generally preferred to "solid mixture" in the geochemical literature. However, the solvent can be distinguished from the solute(s) in a solution, which is not the case for the "solid solutions". Therefore, these should be called "solid mixtures".

Owing to the small amounts of ilmenite and apatite in the considered rock and their refractory behavior during water-rock interaction, these two phases were neglected. The initial surface area of the other minerals was estimated based on their molar fractions and a total initial surface area of 5000 cm^2 exposed to 1000 g of water. As an example, this surface area and this amount of water could pertain to a single fracture (whose opposite faces are 0.4 cm apart) which cuts a cube of rock, whose side is 50 cm. Alternatively, the same surface area belongs to a system made up of 203 spheres, each of radius 1.4 cm, with 1000 g of water occupying the pore spaces (porosity = 0.3). Of course natural systems can be very different from these limiting geometric models. Nevertheless, they are useful to understand the meaning of the solid surface exposed to the aqueous phase. It must be underscored that, during the simulation, the surface area of each solid reactant is automatically changed by the code in proportion to its mass.

Some words of caution are needed here, since the main difficulty in reaction path modeling is the characterization of reaction surface areas of mineral phases, as recognized by many authors (e.g., Lichtner, 1996, 1998; Appelo and Postma, 1996). For instance, the surface of contact between minerals and percolating meteoric waters in soils and rocks may deviate from the surface area in controlled laboratory experiments conducted to determine the dissolution/precipitation rates of minerals. Besides, the surface areas of solid phases computed through an inverse approach by Marini et al. (2000a) was found to change substantially during progressive water-rock interaction and to differ by several orders of magnitude from those obtained on the basis of modal mineralogy, grainsize and intergranular porosity.

10.3.2.1. The dissolution kinetics of solid reactants

The dissolution kinetics of solid reactants has been described by means of transition-state-theory (TST) rate laws (e.g., Aagaard and Helgeson, 1982; Helgeson et al., 1984). Since most of the dissolution rate experiments carried out so far on silicate minerals have been aimed at establishing the dependence of far-from-equilibrium dissolution kinetics on pH, their dissolution reactions can be assumed to involve, consistently with TST (Wieland et al., 1988): (1) a first fast step, consisting in the adsorption of either H^+, or H_2O, or OH^- (depending on pH) on the surface of the dissolving solid and leading to the formation of the activated complex from the reactants and (2) a second, slow step consisting in the decomposition of the activated complex, which generates the reaction products. This second step is therefore rate controlling. TST considers the activated complex as a true chemical species and hypothesizes that it is always in equilibrium with the reactants. Based on TST, the rate of surface-controlled reactions of dissolution and precipitation of a given solid phase per unit surface area, r, can be described by means of the following relation:

$$r = r_+ \cdot \left[1 - \exp\left(\frac{A}{\sigma RT}\right)\right], \qquad (4)$$

where r_+ is the forward (dissolution) rate per unit surface area, σ is the ratio between the rate of decomposition of the activated complex and the overall dissolution rate (σ is also known as Temkin's average stoichiometric number), and *A* is the thermodynamic affinity. We recall that the thermodynamic affinity measures the distance from the equilibrium (saturation) condition with respect to the considered solid phase for a given aqueous solution and it is defined as follows:

$$A = RT \cdot \ln \frac{Q}{K}, \qquad (5)$$

where K is the solubility product of the solid phase, that is the thermodynamic equilibrium constant of the overall dissolution reaction, and Q is the corresponding ion activity product.

Following Oelkers et al. (1994), it can be demonstrated that the far-from-equilibrium forward (dissolution) rate per unit surface area can be expressed as follows:

$$r_+ = k_{+H} \cdot K_H^* \cdot a_{H^+}^{n_H} + k_{+W} \cdot K_W^* + k_{+OH} \cdot K_{OH}^* \cdot \left(\frac{K_W}{a_{H^+}} \right)^{n_{OH}} \qquad (6)$$

where k_{+H}, k_{+W}, and k_{+OH} are the rate constants of the adsorption reactions of H^+, H_2O, and OH^-, respectively, which lead to the formation of the corresponding activated complexes, and K_H^*, K_W^*, and K_{OH}^* represent their thermodynamic equilibrium constants. Usually, only the products $k'_{+H} = k_{+H} \cdot K_H^*$, $k'_{+W} = k_{+W} \cdot K_W^*$, and $k'_{+OH} = k_{+OH} \cdot K_{OH}^* \cdot K_W^{n_{OH}}$ are known through suitable experiments. Thus equation (6) is conveniently re-written as:

$$r_+ = k'_{+H} \cdot a_{H^+}^{n_H} + k'_{+W} + k'_{+OH} \cdot a_{H^+}^{-n_{OH}} . \qquad (7)$$

The first term generally prevails in the acidic region, the second term dominates in the neutral region and the third term prevails in the basic region, thus explaining the typical U-shape of the log-rate of far-from-equilibrium dissolution for most silicates as a function of pH.

The apparent dissolution rate constants $k'_{+i,T}$ at the temperature of interest T = 323.15 K were computed based on their values k'_{+i,T_r} at the reference temperature T_r = 298.15 K by means of the integrated Arrhenius equation:

$$k'_{+i,T} = k'_{+i,T_r} \times \exp\left[\frac{-E_a}{R} \times \left(\frac{1}{T} - \frac{1}{T_r} \right) \right], \qquad (8)$$

where R is the universal gas constant and E_a is the apparent activation energy for the dissolution of the considered solid phases. The word apparent is used to recall that E_a also include the reaction enthalpy terms explaining the temperature dependence of K_H^*, K_W^*, and K_{OH}^*. Values of the apparent kinetic constant for the acidic and neutral dissolution mechanisms at T_r, corresponding apparent activation energies, and reaction order with respect to the H^+ ion for the solid phases of interest were taken from Palandri and Kharaka (2004) and references therein (Table 10.3).

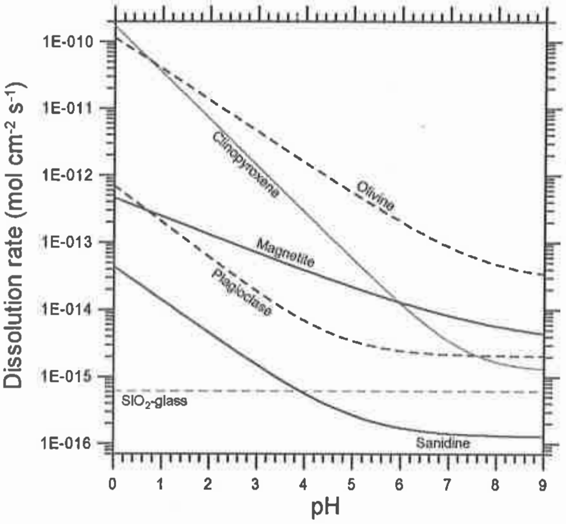

Figure 10.1. Plot of the far-from-equilibrium dissolution rate vs. pH for the primary minerals of interest at 50°C. Dissolution rates were computed based on the rate constants, reaction orders, and apparent activation energies from Palandri and Kharaka (2004) and references therein.

For SiO_2-glass only the apparent dissolution rate constant for the neutral dissolution mechanism was considered, assuming that it is equal to that of amorphous silica, consistent with the experimental results of Oelkers and Gislason (2001). The change in the far-from-equilibrium dissolution rate of the primary minerals of interest with pH, at 50°C, is depicted in Figure 10.1.

10.3.3. The solid product phases

To avoid the formation of unrealistic mineral phases and to maintain the reaction path modeling to a reasonably simple level, only β-cristobalite, gibbsite, goethite, magnetite, pyrite, kaolinite, anhydrite, alunite [$KAl_3(SO_4)_2(OH)_6$], jarosite [$KFe_3(SO_4)_2(OH)_6$], a solid mixture of calcite and siderite, a saponite solid mixture of composition $(Mg_{0.5},Ca_{0.5},Na,K)_{0.33}Mg_3Al_{0.33}Si_{3.67}O_{10}(OH)_2$, and a beidellite solid mixture of composition $(Mg_{0.5},Ca_{0.5},K,Na)_{0.33}Al_{2.33}Si_{3.67}O_{10}(OH)_2$ were allowed to precipitate as secondary (alteration) phases. Solid mixtures were necessarily hypothesized to be ideal, as this is the only solid mixing model supported by the EQ3/6 software package, version 7.2b.

As already recalled, product minerals were assumed to attain instantaneous equilibrium. This choice is dictated by the difficulty of defining the surface area for solid phases which are initially absent in the considered system.

10.3.4. The results of model A

10.3.4.1. The reactants in model A

The amounts of reactant minerals destroyed in model A are shown as a function of time and reaction progress in Figure 10.2. The two phases contributing most chemical components to the considered system through their destruction are olivine, especially for $\xi < 0.01$ moles (i.e., time < 14 years), and plagioclase, above these ξ and time thresholds. The high olivine contribution is due to the high reactivity of this solid phase, whose specific rate of dissolution (in mol cm^{-2} s^{-1}) is much higher than those of the other minerals of interest (see Table 10.3 and Figure 10.1). This causes a high dissolution rate, in terms of mol s^{-1}, in spite of the relatively small abundance and surface area of olivine. In contrast, the high contribution of plagioclase reflects its high abundance and surface area (see Table 10.2), which determine a high dissolution rate, in terms of mol s^{-1}, in spite of its relatively low specific dissolution rate (in mol cm^{-2} s^{-1}). The curves of clinopyroxene and sanidine are relatively similar, although sanidine dissolution ends for ξ of 0.54 moles, that is after 1160 years. Magnetite has a rather complex evolution, in that it turns from reactant to product for $0.00058 < \xi < 0.032$ moles (i.e., between 6 months and 29 years), but it becomes again a reactant after this threshold, until a ξ of 0.16 moles (corresponding to 299 years) when the aqueous solution saturates again with magnetite. At this point, magnetite was dropped from the considered paragenesis, for speeding up the calculations. The slowest dissolving phase is SiO_2-glass owing to its very low specific rate of dissolution (in mol cm^{-2} s^{-1}) at all pH values.

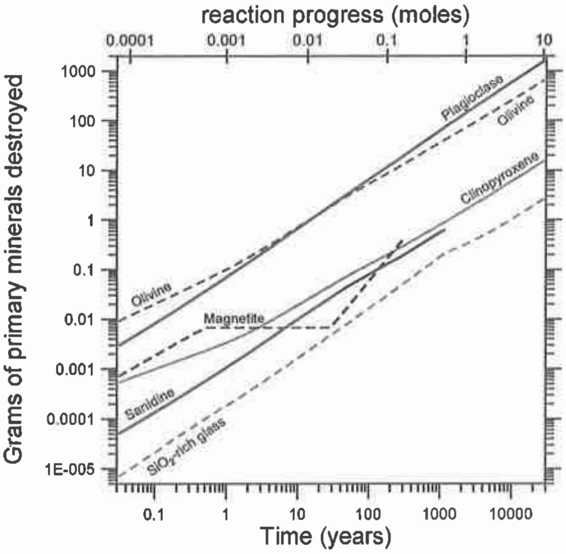

Figure 10.2. *Model A: amounts of reactant minerals destroyed during the computer simulation as a function of time and reaction progress.*

10.3.4.2. The secondary minerals in model A

The amounts of secondary (product) minerals formed in model A are shown as a function of time and reaction progress in Figure 10.3. The most important products are saponite, particularly for $\xi < 0.3$ moles (< 570 years), and beidellite, above this threshold. The siderite-calcite solid mixture is the third most important authigenic mineral. The other clay minerals kaolinite and illite are generated in smaller amounts and their existence is ephemeral. Kaolinite is converted to illite and illite is transformed to β-cristobalite, which is the only stable solid product of this reaction sequence. Pyrite is the first appearing phase, but it is produced in negligible amounts and has ephemeral existence.

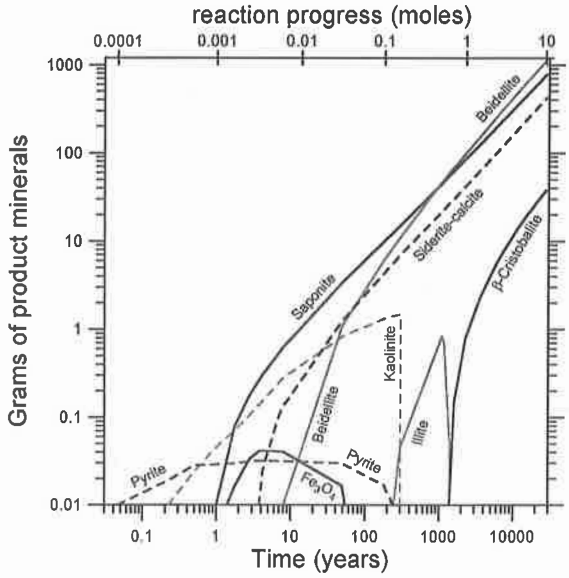

Figure 10.3. *Model A: amounts of secondary minerals formed during progressive rock dissolution as a function of time and the reaction progress variable.*

Magnetite also forms in small amounts and persists for an even shorter time window, as already recalled in the previous section.

10.3.4.3. The aqueous solution in model A

The total concentrations of considered solute species are depicted in Figure 10.4 as a function of time and the reaction progress variable. Also shown in Figure 10.4a is the weight of water, which decreases in the final part of the simulation attaining 990 g at ξ of 1 mol, 948 g at ξ of 5 moles, and 897 g at ξ of 10 moles. This evolution is due to incorporation of water in hydrous minerals, mainly beidellite and saponite, which may lead to dry-up of the system, a phenomenon described by Reed (1997). These changes in the water amount are accompained by mirror variations in the concentration of mobile solutes, e.g., chloride in this case, which is 9.64 ppm at ξ of 1 mol, 10.1 ppm at ξ of 5 moles, and 10.6 at ξ of 10 moles.

In contrast, the concentrations of other solutes experience large changes, mainly reflecting mineral dissolution/precipitation reactions. Silica increases significantly for $\xi < 0.001$ (~ 1 year), that is before attainment of saturation with respect to saponite. Then, when saponite begins to form, the saponite-kaolinite pair acts as an SiO_2-buffer. This is substituted by other SiO_2-buffers during subsequent andesite dissolution, until the aqueous solution saturates with β-cristobalite at ξ of 0.64 moles (1400 years). Nevertheless, dissolved SiO_2 concentration increases significantly above this ξ value owing to the formation of both the $NaHSiO_3^\circ$ aqueous complex and the $HSiO_3^-$ anion. The latter species is increasingly produced through dissociation of silicic acid, at the increasingly high pH values attained in the final part of the simulation, and stabilizes the $NaHSiO_3^\circ$ aqueous complex.

The overall growth in dissolved silica is accompanied by an even more regular increase in Na and $HCO_3(+CO_3)$, which are the main cation and anion, respectively. The increase in HCO_3 concentration at constant f_{CO2}, as assumed in the simulation, brings about a concurrent increase in pH (Figure 10.5), as expected based on the thermodynamic equilibrium constant of the reaction:

$$CO_{2(g)} + H_2O = HCO_3^- + H^+, \qquad (9)$$

which can be rearranged as:

$$pH = \log a_{HCO_3^-} - \log f_{CO_2} - \log K_{CO_{2(g)}} . \qquad (10)$$

The increase in dissolved K (Figure 10.4b) is less pronounced than that of Na, owing to K incorporation in solid phases (clay minerals in the case of K). The same process is even more important for Mg, Ca, and Fe, especially for $\xi > 0.001$ (~ 1 year). In particular, Ca and Fe are significantly sequestered by the siderite-calcite solid mixture. Aqueous Al is maintained at low concentrations throughout the andesite dissolution process by saturation with respect to clay minerals.

Total dissolved sulfate and sulfide undergo remarkable fluctuations which are partly due to precipitation and re-dissolution of pyrite and partly explained by changes in oxygen fugacity. It must be underscored, however, that the log f_{O2} exhibits relatively limited changes, from –61.1 to –63.2, and it does not deviate significantly from the log f_{O2} of sulfate/sulfide iso-activity. This depends on pH as indicated by the linear relation:

$$\log f_{O2} = -60.19 - 0.5 \times pH, \qquad (11)$$

which holds at 50°C, 1 bar and predicts log f_{O2} values of –63.0 at pH 5.6 and –64.7 at pH 9.1.

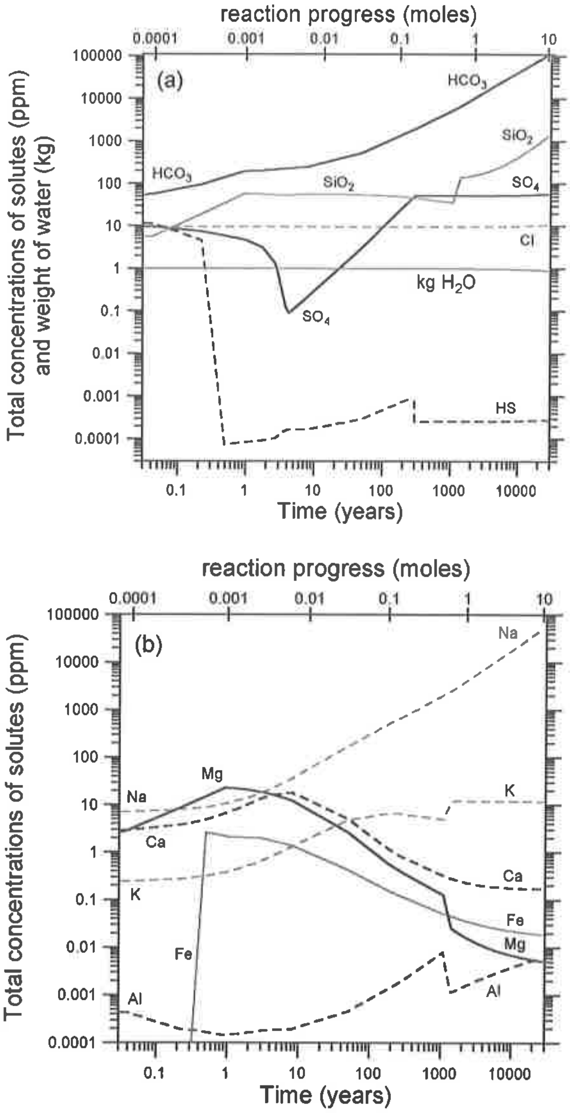

Figure 10.4. Model A: (a) Total concentrations of anionic solutes and silica as a function of time and the reaction progress variable; the water amount is also shown. (b) Total concentrations of cationic solutes as a function of time and the reaction progress variable.

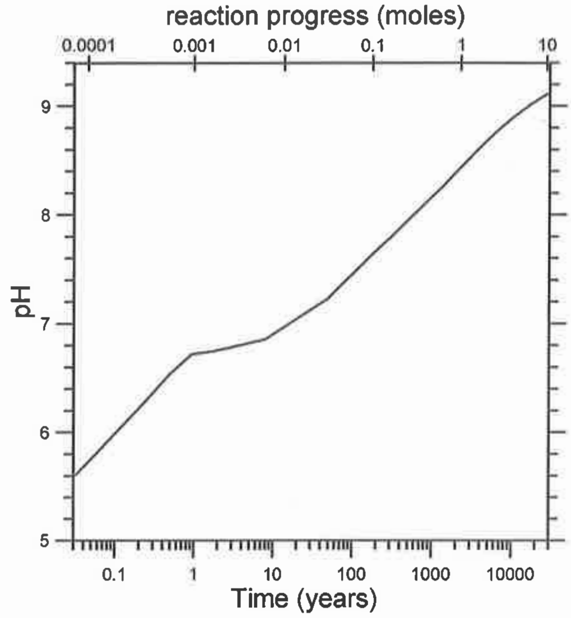

Figure 10.5*. Model A: evolution of pH during progressive andesite dissolution.*

10.3.5. The results of model B

10.3.5.1. The reactants in model B

The amounts of primary minerals destroyed during progressive andesite dissolution in model B are shown in Figure 10.6. Apart from SiO_2-glass, the trends are significantly different from those of model A with the following contributions, in decreasing order, olivine > clinopyroxene > plagioclase > magnetite > sanidine > SiO_2-glass. Since the initial surface area of the minerals are the same in both models, differences are due to the different pH ranges investigated, from 4.5 to 9.1 in model A, but from 0.8 to 5.9 in model B. Consequently the slowest, pH-independent neutral dissolution mechanism prevails through most of model A, whereas the fast, pH- dependent acidic dissolution mechanism dominates most of model B, apart from SiO_2-glass, whose dissolution was assumed to be controlled by the neutral mechanism only.

Indeed, the decrease in slope of the curves in Figure 10.6, for ξ of 0.1 to 0.15 depending on the mineral, marks the transition from the acidic to the neutral dissolution mechanism. Again, no change in slope is observed for SiO_2-glass.

10.3.5.2. The secondary minerals in model B

The amounts of secondary minerals produced during progressive andesite dissolution in model B are presented in Figure 10.7. β-cristobalite and goethite are early appearing solid phases and are the two main product minerals throughout the simulation.

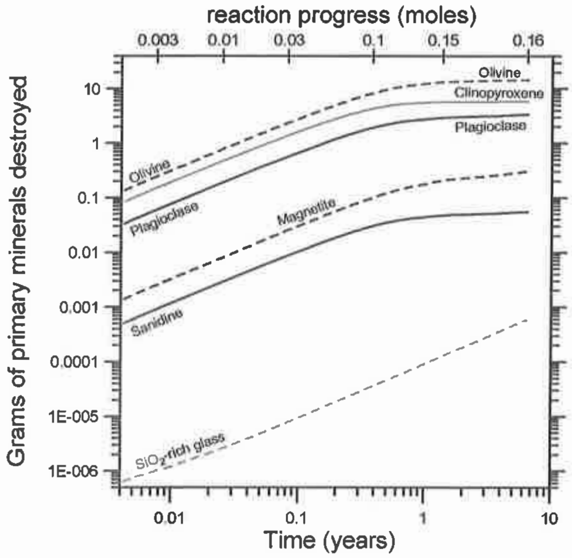

Figure 10.6*. Model B: amounts of reactant minerals dissolved during the computer simulation as a function of time and reaction progress.*

The two sulfate minerals, anhydrite and alunite, are the two following phases, in order of appearance, but they have very different histories. Anhydrite is a stable mineral and persists from pH 1.4 to 5.9, whereas alunite is formed in negligible amounts and has ephemeral existence, in the narrow pH window from 2.5 to 3.3.

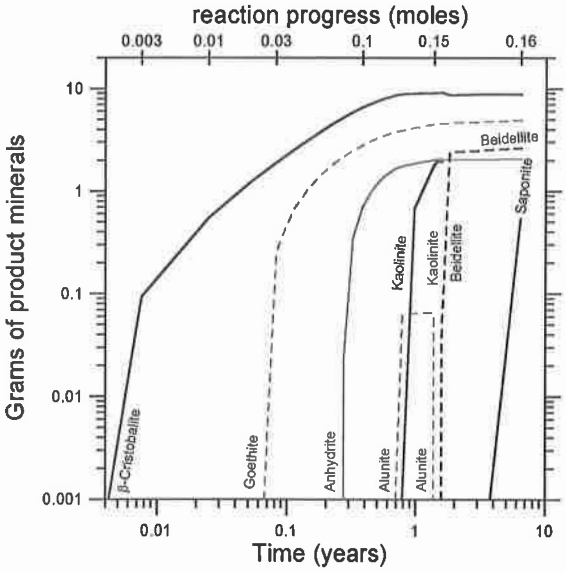

Figure 10.7*. Model B: amounts of product minerals formed during progressive andesite dissolution as a function of time and the reaction progress variable.*

Also kaolinite is an ephemeral mineral and is stable at pH values from 2.9 to 4.9, and for reaction progress and time intervals similar to those of alunite. Kaolinite is converted to beidellite at ξ of 0.152 (1.58 years).

10.3.5.3. The aqueous solution in model B

The total concentrations of anionic solutes plus SiO_2 and those of cationic solutes are shown as a function of time and the reaction progress variable in Figure 10.8a and b, respectively.

Dissolved SiO_2 concentration is kept constant by saturation with respect to β-cristobalite. Aqueous SO_4 is little affected by the precipitation of sulfate minerals, owing to its high concentration, which remains nearly constant throughout the simulation. Bicarbonate content experiences instead a significant increase from 0.002 to 1310 ppm owing to the gradual conversion of CO_2 to HCO_3^-. The increase in HCO_3 concentration is accompanied by a concurrent increase in pH (Figure 10.9) for the reason discussed in section 10.3.4.3.

In contrast to model A, Mg is the prevailing aqueous metal, owing to the dominant roles of olivine and clinopyroxene among the dissolving primary phases. The curves of dissolved Mg and Na in Figure 10.8b mimick those of Mg- and Na-bearing primary minerals (olivine, clinopyroxene, and plagioclase) in Figure 10.6, as these two chemical components do not enter any product solid phase, at least for $\xi < 0.152$ (time < 1.58 years), when beidellite begins to form.

The molar fraction of the Na-component in the beidellite solid mixture is very low (0.006-0.007), whereas that of the Mg-component is close to 0.83. Nevertheless, the concentration of dissolved Mg is so high that it is unaffected by incorporation in beidellite.

The curve of aqueous Ca parallels those of Na and Mg for $\xi < 0.08$ (time < 100 days), when anhydrite starts to precipitate, determining an inflection in the dissolved Ca trend.

An even more pronounced temporary inflection is evident in the curve of aqueous K due to its incorporation in precipitating alunite followed by return of K to the aqueous phase upon re-dissolution of alunite.

Also the curves of aqueous iron and aluminum parallel those of the other dissolved metals, but only for $\xi < 0.025$ (time < 24 days) and for $\xi < 0.130$-0.134 (time < 255-286 days), respectively. The precipitation of goethite and alunite + kaolinite, which begins at these ξ / time values, is responsible for a pronounced decrease in the concentrations of these dissolved metals, from the high values typical of acidic waters to the low contents characteristic of neutral waters.

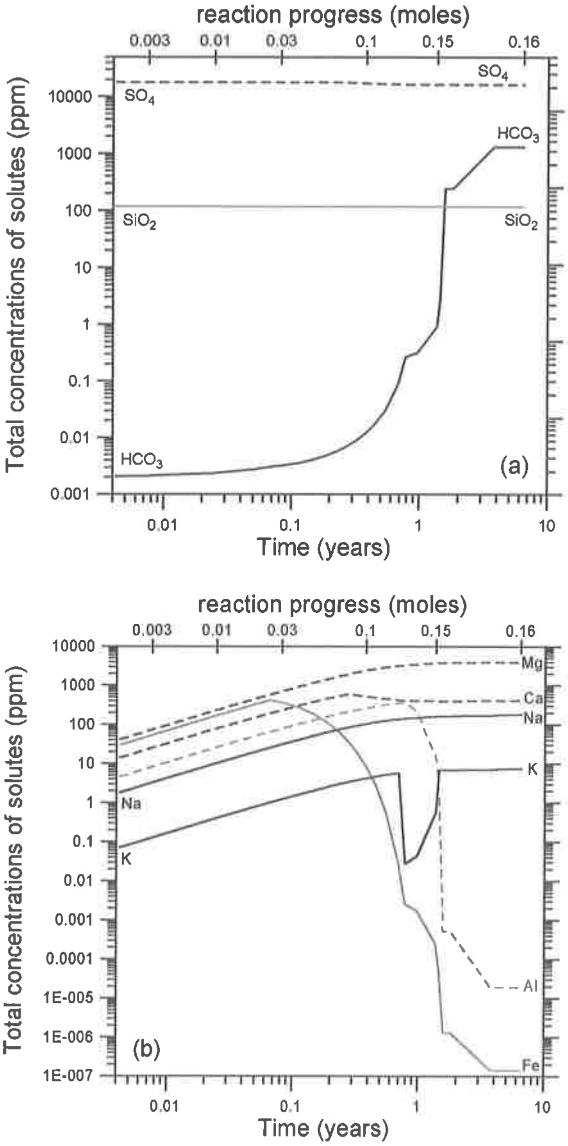

Figure 10.8. Model B: (a) Total concentrations of anionic solutes and silica as a function of time and the reaction progress variable. (b) Total concentrations of cationic solutes as a function of time and the reaction progress variable.

10.3.6. Comparison of model results and field evidences

The secondary minerals produced in model A are in good agreement with the petrographic observations gathered in geothermal wells Nisyros-1 and Nisyros-2 (see section 10.2), suggesting that model A represents a reasonable simulation of the natural processes occurring at shallow depths nearby these two wells. The only differences are represented by the lack of zeolites and anhydrite in the computer simulation, whereas they were recognised as hydrothermal minerals in geothermal wells. As already recalled, the precipitation of zeolite minerals was suppressed in computer experiments to keep the simulation to a relatively simple level, also considering that field knowledge of zeolite minerals is rather poor. Indeed, the zeolite groups include several minerals with different characteristics, in terms of chemical composition, stability, reactivity, etc. However, in the model A run, the aqueous solution becomes oversaturated with respect to several members of this mineral group, such as analcime, clinoptilolite, mesolite, natrolite, and stilbite. In other words, the formation of these zeolites is predicted by computer experiment A. The lack of secondary anhydrite in model A suggests that the anhydrite found in nature has a distinct history with respect to that of other minerals. In other words, it was probably deposited by oxidising aqueous solutions rich in SO_4 and Ca, similar to those generated in model B, that made temporary incursions into a reducing environment usually dominated by neutral waters. As a matter of fact, veins of anhydrite are rather frequent in the area of the hydrothermal craters and could locally extend in nearby zones (Figure 10.10).

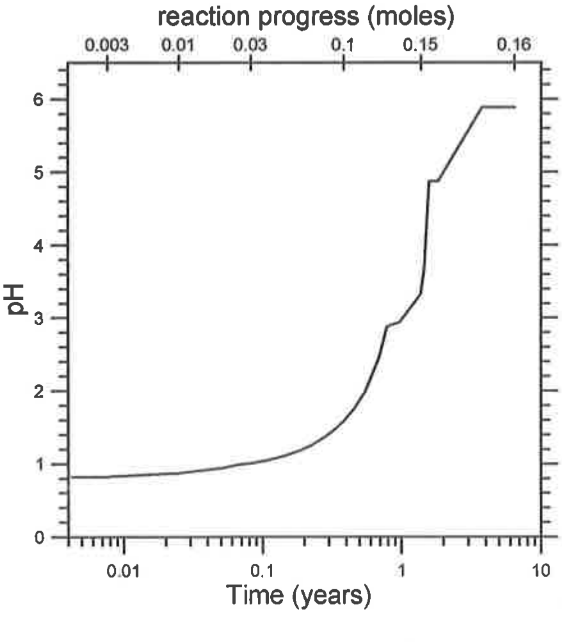

Figure 10.9. *Model B: evolution of pH during progressive rock dissolution.*

In contrast, the persistence of kaolinite and alunite in natural systems affected by acid-sulfate leaching, such as in the area of the hydrothermal craters of Nisyros, is at variance with the results of model B. The persistence of these minerals, which is an inconfutable field evidence, requires open-system conditions or, more specifically, a system which is either continuously or discretely recharged by the aqueous solution of fixed initial composition (i.e., the fumarolic steam condensate). This situation could be modeled adopting the solid-centered flow-through open-system option in EQ6, which will be implemented in future versions of this software package, but is not active in version 7.2b. Nevertheless, we can reasonably assume that open-system conditions must be present in areas affected by acid-sulfate leaching.

Figure 10.10. *Anhydrite veins into a lava block of the Polybotes Megalos hydrothermal debris flow deposit. Anhydrite evidently filled fractures that formed prior to the hydrothermal eruption and was later gypsified upon exposure to the atmosphere (from Marini et al., 1993, modified).*

10.4. The time scale of AA and AAA

Which is the time scale of AA and AAA ? In other words, how long does it take to produce a given percentage of clay minerals in a volcanic rock ? These are important questions to establish the possible role of AA and AAA in causing debris avalanches induced by flank collapse and hydrothermal eruptions.

Let us refer to the andesite example of previous sections. To compute the percentage of clay minerals in that rock, based on the results of models A and B, it is necessary to assume the amount of rock in contact with 1000 g of water at the beginning of the computer experiments. Adopting the set of 203 spheres, each of radius 1.4 cm (see section 10.3.2), the initial mass of andesite is $W_{AND,i}$ = 6355 g. The percentage of clay minerals formed during progressive andesite dissolution is:

$$\text{clay\%} = \frac{\sum_{C} W_C}{W_{AND,i} + \sum_{P} W_P - \sum_{R} W_R} \times 100 \qquad (12)$$

where indices C, P, and R refer to clay minerals, product (secondary) phases, and reactant (primary) phases either produced or destroyed during water-rock interaction. The clay% was computed both for model A and model B. In the first case W_C was computed taking into account the masses of kaolinite, illite, beidellite, and saponite, whereas in the second case only kaolinite was considered to focus on the typical clay mineral of AAA. Since the results of model B refer to a comparatively short time span, they were extrapolated to a much larger time interval based on the linear relationship between clay% and time, t (years):

$$\text{clay\%} = 0.0504 \times t - 0.0387, \qquad (13)$$

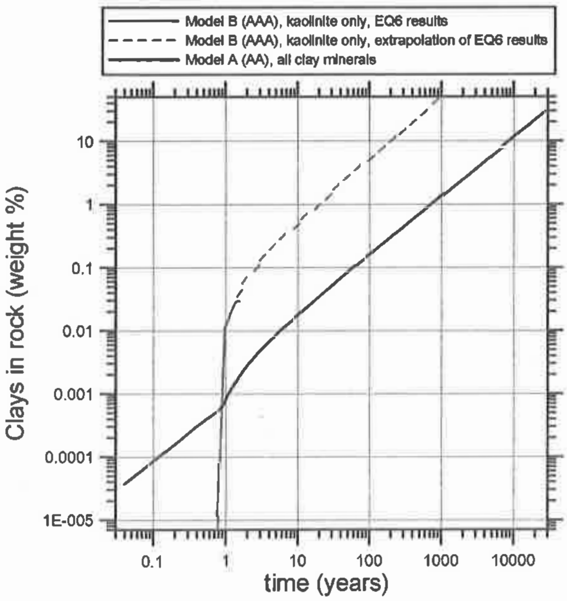

***Figure 10.11**. Percentage of clay minerals formed during progressive andesite dissolution as a function of time for both model A (AA) and model B (AAA).*

which was obtained for n = 16 and has a very high correlation coefficient (R^2 = 0.996). The clay% values computed for AA (model A) and AAA (model B) are shown as a function of time in Figure 10.11, where EQ6 results and their extrapolation for model B are plotted separately.

During progressive dissolution of andesite in a neutral aqueous solution under an f_{CO2} of $10^{-1.4}$ bar and strongly reducing conditions (model A), the percentage of clay minerals in the rock attains 1% in 780 years, 10% in 8500 years, and 30% in 28,500 years. Given enough time, in the order of over 10,000 years, AA can affect a significant fraction of the original rock. Note that the main reactant sustaining AA is CO_2, which must be supplied continuously to the system in order to maintain f_{CO2} at a reasonably high level. Also note that the f_{CO2} assumed in reaction path modeling, $10^{-1.4}$ bar, coincides with the upper f_{CO2} value for soils (Appelo and Postma, 1996 and references therein) but probably underestimate the average f_{CO2} values expected to be present at Nisyros, owing to magma degassing, thermo-metamorphic decarbonation reactions, and hydrothermal activity.

The percentage of clay minerals formed during the interaction of andesite with a strongly acidic aqueous solution under an f_{CO2} of $10^{-0.16}$ bar and strongly oxidising conditions (model B) cannot be evaluated on a sound basis as a different approch to reaction path modeling, e.g., the solid-centered flow-through open-system option (still not available in version 7.2b of EQ6), would be needed. However, extrapolation of the time derivative of the percentage of kaolinite in reacted andesite, based on the data obtained under closed-system conditions, suggests that the kaolinite % could attain 1% in 20 years, 10% in 200 years, and 30% in 600 years. Note that, in this case, a continuous supply not only of CO_2 but also of the strongly acidic aqueous solution (i.e., the fumarolic steam condensate) are required to drive the process. In addition, f_{CO2} must be maintained at a much higher value than in model A. Nevertheless, these requirements are easily met in the area of the hydrothermal craters of Nisyros.

Summing up, AAA appears to be a process more demanding, in terms of chemical reactants, but it proceeds much faster than AA. Given enough time, AA can take place to a significant extent almost everywhere, whereas AAA requires special conditions capable of sustaining acid sulfate leaching.

10.5. Consequences for debris avalanches induced by flank collapse

The extent of AA and AAA can be very different depending on several factors, including temperature, pressure, supply of CO_2, O_2, ..., some of which have been discussed in previous sections. However, the most important factor governing the extent of AA and AAA is the kind of solid medium affected by theses processes (Marinelli, 1978).

In fractured media, such as most lavas (excluding their scoriaceous boundaries), the aqueous solution driving hydrothermal alteration does not penetrate the rock, but circulates only along the fractures and, eventually, the pore space connected with them. Secondary minerals are deposited along these circulation channels and the altered rock is constituted by unaltered or weakly altered blocks wrapped by alteration products.

In porous solid media, such as a lapilli fall deposits and most other pyroclastic and epiclastic deposits as well, the aqueous phase permeates most of the rock and is able to attack almost all its constituting grains. Given enough time (see section 10.4), AA and especially AAA transform the pyroclastic deposit in a sort of mud, perhaps with sparse, unsupported clasts representing the remnants of the largest original clasts. Even pyroclastic deposits of high initial permeability are thus transformed into impermeable layers rich in clay minerals. Note that these represent a relatively large reservoir of liquid water, which plays an important role in the debris avalanche dynamics (see below).

The presence of a strongly argillified, relatively thick pyroclastic layer situated at the bottom of a fragmented rock, such as a lava dome or a thick lava flow, along the steep flanks of the volcano represents the typical situation potentially leading to flank (or sector) collapse and to the consequent generation of a debris avalanche. Note that to generate a debris avalanche rather than a simple landslide, the rock (the lava dome or the thick lava flow, in this case) must have been already fragmented (Ui et al., 2000). This condition is easily attained in volcanoes, owing to the continuos action of rock disaggregation carried out by either the CO_2-rich acid sulfate waters or the CO_2-bearing waters circulating in the volcanic edifice, mostly along a network of faults and fractures of tectonic or volcano-tectonic origin (Siebert et al., 1987). This is the case of Nisyros and other Aegean Islands which are the theater of intense active tectonics (Principe et al., this volume).

The collapse can be triggered by several factors (Day, 1996), including not only high-magnitudo earthquakes, tilting of the volcanic edifice, and intrusion of domes and dykes but also, for coastal volcanoes or volcanic islands, changes in sea-level or erosion along the coast (Principe et al., this volume).

The amounts of clay minerals and water (mostly stored in the clay minerals themselves) play a fundamental role in governing the debris avalanche dynamics. The mixture of clay minerals and water forms a cohesive paste which supports the fine-grained particles and reduces the tension between them. In turn, this cocktail of water, clay minerals, and fine-grained particles is able to support the larger clasts (Rodine and Johnson, 1976). According to different authors, even small amounts of clay minerals (1 to 2 %) are enough to support the debris avalanche dynamics. Based on the reaction path modeling exercise carried out in previous sections, 780 years are required to attain 1% of clay minerals in the case of AA, whereas a much shorter time, 20 years, is needed in the case of AAA. These lapses of time are obviously affected by several uncertainties, but in spite of these possible errors, they can be considered as a twinkling of an eye in the history of a volcano.

10.6. Consequences for hydrothermal eruptions

The hydrothermal craters and hydrothermal-eruption deposits present in the southern Lakkì plain at Nisyros were described and interpreted by Marini et al. (1993), in the light of the Gorceix's letters relative to the 1871-1873 hydrothermal eruptions and the Martelli's description for the small hydrothermal event of 1887, and based on the conceptual geochemical model proposed by Chiodini et al. (1993a).

As recognised by Marini et al. (1993), all the hydrothermal deposits of the southern Lakkì plain have similar characteristics and were probably originated through the same emplacement mechanism. These hydrothermal deposits are made up of unsupported, poorly sorted, from angular to subrounded fragments of pre-existing rocks, with a maximum size of a few meters, dispersed into a prevailing matrix. This is made up of fine-grained fragments produced, at least partially, through pulverization of pre-existing rocks and contains secondary sulfur and gypsum crystals. This matrix constitutes up to 70-80% of the recent deposits emitted from the craters of Phlegethon, Polybotes, and Stephanos, which have not been depleted in fine-grained materials by dissolution and erosion. Indeed, it was noted that the matrix amount decreases with time due to the chemical and physical effects of weathering (see Volentik et al. (b), this volume). The deposit components are affected by AAA preceding the eruptive events and some lava blocks host anhydrite veins up to a few centimeters in width (Figure 10.10).

All the characteristics of the hydrothermal deposits suggest that they were emplaced as debris flows experiencing lateral transport. These debris flows probably have an interstitial mud-water content > 5% by weight, which is the minimum value needed to lubricate the movement of the granular component in this kind of deposits (Cas and Wright, 1987). These debris flows were emplaced during the open-conduit stage of the hydrothermal eruptions, after the initial steam blast, which is chiefly responsible for both opening of the conduit and cratering.

According to Marini and Fiebig (this volume) the conceptual geochemical model of the Nisyros magmatic-hydrothermal systems comprises: (i) a degassing magma body, situated at unknown depth below the caldera of Nisyros and (ii) a deep hydrothermal aquifer hosting high-salinity aqueous solutions with Cl concentrations up to 75,500-78,900 mg/kg, with temperatures up to 340°C or somewhat higher. The gases released from the magma body enter the overlying hydrothermal aquifer from below, supplying matter and heat. Below the area of the hydrothermal craters, the deep hydrothermal liquids rise towards the surface, along faults and fractures, cooling conductively first and through boiling afterwards. The separated vapors are partly discharged by the fumarolic vents, but most steam experiences condensation close to the surface, whereas both CO_2 and heat are released to the atmosphere. The overall flux of vapors (16 kg/s, Caliro et al., 2005) moves along a sort of irregular column, whose shape is controlled by local faults and fractures, situated above the deep hydrothermal aquifer. Contrary to what maintained by Chiodini et al. (1993a), therefore, the shallow hydrothermal aquifer is not present below the area of the hydrothermal craters. However, the shallow hydrothermal aquifer, with temperatures up to 120-180°C, is present in nearby areas, as indicated by the deep geothermal wells Nisyros-1 and Nisyros-2.

Based on this revised conceptual geochemical model, an increase in fluid pressure leading to hydrothermal eruptions may be determined by one of the following mechanisms (Barberi et al., 1992):

(i) Impermeabilization of the cover rocks through self-sealing (Fytikas and Marinelli, 1976; Hedenquist and Henley, 1985). In particular, AAA-induced impermeabiliza-tion takes place at the shallow levels which can be reached by atmospheric O_2. Based on the correlation between the hydrothermal crater diameter and the depth of explosion (Fytikas and Marinelli, 1976), small hydrothermal craters are, therefore, expected for AAA-induced sealing. This could be the case of the 1887 event, that produced the small Polybotes Micros crater. Indeed, no earthquake is reported for this hydrothermal eruption, although the Martelli's (1917) description is rather meagre. Ideally, this type of hydrothermal explosion is similar to the bubbles forming at the flat surface of the "polenta" (Marinelli, oral communication), which is Italian for a thick maize porridge typically served with cheese, meat, or sausages.

(ii) Increase in pressure in the deep hydrothermal aquifer owing to increasing input of magmatic fluids from the underlying magma body. This phenomenon probably took place at Nisyros after the increase in activity that occurred in 1995-1998 including anomalously high seismicity, ground deformations, and significant variations in the chemistry of fumarolic fluids (Chiodini et al., 2002; Shimizu et al., 2005; Caliro et al., 2005; Marini and Fiebig, this volume), although the pressure increase, in this case, was not sufficient to bring about a hydrothermal eruption.

(iii) A sudden uprise of deep hydrothermal fluids along a fracture system opened or re-activated by a seismic event (Lloyd, 1959; Cross, 1963; Fytikas and Marinelli, 1976). Gorceix's letters suggest that tectonic earthquakes triggered the 1873 hydrothermal eruptions.

10.7. Conclusions

The reaction path modeling experiments performed in this study show that very short time spans are required to generate the hydrothermal clay minerals typical of AAA and AA in amounts sufficient to lubricate flank-collapse-induced debris avalanches and hydrothermal debris flow deposits, in spite of the simulation uncertainties, which are mainly related to the reactive surface area of primary dissolving phases.

All the other boundary conditions needed to generate debris avalanches induced by flank collapse (namely tectonically fragmented lava domes and thick lava flows situated on the steep flanks of the volcano and overlying loose pyroclastic deposits) and to trigger hydrothermal eruptions (namely an active, unstable hydrothermal system in a tectonically active area) are locally present, today, at Nisyros. Therefore, the risks related to these two volcanic phenomena have to be taken in serious consideration.

Table 10.1. Total concentrations of relevant solutes, temperature, log f_{O2}, log f_{CO2}, and pH of the two initial aqueous solutions and their parent waters.

	Undiluted, degassed steam condensate	Rainwater	Rainwater-diluted degassed steam condensate (initial sol. in model A)	Undiluted conductively-cooled steam condensate (initial sol. in model B)
T(°C)	100	15	50	50
log f_{O2}	-57.37	-0.678	-61.63	-0.678
log f_{CO2}	-0.875	-3.5	-1.405	-0.161
pH	4.50	7.70	4.49	0.81
m_{Al}	1.00E-20	2.96E-11	1.75E-11	1.00E-20
m_{Ca}	1.00E-20	1.12E-04	6.61E-05	1.00E-20
m_{Cl}	1.00E-20	4.57E-04	2.69E-04	1.00E-20
m_{Fe}	1.00E-20	2.86E-11	1.69E-11	1.00E-20
m_C	1.45E-03	3.02E-04	7.74E-04	1.27E-02
m_K	1.00E-20	1.02E-05	6.03E-06	1.00E-20
m_{Mg}	1.00E-20	2.88E-05	1.70E-05	1.00E-20
m_{Na}	1.00E-20	5.13E-04	3.02E-04	1.00E-20
m_S	1.25E-03	3.02E-05	5.31E-04	1.86E-01
m_{Si}	1.00E-20	6.66E-08	3.92E-08	1.00E-20

Table 10.2a. Whole rock analysis (wt%) of the local andesite considered as solid reactant (from Vanderkluysen et al., 2005)

SiO_2	TiO_2	Al_2O_3	$Fe_2O_{3,tot}$	MnO	MgO	CaO	Na_2O	K_2O	P_2O_5
59.38	1.17	17.06	7.57	0.14	2.48	5.66	4.2	2.1	0.25

Table 10.2b. Computed molar amounts and initial surface area of the local andesite minerals.

Mineral	Plagioclase	SiO_2-glass	Sanidine	Clinopyroxene	Olivine	Magnetite	Ilmenite	Apatite	Total
Molar fraction	0.5895	0.1417	0.1235	0.0489	0.0384	0.0312	0.0156	0.0049	0.9935
Initial surface area (cm^2)	3599	194	783	122	137	164	nd	nd	5000

Table 10.3. Values of the proton-promoted and water-promoted apparent kinetic constants and apparent activation energies and reaction order with respect to the H^+ ion for the solid phases of interest and SiO_2-glass. Kinetic constants are given both at the reference temperature $T_r = 298.15$ K and at the simulation temperature $T = 323.15$ K.

Mineral	k'_{H,T_r} mol cm^{-2} s^{-1}	$k'_{H,T}$ mol cm^{-2} s^{-1}	n_H	$E_{a,H}$ kJ mol^{-1}	k'_{W,T_r} mol cm^{-2} s^{-1}	$k'_{W,T}$ mol cm^{-2} s^{-1}	$E_{a,W}$ kJ mol^{-1}
Plagioclase	1.32E-13$^{(a)}$	7.00E-13	0.541$^{(a)}$	53.5$^{(a)}$	3.39E-16$^{(a)}$	2.03E-15	57.4$^{(a)}$
SiO_2-glass	--	--	--	--	5.89E-17$^{(a,b)}$	6.02E-16	74.5$^{(a,b)}$
Sanidine	8.71E-15$^{(a)}$	4.37E-14	0.500$^{(a)}$	51.7$^{(a)}$	3.89E-17$^{(a)}$	1.27E-16	38.0$^{(a)}$
Clinopyroxene	1.51E-11$^{(a)}$	1.73E-10	0.700$^{(a)}$	78.0$^{(a)}$	1.07E-16$^{(a)}$	1.22E-15	78.0$^{(a)}$
Olivine	1.41E-11$^{(a)}$	1.15E-10	0.470$^{(a)}$	67.2$^{(a)}$	2.29E-15$^{(a)}$	2.70E-14	79.0$^{(a)}$
Magnetite	2.57E-13$^{(a)}$	4.59E-13	0.279$^{(a)}$	18.6$^{(a)}$	1.66E-15$^{(a)}$	2.97E-15	18.6$^{(a)}$

(a) from Palandri and Kharaka (2004) and references therein.
(b) assumed to be equal to those of amorphous silica.

11. Preliminary implications for volcanic hazards at Nisyros (Greece), based on past volcanic activity

Claudia Principe(2), Alain C. M. Volentik(1), Loÿc Vanderkluysen(1),
Johannes C. Hunziker(1), Luigi Marini(3)

(1) Institut de Minéralogie et Géochimie, BFSH-2, Université, CH-1015 Lausanne, Switzerland.

(2) Istituto di Geoscienze e Georisorse, Area della Ricerca CNR-Pisa San Cataldo Via G. Moruzzi 1, I-56124 (Pisa), Italy

(3) Laboratorio di Geochimica, Dip.Te.Ris., Università di Genova, Corso Europa 26, I-16132 Genova, Italy

Abstract - New features of the Nisyros volcanic history, highlighted through the reinterpretation of the volcanic facies of the Lower Pumices (**lp**) and Upper Pumices (**up**) deposits and the discovery of the debris avalanche deposits of Vunàri (**vu$_i$**), generated through a sector collapse that affected the northern flanks of the volcano, have been considered together with already known features for producing a set of hazard maps, each related to a particular kind of volcanic event expected in case of volcanic reactivation on Nisyros island.

11.1. Introduction

The southern Lakkì plain, once studied for possible geothermal exploitation (Geotermica Italiana, 1983; 1984; Dawes & Lagios, 1991; Lagios & Apostolopoulos, 1995; Kavouridis et al., 1999), is known to host about a dozen hydrothermal craters, some of which were created by hydrothermal explosions in historical times. These very recent craters are Alexandros (1871), Polyvotis (1871), and Polyvotis Mikros (1887) (Gorceix, 1873; Martelli, 1917; Marini et al., 1993). In recent years, there has been a concerted effort to assess volcanic hazards related to hydrothermal eruptions, mainly through the study of fumarolic gases (Chiodini et al., 1993; Dotsika & Michelot, 1993; Brombach et al. 2001; 2003; Cardellini et al., 2003; Caliro et al., 2005). However, the discovery of possible ongoing volcanic unrest at Nisyros (Papadopoulos et al., 1998; Lagios et al., 2001; Sachpazi et al., 2002; Chiodini et al., 2002; Sykioti et al., 2003; Gottsmann et al., 2004) and the existence of an evolved magma chamber beneath the volcano (Chonia & Makris, 2000; Marini et al., 2002) further emphasise the need for a volcanic hazard assessment on the island.

In the past, a number of volcanic eruptions of different types occurred on Nisyros Island. Among these, the most devastating events were related to the emplacement of pumice and lapilli fallout, pyroclastic density currents, and minor block and ash flow deposits. Less destructive eruptions consisted in the emission of lava flows and the growth of viscous domes. All these volcanic events bring about a potential risk for the inhabitants of the island upon reactivation of the volcanic-magmatic system in the future, although it is not possible, at present, to predict neither the future kind of event nor its time of occurrence.

In addition to the hazards related to these volcanic eruptions, which are accepted to have occurred on Nisyros based on the existing scientific literature (Vougioukalakis, 2003 and references therein; GEOWARN project site http://www.geowarn.org, and Teschner et al., 2003), new insights on potential hazards result from the discovery in the stratigraphic succession of an other kind of volcanic event, namely the sector collapse that affected the northern flanks of the volcano generating the Vunàri debris avalanche deposits (**vu$_i$**). These deposits show the characteristic hummocky morphology and crop out along the northern coast of Nisyros, between Mandraki and Palì (see Volentik et al.(a), this volume). Note that they were formerly misinterpreted as a block and ash flow deposit caused by dome collapses (Limburg & Varekamp, 1991; Vougioukalakis, 1993; Francalanci et al., 1995).

Moreover, the detailed reconstruction of both the areal distribution and volumes of the different kinds of deposits has shown that the eruptions of the Lower Pumices (**lp**) and Upper Pumices (**up**) have chiefly produced pyroclastic density currents rather plinian fallouts as erroneously interpreted by previous authors.

Of course, the different depositional mechanisms of debris avalanche deposits instead of block and ash flow deposits and of pyroclastic density currents instead of plinian fallouts imply a different hazard zoning.

Hazard maps, to be sound, must be based on the past history of the volcano, the active volcano-tectonic framework, and the present morphology of the volcano under study. Consequently, further important data for their elaboration come from the positioning of past eruptive vents and the definition of active tectonic trends, which are given in this volume (see Volentik et al.(b) and Volentik et al.(c), respectively).

Based on these premises, we present in this section a set of hazard maps (Fig. 11.1), one for each type of volcanic event which has occurred in the past history of Nisyros volcano.

11.2. Hydrothermal explosions

This kind of volcanic hazard has the maximum probability of occurrence in a relatively short period, due to the presence of an active, unstable hydrothermal–magmatic system. As a matter of fact, hyrothermal eruptions took place repeatedly in a very recent past, with the last events in 1871-1873 and 1887 (Marini et al., 1993).

The map of Fig. 11.1-A highlights that hydrothermal events are expected to occur along the active tectonic trends inside the caldera floor (see Volentik et al. (c) this volume) and with the highest probability at the crossing between the 030°N- and the 340°N-trending tectonic elements. Indeed, the hydrothermal craters of Stefanos, Polyvotis, Phlegethon, and Kaminakia share this kind of location.

The area of craterization induced by the Stefanos hydrothermal eruption has been used as an analogue for similar future events and extrapolated along the 030°N- and the 340°N-trending active faults.

The distribution of past deposits indicates that the hazards related to hydrothermal explosions are not only confined to the formation of craters, which mainly occurs during the initial blast phase. The subsequent emission of hot mudflows is an additional hazard induced by this type of event.

Hazards due to hydrothermal explosions are essentially confined to the central and southern Lakkì plain and as such do not represent a major risk for the island's inhabitants. However, this hazardous area is the target of an important tourist flux between May and September (200 to 1000 visitors per day). An eruption during the high season would likely cause a human disaster, and would have a long-term impact on the island's economy. In addition, the entire Lakkì plain is at risk of mudflows. Their occurrence might cause important damages to this herding area of Nisyros and suggest to avoid planning of new buildings and infrastructures on the caldera floor.

To mitigate the hazard related to hydrothermal explosions, fumaroles have been sampled and analysed repeatedly, especially during and after the 1995-1998 seismic crisis (Marini and Fiebig, this volume). Indeed, the eventual gradual pressure build-up in the Nisyros hydrothermal system can be monitored through systematic sampling and analysis of fumarolic effluents and use of suitable geothermometric-geobarometric techniques (Chiodini and Marini, 1998 and references therein). Therefore, the evolution of the hydrothermal system towards critical P,T conditions bringing about a hydrothermal eruption can be established with sufficient prior warning.

11.3. Airfall deposit

The recognition of several fallout layers in the volcano's history (**ka, ms, xo, vs$_n$, lp**) led us to acknowledge this type of risk in case of major explosive eruptions on Nisyros.

In Fig. 11.1-B we modelled a theoretical isopach geometry according to the observed ash and pumice fallout thickness and source position of the **lp** event, which is the major fallout deposit recognised in the island.

The dispersion of a fallout deposit in the case of a Plinian eruption at Nisyros, with the eruptive cloud reaching stratospheric levels, depends on the vertical wind profile in the south-eastern part of the Aegean Sea and on the intensity of the eruption controlling the column height. The shape of the isopachs, on the other hand, depends on the wind intensity. The few fallout thickness data that have been so far collected on the island (see Volentik et al.(b), this volume) seem to indicate a wind direction to the north-east quadrant for past events on Nisyros. The present day wind distribution pattern (Fig. 11.2) agrees with a eastward dispersion of pumice fallout coming from an eruptive columns between 8 and 15 km height. This datum is in agreement with violent strombolian-subplinian and small scale plinian events (Arrighi et al. 2001) as easily is the case of Nisyros past explosive events. Consequently, we used a similar direction for the dispersal axis in the map of Fig. 11.1-B. Of course, this model can be modified according to different wind scenarios.

As the roofs of houses in Greece are most often flat, they are particularly subjected to damage caused by the heavy load of fallout deposits, especially in the case of wet ash deposits generated during phreatomagmatic eruptive episodes. Furthermore, as most roofs on Nisyros are used to collect rainwater, pumice- and ash-falls, even a few centimetres thick, would likely cause water pollution and shortage of fresh water on Nisyros for a whole dry season. Fallout would also generate pollution of grazing grounds, thus causing illnesses and even death of animals. Finally, even if the main town of Mandraki would be little affected by fallout deposition, according to the scenario depicted in the map of Fig. 11.1-B and the present day wind distribution pattern (Fig. 11.2), sea lines bringing goods and fresh water to Nisyros would certainly have to be cut off during the duration of such an eruption.

11.4. Strombolian activity

The off-centred and widespread strombolian activity located along the major tectonic trends observed in the Lies synthem could represent an important risk for the Nisyros inhabitants, which could be further enhanced in the case of water/magma interaction. The strong correlation between volcanic activity and tectonic activity at that time (see Volentik et al.(c), this volume) suggests that opening of several eruptive vents along different active tectonic trends could occur again in the future and have to be seriously considered. Actually, if such an event were to happen again in the future on Nisyros, it could occur anywhere along the fracture network affecting the island.

The hazard map presented in Fig. 11.1-C takes into account:

(1) Spatter cone formation along tectonic trends, with an average dispersion radius of 25 m.

(2) Scoriae cone formation, with an average strombolian fallout dispersion radius of 300 m.

(3) Phreatomagmatic surges related to tuff cones, with an average surge coverage radius of 1.5 km. We considered that magma/water interaction can occur only near the sea or in the caldera floor; in the second case, magma would interact with hydrothermal fluids and previous figures should be considered as minimum estimates (see Marini & Fiebig, this volume for further details on the hydrothermal system).

Although the whole island could be affected by this strombolian eruptive scenario, the building of more than one or two cones at a single time is unlikely. The effect of strombolian eruptions would be limited enough not to affect villages, unless they were to occur within or close to the villages themselves. Mandraki, Emboriò and Nikià could all potentially be the target of such an event, while Palì would be fairly safe.

In case of a surtseyan eruption, however, areas close to the sea or near to the hydrothermal system (which includes all four villages) could be endangered by phreatomagmatic base surges. The edification of a cone in the middle of the Lakkì plain would, however, have limited effects, due to shielding induced by the caldera cliffs. Phreatomagmatic surges would have a devastating impact on structures and life forms, as detailed by Valentine (1998).

11.5. Pyroclastic density currents and lahars

In addition to debris flow deposits, the majority of pyroclastic flow deposits on Nisyros demonstrated to be gravity-controlled (Volentik et al.(b), this volume). Therefore in Fig. 11.1-D the main valleys on the outer slopes of the stratovolcano were recognised as the hazardous sites in case of gravity-controlled flows would occur. In the case of a huge explosive volcanic eruption, assuming the eruptive vent to be located within the caldera depression, pyroclastic flows and secondary debris flows are expected to outpour from the caldera flowing along the main valleys and possibly to produce inward moving backflows, as schematically shown in the map of Fig. 11.1-D.

Diluted density currents are more energetic than gravity-controlled flows and are expected to mantle the pre-existing topography, as is the case of the lag breccia deposits of the Lower Pumices (**lp$_d$**). To maintain the map of Fig. 11.1-D to a reasonably simple level this kind of event was not taken into account.

In any case, it is obvious that the evacuation of the island would be the only action to be undertaken upon occurrence of a huge explosive volcanic eruption.

11.6. Sector collapse and landslides

The occurrence of a catastrophic sector collapse in the recent past of the volcano's history suggests that this type of event could occur again in the future and related hazards have to be taken in serious consideration. The main hazards linked to the emplacement of a debris avalanche are:

(i) the destruction brought about by the debris avalanche itself;

(ii) the possible triggering of a magmatic eruption owing to sudden pressure release on the volcanic system;

(iii) the production of tsunamis if the debris avalanche enter the sea.

At Nisyros, the flank collapse of Vunàri could have been triggered by an ongoing cryptodome or dome formation and/or multiple faulting affecting a pre-existing dome of steep morphology, in the area now occupied by the collapse. The matrix fraction necessary for its formation (Ui et al., 2000) may be easily provided by argillic hydrothermal alteration proceeding along faults and other water circulation pathways (see Principe & Marini, this volume).

Based on these considerations, the potential areas at risk are those dominated by steep topographic highs (lava flows and domes), underlain by unstable tephra units (Vidal & Merle, 2000) and affected by active fault systems. Major sector collapse endanger several areas of the island (Fig. 11.1-E), in particular the zones of Mandraki, Palì and Emboriò that formed by the superposition of deposits with different mechanic properties.

In addition, the occurrence of tsunamis after such an event is highly probable and is expected to affect the nearby islands (Kos, Tilos and Rhodes) as well as the Turkish coast East of Nisyros (Datça Peninsula).

Finally, the presence of active fault zones makes the rocks more fragile and unstable, especially in association with steep topographies. In the case of seismic activity, which is recurrent on Nisyros, landslides could occur all around the caldera wall, and along the cliffs of the north-eastern coast of Nisyros. They represent the most direct hazard at present, in particular for the two villages located exactly on the caldera rim, i.e., Emboriò and Nikià. Similarly, the western part of the harbourtown of Mandraki could be affected by landslides or rock fall from the pillow lava cliffs, i.e., along the coast and the hill of the Aghia Spiliani Monastery (Kazilis & Zaccas 1988).

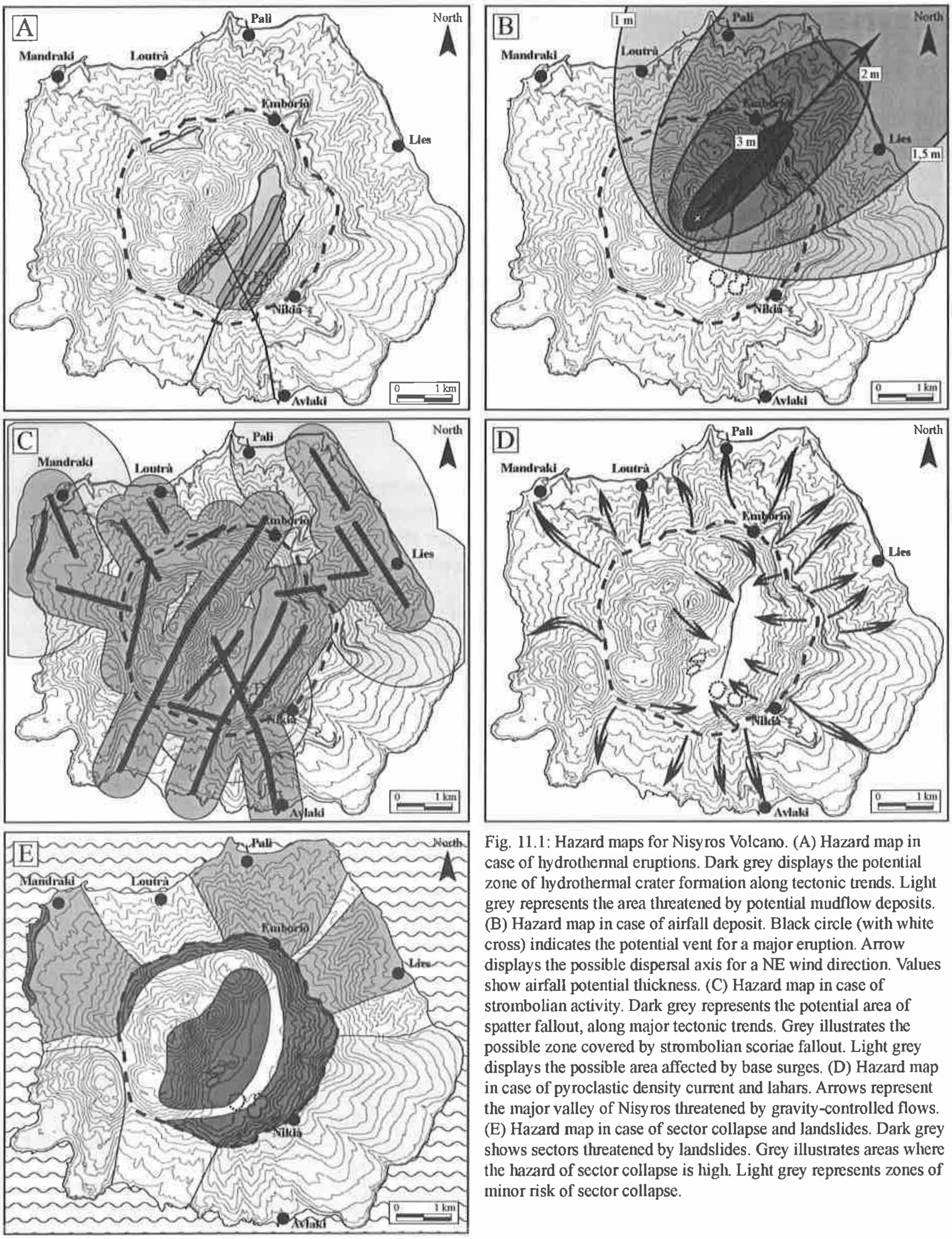

Fig. 11.1: Hazard maps for Nisyros Volcano. (A) Hazard map in case of hydrothermal eruptions. Dark grey displays the potential zone of hydrothermal crater formation along tectonic trends. Light grey represents the area threatened by potential mudflow deposits. (B) Hazard map in case of airfall deposit. Black circle (with white cross) indicates the potential vent for a major eruption. Arrow displays the possible dispersal axis for a NE wind direction. Values show airfall potential thickness. (C) Hazard map in case of strombolian activity. Dark grey represents the potential area of spatter fallout, along major tectonic trends. Grey illustrates the possible zone covered by strombolian scoriae fallout. Light grey displays the possible area affected by base surges. (D) Hazard map in case of pyroclastic density current and lahars. Arrows represent the major valley of Nisyros threatened by gravity-controlled flows. (E) Hazard map in case of sector collapse and landslides. Dark grey shows sectors threatened by landslides. Grey illustrates areas where the hazard of sector collapse is high. Light grey represents zones of minor risk of sector collapse.

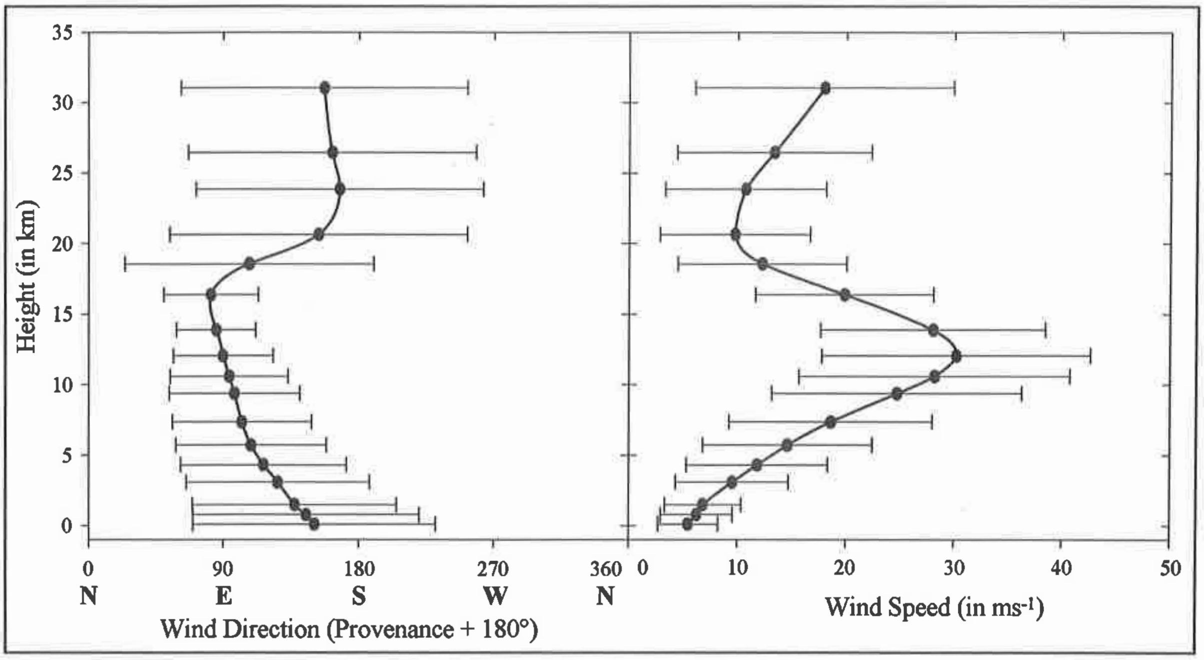

Fig. 11.2: Wind profile for the closest station of wind data acquisition, located at: 35°00'N; 27°50'E. Data represent the mean of the wind directions and wind velocities from January 1st, 2000 to December 31st, 2004, with standard deviation. Data from NOAA: http://www.cdc.noaa.gov/cdc/data.ncep.reanalysis.html.

12. References

Aagaard P., Helgeson H. C. (1982) Thermodynamic and kinetic constraints on reaction rates among minerals and aqueous solutions. I. Theoretical considerations. *Am. J. Sci.*, **282**, 237-285.

Allen S.R., McPhie J. (2000) Water-settling and resedimentation of submarine rhyolitic pumice at Yali, eastern Aegean, Greece. *J. Volcanol. Geotherm. Res.*, **95**, 285-307.

Allen S.R., Cas R.A.F. (2001) Transport of pyroclastic flows across the sea during the explosive, rhyolitic eruption of the Kos Plateau Tuff, Greece. *Bull. Volcanol.*, **62**, 441-456.

Apostolopoulos G., Louis I., Lagios E. (1997) Case history. The self-potential method in the geothermal exploration of Greece. *Geophysics*, **62**, 1715-1723.

Appelo C.A.J., Postma D. (1996) *Geochemistry, groundwaters and pollution*. A.A. Balkema. Rotterdam.

Arnórsson S. (1987) Gas chemistry of the Krísuvík geothermal field, Iceland, with special reference to evaluation of steam condensation in upflow zones. *Jökull*, **37**, 32-47.

Arrighi S., Principe C., Rosi M. (2001) Violent strombolian and subplinian eruptions at Vesuvius during post-1631 activity. *Bull. Volcanol.*, **63**, 126-150.

Aubert M., Lima E. (1986) Hydrothermal activity detected by self-potential measurements at the N-S volcanic axis between the volcanoes of "Nevado de Colima" and "Volcan de Fuego de Colima", Mexico. *Geofis. Int.* **25**, 575-586.

Bachmann O., Dungan M. A. (2002) Temperature-induced aluminium zoning in hornblendes of the Fish Canyon magma, Colorado. *Am. Mineral.*, **87**, 1062-1076.

Barberi F., Bertagnini A., Landi P., Principe C. (1992) A review on phreatic eruptions and their precursors. *J. Volcanol. Geotherm. Res.*, **52**, 231-246.

Barberi F., Navarro J. M., Rosi M., Santacroce R., Sbrana A. (1988) Explosive interaction of magma with ground water: insights from xenoliths and geothermal drillings. *Rend.Soc. It. Min. Petr.*, **43**, 901-926.

Baubron J.C., Allard P., Sabroux J.C., Tedesco D., Toutain J.P. (1991) Soil gas emanation as precursory indicators of volcanic eruptions. *J. Geol. Soc.*, **148**, 571-576.

Berner E.K., Berner R.A. (1996) *Global environment: water, air, and geochemical cycles*. Prentice Hall. Upper Saddle River.

Berner R.A., Lasaga A.C., Garrels R.M.(1983) The carbonate-silicate geochemical cycle and its effect on atmospheric carbon dioxide over the past 100 million years. *Am. J. Sci.*, **283**, 641-683.

Bertrami R., Cioni R., Corazza E., D'Amore F., Marini L. (1985). Carbon monoxide in geothermal gases. Reservoir temperature calculations at Larderello (Italy). *Geothermal Resources Council Transactions*, **9-I**, 299-303.

Bohla M., Keller J. (1987) Petrology of plinian eruptions of Nisyros volcano, Hellenic Arc. *Terra Cognita* **7**, 171.

Bottinga Y. (1969) Calculated fractionation factors for carbon and hydrogen isotope exchange in the system calcite – carbon dioxide – graphite – methane – hydrogen – water vapor. *Geochim. Cosmochim. Acta*, **33**, 49-64.

Brombach T. (2000) Fluid geochemistry of hydrothermal systems in volcanic island arcs: Guadeloupe (Lesser Antilles) and Nisyros (Greece). PhD. Thesis, University of Lausanne.

Brombach T., Hunziker J.C., Chiodini G., Cardellini C., Marini L. (2001) Soil diffuse degassing and thermal energy fluxes from the southern Lakki plain, Nisyros (Greece). *Geophys. Res. Letters*, **28**, 69-72.

Brombach T., Caliro S., Chiodini G., Fiebig J., Hunziker J.C., Raco B. (2003) Geochemical evidence for mixing of magmatic fluids with seawater, Nisyros hydrothermal system, Greece. *Bull. Volcanol.*, **65**, 505-516.

Büttner A. (2004) *Geochronology and multi-isotope geochemistry of three Quaternary volcanoes: Nisyros-Yali (Greece), Monte Vico and Monte Vulture (Italy)*. PhD Thesis, University of Bern.

Büttner A., Kleinhannes I. C., Rufer D., Hunziker J. C., Villa I. M. (2005) Magma generation at the easternmost section of the Hellenic arc: Hf, Nd, Pb and Sr isotope geochemistry of Nisyros and Yali volcanoes (Greece). *Lithos*, **83**, 29-46.

Byrdina S., Friedel S., Wassermann J., Zlotnicki J. (2003) Self-potential variations associated with ultra-long-period seismic signals at Merapi volcano. *Geophys. Res. Let.*, **30**, No. 2156.

Caliro S., Chiodini G., Galluzzo D., Granieri D., La Rocca M., Saccorotti G., Ventura G. (2005) Recent activity of Nisyros volcano (Greece) inferred from structural, geochemical and seismological data. *Bull. Volcanol.*, **67**, 358-369.

Cardellini C., Chiodini G., Frondini F. (2003) Application of stochastic simulation to CO_2 flux from soil: Mapping and quantification of gas release. *J. Geophys. Res.*, **108**(B9), 2425.

Carey S., Sigurdsson H. (1989) The intensity of plinian eruptions. *Bull. Volcanol.*, **51**, 28-40.

Cas R.A.F., Wright J.V. (1987) *Volcanic successions: Modern and Ancient: A Geological Approach to Processes, Products and Successions*. Allen & Unwin, London, 528 pp.

Chiodini G., Marini L. (1998) Hydrothermal gas equilibria: The H_2O-H_2-CO_2-CO-CH_4 system. *Geochim. Cosmochimic. Acta*, **62**, 2673-2687.

Chiodini G., Cioni R., Falsaperla S., Montalto A., Guidi M., Marini L. (1992a). Geochemical and seismological investigations at Vulcano (Aeolian Islands) during 1978-1989. *J. Geophy. Res.*, **97**, 11025-11032.

Chiodini G., Cioni R., Guidi M., Marini L., Raco B., Taddeucci G. (1992b) Gas geobarometry in boiling hydrothermal systems: a possible tool to evaluate the hazard of hydrothermal explosions. *Acta Vulcanologica, Marinelli Volume*, **2**, 99-107

Chiodini G., Cioni R., Leonis C., Marini L., Raco B. (1993a). Fluid geochemistry of Nisyros island, Dodecanese, Greece. *J. Volcanol. Geotherm. Res.*, **56**, 95-112.

Chiodini G., Cioni R., Marini L. (1993b). Reactions governing the chemistry of crater fumaroles from Vulcano Island, Italy, and implications for volcanic surveillance. *Appl. Geochem.*, **8**, 357-371.

Chiodini G., Cioni R., Guidi M., Raco B., Marini L. (1998) Soil CO_2 flux measurements in volcanic and geothermal areas. *Appl. Geoch.*, **13**, 543-552.

Chiodini G., Frondini F., Kerrick D.M., Rogie J., Parello F., Peruzzi L., Zanzari A.R. (1999) Quantification of deep CO_2 fluxes from Central Italy. Examples of carbon balance for regional aquifers and of soil diffuse degassing. *Chem. Geol.*, **159**, 205-222.

Chiodini G., Allard P., Caliro S., Parello F. (2000) ^{18}O exchange between steam and carbon dioxide in volcanic and hydrothermal gases: isotopic and genetic implications. *Geochim. Cosmochim. Acta*, **64**, 2479-2488.

Chiodini G., Brombach T., Caliro S., Cardellini C., Marini L., Dietrich V. (2002) Geochemical indicators of possible ongoing volcanic unrest at Nisyros Island (Greece). *Geophys. Res. Letters*, **29**, 6-1/6-4.

Chonia T., Makris J. (2000) Seismic and seismicity observations at the active volcano of Nisyros, East Aegean Sea. European Geophysical Society, 25th General Assembly.

Commissione per la cartografia geologica e geomorfologica del CNR (1992) Carta Geologica d'Italia 1:50'000 - Guida al Rilevamento. *Quaderni del Servizio Geologico Nazionale*, **III**(1), 203 pp.

Cross D. (1963) Soils and geology of some hydrothermal eruptions in the Waiotapu district. *N. Z. J. Geol. Geophys.*, **6**, 70-87.

D'Amore F., Panichi C. (1980) Evaluation of deep temperature of hydrothermal systems by a new gas-geothermometer. *Geochim. Cosmochim. Acta*, **44**, 549-556.

Davis E. (1967) Zur Geologie und Petrologie der Insel Nisyros und Jali (Dodecanes). *Praktika Akad. Athen.* **42**, 235-252.

Dawes G.J.K., Lagios, E. (1991) A magnetotelluric survey of the Nissyros geothermal field (Greece). *Geothermics*, **20**, 225-235.

Day S.J. (1996) Hydrothermal pore fluid pressure and the stability of porous, permeable volcanoes. In: McGuire W.J., Jones A.P., Neuberg J. (Eds.). *Volcano Instability on the Earth and Other Planets*, *Geol. Soc. Sp. Pub.*, **110**, 77-93, London.

De Rita D., Fabbri M., Giordano D., Rodani S., Trigari, A. (2000) L'utilizzo delle Unità Stratigrafiche a Limiti Incomformi in Ambiente vulcanico e vulcanoclastico: proposta di una metodologia di terreno e di organizzazione informatica dei dati. *Boll. Soc. Geol. It.*, **119**, 749-760.

Desio A. (1931) Le Isole Italiane dell'Egeo – Studi geologici e geografici-fisici. *Memorie descrittive della Carta Geologica d'Italia.* R.Ufficio Geologico d'Italia.

Dietrich V.J., Kipfer R., Schwandner F. (1998) Mantle-derived noble gases in the south Aegean volcanic arc: indicators for incipient magmatic activity and deep crustal movements. *Newsl. Eur. Cent. Prev. Forecast. Earthquakes*, **2**, 28-32.

Di Paola G.M. (1974) Volcanology and petrology of Nisyros Island (Dodecanese, Greece). *Bull. Volcanol.*, **38**, 944-987.

Dotsika E. (1992) *Utilisation du geothermometre isotopique sulfate-eau en milieu de haute temperature sous influence marine potentielle: les systemes geothermaux de Grece*. These en Sciences, Université Paris Sud, No 1781.

Dotsika E., Michelot J. L. (1993) Hydrochemistry, isotope contents and origin of geothermal fluids at Nisyros (Dodecanese). *Bull. Geol. Soc. Greece*, **XXVIII**, 293-304 (In Greek, with English abstract).

Druitt T.H. (1985) Vent evolution and lag breccia formation during the Cape Riva eruption of Santorini, Greece. *J. Geol.*, **93**, 439-454.

Druitt T. H., Sparks R. S. J. (1984) On the formation of calderas during ignimbrite eruptions. *Nature*, **310**, 679-681.

Elliott D.C., Sealock L.J. Jr. (1983) Aqueous catalyst systems for the water-gas shift reaction. 1. Comparative catalyst studies. *Ind. Eng. Chem. Prod. Res. Dev.*, **22**, 426-431.

Elliott D.C., Hallen R.T., Sealock L.J. Jr. (1983) Aqueous catalyst systems for the water-gas shift reaction. 2. Mechanism of basic catalysis. *Ind. Eng. Chem. Prod. Res. Dev.*, **22**, 431-435.

Elliott D.C., Sealock L.J. Jr., R.S. Butner (1986) Aqueous catalyst systems for the water-gas shift reaction. 3. Continuous gas processing results. *Ind. Eng. Chem. Prod. Res. Dev.*, **25**, 541-549.

Ellis A.J. and Mahon W.A.J. (1977) *Chemistry and Geothermal Systems*, Academic Press, 392 pp.

Faure G. (1986) *Principles of Isotope Geology*, 2^{nd} ed. Wiley, New York, 589 pp.

Fiebig J., Chiodini G., Caliro S., Rizzo A., Spangenberg J., Hunziker J.C. (2004) Chemical and isotopic equilibrium between CO_2 and CH_4 in fumarolic gas discharges: Generation of CH_4 in arc magmatic-hydrothermal systems. *Geochim. Cosmochim. Acta*, **68**, 2321-2334.

Fisher R.V., Schmincke, H.-U. (1984) *Pyroclastic rocks*. Springer, Berlin.

Fournier R.O. (1979) Geochemical and hydrological considerations and the use of enthalpy-chloride diagrams in the prediction of underground conditions in hot-spring systems. *J. Volcanol. Geotherm. Res.*, **5**, 1-16.

Francalanci L., Varekamp J.C., Vougioukalakis G., Defant M.J., Innocenti F., Manetti P. (1995) Crystal retention, fractionation and crustal assimilation in a convecting magma chamber, Nisyros Volcano, Greece. *Bull. Volcanol.*, **56**, 601-620.

Fraser D. C. (1969) Contouring of VLF-EM data. *Geophysics*, **34**, 958-967.

Fytikas M., Marinelli G. (1976) *Geology and geothermics of the Island of Milos (Greece)*. International Congress on Thermal Waters, Geothermal Energy and Volcanism in the Mediterranean Area, Athens, 58 pp.

Gansecki C. (1991) *Petrology of the domes and inclusions of Nisyros volcano, Dodecanese islands, Greece*. BA Thesis, Wesleyan University, Middletown, CT, 97 pp.

Geotermica Italiana (1983) *Nisyros 1 geothermal well*. Unpublished PPC-EEC report, pp106.

Geotermica Italiana (1984) *Nisyros 2 geothermal well*. Unpublished PPC-EEC report, pp44.

Gex P. (1992) Etude géophysique des environs du cratère de Vulcano, Italie. *Bull. Soc. Vaud. Sc. Nat.*, **319**, 157-172.

Giggenbach W.F. (1980) Geothermal gas equilibria. *Geochim. Cosmochim. Acta*, **44**, 2021-2032.

Giggenbach W.F. (1987) Redox processes governing the chemistry of fumarolic gas discharges from White Island, New Zealand. *Appl. Geochem.*, **2**, 143-161

Giggenbach W.F. (1988) Geothermal solute equilibria. Derivation of Na-K-Mg-Ca geoindicators. *Geochim. Cosmochim. Acta* **52**, 2749-2765.

Giggenbach W.F. (1991) Chemical techniques in geothermal exploration. In *Application of Geochemistry in Geothermal Reservoir Development*. (F. D'Amore, co-ordinator), UNITAR, 119-144.

Giggenbach W.F. (1996) Chemical composition of volcanic gases. In: *Monitoring and Mitigation of Volcano Hazards* (R. Scarpa and R.I. Tilling, Eds.) Springer, 221-256

Giggenbach W.F. (1997) Relative importance of thermodynamic and kinetic processes in governing the chemical and isotopic composition of carbon gases in high-heatflow sedimentary basins. *Geochim. Cosmochim. Acta* **61**, 3763-3785.

Giggenbach W.F., Stewart M.K. (1982) Processes controlling the isotopic composition of steam and water discharges from steam vents and steam-heated pools in geothermal areas. *Geothermics* **11**, 71-80.

Giggenbach W.F., Sano Y., Wakita H. (1993) Isotopic composition of helium, and CO_2 and CH_4 contents in gases produced along the New Zealand part of a convergent plate boundary. *Geochim. Cosmochim Acta*, **57**, 3427-3455.

Giggenbach W.F., Sheppard D.S., Robinson B.W., Stewart M.K., Lyon G.L. (1994) Geochemical structure and position of the Waiotapu geothermal field, New Zealand. *Geothermics* **23**, 599-644.

Gorceix M. H. (1873) Sur l'état du volcan de Nisyros au mois de mars 1873. *Compte Rendu Séances Acad. Sci. Paris* **LXXVII**, 597-601.

Gottsmann J., Wooller L. K., Rymer H. (2004) The restless Nisyros caldera, Greece: Probing sub-surface dynamics via a new GPS and Gravity Network. Eur. Geosc. Un. Meet. Nice.

Hammarstrom J. M., Zen, E-a (1986) Aluminum in hornblende: An empirical igneous geobarometer. *Am. Mineral.*, **71**, 1297-1313.

Hanus V., Vanek J. (1993) Seismically active fracrure zones related to the eastern segment of the Hellenic subduction. *J. Geodynamics*, **17**, 39-56.

Hardiman J.C. (1999) Deep sea tephra from Nisyros Island, eastern Aegean Sea, Greece. In: C.R. Firth and W.J. McGuire (Editors), *Volcanoes in the Quaternary*. Geological Society Special Publications, London.

Hedenquist J.W., Henley R.W. (1985) Hydrothermal eruptions in the Waiotapu geothermal system, New Zealand: their origin, associated breccias, and relation to precious metal mineralization. *Econ. Geol.*, **80**, 1640-1668.

Helgeson H.C. (1968) Evaluation of irreversible reactions in geochemical processes involving minerals and aqueous solutions: I. Thermodynamic relations. *Geochim. Cosmochim. Acta*, **32**, 853-877.

Helgeson H.C. (1979) Mass transfer among minerals and hydrothermal solutions. In: Barnes, H. L. (Ed.). *Geochemistry of hydrothermal ore deposits*, Wiley, New York, pp. 568-610.

Helgeson H.C., Delany J.M., Nesbitt H.W. and Bird D.K. (1978) Summary and critique of the thermodynamic properties of rock-forming minerals. *Am. J. Sci.*, **278A**, 229 p.

Helgeson H. C., Murphy W. M., Aagaard P. (1984) Thermodynamic and kinetic constraints on reaction rates among minerals and aqueous solutions. II. Rate constants, effective surface area, and the hydrolysis of feldspar. *Geochim. Cosmochim. Acta*, **48**, 2405-2432.

Henley, R.W. and Ellis, A.J. (1983) Geothermal systems, ancient and modern: a geochemical review. *Earth Science Review* **19**, 1-50.

Henley R.W., Truesdell A.H., Barton P.B. Jr, Whitney J.A. (1984) Fluid-mineral equilibria in hydrothermal systems. *Reviews in Economic Geology* **1**, 267 pp.

Holgate R.H., Webley P.A., Tester J.W. (1992) Carbon monoxide oxidation in supercritical water : the effects of heat transfer and the water-gas shift reaction on observed kinetics. *Energy & Fuels*, **6**, 586-597.

Hollister L. S., Grissom G. C., Peters E. K., Stowell H. H., Sisson V. B. (1987) Confirmation of the empirical correlation of Al in hornblende with pressure of solidification of calc-alkaline plutons. *Am. Mineral.*, **72**, 231-239.

Holloway J.R., Blank J.G. (1994) Application of experimental results to C-O-H species in natural melts. In "Volatiles in magmas" (M.R. Carroll and J.R. Holloway, Editors), *Reviews in Mineralogy*, **30**, 187-230.

Horita J. (2001) Carbon isotope exchange in the system CO_2-CH_4 at elevated temperatures. *Geochim. Cosmochim Acta*, **65**, 1907-1919.

Horita J., Wesolowski D.J. (1994) Liquid-vapor fractionation of oxygen and hydrogen isotopes of water from the freezing to the critical temperature. *Geochim. Cosmochim. Acta* **58**, 3425-3437.

Innocenti S., Francalanci L., Vougioukalakis G.E. (2002) Changes in the Eruptive Activity of Nisyros, Dodecanese, Greece: Insights from Panagia Kyra' Pyroclastic Series. Am. Geophys. Union Chapman Conf. on Volcanism and the Earth's Atmosphere, The Thera Foundation Conference Center, Santorini, Greece.

Isaaks E.H., Srivastava R.M. (1989) *An Introduction to applied geostatistics*. Oxford University Press, 561 pp.

Istituto Idrografico della Marina (1939) Nisiro e isole minori (Mediterraneo – Isole dell'Egeo). Dai rilievi effettuati nel 1933 dalle navi Magnaghi (Comandante il Capitano di Fregata M.Bonetti) e Milazzo (Comandante il Capitano di Corvetta M.Grassi) e da quelli dei Tenenti di Vascello G. Ghiglieri e G. Andreani. Scala 1:30.000.

Johnson J.W., Oelkers E.H., Helgeson H.C. (1992) SUPCRT 92: A software package for calculating the standard molal thermodynamic properties of minerals, gases, aqueous species, and reactions from 1 to 5000 bars and 0 to 1000°C. *Computers & Geosciences* **18**, 899-947.

Johnson M. C., Rutherford M. J. (1989) Experimental calibration of the aluminum-in-hornblende geobarometer with application to Long Valley caldera (California) volcanic rocks. *Geology*, **17**, 837-841.

Kavouridis T., Kuris D., Leonis C., Liberopoulou V., Leontiadis J., Panichi C., La Ruffa G., Caprai A. (1999) Isotope and chemical studies for a geothermal assessment of the island of Nisyros (Greece). *Geothermics*, **28**, 219-239.

Kazilis N.G., Zaccas M. (1988) The engineering geology of Nisyros Castle and its impact in stabilizing the cliffs of Panagia Spiliani Monastery, Nisyros Island, Greece. In: M. Koukis (Ed.), *Engineering Geology of Ancient Works, Monuments and Historical Sites.* Balkema, Rotterdam, 101-104.

Keller J. (1971) The major volcanic events in recent eastern mediterranean volcanism and their bearing on the problem of Santorini ash layers. *Int. Sci. Congr. Volcano of Thera,* **1**, 152-169.

Keller J. (1982) Mediterranean island arcs. In: R.S. Thorpe (ed), *Andesites*. Wiley, New York, 307-325.

Keller J., Rehren T., Stadlbauer E. (1990) Explosive volcanism in the Hellenic Arc: a summary and review. In: D.A. Hardy, J. Keller, V.P. Galanopoulos, N.C. Flemming and T.H. Druitt (Eds), *Thera and the Aegean World.* Proc. 3d Int. Congr. The Thera Foundation, London, 13-26.

Kerrick D.M., McKibben M.A., Seward T.M., Caldeira K. (1995) Convective hydrothermal CO_2 emission from high heat flow regions. *Chem Geol.*, **121**, 285-293.

Koutroupis N. (1983) Geothermal exploration in the Island of Nisyros. Nisyros 1 geothermal well. In: A.S. Strub and P. Ungemach (Eds.), *Proceedings of the Third International Seminar on the Results of EC Geothermal Energy Research.* Reidel, Dordrecht, 440-446.

Lagios E., Apostolopoulos G. (1995) Integrated geophysical study of the geothermal system in the southern part of Nisyros Island, Greece. *J. Appl. Geophys.*, **34**, 55-61.

Lagios E., Chailas S., Giannopoulos J., Sotiropoulos P. (1998) Surveillance of Nisyros volcano. Establishment and remeasurement of Radon and GPS networks. Proc. 8th Int. Cong. Geol. Soc. Greece, Patras, 27-29 May, (Athens: ERE) **35**, 215-217.

Lagios E., Dietrich V., Stavrakakis G., Parcharides I., Sakkas V., Vassilopoulou S. (2001) Will Nisyros Volcano (GR) become active? Seismic unrest and crustal deformation. *European Geologist*, **12**, 44-50.

Langmuir C. H., Vocke R. D. Jr., Hanson G. N., Hart S. R. (1978) A general mixing equation with applications to Icelandic basalts. *Earth Planet. Sci. Letters*, **37**, 380-392.

La Ruffa G., Panichi C., Kavouridis T., Liberopoulou V., Leontiadis J., Caprai A. (1999) Isotope and chemical assessment of geothermal potential of Kos Island, Greece. *Geothermics*, **28**, 205-217

Lemmon E.W., McLinden M.O., Friend D.G. (2003) Thermophysical Properties of Fluid Systems. In: *NIST Chemistry WebBook, NIST Standard Reference Database Number 69*, Eds. P.J. Linstrom and W.G. Mallard, National Institute of Standards and Technology, Gaithersburg MD (http://webbook.nist.gov/).

Lichtner P.C. (1996) Continuum formulation of multicomponent-multiphase reactive transport. In: Lichtner, P.C., Steefel, C.I., Oelkers, E.H. (Eds.). *Reactive transport in porous media, Reviews in Mineralogy*, **34**, 1-81.

Lichtner P.C. (1998) Modeling reactive flow and transport in natural systems. In: Marini, L., Ottonello, G. (Eds.). *Proceedings of the Rome Seminar on Environmental Geochemistry*, Pacini, Pisa, pp. 5-72.

Limburg, E.M., Varekamp J.C. (1991) Young pumice deposits on Nisyros, Greece. *Bull. Volcanol.*, **54**, 68-77.

Lloyd E.F. (1959) The hot springs and hydrothermal eruptions of Waiotapu. *N. Z. J. Geol. Geophys.*, **2**, 141-176.

Lodise L. (1987) *Petrology and geochemistry of Nisyros volcano (Dodecanese, Greece).* MS Thesis, Wesleyan University, Mddletown, CT, USA, 245 pp.

Makris J., Stobbe C. (1984) Properties and state of the crust and upper mantle of the eastern Mediterranean Sea deduced from geophysical data. *Marine Geology*, **55**, 345-361.

Marinelli G. (1978) Le problème de la perméabilité des roches d'origine volcanique dans la recherche d'un champ géothermique. Implications de l'Hydrogéologie dans les autres Sciences de la Terre (I.H.E.S. Symposium), Montpellier (France), 11-16 Septembre 1978. *Mémoire hors série CERGH-USTL Montpellier*, 397-404.

Marinelli G., Marini L., Merla A., Sini R., Ungemach P. (1983). Geothermal exploration in the island of Nisyros, Dodecanese, Greece. In: A.S. Strub and P. Ungemach (Eds.), *Proceedings of the Third International Seminar on the Results of EC Geothermal Energy Research.* Reidel, Dordrecht, 203-205.

Marini L., Principe C., Chiodini G., Cioni R., Fytikas M., Marinelli G. (1993). Hydrothermal eruptions of Nisyros (Dodecanese, Greece). Past events and present hazard. *J. Volcanol. Geotherm. Res.*, **56**, 71-94.

Marini L., Chiappini V., Cioni R., Cortecci G., Dinelli E., Principe C., Ferrara G. (1998). Effect of degassing on sulfur contents and $\delta^{34}S$ values in Somma-Vesuvius magmas. *Bull. Volcanol.*, **60**, 187-194.

Marini L., Ottonello G., Canepa M., Cipolli F. (2000a). Water-rock interaction in the Bisagno Valley (Genoa, Italy): application of an inverse approach to model spring water chemistry. *Geochim. Cosmochim. Acta*, 64, 2617-2635.

Marini L., Bonaria V., Guidi M., Hunziker J.C., Ottonello G., Vetuschi Zuccolini M. (2000b) Fluid geochemistry of the Acqui Terme-Visone geothermal area (Piemonte, Italy). *Appl. Geochem.* **15**, 917-935.

Marini L, Gambardella B., Principe C., Arias A., Brombach T., Hunziker J.C. (2002) Characterization of magmatic sulfur in the Aegean island arc by means of the $\delta^{34}S$ values of fumarolic gases, elemental sulfur, and hydrothermal gypsum of Nisyros and Milos islands. *Earth Planet. Sci. Letters*, **200**, 15-31.

Martelli A. (1917) Il gruppo eruttivo di Nisiro nel mare Egeo. *Società dei XL*, ser. 3, **XX**, 79-165.

Massenet F., Van Ngoc P. H. (1985) Mapping and surveillance of active fissure zones on a volcano by the self-potential method, Etna, Sicily. *J. Volcanol. Geotherm. Res.*, **24**, 315-338.

Matheron G. (1965) *Les variables régionalisées et leur estimation.* Masson, Paris, 306 pp.

Meijer P.Th., Wortel M.J.R. (1997) Present-day dynamics of the Aegean region: A model analysis of the horizontal pattern of stress and deformation. *Tectonics*, **16**, 879-895.

Michel S., Zlotnicki J. (1998) Self-potential and magnetic surveying of La Fournaise volcano (Reunion Island): Correlations with faulting, fluid circulation, and eruption. *J. Geophys. Res.*, **103 (B8)**, 17845-17857.

Minissale A., Duchi V., Kolios N., Nocenti M., Verrucchi C. (1997) Chemical patterns of thermal aquifers in the volcanic islands of the Aegean arc, Greece. *Geothermics*, **26**, 501-518.

Nakamura K., Uyeda S. (1980) Stress gradient in arc-back arc regions and plate subduction. *J. Geophys. Res.*, **85**, 6419-6428.

Nimis P. (1996) Structure simulation of experimental C2/ c pyroxenes; a revised geobarometer for basic magmas. *Terra Abstracts*, **8**, 48.

Nimis P. (1999) Clinopyroxene geobarometer of magmatic rocks. Part 2. Structural geobarometers for basic to acid, tholeiitic and mildly alkaline magmatic systems. *Contrib. Mineral. Petrol.*, **135**, 62-74.

Nimis P., Ulmer P. (1998) Clinopyroxene geobarometry of magmatic rocks; Part 1. An expanded structural geobarometer for anhydrous and hydrous, basic and ultrabasic systems. *Contrib. Mineral. Petrol.*, **133**, 122-135.

Oelkers E.H., Gislason S.R. (2001) The mechanism, rates and consequences of basaltic glass dissolution: I. An experimental study of the dissolution rates of basaltic glass as a function of aqueous Al, Si, and oxalic acid concentration at 25°C and pH = 3 and 11. *Geochim. Cosmochim. Acta*, **58**, 2011-2024.

Oelkers E. H. , Schott J., Devidal J.-L. (1994) The effect of aluminum, pH, and chemical affinity on the rates of aluminosilicate dissolution reactions. *Geochim. Cosmochim. Acta*, **58**, 2011-2024.

Ohmoto H., Goldhaber M.B. (1997) Sulfur and carbon isotopes. In: Barnes H.L. (Editor) *Geochemistry of hydrothermal ore deposits*, Wiley, New York, pp 517-612.

Orkustofnun-Virkir (1986) *Nisyros geothermal development. Nisyros well NIS-2. Production characteristics and fluid composition.* Unpublished PPC report, 97 pp.

Ottonello G. (2001) The inverse modeling of water-rock interaction. *Proceedings of the X Water-Rock Interaction Conference.* **1**,14.

Ozima M., Podosek F.A. (2002) *Noble Gas Geochemistry.* Cambridge University Press, Cambridge, 286 pp.

Palandri J. L., Kharaka Y. K. (2004) *A compilation of rate parameters of water-mineral interaction kinetics for application to geochemical modeling.* U. S. Geological Survey, Open File Report 2004-1068.

Panichi C., La Ruffa G. (2001) Stable isotope geochemistry of fumaroles: an insight into volcanic surveillance. *J. Geodynamics*, **32**, 519-542.

Panichi C., La Ruffa G., Kavouridis T., Leontiadis J., Leonis C., Liberopoulou V., Dotsika E. (2000) Geochemical assessment of the thermal fluids emerging along the Aegean volcanic arc (Greece). *Proc. World Geother. Cong., Kyushu – Tohoku*, 1565-1570.

Papadopoulos G.A., Sachpazi M., Panopoulou G., Stavrakakis G. (1998) The volcanoseismic crisis of the 1996-97 in Nisyros, SE Aegean Sea, Greece. *Terra Nova,* **10**,151-154.

Papanikolaou D.J., Lekkas E.L., Sakellariou D. (1991) Geological structure and evolution of the Nisyros Volcano. *Bull. Geol. Soc. Greece*, **XXV**, 405-419. (In Greek, with English abstract).

Papazachos B.C., Panagiotopoulos D.G. (1993) Normal faults associated with volcanic activity and deep rupture zones in the Southern Aegean volcanic arc. *Bull. Geol. Soc. Greece*, **28**, 243-252.

Papazachos C.B., Kiratzi A.A., Papazachos B.C. (1993) Rates of active crustal deformation in the Aegean and the surrounding area *Bull. Geol. Soc. Greece*, **28**, 21-32.

Parkinson K.J. (1981) An improved method for measuring soil respiration in the field. *J. Appl. Ecology*, **18**, 221-228.

Pe-Piper G., Piper D.J.W. (2002) *The igneous rocks of Greece, The anatomy of an orogen.* Gebrueder Borntraeger, Stuttgart, 573 pp.

Pe-Piper G., Piper D.J.W. (2005) The South Aegean active volcanic arc: relationships between magmatism and tectonics. In: Fytikas M. and Vougioukalakis G. (Eds.), The South Aegean Volcanic Arc. *Developments in Volcanology*, **7**, Elsevier (in press).

Pe-Piper G., Piper D.J.W., Perissoratis C. (2005) Neotectonics and the Kos Plateau Tuff eruption of 161ka, South Aegean arc. *J. Volcanol. Geotherm. Res.,* **139**, 315-338.

Piper D.J.W., Perissoratis C. (2003) Quaternary neotectonics of the South Aegean arc. *Marine Geology*, **198,** 259-288.

Rapolla A. (1974) Natural electric field survey in the three southern Italy geothermal areas. *Geothermics*, **3**, 118-121.

Reed M.H. (1997) Hydrothermal alteration and its relationship to ore fluid composition. In: Barnes H.L. (Ed.) *Geochemistry of hydrothermal ore deposits*, Wiley, New York, 303-365

Regio Decreto-Legge del 15 ottobre 1925 n.1854: Acquisto della cittadinanza italiana degli abitanti del Dodecaneso in base alle disposizioni del trattato di Losanna (Ouchy) pubblicato sulla G.U. n.258 del del 6 novembre 1925.

Rehren T. (1988) *Geochemie und Petrologie von Nisyros (östliche Agais).* PhD Thesis, Universität Freiburg, 167 pp.

Rodine J.D., Johnson A.M. (1976) The ability of debris, heavily freighted with coarse clastic materials, to flow on gentle slopes. *Sedimentology*, **23**, 213-234.

Ross L. (1843) *Reisen auf den griechischen Inseln der agaischen Meeres.* Bd II, Stuttgard 69 pp.

Sachpazi M., Kontoes C., Voulgaris N., Laigle M., Vougioukalakis G., Sikioti O., Stavrakakis G., Baskoutas J., Kalogeras J., Lepine, J.C. (2002) Seismological and SAR signature of unrest at Nisyros caldera, Greece. *J. Volcanol. Geotherm. Res.*, **116**, 19-33.

Salvador A. (1987) Unconformity-bounded stratigraphic units. *Geol. Soc. Am. Bull.*, **98**, 232-237.

Sano Y., Marty B. (1995) Origin of carbon in fumarolic gas from island arcs. *Chem. Geol.*, **119**, 265-274.

Sano Y., Wakita H. (1985) Geographical distribution of ^{3}He/^{4}He ratios in Japan: Implications for arc tectonics and incipient magmatism. *J. Geophys. Res.*, **90**, 8729-8741.

Sato M., Mooney H.M. (1960) The electrochemical mechanism of sulphide self-potentials. *Geophysics*, **25**, 226-249.

Seward T.M, Kerrick D.M. (1996) Hydrothermal CO_2 emission from Taupo Volcanic Zone, New Zealand. *Earth Planet. Sci. Letters*, **139**, 105-113.

Shimizu A., Sumino H., Nagao K., Notsu K., Mitropoulos P. (2005) Variation in noble gas isotopic composition of gas samples from the Aegean arc, Greece. *J. Volcanol. Geotherm. Res.*, **140**, 321-339.

Siebert L., Glicken H., Ui T. (1987) Volcanic hazards from Bezymianny- and Bandai-type eruptions. *Bull. Volcanol.*, **49**, 453-459.

Simaiakis K. (1992) *Neotectonic study of Nisyros*. 6843, Institute of Geology and Mineral Exploration (IGME), Athens.

Sinclair A.J. (1974) Selection of threshold values in geochemical data using probability graphs. *J. Geochem. Explor.*, **3**, 129-149.

Smith P.E., York D., Chen Y., Evensen N.M. (1996) Single crystal ^{40}Ar-^{39}Ar dating of a Late Quaternary paroxysm on Kos, Greece: Concordance of terrestrial and marine ages. *Geophys. Res. Lett.*, **23**, 3047-3050.

Sparks R.S.J., Self S., Walker G.P.L. (1973) Products of Ignimbrite Eruptions. *Geology*, **1-3**, 115-118.

Sparks R.S.J., Wilson L. (1976) A model for the formation of ignimbrite by gravitational column collapse. *J. Geol. Soc. London*, **132**, 441-451.

Stavrakakis G., Papoulia I. (1998) Seismicity of Nisyros. *Newsl. Eur. Cent. Prev. Forecast. Earthquakes*, **2**, 14-16.

Stiros S.C. (2000) Fault pattern of Nisyros volcano (Aegean Sea, Greece): structural, coastal and archeological evidences. In: McGuire W.C., Griffiths D.R., Hancock P.L., Stewart I.S. (eds) *The archaeology of geological catastrophes*. Geol. Soc., London, Spec. Publ. **171**, 385-397.

St. Seymour K., Vlassopoulos D. (1989) The potential for future explosive volcanism associated with dome growth at Nisyros, Aegean Volcanic Arc, Greece. *J. Volcanol. Geotherm. Res.*, **37**, 351-364.

St. Seymour K., Vlassopoulos D. (1992) Magma mixing at Nisyros volcano, as inferred from incompatible trace-elements systematics. *J. Volcanol. Geotherm. Res.*, **50**, 273-299.

Sykioti O., Kontoes C.C., Elias P., Briole P., Sachpazi M., Paradissis D., Kotsis I. (2003) Ground deformation at Nisyros volcano (Greece) detected by ERS-2 SAR differential interferometry. *Int. J. Remote Sensing*, **24**, 183-188.

Taran, Y.A., Fischer, T.P., Cienfuegos, E., Morales, P. (2002) Geochemistry of hydrothermal fluids from an intraplate ocean island: Everman volcano, Socorro Island, Mexico. *Chem. Geol.* **188**, 51-63.

Tarantola A. (1987) *Inverse model theory: Methods of data fitting and model parameter estimation*, Elsevier, 867 pp.

Teschner M., Vougioukalakis G.E., Faber E., Poggenburg J., Chatzigiannis G. (2003) Real time monitoring of Nisyros fumaroles: The South Aegean Active Volcanic Arc: Present Knowledge and Future Perspectives (SAAVA 2003), Int. Conf., Milos Island, Greece.

Thy P. (1991a) High and low pressure phase equilibria of a mildly alkalic lava from the 1965 Surtsey eruption; experimental results. *Lithos*, **26**, 223-243.

Thy P. (1991b) High and low pressure phase equilibria of a mildly alkalic lava from the 1965 Surtsey eruption; implications for the evolution of mildly alkalic and transitional basalts in the southeastern propagating rift zone of Iceland. *Lithos*, **26**, 253-269.

Traversi C. (1965) Storia della cartografia Italiana delle Isole Egee e dell'Albania. Istituto Geografico Militare, Firenze, 150 pp.

Ui T., Takarada S., Yoshimoto M. (2000) Debris Avalanches. In: Sigurdsson H. (Ed.) *Encyclopedia of Volcanoes*, Academic Press, New York, 617-626.

Valentine G.A. (1998) Damage to structures by pyroclastic flows and surges, inferred from nuclear weapons effects. *J. Volcanol. Geotherm. Res.*, **87**, 117-140.

Vanderkluysen L., Volentik A. (2001) *Etude géophysique et hydrothermalisme du complexe volcanique de Nisyros, Grèce*. Diploma Thesis, Université de Lausanne, 115 pp.

Vanderkluysen L., Volentik A. (2002) *Volcanological and Petrological Evolution of the Volcanic Island of Nisyros, Greece*. Master's (DEA) Thesis, Université de Lausanne, 200 pp.

Vanderkluysen L., Volentik A., Principe C., Hunziker J.C., Hernandez J. (2005) Stratigraphy, evolution, and preliminary hazard assessment of Nisyros volcano, Greece. *J. Volcanol. Geotherm. Res.* (submitted)

Varekamp J.C. (1993) Some remarks on volcanic vent evolution during plinian eruptions. *J. Volcanol. Geotherm. Res.*, **54**, 309-318.

Vidal N., Merle O. (2000) Reactivation of basement faults beneath volcanoes: a new model of flank collapse. *J. Volcanol. Geotherm. Res.*, **99**, 9-26.

Vinci A. (1983) A new ash layer "Nisyros layer" in the Aegean sea sediments. *Boll. Oceanol. Teor. Appl.*, **1**, 341-342.

Vetuschi Zuccolini M. (2002) Interpolation algorithms and stochastic simulations for the evaluation of the total budget of terrestrial CO2 and the visualization of uncertainties. *Proceedings of the Arezzo Seminar on Fluid Geochemistry* (A. Buccianti, L. Marini, G. Ottonello, O. Vaselli, Eds.), August 29th-September 1st, 2000, 160-173.

Volentik A., Vanderkluysen L., Principe C. (2002) Stratigraphy of the caldera walls of Nisyros volcano, Greece. *Eclogae Geol. Helvetiae*, **95**, 223-235.

Vougioukalakis G. E. (1984) *Studio vulcanologico e chimico-petrografico dell'isola di Nisyros (Dodecanneso, Grecia).* Tesi di laurea, Università di Pisa.

Vougioukalakis G.E. (1993) Volcanic stratigraphy and evolution of Nisyros Island. *Bull. Geol. Soc. Greece*, **XXVII**, 239-258 (In Greek, with English abstract).

Vougioukalakis G.E. (1998) *Blue volcanoes: Nisyros.* Regional Council of Mandraki.

Vougioukalakis G.E. (2003) Passive fissuring in long-dormant caldera volcanoes: The Nisyros case, The South Aegean Active Volcanic Arc: Present Knowledge and Future Perspectives (SAAVA 2003), Int. Conf., Milos Island, Greece.

Vrouzi F. (1985) Research and development of geothermal resources in Greece: present status and future prospects. *Geothermics*, **14**, 213-227.

Walker G.P.L. (1985) Origin of coarse lithic breccias near ignimbrite source vents. *J. Volcanol. Geotherm. Res.*, **25**, 157-171.

Walker G.P.L., Wilson L., Bowell E.L.G. (1971) Explosive volcanic eruptions. I. The rate of fall of pyroclasts. *Geophys. Jour. Royal Astronom. Soc.*, **22**: 377-83.

Wieland E., Wehrli B., Stumm W. (1988) The coordination chemistry of weathering: III. A generalization on the dissolution rates of minerals. *Geochim. Cosmochim. Acta*, **52**, 1969-1981.

Williams S. N., Schaefer J.S., Calvache M.L.V., Lopez D. (1992) Global carbon dioxide emission to the atmosphere by volcanoes. *Geochim. Cosmochim. Acta*, **56**, 1765-1770.

Wilson L. (1976) Explosive volcanic eruptions. III. Plinian Eruption Columns. *Geophys. Jour. Royal Astronom. Soc.*, **45**: 543-556.

Wilson L., Sparks R. S. J., Walker G. P. L. (1980) Explosive volcanic eruptions. IV. The control of magma properties and conduit geometry on eruption column behavior. *Geophys. Jour. Royal Astronom. Soc.*, **63**: 117-148.

Wolery, T.J. (1979) *Calculation of chemical equilibrium between aqueous solutions and minerals: the EQ3/6 software package.* Report UCRL-52658, Lawrence Livermore National Laboratory. Livermore.

Wolery T.J. (1992) *EQ3NR, A computer program for geochemical aqueous speciation-solubility calculations: Theoretical manual, user's guide and related documentation (version 7.0).* Report UCRL-MA-110662 PT III. Lawrence Livermore National Laboratory, Livermore.

Wolery T.J., Daveler S.A. (1992) *EQ6, A computer program for reaction path modeling of aqueous geochemical systems: Theoretical manual, user's guide, and related documentation (version 7.0).* Report UCRL-MA-110662 PT IV. Lawrence Livermore National Laboratory, Livermore.

Wyers G. P., Barton M. (1989) Polybaric evolution of calc-alkaline magmas from Nisyros, Southeastern Hellenic Arc, Greece. *J. Petrol.*, **30**, 1-37.

Yoshida K., Wakai C., Matubayasi N., Nakahara M. (2004) NMR spectroscopic evidence for an intermediate of formic acid in the water-gas-shift reaction. *J. Phys. Chem. A*, **108**, 7479-7482.

Zlotnicki J., Le Mouel J. L., Gvishiani A., Agayan S., Mikhailov V., Bogoutdinov S., Kanwar R., Yvetot P. (2005) Automatic fuzzy-logic recognition of anomalous activity on long geophysical records: Application to electric signals associated with the volcanic activity of La Fournaise volcano (Reunion Island). *Earth Planet. Sci. Lett.*, **234**, 261-278.

GEOLOGICAL MAP OF NISYROS VOLCANO (GREECE)

Alain C. M. Volentik(1), Claudia Principe(2), Loÿc Vanderkluysen(1) and Johannes C. Hunziker(1)

(1) Institut de Minéralogie et Géochimie, Université de Lausanne -Switzerland-, (2) Istituto di Geoscienze e Georisorse, CNR di Pisa -Italy-

0 500 m 1 km 2 km

Scale 1 12500

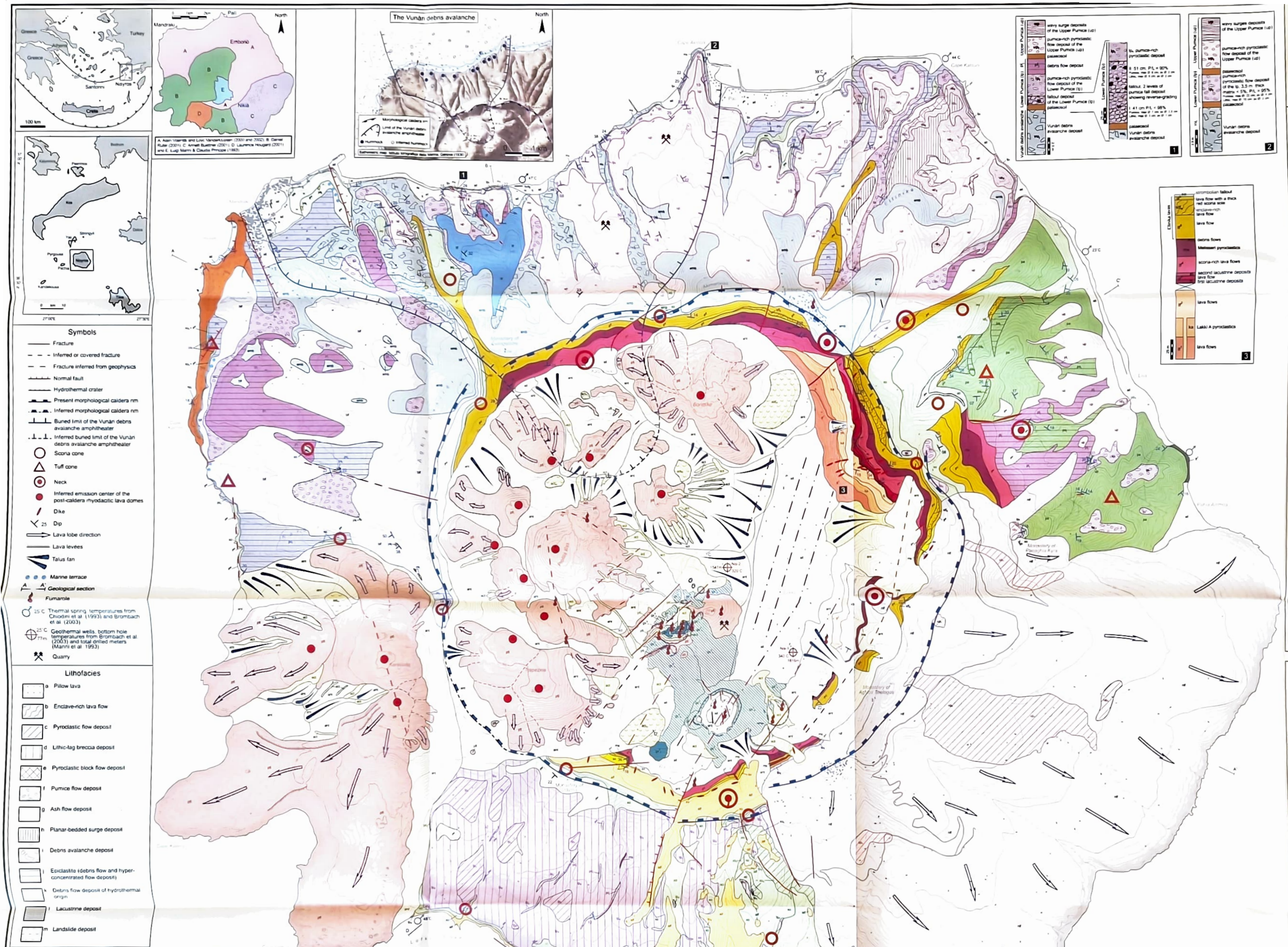

Symbols

- Fracture
- Inferred or covered fracture
- Fracture inferred from geophysics
- Normal fault
- Hydrothermal crater
- Present morphological caldera rim
- Inferred morphological caldera rim
- Buried limit of the Vunàn debris avalanche amphitheater
- Inferred buried limit of the Vunàn debris avalanche amphitheater
- Scoria cone
- Tuff cone
- Neck
- Inferred emission center of the post-caldera rhyodacitic lava domes
- Dike
- 25 Dip
- Lava lobe direction
- Lava levées
- Talus fan
- Marine terrace
- A A' Geological section
- Fumarole
- 25 C Thermal spring, temperatures from Chiodini et al. (1993) and Brombach et al. (2003)
- 25 C 77m Geothermal wells, bottom hole temperatures from Brombach et al. (2003) and total drilled meters (Manni et al. 1993)
- Quarry

Lithofacies

- a Pillow lava
- b Enclave-rich lava flow
- c Pyroclastic flow deposit
- d Lithic-lag breccia deposit
- e Pyroclastic block flow deposit
- f Pumice flow deposit
- g Ash flow deposit
- h Planar-bedded surge deposit
- i Debris avalanche deposit
- j Epiclastite (debris flow and hyper-concentrated flow deposit)
- k Debris flow deposit of hydrothermal origin
- l Lacustrine deposit
- m Landslide deposit

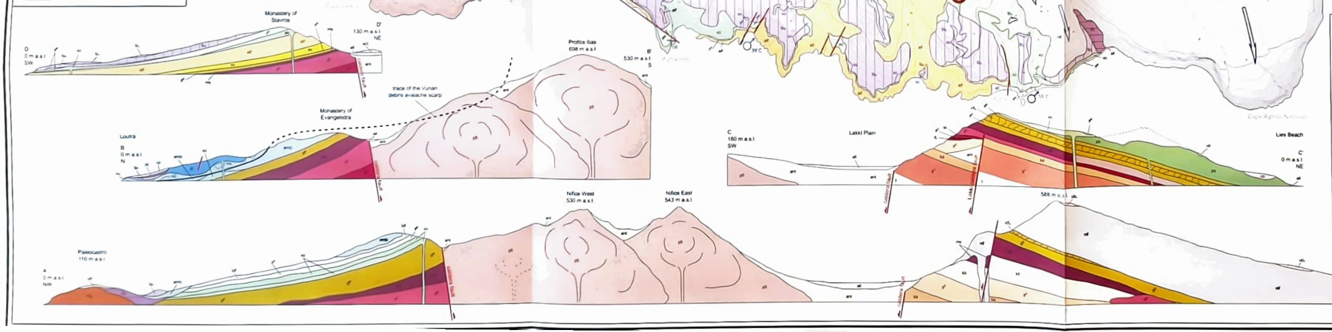

Legend

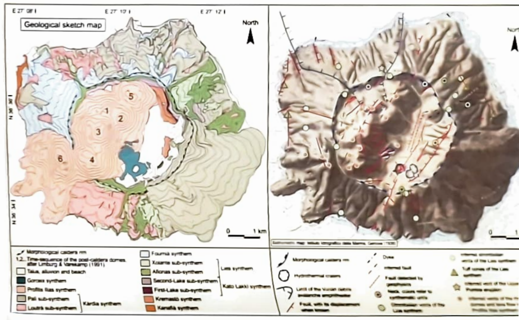

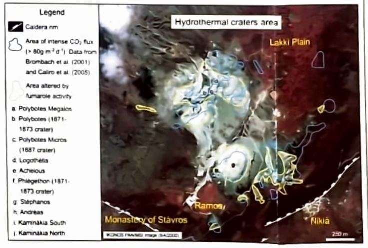

Legend

- Caldera rim
- Area of intense CO_2 flux ($> 80 g m^{-2} d^{-1}$). Data from Brombach et al. (2001) and Caliro et al. (2005)
- Area altered by fumarole activity
- a: Polybotes Megalòs
- b: Polybotes (1871-1873 crater)
- c: Polybotes Micròs (1887 crater)
- d: Logothètis
- e: Achelous
- f: Phlègethon (1871-1873 crater)
- g: Stèphanos
- h: Andrèas
- i: Kaminàkia South
- j: Kaminàkia North

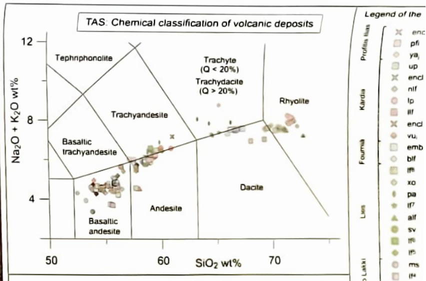

Mapping was carried out onto 1:10,000 topographic maps between 1999 and 2002, with the financial aid of the Immanuel Friedlaender Foundation for Volcanology (Switzerland) and the Swiss Academy for Science. We are grateful to Lorenz Hurni (Institute of Cartography, Swiss Federal Institute of Technology, ETH-Hönggerberg, Zürich, Switzerland) who kindly provided the digital topographic map (equidistance: 10 meters) of Nisyros Volcano.
Digital cartography by Alain C. M. Volentik.
Printed with the financial aid of the Swiss Federal Office of Education and Science, contract number 99.0058/2, and of the IGG-CNR (Pisa, Italy).
Printed in July 2005 by Chabloz Imprimerie, Lausanne, Switzerland.